Summary Report

On the

Preliminary Design

Of the

ITER In-Vessel Coil System

October 2010

T. Bohm[1], A. Brooks[2], L. Bryant[2], J. Chrzanowski[2], E. Daly[3], R. Feder[2], J. Feng[4], M. Gomez[2], I. Griffiths[5], P. Heitzenroeder[2], M. Kalish[2], A. Lipski[2], M. Mardenfeld[2], M. Nakahira[3], C. Neumeyer[2], R. Pillsbury[6], M. Sawan[1], M. Schaffer[7], R. Simmons[2], H. Stone[8], P. Titus[2], I. Zatz[2], R. Walsh[9]

[1]University of Wisconsin

[2] Princeton Plasma Physics Laboratory

[3] ITER International Organization

[4] Massachusetts Institute of Technology[5] Oxford University

[6] Sherbrooke Consulting

[7] General Atomics

[8] Princeton University

[9] National High Magnetic Field Laboratory

Executive Summary

STAC has recommended (PCR-166) study of in-vessel coils (IVCs) to suppress "Edge Localized Modes" (ELMs) and to enhance robustness of "Vertical Stabilization" (VS). A "Conceptual Design Review" (CDR) was conducted in September 2009. An ITER "Task Agreement" (TA) was issued in March 2010 to support the US-DA/PPPL team's development of the preliminary design leading to a "Preliminary Design Review" (PDR). This report presents the preliminary design of the IVCs along with the results of design-basis analysis and R&D.

The in-vessel radiation and temperature environment is severe and conventional electrical insulation materials and processes cannot be used. Mineral insulated conductor technology is the only viable choice but it does not exist in the large cross section (59 mm OD) required for the ELM and VS coils so that R&D programs are necessary to develop conductor fabrication and joining techniques. Thus the use of a "Stainless Steel Jacketed Mineral Insulated Conductor" (SSMIC) is the key feature of the design.

The ELM coils consist of nine toroidal sectors of three (upper, midplane, and lower) 6-turn rectangular "picture frame coils", total of 27 coils mounted to the vacuum vessel and positioned behind the blanket shield modules. The ELM coil structural design is driven by fatigue considerations arising from thermal cycling. To achieve the required fatigue lifetime the ELM SSMIC conductors use a CuCrZr conductor which is cooled by water flowing at 3 m/s. The ELM coils are rated 180V and 15kA per turn, DC to 5Hz. Each ELM coil will be driven by a 12-pulse 4-quadrant thyristor AC/DC converter.

The VS coils consist of one upper and one lower 4-turn solenoidal "ring" coil connected in an anti-series "saddle" arrangement. The coils are mounted to the vacuum vessel and positioned behind the blanket shield modules. The VS SSMIC conductors use Cu which is cooled by water flowing at 3 m/s. The VS coils are rated 2.4kV and 9kA rms per turn based on a 10 second

periodic pulsed waveform with a peak current 60kA peak as required during VDEs. The VS coils can deliver rated amp-turns with one turn out of circuit and bypassed. The VS coils will be driven by two H-bridge chopper power supplies each rated 1.2kV and interleaved in series with the upper and lower coils.

At the time of issue of this report the R&D to produce the SSMIC, perform electrical and mechanical characterization tests, and develop joining techniques is not yet complete. At the conclusion of the TA when all R&D results are completed the results will be incorporated into the design and analysis and a revision of the report will be issued.

TABLE OF CONTENTS

TABLE OF FIGURES

LISTING OF TABLES

1 INTRODUCTION

1.1 BACKGROUND

As part of the Design Review process (2006-2008) which was initiated following the signing of the ITER Agreement and the start of the ITER Project, the Science and Technology Advisory Committee (STAC), which advises the ITER Council, identified a list of physics issues needing attention. Amongst these were two which may be solved by the deployment of "In-Vessel Coils" (IVCs) with strong coupling to the plasma. The first issue concerns "Edge Localized Modes" (ELMs) and the second concerns "Vertical Stabilization" (VS).

An ELM is a disruptive instability occurring in the edge region of a tokamak plasma due to the quasi-periodic relaxation of a transport barrier previously formed during an L --> H transition. ELMs result in impulsive bursts of energy deposition on to the "Plasma Facing Components" (PFCs) causing a reduction in their lifetime through processes including erosion, thermal fatigue, and cracking. Without mitigation the ELM energy deposition on ITER can potentially exceed the allowable level by a factor of 10-20. Various experiments have shown that the application of "Resonant Magnetic Perturbations" (RMPs) produced by in-vessel non-axisymmetric coils can be used to suppress the ELMs.

The elongated plasma of ITER is inherently unstable and requires feedback control to maintain vertical position[1]. Vertical stabilization (VS) is nominally provided by eddy current flow in passive structures which resist plasma motion along with feedback control of the "Poloidal

[1] Humphreys, D.A. et al. "Experimental vertical stability studies for ITER performance and design guidance." 2009 Nucl. Fusion 49 115003

Field" (PF) coils which produce a radial component of field and vertical force on the plasma. However, analysis indicates that the capability of these features, measured by the ability to recover from an initial displacement in vertical position, is not reliable or robust. Considering that loss of vertical plasma position control in ITER will cause large thermal loads on PFCs and can lead to plasma disruption events which produce large electromagnetic loads and other undesirable consequences, then need for a set of in-vessel coils to provide additional vertical stabilization capability has been recommended.

An ITER "Project Change Request" (PCR-166[2]) was initiated in June 2008 to study the implementation of IVCs, consisting of ELM and VS coils, to address the above issues. Since then the design has progressed based on design iterations developed first by the ITER "International Organization" (IO) and then by the US "Domestic Agency" (DA) team led by the Princeton Plasma Physics Lab (PPPL). A "Conceptual Design Review"[3] (CDR) was conducted in September 2009. An ITER "Task Agreement" (TA) was issued[4] in March 2010 to support the US-DA/PPPL team's development of the preliminary design leading to a "Preliminary Design Review" (PDR). Plans for ELM[5] and VS[6] control have been refined by STAC and are consistent with the latest IVC design.

---

[2] "PCR-166: In-Vessel ELM-VS Control Coils", ITER_D_ 2FHA27, June 2008

[3] "ITER In-Vessel Coils CDR Committee Report, ITER In-Vessel Coils, Conceptual Design Review, September 29-30, 2009", ITER_D_2YHXW3, October 2008

[4] "Support for Preliminary Design of the ITER In-Vessel Coils", Task Number C15TD70FU, ITER_D_3CNGUT, March 2010

[5] "ITER Council, STAC 8th Meeting, Plan for ELM Mitigation in ITER", ITER_D_35G2DD, May 2010

[6] "ITER Council, STAC 8th Meeting, Vertical stability in ITER: in-vessel coils and back-up options", ITER_DO33H67F, May 2010

This report presents the preliminary design of the IVCs along with the results of design-basis analysis and R&D. It is intended to serve as a repository of background information in support of the PDR, and is a deliverable item according to the TA.

At the time of writing this report, PCR-166 has not yet been approved. However, the ELM and VS IVCs are mentioned in the ITER "Project Requirements" (PR) document[7] and are identified as comprising Plant Breakdown Structure (PBS) element PBS-15-IV.

1.2 SCOPE

This report focuses primarily on the IVCs whose scope is defined by the "System Requirements Document" (SRD[8]) for PBS15-IV. This includes the ELM and VS coils and their feeders located inside the vacuum vessel, the feed-thrus at the ports, the terminations with the electrical and water supply systems, and local I&C. Note that the DC bus bars, the power supplies, and the cooling water system components are not included in this scope. However they are addressed to a limited extent herein as necessary to characterize the overall ELM and VS system performance.

1.3 REPORT FORMAT

The chapters of this report are ordered in the following sequence:

- Requirements
- Design
- Performance
- R&D
- Fabrication

---

[7] "Project Requirements (PR)", ITER_D_ 27ZRW8

[8] "System Requirements Document (SRD), In-Vessel Coils", ITER_D_2MFYMW

- Installation
- Cost/schedule

The intent is to present the work in same manner that it progresses.

2 REQUIREMENTS

2.1 PHYSICAL ENVELOPE

As shown in Figure 2-1 the Vertical Stabilization and ELM coils are required to fit tightly within the space envelope defined by the Vacuum Vessel and Blanket Shield Modules.

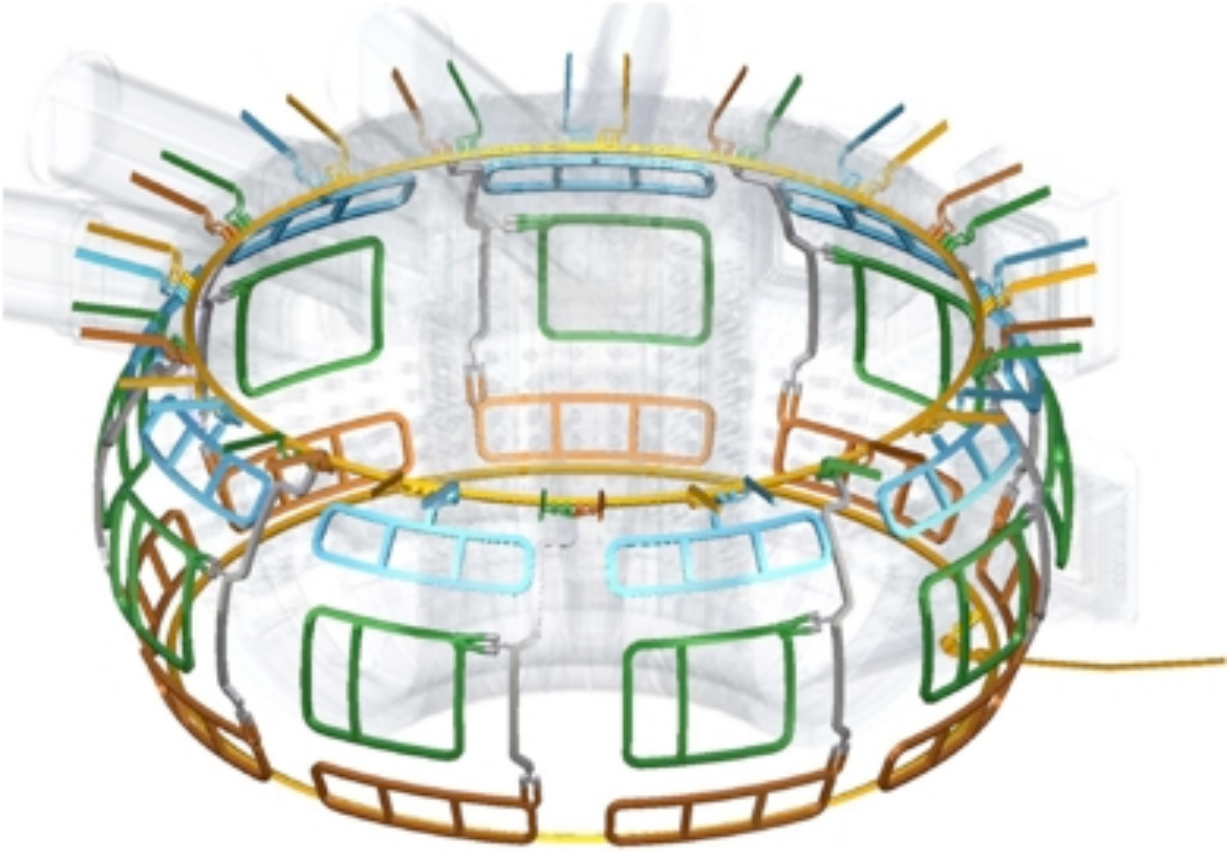

Figure 2-1 ITER In-Vessel Coil System

Coolant supply and return piping as well as electrical feeders and additional cabling must also be integrated into the available space (Figure 2-2).

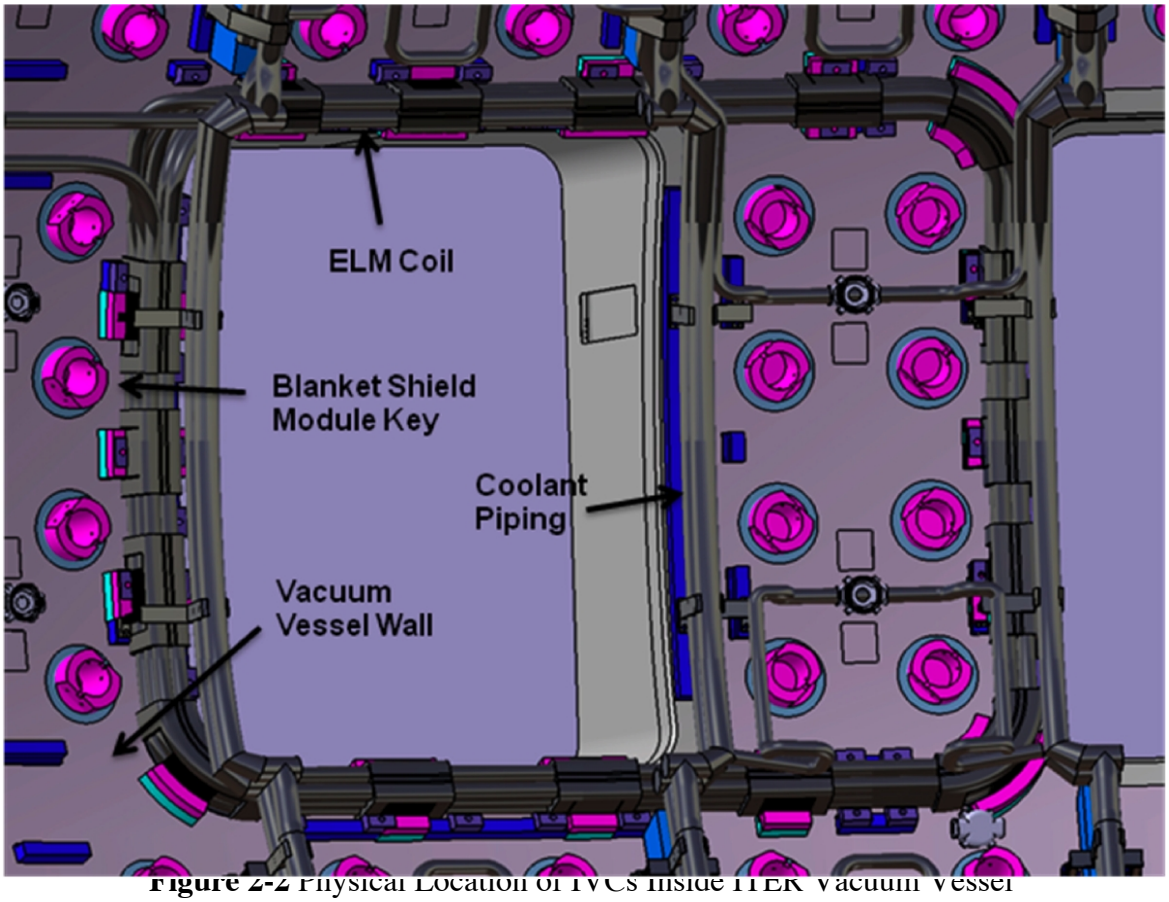

Figure 2-2 Physical Location of IVCs Inside ITER Vacuum Vessel

The physical envelope is controlled with a CMM or Configuration Management Model provided by the I/O. The design of the IVCs must fall within the envelope defined by the CMM. Clearances between the IVCs and blanket shield module cutouts are maintained at 20mm. The clearance between the IVCs and the vacuum vessel surface as well as to any cabling conduit or pipe is also maintained at 20mm. See Figure 2-3.

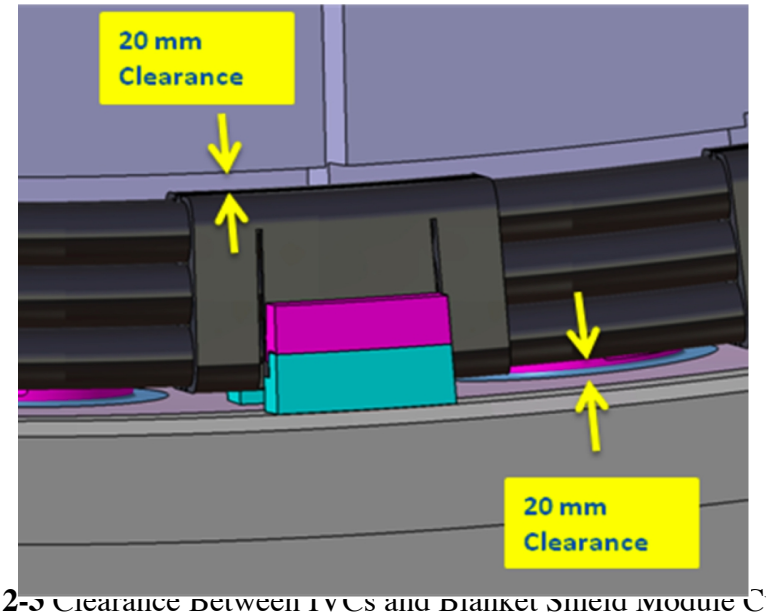

Figure 2-3 Clearance Between IVCs and Blanket Shield Module Cut-Outs

A larger clearance equal to 40mm is required around the blanket shield module keys to provide adequate clearance for inspection. See Figure 2-4.

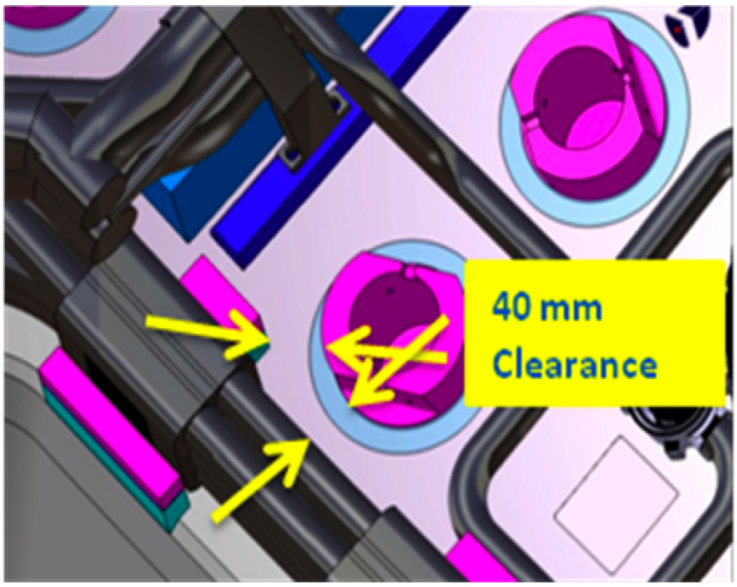

Figure 2-4 Clearance Between IVCs and Blanket Shield Module Keys

The ELM coils must also be sized to enter the vessel through the equatorial ports during initial assembly. The VS Coils must be sized so that the individual pieces of the coil are capable of fitting through the equatorial ports allowing for in vessel assembly of the VS Coils.

2.2 ELECTROMAGNETIC

2.2.1 Plasma control functions

2.2.1.1 ELM Coil Function

The primary objective of the ELM coils is to produce RMPs to suppress ELMs. A secondary objective is to perform a "Resistive Wall Mode" (RWM) function which would permit plasma operation at higher pressure (β). The RWM function is mentioned in the PR and SRD but is not quantified and is limited to whatever spare capacity may remain after the ELM function is served. Therefore the RWM function is not a design-driver.

As shown in Figure 2-5 there are three ELM coils in each of the nine sectors of the machine, referred to as the "Upper", "Equatorial", and "Lower" coils. These rectangular "picture frame" coils each produce a field which is normal to the plane of the coils and the plasma surface and radial with respect to the plasma center along its magnetic axis.

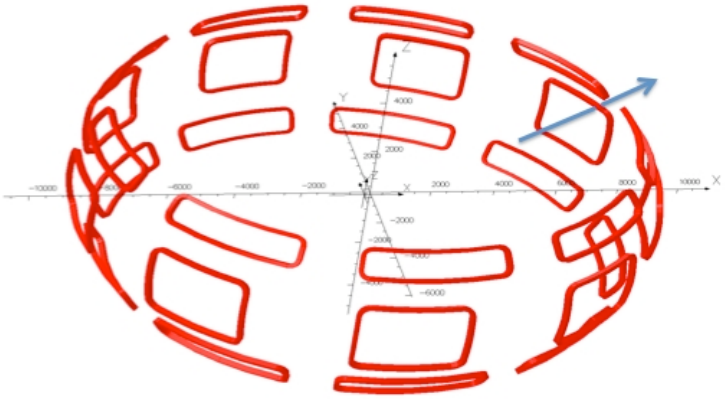

Figure 2-5 ELM Coil Arrangement

By controlling the current in the nine individual coils of either of the three coil sets a non-axisymmetric field pattern can be created along any toroidal path. Fourier decomposition of the field pattern along such a toroidal path leads to coefficients corresponding to the amplitude of sine waves of varying periodicity along the toroidal path, referred to as toroidal mode numbers "n". Thus n=0 refers to a constant field around the toroidal path, n=1 to a sinusoidal field pattern with one period around the toroidal path, n=2 to a sinusoidal field pattern with two periods and so on. Similarly, with individual control of the three sets of nine coils a poloidal variation in the field can be created which can be decomposed into poloidal mode numbers "m". Thus the net radial field perturbation is helical and can be aligned with the field lines at the edge of the plasma. The fidelity of the field produced by the coils depends on the desired m and n numbers versus the number of individual coils deployed in the poloidal and toroidal direction, respectively. The more coils, the higher the fidelity. The PR requires the capability to produce RMPs with $n \leq 4$ and extensive physics analysis[9,10] has determined that a coil array of 3 x 9 has sufficient fidelity to do so. In addition to production of the aforementioned field patterns on a static basis it is necessary to rotate them toroidally up to 5 rotations per second (5Hz). This means that the current in any one ELM coil can range from DC to sinusoidal at 5Hz. Thus the 9 x 3 = 27 individual ELM coil currents are sine waves at the applicable rotation frequency, suitably displaced in phase to achieve the required m and n field pattern.

To first approximation the phase angle of the sinusoidal current in the coils of any one of the three sets of nine coils is n*k*360/9 = n*k*40 degrees where n is the toroidal mode number of the desired field pattern and k is the sector number, k=1,9. In this case, with symmetrically displaced sine waves of coil current, the total net input power is constant even though the

---

[9] "Study of in-vessel non-axisymmetric ELM suppression coil concepts for ITER", M. Schaffer et al, Nuclear Fusion 48 (2008)

[10] "Final Report on Impact of Proposed "Modified Baseline" and "Alternate Vacuum Vessel" Designs on ITER ELM Coils", ITER_D_35CULK, July 2009

individual coil power is oscillatory. Moreover the total net input power is equal to ½ of the product of peak coil power multiplied by the number of coils. These aspects are important for the electric power system because an oscillatory net load would be undesirable.

Figure 2-6 an idealized condition where one of the three sets of ELM coils produces n=1, 2 and 3 mode patterns. The figures in the left column show the currents in the nine coils at one instant in time, and the mode patterns are evident. The figures in the center column show the sinusoidal currents in the nine coils over one period of the waveform (0 – 5Hz). The figures in the right column show the instantaneous power in the nine coils and the total power, which is constant.

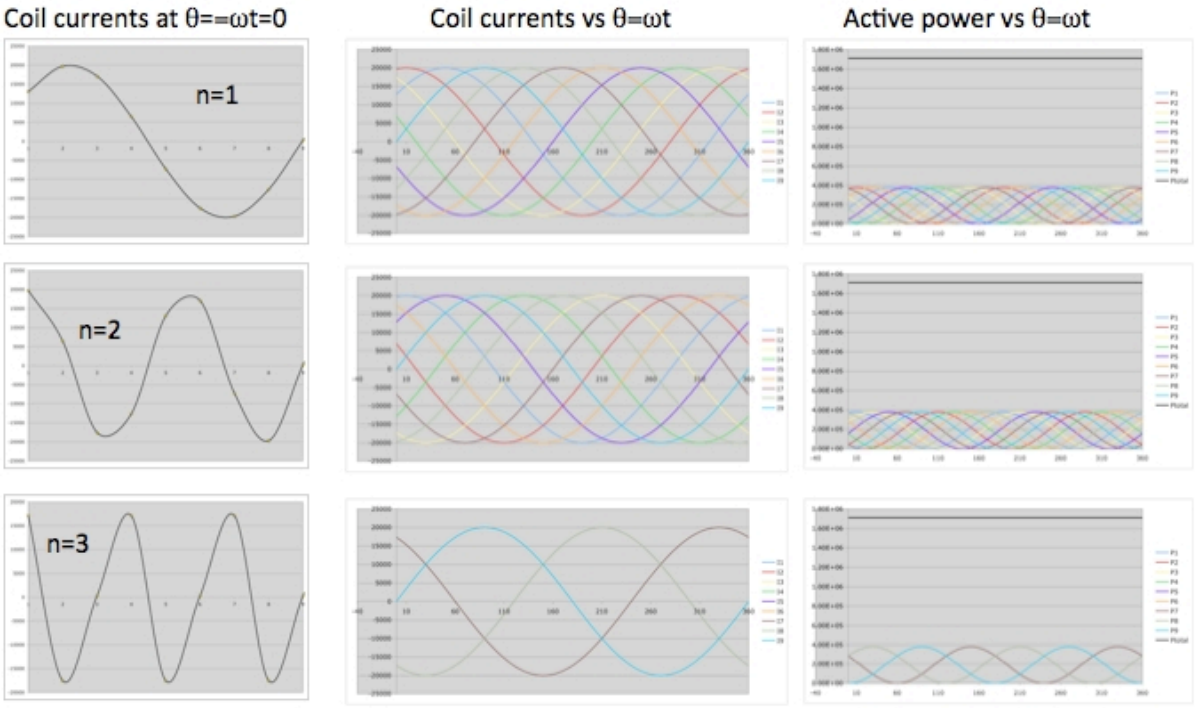

Figure 2-6 Pattern of ELM Coil Currents and Power For n=1,2,3

Figure 2-7 shows a typical field pattern from physics analysis of n=4 ELM suppression and Figure 2-8 shows the corresponding coil current amplitudes.

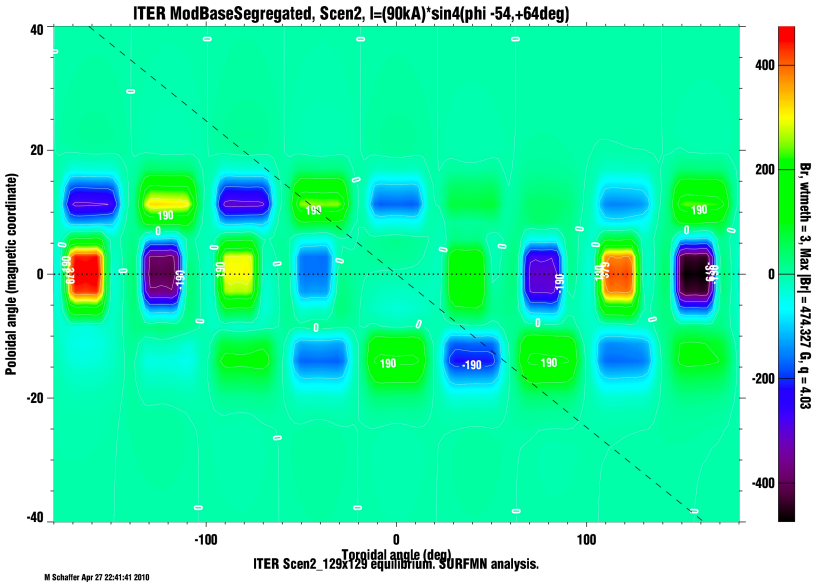

Figure 2-7 Field Normal To Plasma Surface vs. Toroidal and Poloidal Angle for n=4 ELM Suppression (courtesy of M. Schaffer)

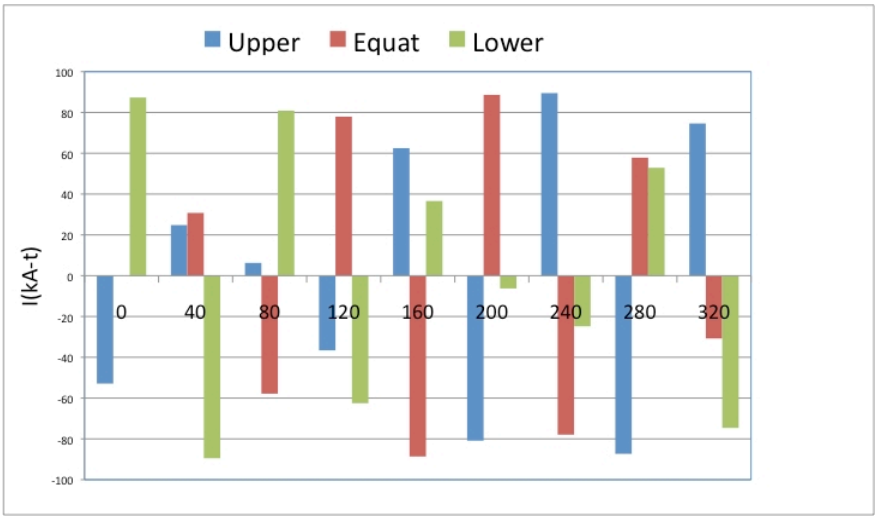

Figure 2-8 ELM Coil Currents for n=4 Suppression (courtesy of M. Schaffer)

2.2.1.2 VS Coil Function

Operation of the VS can be explained via Figure 2-9. The upper and lower VS coil windings are connected in a "saddle" configuration, meaning that current flow in the series loop formed by the upper and lower windings is in the opposite direction viewed from above (lower coil clockwise, upper coil counter-clockwise viewed from above as depicted in Figure 2-9). As depicted, current flow in the plasma is in the same direction as the upper VS winding. Two phenomena are noteworthy.

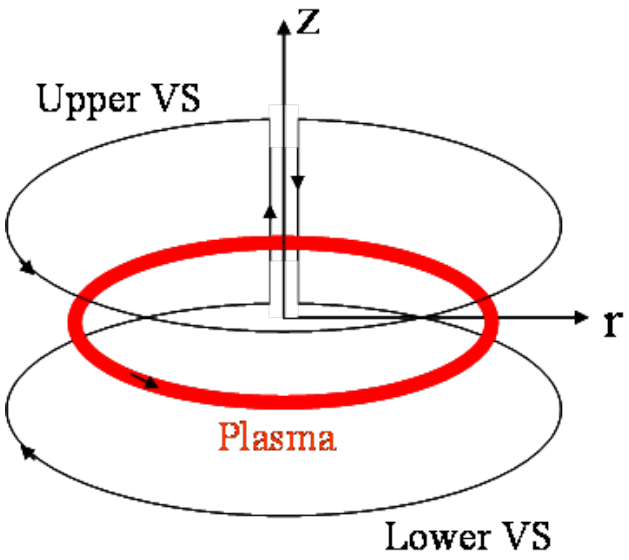

Figure 2-9 Vertical Stabilization (VS) Concept

First, recalling that the force between currents flowing in the same direction is attractive and between currents in the opposite direction repulsive, the force on the plasma current from both the upper and lower VS currents as shown is in the upward z direction. Thus if the plasma vertical position is below the desired z value it can be pushed up with current flow in the VS as shown. Conversely if the plasma vertical position is above the desired z value it can be pushed down with current flow in the VS opposite to what is shown.

Second, if the plasma drifts upward or downward it will induce current in the VS windings which tends to conserve the flux linkage of each winding. Thus a downward drift will induce

current in the same direction of the plasma in the upper VS and the opposite direction in the lower as shown resulting in an upward force on the plasma which opposes the drift. An upward drift would cause the opposite polarity of induction and force.

These two effects indicate that the saddle connection of the VS coils tends to stabilize the vertical position by induction, and the connection of a power supply in the VS loop allows for generation of current flow which can stabilize the vertical position in a feedback loop.

Finally, it is noted that with the saddle connection, the net flux linkage with the Central Solenoid (CS) coil set and the PF coil set is nullified (to the extent that these coils and the VS coils are symmetric about the midplane). This means that the mutual coupling to VS from many of the CS and PF operations (e.g. plasma initiation, radial position control) is nullified which is advantageous because it reduces the requirements on the VS power supply which would otherwise have to compensate.

Moving beyond the above-simplified explanation of VS operation, extensive simulations have been performed by the ITER project to assess the VS performance and requirements[11]. In fact there are three systems which contribute to VS, called VS-1, VS-2, and VS-3. VS-1 is a power supply which acts on PF coils 2-5 to produce a radial field at the plasma for vertical position control. Similarly VS-2 is a power supply which drives a difference current between CS2U and CS2L resulting in a radial field at the plasma for vertical position control. VS-3 is the in-vessel VS coil system which is the subject of this report. Note that both VS-1 and VS-2 act on coils which are outside the vacuum vessel so that their control actions are relatively slow compared to VS-3. The combined action of VS-1, VS-2, and VS-3 are available to ITER for vertical stabilization.

The parameter, $\Delta Z_{max}/a$, has been identified as a figure of merit for characterizing the effectiveness of the vertical stabilization, where ΔZ_{max} is the maximum "sudden" plasma

[11] "Preliminary study of the VS in-vessel coils "April 2010"", ITER_D_33DPE7

displacement, which can be stabilized and "a" is the plasma minor radius. Thus, the larger the value of $\Delta Z_{max}/a$, the greater the vertical control capability and robustness. The PR requires that, with VS-1 and VS-3 only, "the system stabilizing plasma vertical displacements shall be capable of restoring the plasma to its specified vertical position after a maximum uncontrolled vertical drift with target value of 16 cm for a nominal full aperture plasma with li < 1.2".

2.2.2 **Current and voltage waveforms**

2.2.2.1 ELM current and voltage waveforms

Per the SRD, each ELM coil shall be designed to carry a current of 90kA-turn over a range from continuous DC to 5Hz sinusoidal which is derived in the physics analysis[12]. Although it is unlikely that ELM suppression will be a continuous mode of operation during an ITER pulse the coil requirement is assumed to be continuous.

The voltage rating of the ELM coil shall be determined based on the required coil current and circuit impedance at 5Hz. This is derived in later sections of this report.

2.2.2.2 VS current and voltage waveforms

Per the SRD, each VS coil shall be designed to carry a periodic transient current waveform as derived[13] from the underlying physics analysis based on a simulation of a "Vertical Displacement Event" (VDE). Over one period the waveform consists of two components as follows:

---

[12] "Final Report on Impact of Proposed "Modified Baseline" and "Alternate Vacuum Vessel" Designs on ITER ELM Coils", ITER_D_35CULK, July 2009

[13] "Definition of VS3 Current Requirements" ITER_D_33T879

$$I = I_{vde} + I_{noise}$$

$$I_{vde} = A\left(\varepsilon^{-t/\tau_1} - \varepsilon^{-t/\tau 2}\right) \rightarrow t \geq t_{delay}$$

$$I_{noise} = I_{noise\_rms}\sqrt{2}\sin(2\pi f t)$$

Waveform parameters are given in Table 2-1.

Table 2-1 VS Waveform Parameters

A	2.98E+05	Amp-turn
τ_1	0.304	second
τ_2	0.016	second
I_{noise_rms}	11628	Amp-turn
f	30.0	Hz

One period of the design-basis waveform is shown in Figure 2-10 and Figure 2-11.

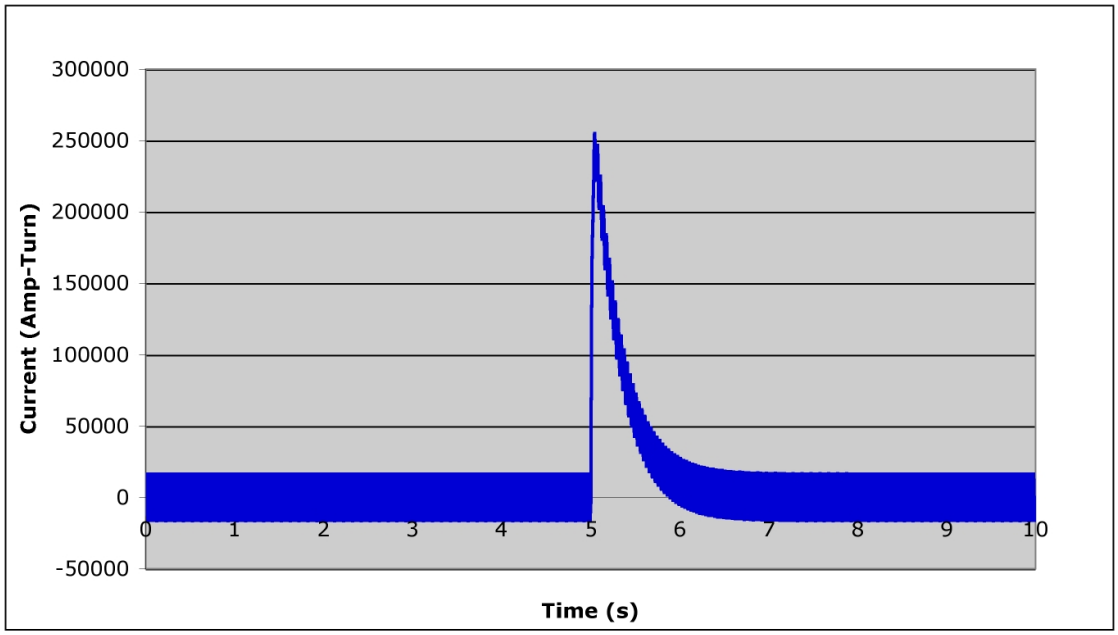

Figure 2-10 VS Design-Basis Current Waveform

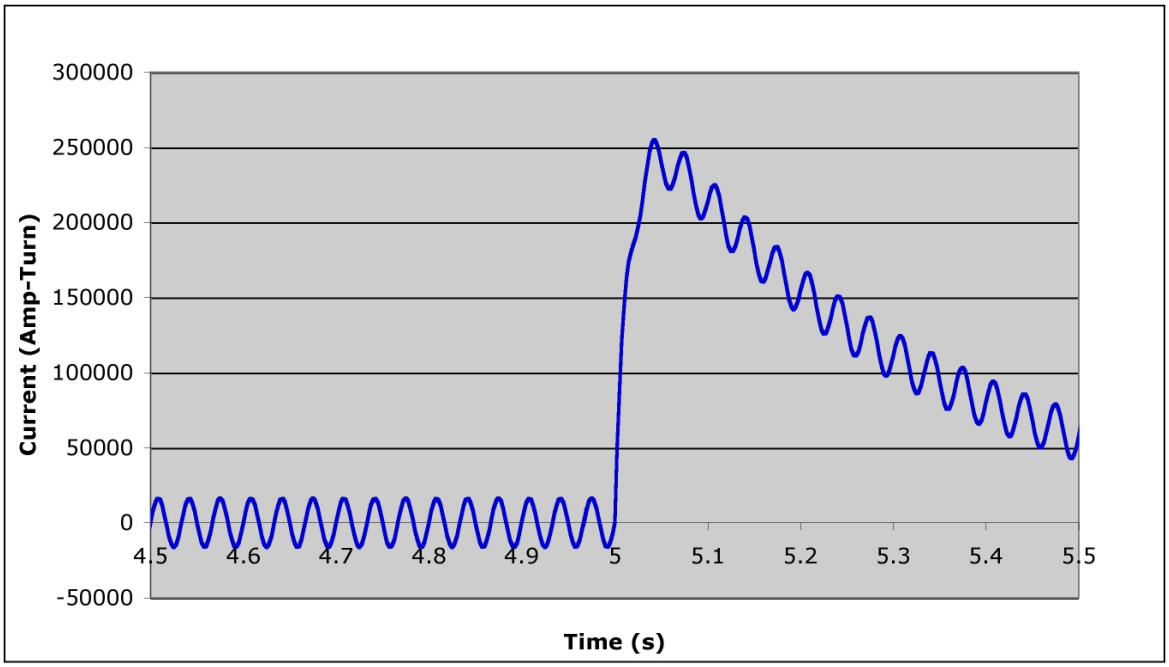

Figure 2-11 VS Design-Basis Current Waveform (zoom)

The peak value of I_{vde} = 240kAt. The $\int i^2(t)dt$ of the composite waveform taken over the 10 sec period is 12845 kAt^2-sec. For the noise component a frequency of 30Hz was assumed, somewhat arbitrarily. At this frequency the voltage required to drive the noise current is 50% of the assumed maximum voltage. Note that, for the sinusoidal noise component, the rms value is independent of frequency.

In accordance with the PR the frequency and number of occurrences per pulse of the waveform shall be ≤0.1 Hz (10 sec period) and three, respectively. The total number of these events shall be no more than 30000 over the lifetime of ITER.

The voltage rating of the VS coil shall be 575 volt per turn based on the underlying physics analysis[14].

2.2.3 Plasma interaction

The IVCs must be designed to withstand the forces during both normal operation and for a range of plasma disruption events. The forces acting on the IVCs across five different 15 MA DT normal operating scenarios have been analyzed. Five DINA-based scenarios are from the Excel file "Contents of PF Scenario database" (ITER IDM (https://user.iter.org/?uid=34263N). They are: (1) 15MA DT-DINA2010-03 (v2); (2) 15MA DT-DINA2010-03b; (3) 15MA DT-DINA2010-04b; (4) 15MA DT-DINA2010-04c; and (5) 15MA DT-DINA2010-05b. These forces were analyzed using OPERA[15] in quasi-static mode. That is, there are no induced currents in conducting structures. An initial scan for a fixed set of IVC currents across all scenarios was performed. Then for a single scenario (1) all combinations of maximum IVC coil currents were evaluated.

---

[14] "Preliminary study of the VS in-vessel coils "April 2010"", ITER_D_33DPE7

[15] Vector Fields Software for Electromagnetic Analyses, Cobham Technical Services, Kidlington, UK

In addition to the normal operational scenarios, plasma disruption events were analyzed using OPERA with a one-ninth (40°) model of the vacuum vessel and IVCs. TF and PF coils were assumed to be a constant current during the plasma disruptions. The IVCs are assumed to be shorted at the start of disruption event. The plasma is modeled as a number of stationary co-axial solenoids with time-varying currents to model both the motion and current quench. The plasma disruption events analyzed were based on the 2007 DINA simulations. A single 2010 simulation was analyzed to compare the impact on IVC currents and forces. The plasma disruption events analyzed were: (a) 2007 MD_UP with a 36 ms linear current quench; (b) 2007 VDE_UP with a 36 ms linear current quench; (c) 2007 VDE_DN with a 36 ms linear current quench; and (d) the 2010 VDE_DN with a 16 ms exponential current quench. The linear current quench produces higher loads on the vacuum vessel walls.[16]

Several possible sets of initial currents in the IVCs at the start of the disruption event were investigated. The initial VS coil currents were assumed to be zero for all cases since the interaction of the VS with the plasma will greatly impact the motion and nullify the physics basis of the disruption. It is felt the ELM coils on the other hand could potentially have any value of current at the time of the disruption. In these analyses, the ELM coil chosen is the one that will provide the worst-case current/force during the event.

2.3 FAILURE MODES

Because of the difficulty of repair and replacement, the IVCs are designed to operate in degraded modes as follows:

- In case of an ELM coil failure which compromises its ability to perform its normal electrical function but does not compromise its ability to withstand the in-vessel electromagnetic and vacuum environment, removal of the coil from the tokamak shall not be required.

[16]Load Specification fro the ITER Vacuum Vessel (ITER_D_2F52JY v2.2 – sec 5.2)

- In case of a VS coil failure which compromises the ability of a single turn to perform its normal electrical function but does not compromise that turn's ability to withstand the in-vessel electromagnetic and vacuum environment, removal of that turn from the tokamak shall not be required, and the remaining turns shall be capable of delivering the full rated current waveforms described herein.

2.4 RADIATION ENVIRONMENT

2.4.1 Radiation Limits for Vacuum Vessel, Toroidal Field Coils, Accessible Areas

Some blanket/shield modules have to be modified to provide cavities to accommodate the IVCs and feeders. This added void space and the different shielding performance of the IVCs compared to the shield module could alter the shielding performance. The combined modified blanket/shield modules and IVCs and feeders must provide adequate nuclear shielding for the vacuum vessel (VV) and coils outside the VV such as the TF coils (TFC)[17].

The requirement to allow for re-welding of the VV throughout ITER's operational lifetime is that the cumulative helium production in the SS316 should not exceed 1 appm. The combined modified blanket/shield modules must also provide adequate nuclear shielding to allow for re-welding of the coil and feeder casing throughout ITER's operational lifetime. However, the design might allow for replacing rather than re-welding these components which will eliminate such a requirement. For thin welds in thin tubes the limit on cumulative helium production is relaxed to 3 appm. Detailed 3-D nuclear analysis for the present design is presented in Section 4.1 to quantify the expected cumulative helium production.

The combined modified blanket/shield modules and IVCs and feeders, in conjunction with the vessel, shall limit the insulator dose in coils outside the VV to less than 10^7 Gy. The peak nuclear heating in the winding pack of the superconducting coils should be less than 1 kW/m^3. In

[17] System Requirement Document, SRD-15-IV (In-Vessel Coils), ITER_D_2MFYMW v1.5 (May 2010).

addition, the peak nuclear heating in the superconducting coil case and structures should be limited to less than 2 kW/m^3. The integrated nuclear heating in the 18 TF coils should be less than 14 kW.

It should be noted that shielding of the outboard legs of the TF coils is affected only by the VS coils and toroidal legs of the ELM coils that replace part of the shield modules protecting these TF coils. The IVCs cover only ~10% of the TF coils. We performed simple calculations to address the impact of the IVCs on TFC nuclear parameters. In this analysis a homogenized mixture was used for the ELM coil and surrounding void. The void corresponds to ~30% of the space. This void is equivalent to reducing the effective shielding thickness by ~5.4 cm. The calculations indicated that the TFC nuclear parameters increase by a factor of ~2.5 at the locations where the shield is perturbed by the ELM coils. Since the IVCs cover less than ~10% of the inner surface of the outboard TF coils, the expected impact on outboard TFC heating is only ~15%. Calculated total TFC heating for a model without IVCs[18] gave a total of 19.4 kW with only ~1.7 kW in the outboard legs. If we make the very conservative assumption that the calculated 1.7 kW is all due to the bulk shielding and not port streaming, we get IVCs effect of only 0.26 kW. It remains to be investigated whether the factor of ~2.5 increase in local values of heating and insulator dose will result in violating the TFC design requirements. However we note that peak local nuclear parameters (insulator dose, winding pack heating, fast neutron fluence) in the outboard leg of the TFC are much lower than the design limits with a margin >10.The Nuclear Analysis Report [ITER Report ITER_D_22F2ST] reports peak inboard fast neutron fluence of ~2.3x1021 n/m2, insulator dose of 3.2 MGy, and 0.2 kW/m3 power density which are a factor of 2-5 below the design limit. Peak values at outboard are a factor of ~200 lower because of the ~40 cm thicker VV. Since IVCs affect only OB TFC, the design limits remain satisfied by a large margin. Therefore, introducing the IVCs will not compromise the TFC shielding.

[18] ITER_D_2LF7NM v 1.0, 21 October 2009.

The combined modified blanket/shield modules and IVCs and feeders, in conjunction with the in-vessel components and port-mounted equipment, shall limit the dose rate in accessible areas of the cryostat to a level that would allow hands-on maintenance. The dose rate should be as low as reasonably achievable, with a target of 100 micro Sv/hr, and in any case less than 2 mSv/hr, after a decay period of 12 days. This requirement will be verified with detailed activation calculations upon convergence on a reference design for the IVCs.

2.4.2 **Radiation Limits for IVC**

The IVCs are normal Cu conductors cooled by water and utilize ceramic compacted powder insulators (MgO or spinel). Radiation limits for such components are not defined for ITER. However, previous reviews of radiation limits for normal conducting magnets in fusion environment are available and are used here as guidance to determine the expected radiation effects as discussed in Sections 4.3 and 4.1.1[19,20]For the insulator, the degradation of mechanical and structural performance under long-term neutron fluence is an issue. Swelling in solid ceramics with cubic structure (e.g. MgO and $MgAl_2O_4$) is isotropic under neutron irradiation. Fracture toughness increases at elevated fluences for such ceramics. The fluence limit is determined only by the maximum swelling that can be tolerated. A maximum swelling of 3% corresponds to fast neutron (E>0.1 MeV) fluences of $1.1x10^{22}$ and $4x10^{22}$ n/cm^2 for polycrystalline solid MgO and spinel, respectively. This corresponds to ~10^{11} Gy of cumulative absorbed dose. However, higher neutron fluence can be tolerated for compacted powder ceramics since each grain is affected individually. Resistivity degradation in the ceramic insulator is another concern. Under large instantaneous neutron and gamma dose rates, ceramic insulators exhibit a significant and instantaneous decrease in their resistivity. Compacted powder ceramics show a greater effect than those in solid. Dose rates calculated from the 3-D analysis in

---

[19] L.J. Perkins, "Materials Considerations for Highly Irradiated Normal-Conducting Magnets in Fusion Reactor Applications," J. of Nuclear Materials, vol. 122&123, pp. 1371-1375 (1984).

[20] M. Sawan, H. Khater, and S. Zinkle, "Nuclear Features of the Fusion Ignition Research Experiment (FIRE)," Fusion Engineering & Design, vol. 63-64, pp 547 - 557 (2002).

Section 4.3 will be used to determine the expected conductivity increase as discussed in Section 4.4.

Upon irradiation, the electrical resistivity of the copper conductor will increase. It is important to determine this radiation-induced resistivity as it will affect the I^2R dissipated power. The increase in electrical resistivity results from displacement damage (production of defects and dislocations) and solute transmutation products. This increase is to be compared to the un-irradiated resistivity of ~16 nΩm. At high doses, the displacement damage component approaches rapidly a constant saturation value due to displacement cascade overlap effects with a saturation value of 1-4 nΩm depending on purity and Cu alloy used. Most of these effects could be annealed by baking at 200-300° C. The transmutation products are Ni, Zn, Co and they build up as impurities with time resulting in changing conductor resistivity. The expected increase in resistivity will be quantified in Section 4.2 based on the calculated damage parameters in the copper conductor. Another concern is the degradation in mechanical and structural properties of the Cu conductor. This depends on the amount of cumulative atomic displacements produced (dpa) and the operating temperature. Notice that damage level at the conductors of the IVCs is about an order of magnitude lower than that in the CuCrZr FW heat sink. Two issues are of concern; the low temperature embrittlement and thermal creep at high temperatures. For the water cooled IVCs, high temperature creep might not be an issue. However, low temperature embrittlement might be a concern (at <150°C). Periodic annealing at ~300°C will help alleviating this problem. The dpa levels determined from the 3-D neutronics calculations will help along with the operating temperature to assess the expected degradation in mechanical and structural properties of the copper conductor.

2.5 SAFETY

The IVC coils and feeders are considered as non-Safety Important Components (non-SIC), and there is no safety credit function associated with them. Nonetheless, under any normal, upset, emergency, or fault condition, no combination of loads shall lead to damage to SIC components,

including: vacuum vessel confinement barrier, primary cooling system lines for the vacuum vessel and IVC components, fuelling system lines, or cryostat confinement barriers that could result in release of radioactivity exceeding the specified limits.

3 DESIGN

3.1 CONDUCTOR

The design of the conductor serves as the basis of the entire coil system design. The considerations and procedure for choosing the conductor technology and geometry is described in the following sections.

3.1.1 Choice of conductor technology

The operating environment of the IVC conductors is severe in terms of radiation and temperature and precludes the use of organic insulating materials and conventional methods for coil fabrication. Efforts to demonstrate sufficient radiation resistance of "ceramic polymer" as was proposed at the IVC CDR fell short of requirements[21]. Therefore the chosen technology is "Stainless Steel Jacketed Mineral Insulated Conductors" (SSMIC). Application considerations are discussed in the following sections.

3.1.1.1 Radiation considerations

The closest prior experience in terms of radiation effects is that of the high-energy physics community. A comprehensive study by CERN[22] evaluated a wide variety of technologies and application issues and serves as an excellent reference. Their summary of radiation resistance is shown in Figure 3-1. Note that the ITER IVC radiation fluence is of order 3000MGy which falls between the 10^9 and 10^{10} Gy divisions at the extreme right of the figure where choices are very

[21] "Fabrication, Characterization Testing, and Irradiation of Ceramic Polymer Composite Materials at 373 K", Final Test Report for Purchase Order No. 090501, Composite Technology Development (CTD), 2009.

[22] "Radiation-Resistant Magnets", CERN-82-05, 1982

limited. The prime candidate for the mineral insulation is compacted Magnesium Oxide (MgO) powder which is viable at these fluences.

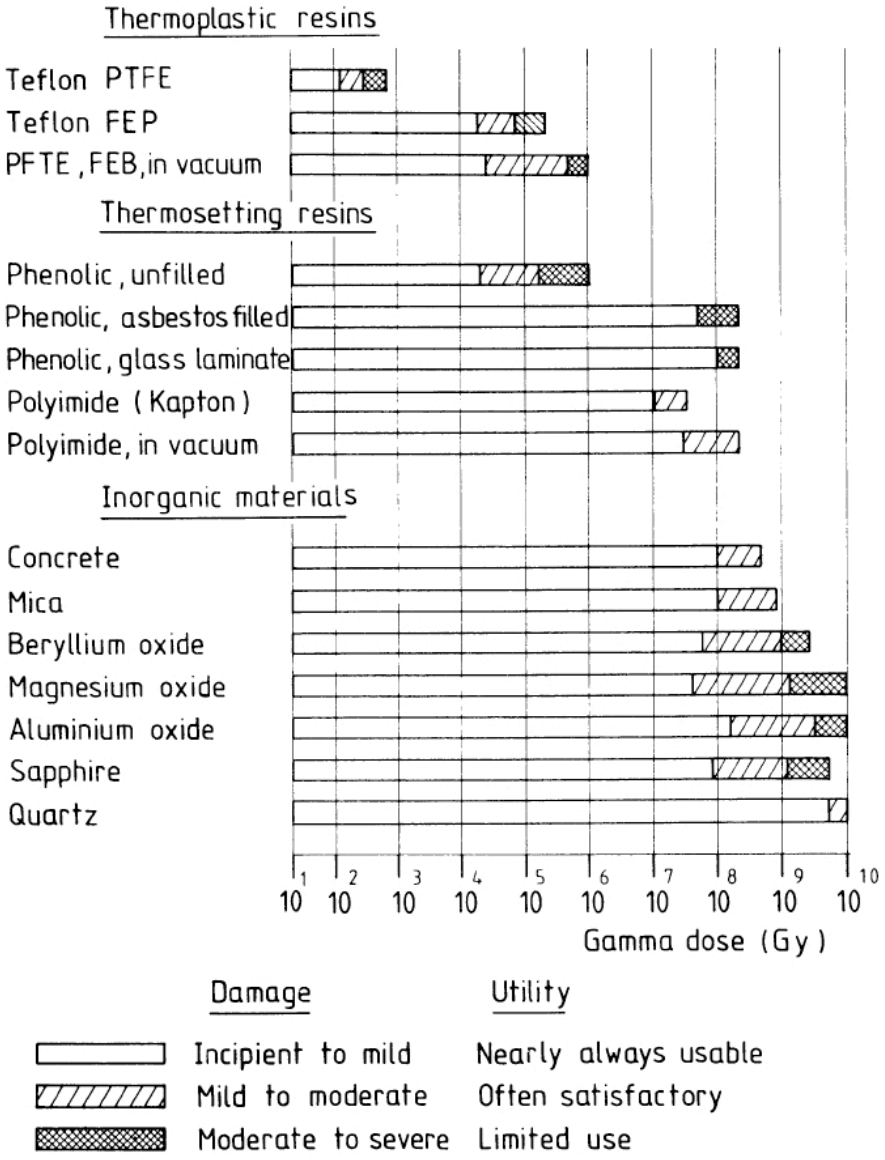

Figure 3-1 Radiation Resistance of Various Insulating Materials

An additional important overview study was performed by MIT[23] which identified the "mineral insulated conductor" (MIC) approach as viable and highlighted important application issues.

Magnets using MIC in high radiation fields were pioneered by the accelerator community beginning in the 1960s, mainly at the meson factories LAMPF[24,25,26], SIN, and TRIUMF. Although precise data is not available it is estimated that the fluence seen by these magnets, which have been in operation for decades, exceeds the ITER requirement by a factor of 10-100. More recently, MIC magnets have been deployed at KEK[27,28] in Japan and at the NCSL[29,30,31] and SNS in the US.

Various fusion-based studies[32,33,34,35,36] have also been performed which add to the knowledge base of application issues.

---

[23] "Design Practice and Operational Experience of Highly Irradiated, High Performance Normal Magnets", Schultz, Journal of Fusion Energy, Vol. 3, No. 2, 1983

[24]" Mineral Insulated Magnets for High Radiation Environment", Harvey, IEEE Proeedings of PAC, 1969

[25] "Radiation Hardened Magnets Using Mineral Insulated Conductors", Harvey, LA-5306-MS, 1973

[26] "Radiation Hardening of Magnet Coils", Harvey, SLAC-PUB-4910, 1989

[27] "Development of Radiation-Resistant Magnet Coils for High-IntensityBeam Lines: Part II-completely inorganic insulated coils", Yamanoi, IEEE Transactions on Magnetics Vol 32 No 4 p2147

[28] "Development of radiation resistant magnet in KEK", Kusano, 2004

[29] "Radiation resistant Magnet R&D at the NSCL", Zeller, Proceedings of the 2003 Particle Accelerator Conference p 161

[30] "A Radiation Resistant Dipole Using Metal-Oxide Insulated CICC", De Lauter, IEEE Transactions on Applied Superconductivity Vol 17 No 2 p 1087

[31] "Final Report on Radiation Resistant Magnets", Zeller, DOE Grant DE-FG02-03ER41254, 2005

[32] "Sizing of the Thermal and Electrical Systems for An FED Bundle Divertor Design with MgO Insulation", Schultz, MIT, 1980

The JT60-SA project[37] is now developing SSMIC in conjunction with the Okazaki Company[38] in Kobe, Japan, albeit about half the diameter of what is required for the ITER IVC.

The prior experience described above highlights the key issues with respect to the application of MIC in a radiation field, namely structural degradation, "Radiation Induced Conductivity" (RIC), and "Radiation Induced Electrical Degradation" (RIED). Structural degradation of the mineral insulation is not perceived to be an issue because, while some swelling will occur, the compacted mineral powder has a void fraction substantially greater than the expected swelling. An assessment of RIC and RIED is given in later sections of this report.

3.1.1.2 Temperature considerations

The ITER IVC will experience temperatures as high as 150ºC during operation and ~ 240ºC during bakeout. While these temperatures would challenge conventional insulation systems they are not a problem for MIC which is typically used in heating elements and fireproof wiring. Commercial cables are typically rated for continuous operation at 250ºC, transient operation up to 1000ºC

---

[33] "Radiation Dose Rate Resistivity Degradation in Ceramic Insulators and Assessment of the Consequences in Fusion Reactor Applications", Perkins, 1982, UWFDM-469

[34] "Materials Considerations for Highly Irradiated Normal-Conducting Magnets in Fusion Reactor Applications", Perkins, Journal of Nuclear Materials 122 & 123 (1984) 1371-1375

[35] "Improved Mineral Insulation Cables for High Radiation Environments", Snead, CRADA ORNL 94-0301

[36] "Generic Diagnostic Issues for a Burning Plasma Experiment", Vayakis, Fusion Science and Technology Vol. 53 Feb. 2008

[37] "Improvement and R&D of MIC", Takechi, 2010

[38] "Okazaki Product Examples", 2010

3.1.2 Selection of conductor geometry, number of turns and "Design Point"

A common trade-off in coil design involves the selection of the number of turns. Figure 3-2 shows the factors typically considered.

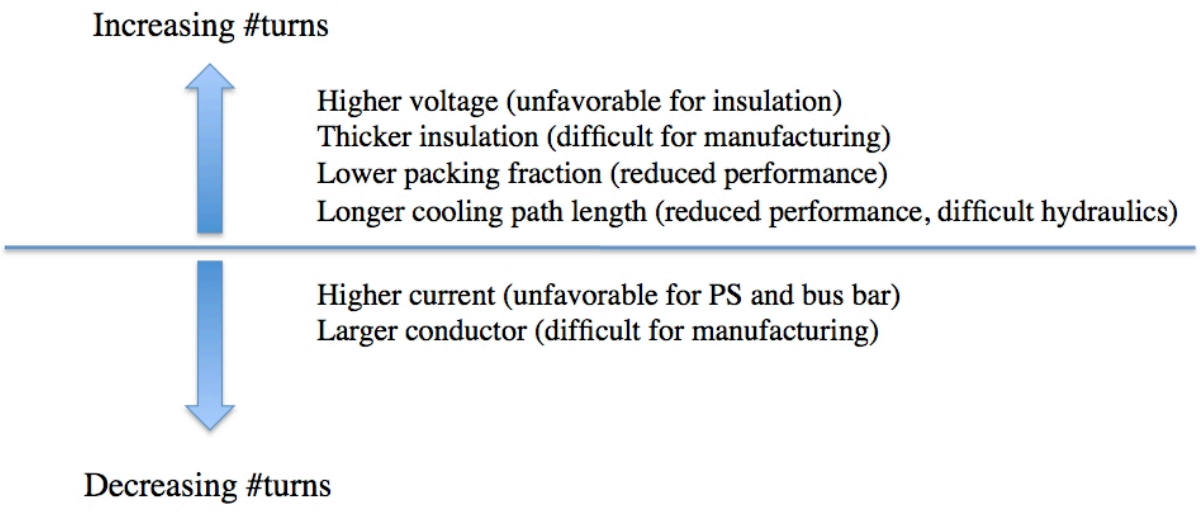

Figure 3-2 Considerations related to the selection of number of turns

For the ITER IVCs the selection of then number of turns in the ELM coil was not constrained but for the VS, a scheme was already developed based on 4 turns with each turn penetrating a port and routed to the power supply area allowing the option to abandon failed turn(s) and operate he others. Deviation from this approach was not practical, so other numbers of turns were not considered.

A key parameter related to the number of turns is the insulation thickness which must consider the following issues:

- Electrical breakdown
  - Basic dielectric strength limitation
  - Thermal runaway
    - Ohmic resistance highly dependant on RIC and operating temperature

  - Current through insulation depends on resistance and capacitive displacement currents (high frequency chopper power supply may cause substantial AC component)

- Thermal conductivity
  - Removal of nuclear heat deposited on structures
- Structural behavior
- Ground fault detection
  - Low stray resistance due to RIC and temperature will limit sensitivity detection
- Manufacturing feasibility
  - Limited prior experience with large size MIC
- Winding feasibility (minimum bend radius)
  - Maintain adequate thickness at bends

For the ITER IVCs the starting point for selection of insulation thickness was as follows. For ELM, the thickness chosen is the same as that used in the largest commercially available MIC cable from the world's largest manufacturer of same (Tyco Industries) which is a 500MCM, 600V ac power cable. Considering the ELM operating voltage (to be derived in later sections) this would seem to offer sufficient margin on dielectric strength, allowing (qualitatively) the lower temperature in the ITER application to trade off against the presence of the radiation field not present in the commercial application. For the VS, considering that the voltage is substantially higher than ELM, twice the ELM thickness has been chosen. The corresponding electrical field for ELM and VS is discussed in a later section of this report.

With the insulation thickness set, a trade study was performed to evaluate different conductor geometries and designs to arrive at "Design Points" (DPs) for the ELM and VS conductors and coils. Features of the study are summarized below.

- Calculation using XL solver
  - Compute water temperature rise based on ohmic + nuclear heat input to flowing water
  - Neglect film resistance and delta T between water and Cu
  - Assume copper and water properties based on average of T_inlet and T_outlet
- Manual inputs
  - Conductor shape (rectangular or circular)
  - Conductor material (100% IACS Cu, 80% IACS CuCrZr (ELM only))
  - # turns
  - Coolant inlet temperature (100°C)
  - Allowable coolant temperature rise (30,40,50°C)
  - Allowable water flow rate (3, 4,6,8 m/s)
- Solver variables
  - Fraction of overall coil envelope taken by conductor + insulation + jacket
  - Cooling hole diameter and straight for racetrack (rectangular only)
  - Coolant flow rate
- Constraints
  - Flow rate ≤ allowable
  - Cooling hole dimension ≤ 2/3 conductor width, height (rectangular) or diameter (circular)
- Fixed
  - Coil cross section envelope 128 x 193 mm (ELM), 158 x 173 mm (VS)
  - Length per turn 10m (ELM), 48m (VS)
  - 2 turns across width (allowing central “backbone”)
  - 2mm jacket thickness, 2.5mm insulation thickness (ELM), 5mm thickness (VS)
  - 96kA-turn continuous and rms ELM), 27kA-turn continuous VS
  - nuclear heating 0.5 watt/cc

A large number of cases were considered, after which DPs were chosen for ELM and VS for detailed analysis. After several iterations the present DPs were arrived at. These are published on a web site http://www.pppl.gov/~neumeyer/ITER_IVC/Design_Point.html and summarized in the appendices of this report. The DP XL spreadsheets "ELM_Design_Point_YYMMDD.xls" and "VS_Design_Point_YYMMDD.xls", where YYMMDD is year, month, day of revision, contain all of the calculations and are downloadable from the web site.

3.1.3 **Summary description of conductor**

SSMIC is used for both the ELM and VS coils. The VS uses Cu conductor whereas the ELM requires a Copper-Chromium-Zirconium (CuCrZr) alloy to provide adequate lifetime based on fatigue considerations. Another major difference is the insulation thickness required to handle the higher voltages required by the VS coils. The stainless steel (SS) jacket is ITER-Grade (IG) 316LN. Figure 3-3 is a depiction of the SSMIC design. Table 3-1 provides the radial dimensions of each conductor type.

Electrical and mechanical tests to date have been on commercially available 500 MCM copper jacketed conductor (MgO), to get preliminary data and we plan to test the full-scale prototypes. The results are reported in section 10.

Currently, full-scale prototype cable lengths using both insulation material candidates are being produced by two vendors (ASIPP in China and TYCO in Canada). Complete results will be available after the PDR. While we do not anticipate large differences in the results, we will update the analyses based on the complete full-scale test results following the PDR.

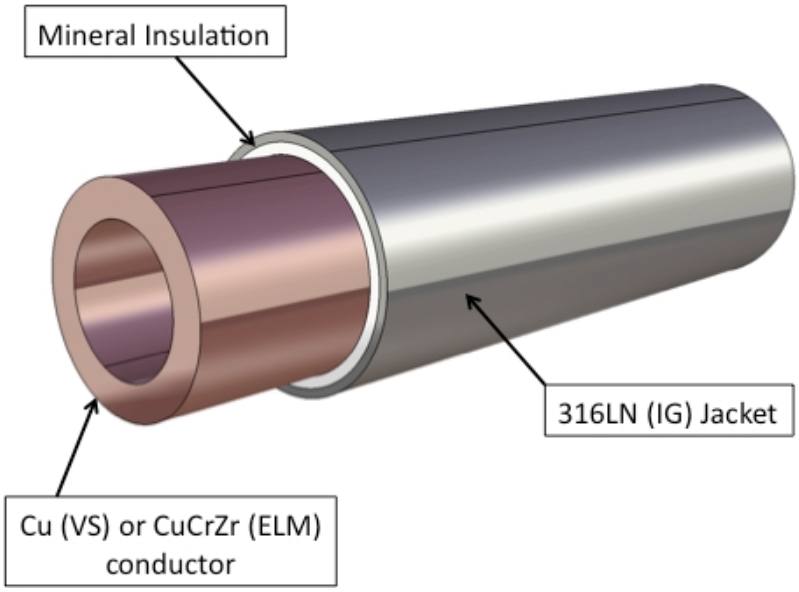

Figure 3-3 SSMIC Depiction

Table 3-1 SSMIC Dimensions

	ELM	**VS**
SS [316 LN (IG)] Jacket Outer Diameter	59 mm	59 mm
SS [316 LN (IG)] Jacket Inner Diameter	57 mm	57 mm
Conductor Material	CuCrZr [CDA 18150]	Cu [CDA 10700]
Conductor Outer Diameter	50 mm	45 mm
Conductor Inner Diameter	33.3 mm	30 mm
Mineral Insulation thickness	2.5 mm	5.0 mm

There are two options for the insulation: Magnesium Oxide (MgO) and spinel ($MgAl_2O_4$). While the likely insulation will be the MgO, as it is the most commonly used insulation in industry,

there is a major drawback in that it is very hydroscopic. Accordingly, efforts are underway to develop methods to immediately seal the ends of the cable once they are baked out. The $MgAl_2O_4$ is appears to be a viable option as it is not hydroscopic, however, its thermal conductivity is not as good as MgO (MgO: 15 W/cm-deg vs. MgAl2O4: 45 W/cm-deg)[39]. In addition, the database on performance in a radiation field may be limited.

3.2 COILS

3.2.1 Overview

The In-Vessel Coils, shown in Figure 2-1, consist of (27) ELM coils and (2) VS coils.

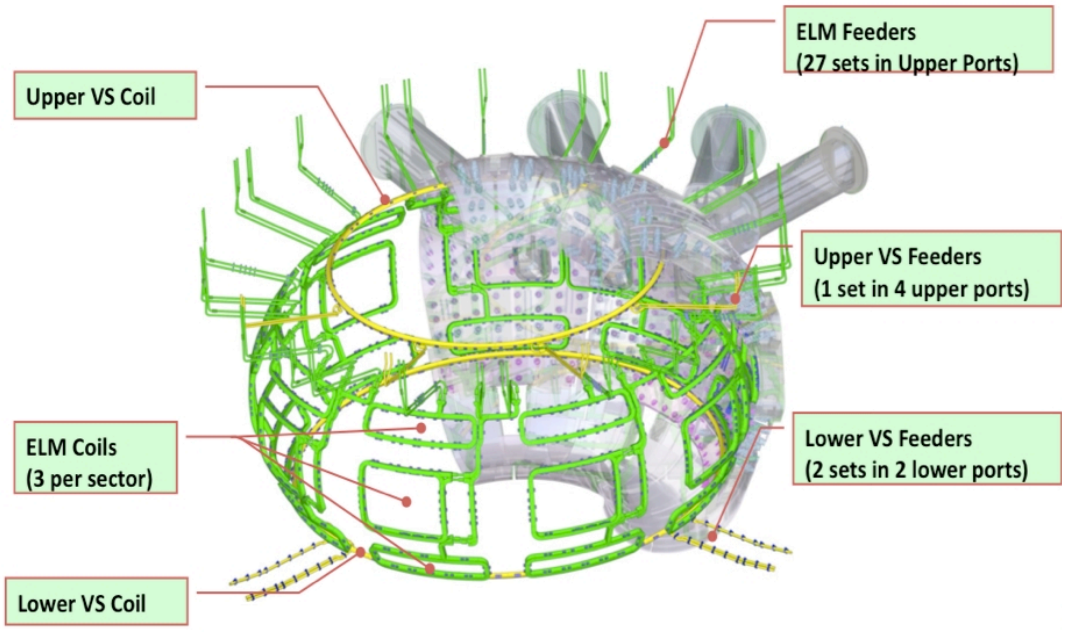

Figure 3-4 The In-Vessel Coil (IVC) System

[39] Physical Review, Volume 126, No. 2, April 15, 1962

Both the ELM and VS coils are wound from Stainless Steel Jacketed, Mineral Insulated Conductor (SSMIC) as described in section 3.1.3 so that they can withstand the total neutron dose and the operational and bakeout temperature requirements. Note that copper alloy CuCrZr is used in the SSMIC for the ELM coils because of their more demanding fatigue conditions and that the MgO thickness in the SSMIC for the VS coils is twice as thick (5 mm vs. 2.5 mm) because of the higher voltage requirements of the VS coils (2.4 kV for VS; 0.18 kV for ELM).

3.2.2 ELM Coils

Error! Reference source not found. shows the ELM coils installed in a typical vacuum vessel sector. The same coil designs are used in a neutral beam sector, shown in **Error! Reference source not found.**, to preserve coil symmetry. Installation will be hands on, possibly using the RH equipment to assist in the installation process.

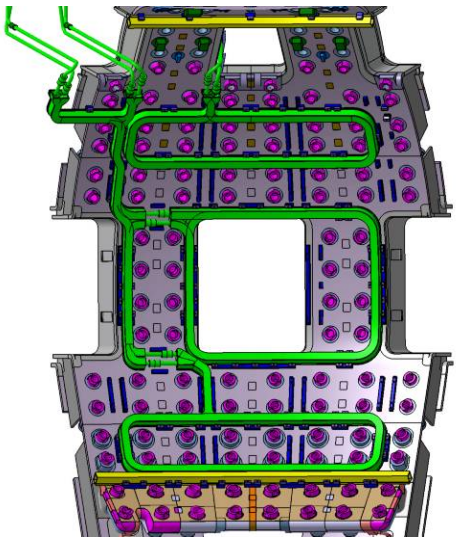

Figure 3-5 ELM Coils Installed In Standard Sector

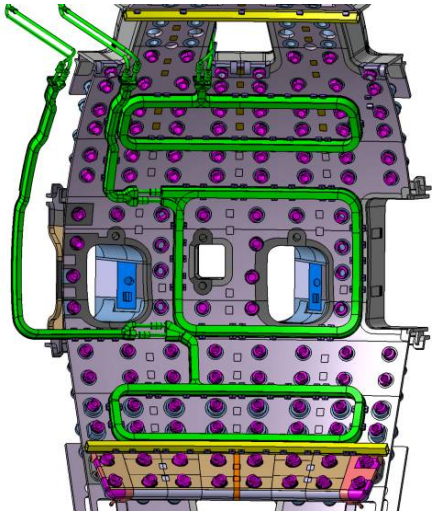

Figure 3-6 ELM Coils Installed in Neutral Beam Sector

All ELM coils are similar in construction; some critical characteristics are listed below:

- Each sector has one upper, 1 equatorial, and 1 lower ELM coil.
- 6 turns/coil
- Max. +/- 15 kA (+/- 90 kAt/coil) DC-5 Hz.
- Max. design voltage to ground 180 V (i.e., the power supply voltage).
- 1 flow path/coil (total flow path is coil + it's associated feeder). A flow velocity of 3 m/s is used to minimize flow erosion concerns.
- Feeders (section 3.3) use the same SSMIC as used in the coil to supply water and power to each coil; connections between the coils and feeders are welded and brazed for reliability (see section 11.2)
- Plan to seek qualification as RH Class 3: ***Class 3 components are those that do not require scheduled maintenance and are unlikely to require unscheduled maintenance (P<0.01) during the lifetime of ITER. The procedure for maintenance of Class 3 components shall be defined prior to ITER construction.***

Coolant manifolds for the blanket modules are located above the ELM coils, as shown in **Error! Reference source not found.**. They are independently supported from the vacuum vessel wall

by separate support brackets; no forces are transmitted between the ELM coils and manifolds. The ELM coils, blanket manifolds, and VV wall are protected by the blanket/shield modules which are also independently supported from the vessel by their supports, shown as circular objects (Refer to **Error! Reference source not found.**). Pockets are provided in the blanket-shield modules to accommodate the coils. Details of the overall size, weight, and materials are given in **Error! Reference source not found.**.

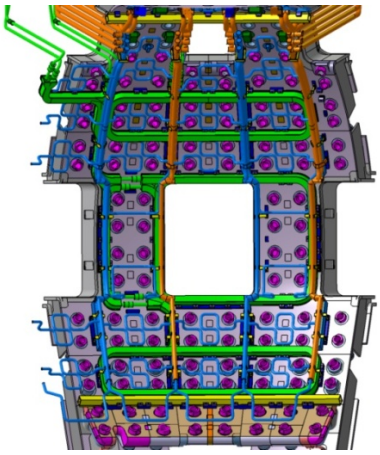

Figure 3-7 Blanket/shield modules are installed in front of the ELM coils and manifolds

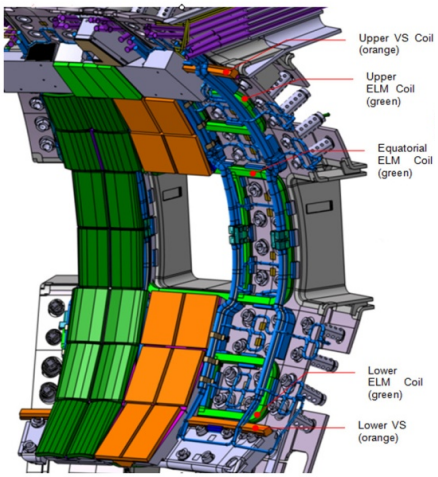

Figure 3-8 Blanket/shield coolant manifolds are mounted in front of the ELM coils

Mass [tonne]:	• Upper ELM Coil = 2.1 • EQ ELM Coil = 2.3 • Lower ELM Coil = 2.2 • In-vessel Feeder = 1.3
Outside dimensions [m]:	• Upper ELM Coil = 0.9H×4.0W×0.3T • EQ ELM Coil = 2.4H×3.1W×0.5T • Lower ELM Coil = 1.0H×4.2W×0.3T • In-vessel Feeder = 4.8H×1.0W×0.5T H=Poloidal, W=Toroidal, T= Radial
Material(s):	• Conductor = CuCrZr-IG alloy • Insulation = MgO Powder • Outer Jacket = 316L(N)-IG • Clamps = 316L(N)-IG • Bolts = 316L(N)-IG with MoS2 lubricant coating • Rails - Body = 316L(N)-IG - Threaded Insert = C63200 Ni-Al bronze

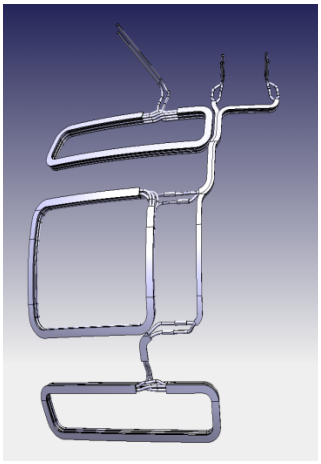

Figure 3-9 ELM Coil Sizes, Weights, and Materials

The coils will be made by precisely forming the SSMIC into a six turn coils with poloidal and toroidal contours matched to the vacuum vessel, as described in section 0. A minimum 200 mm bend radii us used on all SSMIC bends to preserve the electrical integrity of the mineral insulation. Bend tests are planned on the SSMIC prototypes to verify this bend radius. The coil support assembly components will be carefully positioned around the formed SSMIC coil, and the components joined by welding. The supports will be brazed to the SSMIC using local heating furnaces. Brazing avoids slippage between the SSMIC and supports and ensures good thermal conduction so that nuclear heating of the supports to be transported to the water-cooled SSMIC.

The EM forces acting on the coil are described in detail in section 6. The largest forces by far are due to I_{ELM} x $B_{toroidal}$. This results in forces either pushing or pulling the poloidal legs of the coil normal to the vessel wall. If the thermal expansion of the coil due to Joule heating during operation is inhibited, significant stresses will develop along the length of the conductor. These thermal stresses determine the value of the mean stress, and the EM loads determine the value of the range stress which are the primary quantities in fatigue life evaluation. The EM loads are determined by the operating requirements and there is not much that can be done about them. However, the thermal stress can be controlled by allowing thermal expansion to occur rather than thermal stresses to build up. For this reason, a flexible coil support design, shown in **Error!**

Reference source not found. and **Error! Reference source not found.** is used. Flexible leaf spring elements which are integral parts of the support clamps (i.e., machined from one block of Inconel 718) connect the coils to the VV. The leaf springs are broken up by a series of cuts to reduce their stiffness in the axial direction and to allow thermal growth in these directions. In this manner, the support provides flexibility to permit thermal expansion in the plane of the coil while still providing a strong load path normal to the vessel wall to react EM loads. Note that custom fitted shims are used to vertically align the position of the coils. Captured swing clamps are used to facilitate RH operations, in the unlikely case that a coil had to be replaced remotely. **Error! Reference source not found.** shows an equatorial ELM coil assembled to the vessel via the flexible supports and clamps.

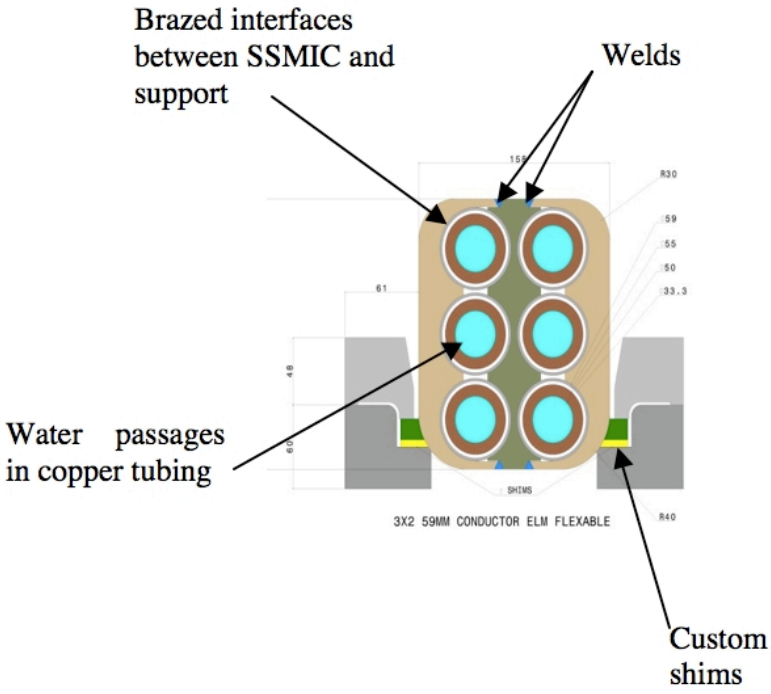

Figure 3-10 ELM Coil Support Details

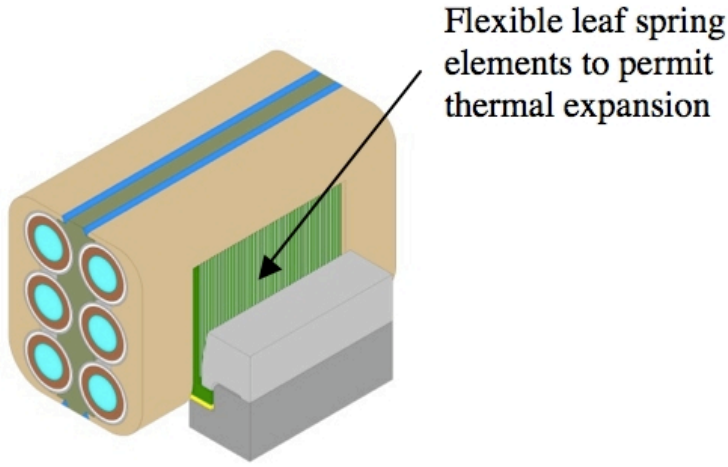

Figure 3-11 Side View of an ELM Support

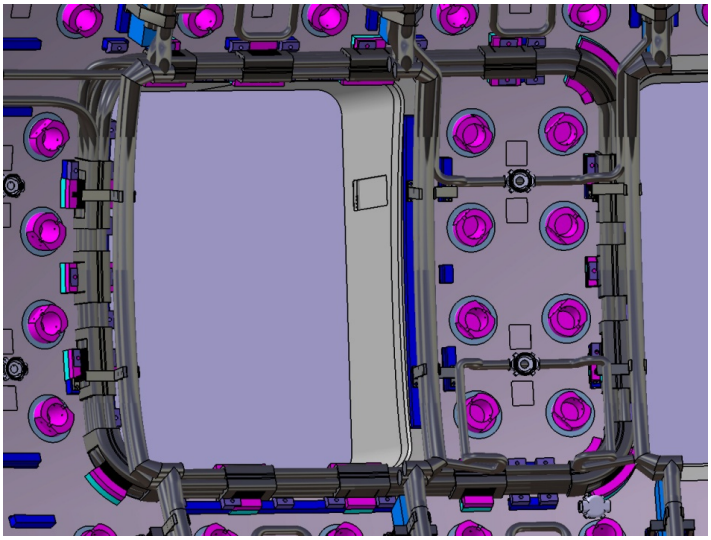

Figure 3-12 Installed View of an Equatorial ELM Coil

3.2.2 VS Coils

The VS coils are wound of SSMIC but, as described in the overview (section **Error! Reference source not found.**), differs from that used in the ELM coils in copper alloy and insulation thickness Each coil has four turns, with each turn having its own individual feeders. This arrangement allows each turn to be an individual flow path and also allows individual turns to be bypassed in the event of a failure of one of the coil turns. It is planned to seek qualification as RH Class 3, based on this ability to recover from a turn failure and the robust design of the coils.

The upper coil has a major diameter of 12.199 m; the lower coil has a diameter of 15.242 m. The differing diameters are required to satisfy integration demands. A VS coil cross-section is shown **Error! Reference source not found.**. Presently the support scheme is similar in concept to that used for the ELM coils. However, the support requirements for the VS coils are less demanding than the ELM coils, and, as discussed in the analysis (section 8.1.2), design simplifications may be possible. The VS coils will be assembled in the vacuum vessel from prefabricated components, as described in Sect. 11.

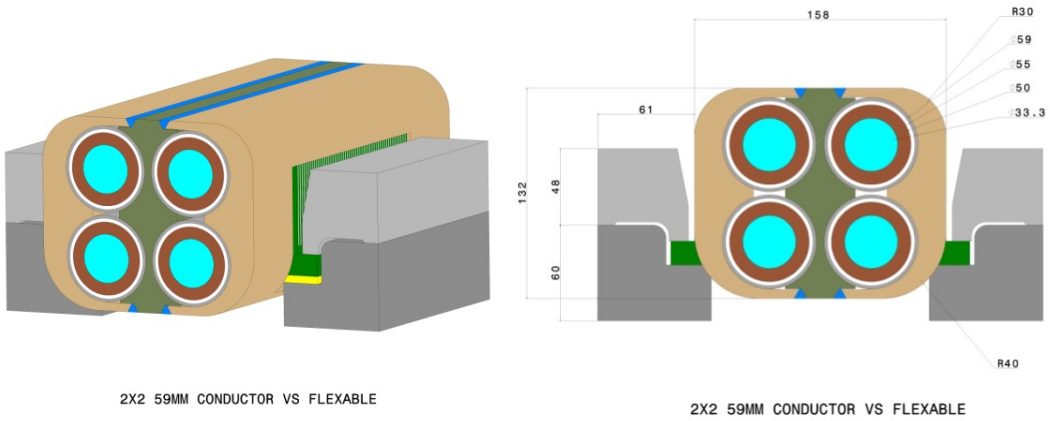

Figure 3-13 VS Coil Details

3.3 FEEDERS

The ELM Feeders described in this section connect the DC Bus Bar (which enters the VV through the Upper Port) to the mid (equatorial) and lower ELM coils. The feeders run down along and are mounted to the VV Inner Shell. There is a separate feeder for each of the nine sectors with each feeder powering a single mid and lower ELM coil. The coil/feeder joints are described separately in the following section. CAD models of the ELM Feeders are TBD.

The design of the ELM Feeders follows the general design of the ELM coils. They use the same "Stainless Steel Jacketed Mineral Insulated Conductors " (SSMIC) as the ELM coils with a Copper-Chromium-Zirconium (CuCrZr) conductor as described in section 3.1.3. They also use similar flexible supports to accommodate thermal growth while providing support from EM

loads. There are two conductors per coil (in and out) arranged side by side to minimize both stray magnetic fields and Lorentz forces. The feeds for the middle ELM and lower ELM are also clustered together in part due to space limitations but also to provide more structural rigidity.

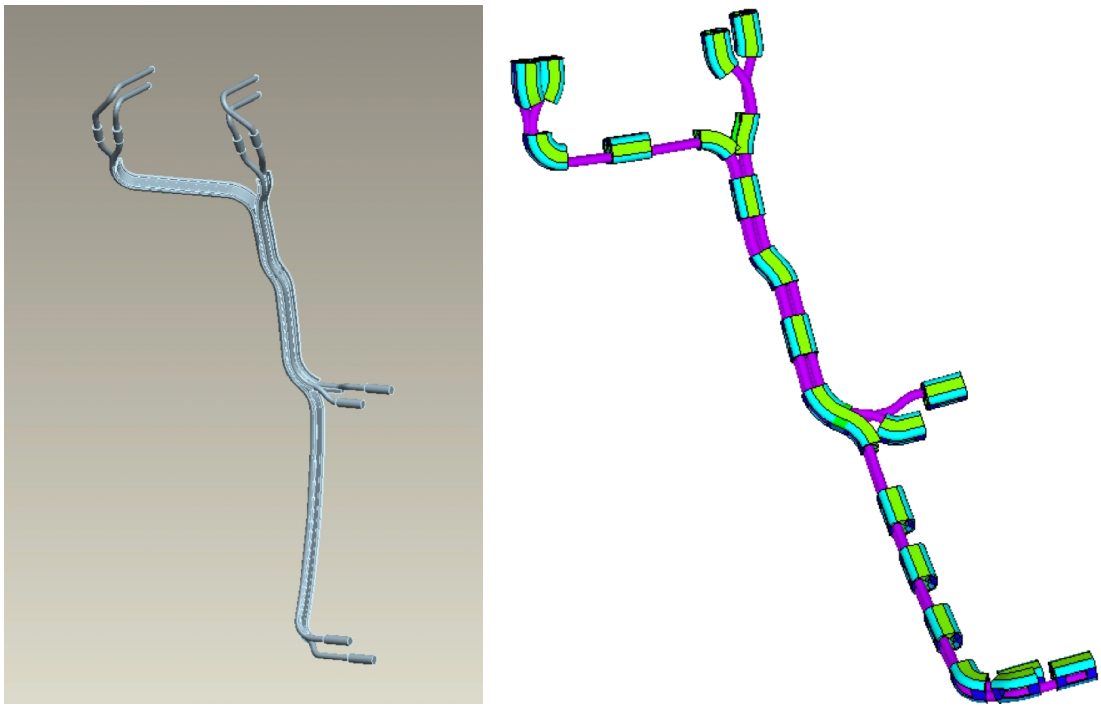

Figure 3-14 CDR Design, Left and PDR Design, Right

The initial design of the feeders shown at the CDR (shown above in Figure 3-14 left, rendered in ProE) used a continuous tree support as did the early ELM coil design. This was perceived as difficult to fabricate but also produced large thermal stress resulting from temperature gradients in the continuous tree from plasma face to VV shell induced by the nuclear heating. The present design concept (above right, rendered in ANSYS) uses discrete flexible supports spaced to minimize the free span of conductor. A design goal of 300mm was established base on preliminary analysis. The bends are fully supported with the free spans occurring on the (relatively) straight sections. Free span 90 degree bends were found to be ineffective at relieving thermal growth and instead induced large stresses at the tangency points. Full U-bends would be preferred but space limitations do not permit their use.

The feeders require several different styles of flexible supports to accommodate the clustering of all four conductors where they are routed together, or just two where they branch off to the separate coils or buss pairs, or just one where they further separate to make up the connections as shown schematically below. Not shown are the flexible members which attach the supports to the VV wall. As with the ELM coils, there is a central tree to which the conductors are brazed to and two outer clam shells, also brazed to the conductors which are then welded top and bottom.

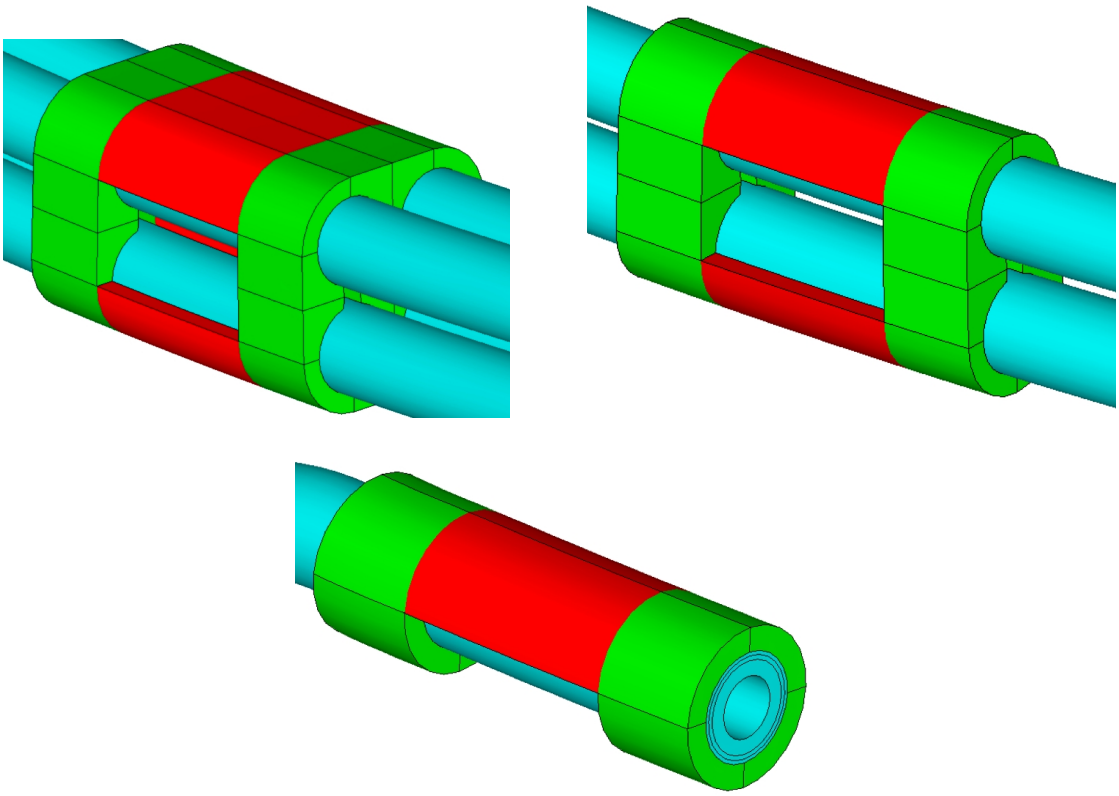

Figure 3-15 Feeder Flexible Supports for Four, Two, and One Conductors

The above show only the straight sections. There are similar supports at each of the corner bends.

The water flow direction in the feeder is chosen to put the two warm outlets at the base of the supports (i.e. VV side) and the two cold inlets at the top (ie. plasma side). This has the advantage of putting better cooling where the nuclear heating is greatest, minimizing thermal gradients in the support.

Where the conductors are tied together in either a four or two tube arrangement, there would be not net EM force but there will be in the single conductors where they branch off and also in-between supports.

3.4 COIL/FEEDER JOINTS

Joints utilizing induction brazed copper connections and welded jacket connections were adapted after consideration of a number of joint configurations, including bolted joints and hybrid bolted/soldered joints. Based on these joints studies, it was concluded that brazed and welded joints are the only ones that have the requisite reliability needed required twenty-year lifetime with no maintenance. R&D studies are underway (see section) to develop and demonstrate the joining and nondestructive testing methods to be used for the feeder joints. A typical coil/feeder joint is shown in Figure 3-16.

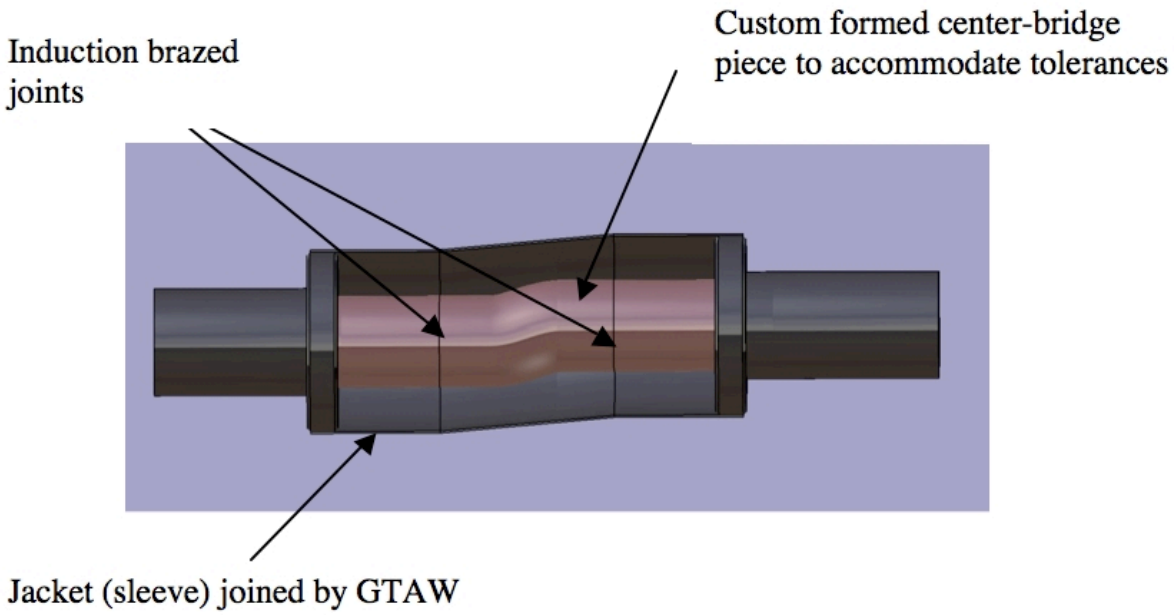

Figure 3-16 Coil-Feeder Joint

During the initial installation, laser scanners will be used to accurately map the locations of the feeder terminations relative to the coil terminations. A custom fitted bridge piece is used to accommodate misalignment between the feeder and coil connection. This information will permit the custom bridge piece to be designed using CATIA. The bridge piece will be formed

using progressive forming dies. Both planar and scarf joint interfaces are being considered. Split induction coils will be used to heat the joints for silver brazing. NDT testing is likely to be a combination of joint resistance, helium leak testing, ultrasonic testing, and X-ray examination. Both split and slide over configurations are being considered for the stainless steel jacket, which will be joined by GTAW (gas tungsten arc welding) using orbital welders in combination specially developed weld equipment and techniques for longitudinal seams. The weld joints will likely be subject to helium leak testing in combination with x-ray examination. The annulus between the sleeve and copper bridge piece may be filled with mineral powder introduced through ports or, alternatively, split ceramic insulating sleeves may be used between the sleeve and copper bridge piece.

3.5 DC BUS BAR

Although the DC bus bar is out of scope of the TA it is necessary to rough out a design and estimate electrical parameters in order that the overall loop impedance and required power supply voltage can be determined.

The ELM and VS bus bar provides a connection between the feed-thrus at the machine ports to the power supplies which are located on an upper level of the Tokamak Complex. The IO has performed layout studies as shown in Figure 3-17 and Figure 3-18 and has supplied the lengths[40]. For ELM the average length per pole is 30m and for VS it is 47m per pole. Note that, for ELM, the DC bus consists of 2 poles per coil circuit, one (+) and one (-). However, for VS, there are actually 16 poles in the circuit because each of the 4 turns in the upper and lower coils has its (+) and (-) poles routed to the power supply area. See Figure 3-19. So the total for VS is 2 poles per turn * 4 turns per coil * 2 coils = 16 poles.

[40] e-mail from E. Daly 3/25/10 and ELM_VS3_LENGTH-Updated.ppt

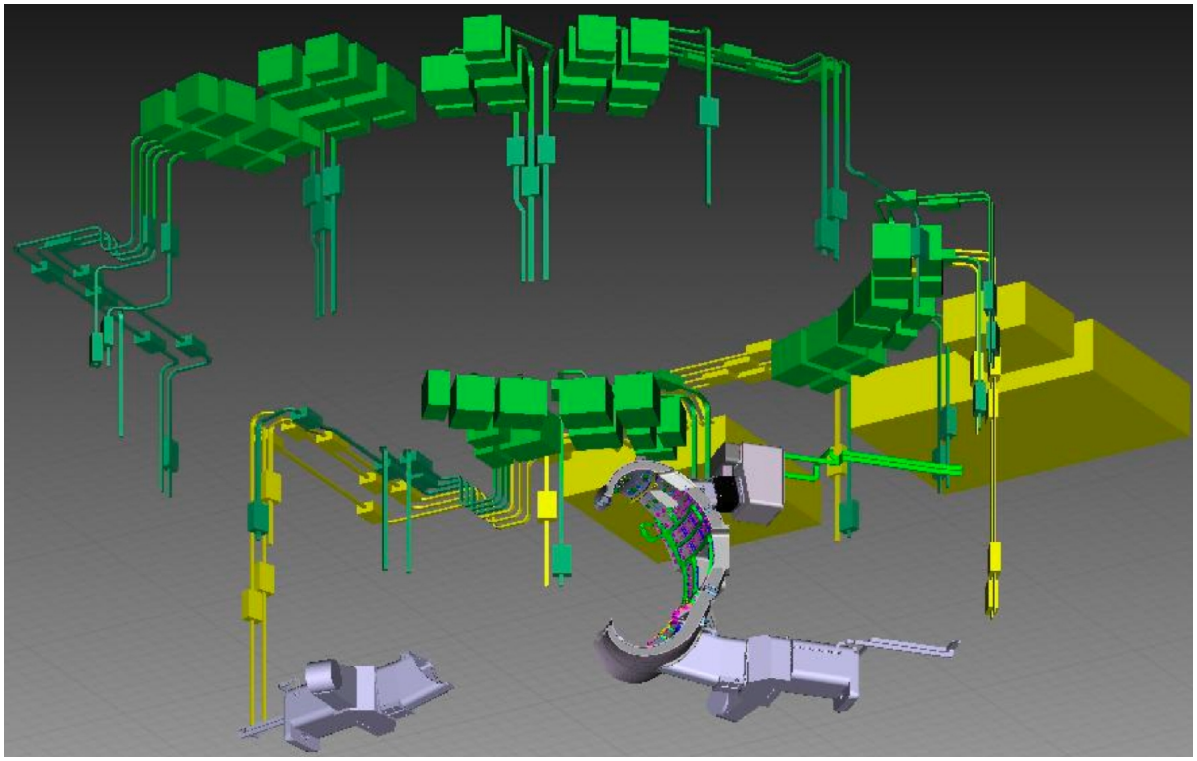

Figure 3-17 Arrangement of DC Bus Bars and Power Supplies

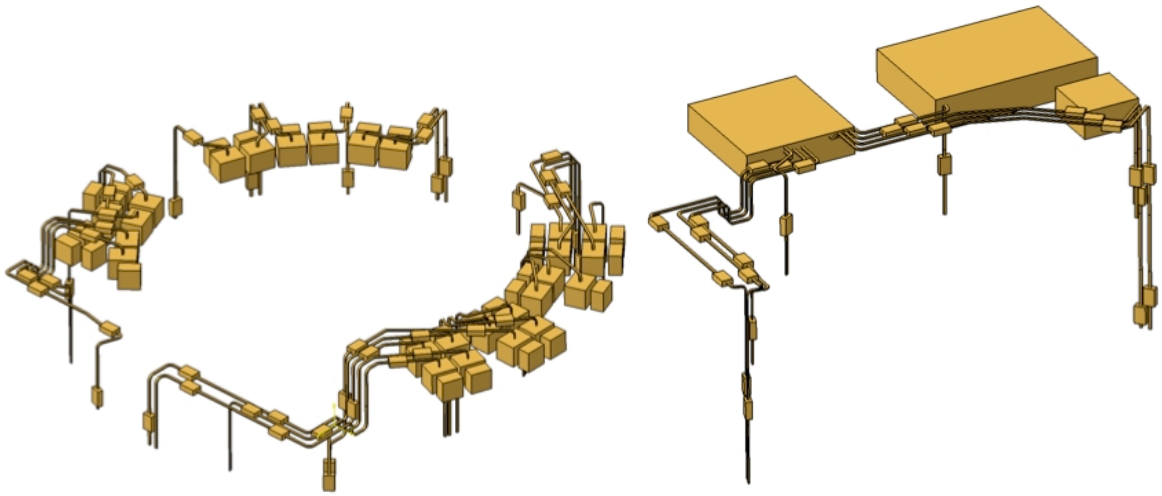

Figure 3-18 ELM (left) and VS (right) DC Bus Bar

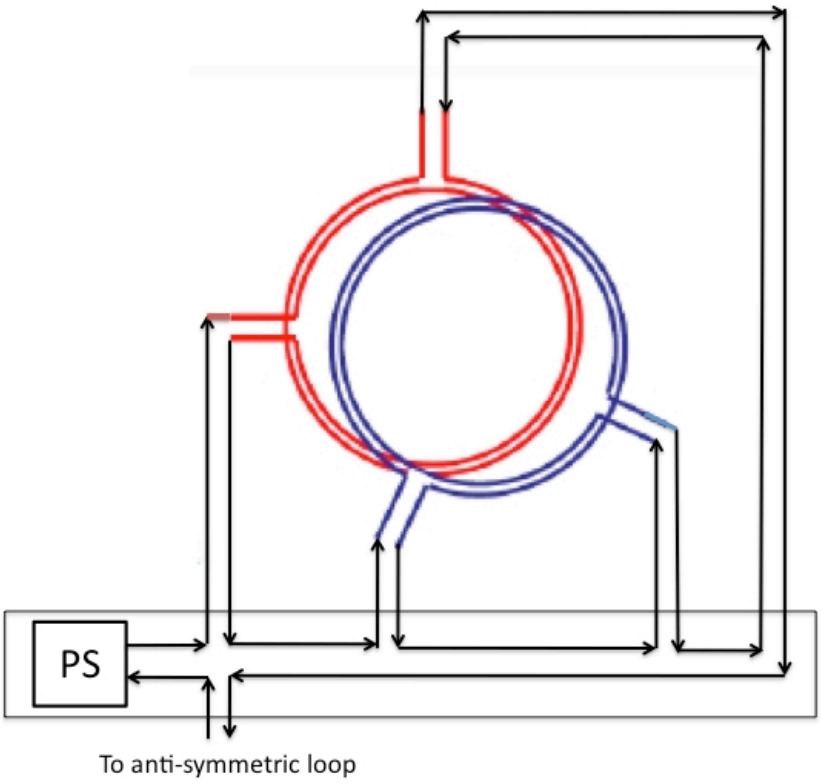

Figure 3-19 VS DC Bus Bar Connections to Individual Coil Turns

When sizing the bus bars it was decided to utilize copper conductor with a cross section of 50 mm x 100 mm and a 17.5mm cooling hole. This is similar to the largest standard size available from Luvata, a major producer (http://www.luvata.com/en/Products--Markets/Products/Hollow-Conductors/) of copper conductors. Based on a extrusion billet size of 250kG this corresponds to individual sections of approximately 6m length. Copper conductor is favorable for this application due to the higher achievable current density (more compact size) compared to aluminum as well as the fact that the local component cooling water system will cool other copper components in the power supplies and mixed metals must be avoided. Two options for the configuration were considered:

- 2 parallel conductors per pole with 1 water loop which goes from the "Power Supply" (PS) area through one pole to the VV port interface and then back through the other pole to the PS area
    - set water flow to limit water ΔT to 10°C to limit thermal stresses between the poles in case they are bundled
- 1 conductor per pole with 2 water loops, one water loop per pole.
    - set the water flow to limit dT to 25C
    - additional piping would be needed to return the water to the PS area from the VV interface

The first option was selected.

The DC bus bar details are published on a web site:

http://www.pppl.gov/~neumeyer/ITER_IVC/Design_Point.html

and summarized in the appendices of this report. The DP XL spreadsheets "ELM_Design_Point_YYMMDD.xls" and "VS_Design_Point_YYMMDD.xls", where YYMMDD is year, month, day of revision, contain all of the calculations and are downloadable from the web site. Overall circuit parameters are summarized in later sections of this report.

3.6 COOLING WATER SYSTEM

Cooling water is provided by the Tokamak Cooling Water System (TCWS – PBS26) and is not within the scope of the IVC WBS. The cooling water is required to reject the heat in the coils from both the nuclear heating and the resistive heating generated during pulsed operation. The TCWS also provides hot water during bakeout operations at which time the coils are heated to 240C over the course of 100hrs.

Table 3-2 summarizes the parameters for the interface with the cooling water system.

Table 3-2 IVC water supply from the TCWS

	Normal Operation	**During Baking**
Inlet water temperature	100 C	240 C
Maximum outlet temperature	167 C	240 C
Inlet pressure	3.0 MPa	4.4 MPa

The pressure loss through the coils must not exceed 1MPa to keep the coil discharge pressure from dropping below the vapor pressure of water at the operating temperature. The required pressure drop to maintain 3 m/s in the coils is approximately 0.25MPa. This leaves adequate margin with respect to providing larger flows at a larger pressure drop without dropping below the vapor pressure limit. The available pressure provided by the TCWS is well in excess of the pressure necessary to achieve the flow rate required for rejecting the heat. The flow to both the ELM and VS coils will be throttled at the cooling water discharge so that the pressure drop across the coils is maintained at the required value.

4 RADIATION EFFECTS

4.1 ELM COIL NUCLEAR FLUX, FLUENCE AND HEATING

4.1.1 Introduction to ELM Coil Analysis

For the ELM coil analysis, initial 1-D and simplified homogenized 3-D analyses[41,42] were performed to determine radiation parameters expected in both poloidal and toroidal legs of the ELM coils. This work examines a more detailed 3x2 ELM coil along the toroidal and poloidal leg. Results were normalized for the peak outboard neutron wall loading of 0.75 MW/m^2 to be conservative (as shown in Figure 4-1). Cumulative end-of-life parameters were calculated for the 0.3 MWa/m^2 total average FW fluence (based on 0.56 MW/m^2 average NWL that corresponds to 0.54 FPY). For the toroidal and poloidal leg analysis, the MCNPX-2.7a Monte Carlo transport code[43] was used with the continuous energy FENDL-2.1 cross section library[44].

---

[41] T.D. BOHM and M.E.SAWAN, "Neutronics Analysis for Gap Streaming Effect on ITER ELM Coils", powerpoint memo July 28, 2008.

[42] M.E. SAWAN and T.D. BOHM, "ELM Coils: Nuclear Environment and Shielding Issues", presented at the 5th ITER Neutronics Meeting, February 8-9, Aix-en-province, France, ITER_D_35SK5T, 2010.

[43] D. PELOWITZ, editor, "MCNPX User's Manual version 2.6.0", *Los Alamos National Laboratory Report*, LA-CP-07-1473, April (2008)

[44] D.L. ALDAMA and A. TRKOV, "FENDL-2.1, Update of an Evaluated Nuclear Data Library for Fusion Applications," Report INDC(NDS)-467, International Atomic Energy Agency (2004)

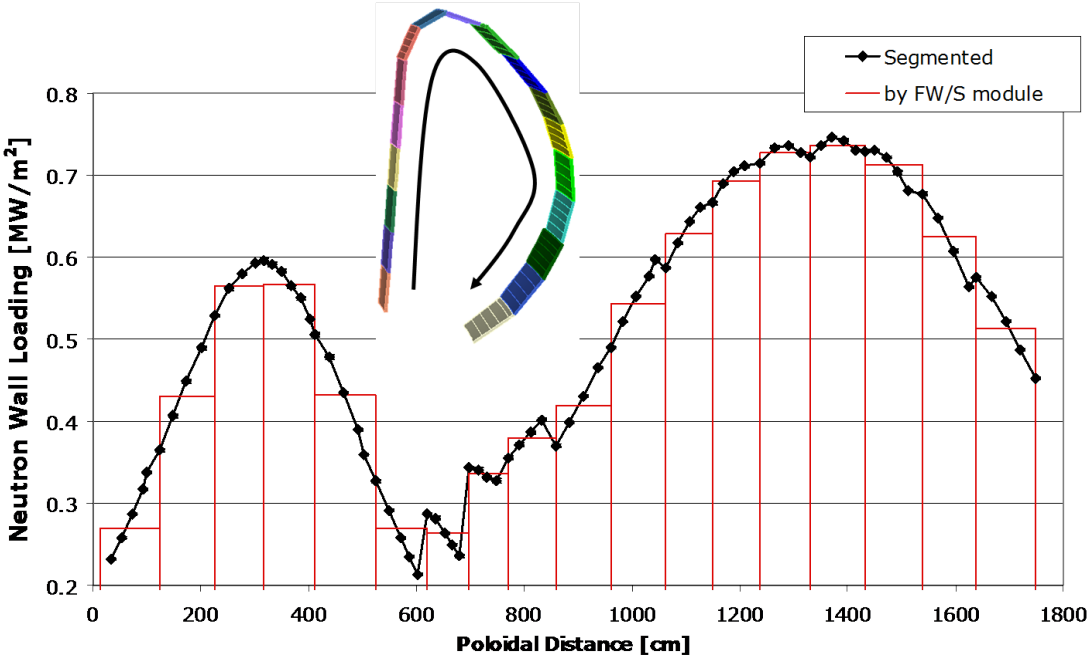

Figure 4-1 Neutron Wall Loading versus Poloidal Distance/FWS Module

4.1.2 **Analysis of the toroidal leg of the ELM coil**

Figure 4-2 shows the location of the toroidal leg geometry that was chosen for analysis. This section of the toroidal leg was chosen because one of the turns of the coil is directly in line with the FWS modules' toroidal gap which is likely to cause a peak in radiation damage parameters to the coil. A partially homogenized 3-D MCNP model of the ITER machine was created. This model is a cylindrical 5 degree sector, 45 cm in height, and includes homogenized inboard and outboard components of ITER along with the detailed geometry of the 3x2 ELM coil. There are reflecting boundaries at the top and bottom of the model as well as at the 0 degree and 5 degree wedge boundaries. There is a 2 cm toroidal gap between the FWS modules. The source is modeled as a uniform 14.1 MeV neutron source in the interior region (r=519-719 cm) of the plasma. Figure 4-3 shows a close up 3-D view of the MCNP model of the toroidal leg of the 3x2 ELM coil that was developed. The coil model uses pure Cu conductor with compacted powder Spinel (MgO-Al2O3) insulator (rho= 3.38 g/cm^3) and SS-316L(N)-IG casings. For this analysis, the 54 mm coil was modeled (this is the outside diameter of the SS casing).

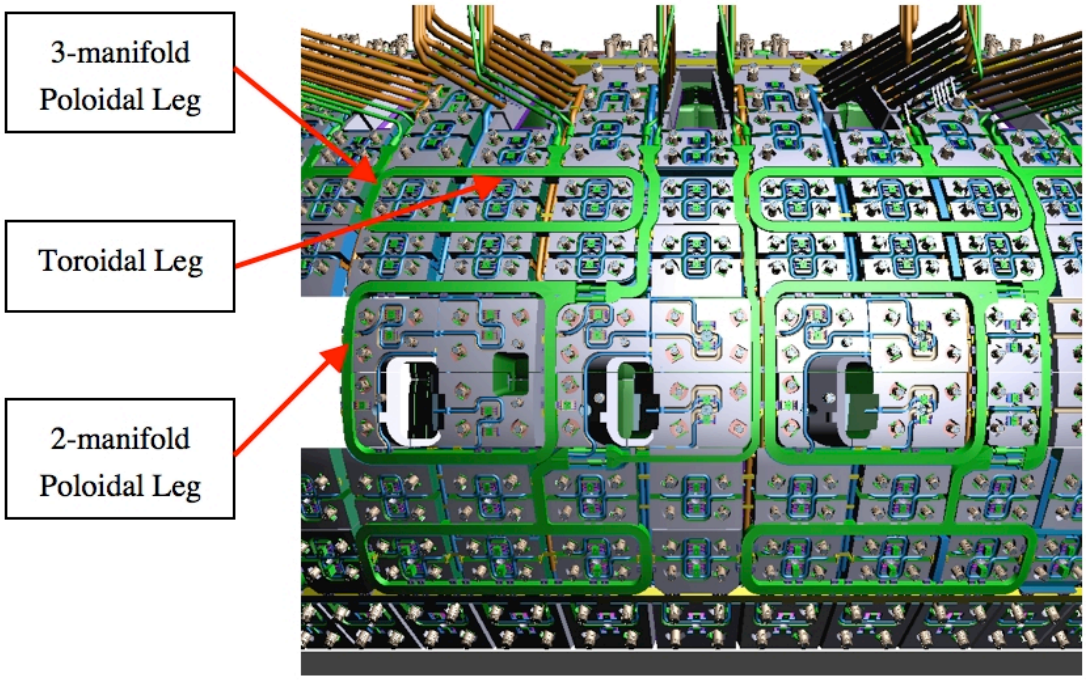

Figure 4-2 Location of the ELM coil leg geometry

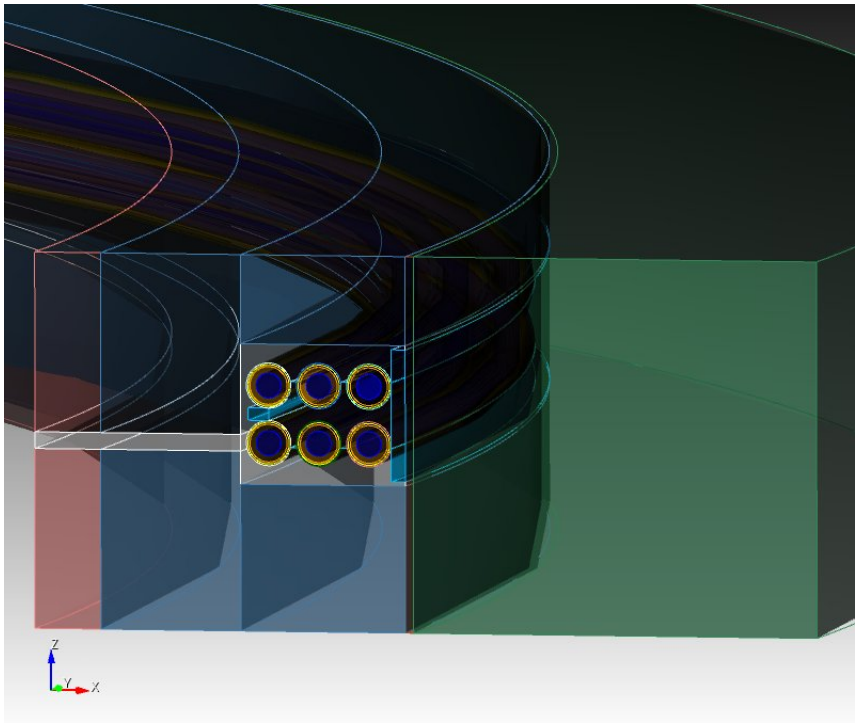

Figure 4-3 MCNP model of the toroidal leg of the ELM coil

Error! Reference source not found. shows the nuclear heating (in W/cm3) in the toroidal leg. The nuclear heating peaks in the Cu conductor nearest the FWS module gap at 1.68 W/cm3. Figure 4-5 shows the heating profile along two sections of the ELM coil. The profiles are taken along the dotted lines as indicated in the inset figure in the graph. These profiles clearly show the low nuclear heating in the water coolant channels as well as the high heating in the Cu conductors. The profiles also clearly show that there is higher heating in the lower turns as compared to the upper turns at a given distance from the plasma. This is expected since the lower turns are directly in line with the toroidal gap.Table 4-1 gives the cell (volume) averaged heating by component for the toroidal ELM. Figure 4-6 shows the corresponding cell number for each component. These nuclear heating results can then be used as input for thermal stress analysis and computational fluid dynamics codes (CFD) for further engineering analysis.

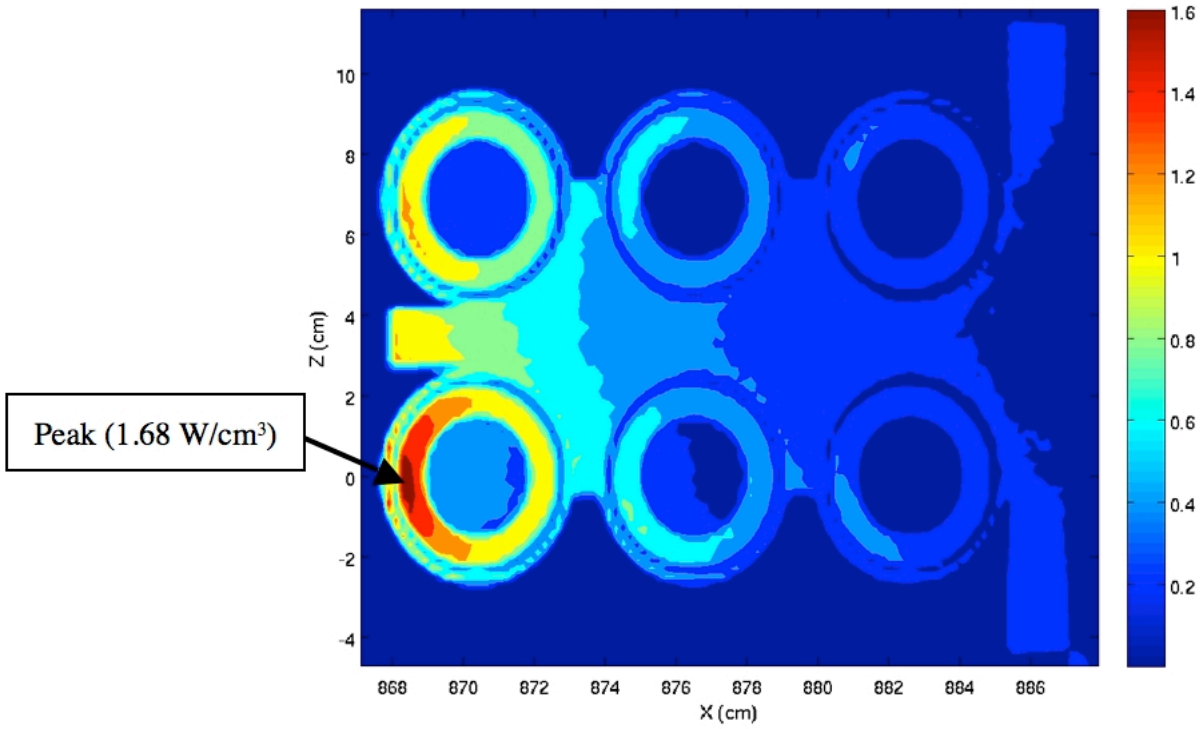

Figure 4-4 Nuclear heating (W/cm3) in the toroidal leg of the ELM coil

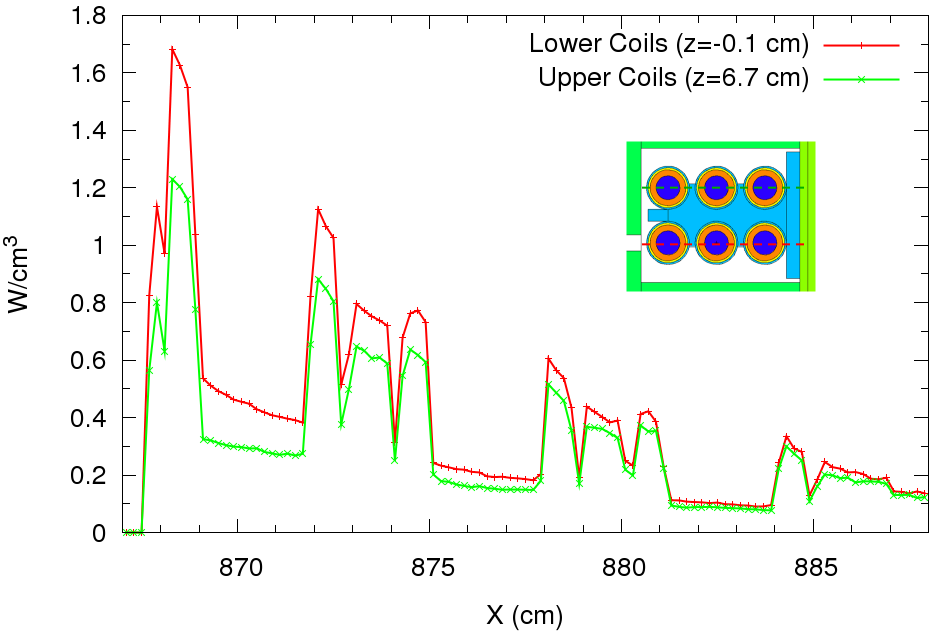

Figure 4-5 Nuclear Heating profiles in toroidal leg

Table 4-1 Cell (volume) averaged heating in toroidal ELM coil

Cell	Component	Heating (W/cm3)
101	bracket	0.212
102	spacer	0.445
103	stub	1.075
111	case1	0.902
112	case2	0.476
113	case3	0.273
114	case4	1.075
115	case5	0.555
116	case6	0.311
121	insulator1	0.368
122	insulator2	0.199
123	insulator3	0.110
124	insulator4	0.476
125	insulator5	0.241
126	insulator6	0.131
131	conductor1	1.004
132	conductor2	0.549
133	conductor3	0.310

134	conductor4	1.252
135	conductor5	0.639
136	conductor6	0.363
141	coolant1	0.295
142	coolant2	0.157
143	coolant3	0.086
144	coolant4	0.450
145	coolant5	0.205
146	coolant6	0.105

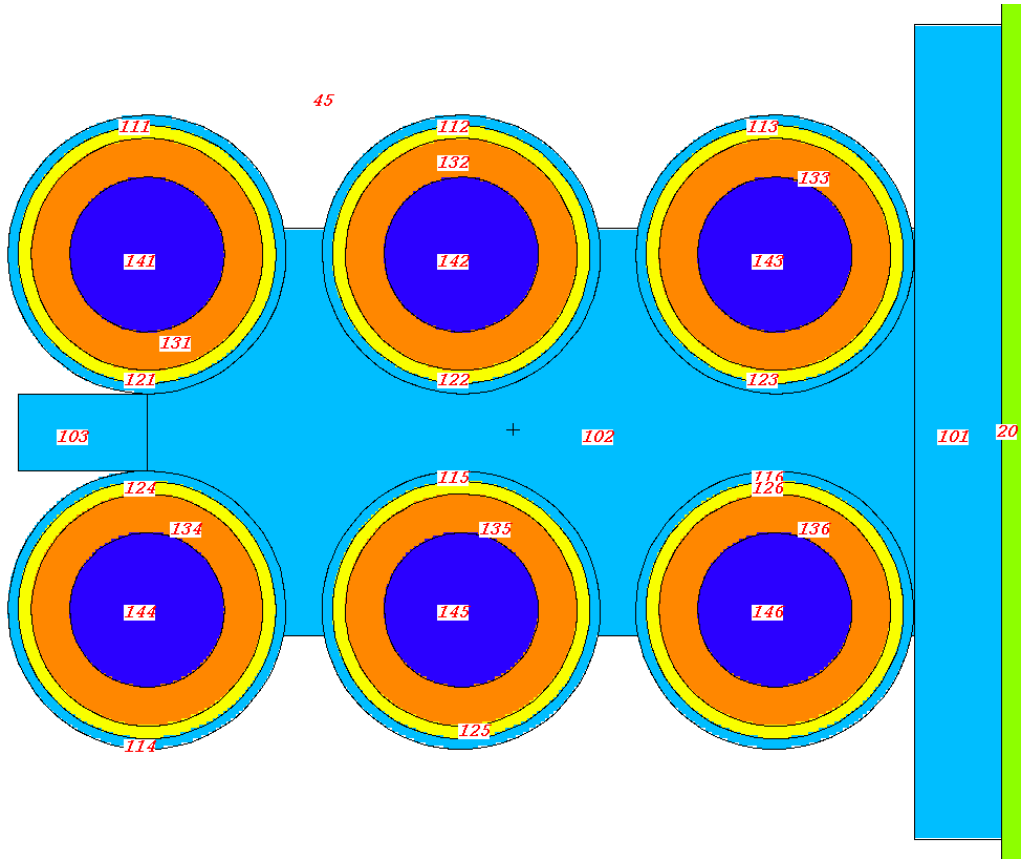

Figure 4-6 Cell numbers indicating ELM components

Peak radiation damage values for the toroidal leg in the turn nearest the FWS module gap are given in Table 4-2.

Table 4-2 Peak radiation damage parameters in toroidal ELM leg

	Current	**Homogenized (2008)**
Spinel Insulator		
Fast neutron fluence (n/cm^2)	2.77e20	2.22e20

Dose rate (Gy/sec)	203	160
SS casing		
He production (appm)	4.68	-
Cu conductor		
Cu dpa (dpa)	0.259	0.229
Nuclear heating (W/cm^3)	1.59	1.11

These values are volume averaged in the region nearest the gap as indicated in **Error! Reference source not found.**. Also shown in the table are the values from the previous homogenized analysis. He production in SS was also calculated in the "stub" of the Christmas tree support structure of the ELM and at the vacuum vessel just below the "bracket". Here the He production cumulative values are 2.12 appm and 0.68 appm respectively. The ITER recommended limits for re-weldability are 3 appm for thin plate or tube welds and 1 appm for thick plate welds. From Table 2, the peak He production in the SS casing was 4.68 appm, therefore the casing will not meet the re-weldability limit. However, the casing is not intended to be re-welded. The vacuum vessel meets the 1 appm limit for re-weldability along the toroidal leg.

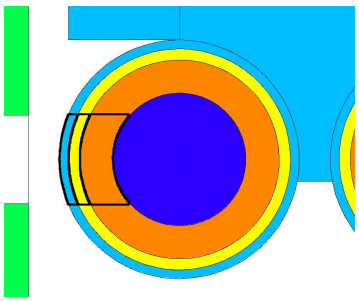

Figure 4-7 Tally volumes used for calculating peak radiation values

4.1.3 Analysis of the poloidal leg of the ELM coil

4.1.3.1 3-manifold version

Figure 4-2 shows the location of the 3-manifold poloidal leg geometry that was chosen for analysis. The radial build used to create the poloidal MCNP model is the same as the toroidal model. For the poloidal model, the geometry is a cylindrical 10 degree sector, 100 cm in height, and includes homogenized inboard and outboard components of ITER along with the detailed

geometry of the 3x2 ELM coil. There are reflecting boundaries at the top and bottom of the model as well as at the 0 degree and 10 degree wedge boundaries. There is a 2.5 cm poloidal gap between the FWS modules. As in the toroidal model, the source is modeled as a uniform 14.1 MeV neutron source in the interior region (r=519-719 cm) of the plasma. **Error! Reference source not found.** shows a close up 3-D view of the MCNP model of the poloidal leg of the 3x2 ELM coil that was developed. The coil model is the same as in the toroidal analysis and the manifold model includes SS pipes filled with water. Notice that a large void space exists behind the manifold pipes and adjacent to the ELM coil.

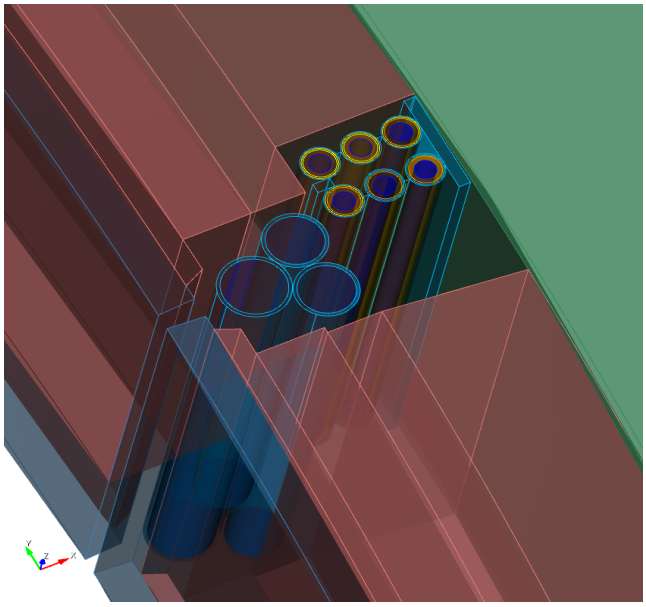

Figure 4-8 MCNP model of the 3 manifold poloidal leg of the ELM coil

Figure 4-9 shows the nuclear heating (in W/cm^3) in the poloidal leg. The nuclear heating peaks in the Cu conductor nearest the FWS module gap at 2.52 W/cm^3. This is 50% higher than that seen in the toroidal leg. The higher heating is expected since the poloidal gap is larger than the toroidal gap (2.5 cm versus 2 cm) and more shield material is removed to make room for the water manifolds. Additionally, the presence of the water softens the neutron spectrum allowing more gammas to be produced which contribute the largest portion of the heating in SS and Cu. Figure 4-10 shows the heating profile along two sections of the ELM coil. The profiles are taken along the dotted lines as indicated in the inset figure in the graph. These profiles clearly show

the higher heating in the turns of the coil nearest the gap. Table 4-3 gives the cell (volume) averaged heating by component for the poloidal ELM. Figure 4-6 shows the corresponding cell number for each component. Looking at the tabulated values, nuclear heating is 20-150% higher in the ELM coil components for the 3-manifold poloidal leg as compared to the toroidal leg.

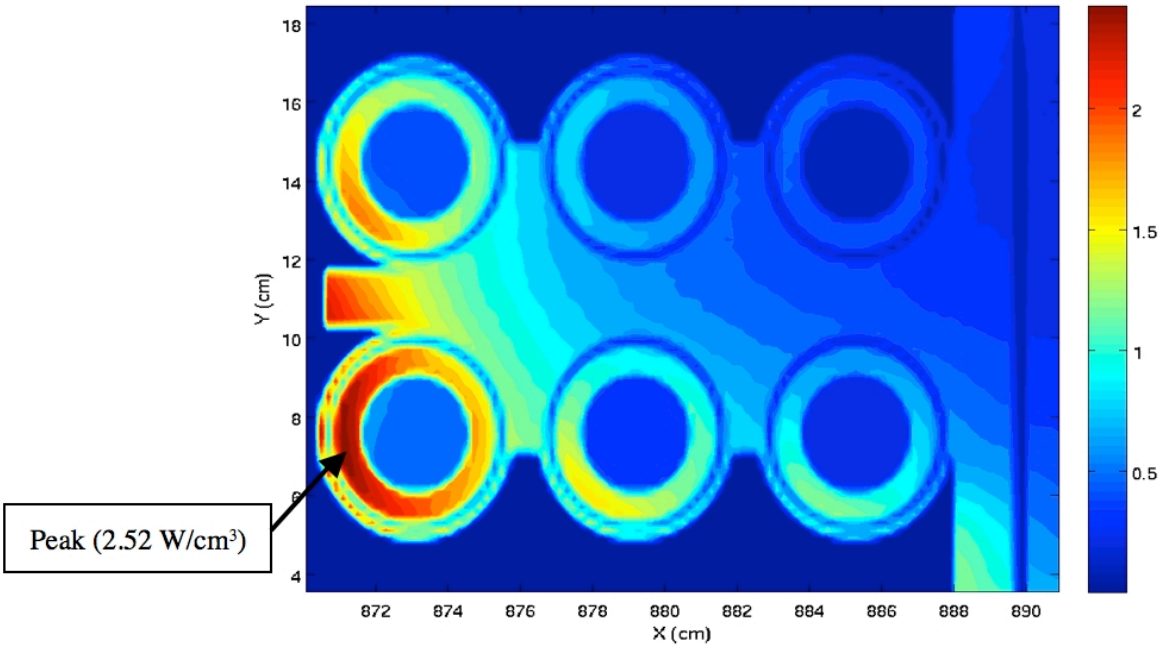

Figure 4-9 Nuclear Heating (W/cm3) in the 3-manifold poloidal leg of the ELM coil

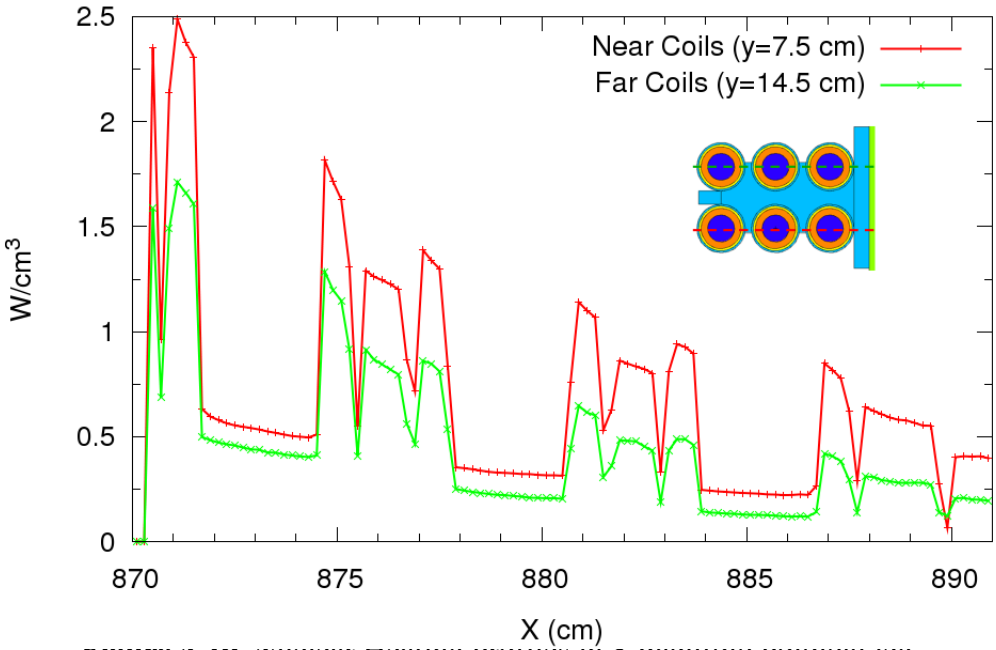

Figure 4-10 Nuclear Heating profiles in 3-manifold poloidal leg

Table 4-3 Cell (volume) averaged heating in 3-manifold poloidal ELM coil

101	bracket	0.503
102	spacer	0.708
103	stub	1.830
111	case1	1.265
112	case2	0.653
113	case3	0.398
114	case4	1.804
115	case5	1.071
116	case6	0.795
121	insulator1	0.545
122	insulator2	0.276
123	insulator3	0.163
124	insulator4	0.745
125	insulator5	0.440
126	insulator6	0.321
131	conductor1	1.426
132	conductor2	0.724
133	conductor3	0.448

134	conductor4	1.999
135	conductor5	1. 203
136	conductor6	0.884
141	coolant1	0.442
142	coolant2	0.227
143	coolant3	0.130
144	coolant4	0.542
145	coolant5	0.330
146	coolant6	0.234

Peak radiation damage values for the 3-manifold poloidal leg in the turn nearest the FWS module gap are given in Table 4-4. These values are volume averaged in the region nearest the gap as indicated in Figure 4-11. The fast neutron fluence in the insulator peaks in the upper segment of the indicated insulator region whereas the other radiation damage parameters peak in the regions nearest the manifold. He production in SS was also calculated in the manifold pipes, the "stub" of the Christmas tree support structure of the ELM coils, and at the vacuum vessel below the ELM "bracket". For the manifolds, the volume averaged He production in the SS pipe is ~23 appm for the plasma facing manifold and ~11 appm for the two manifolds located away from the plasma. For the "stub", the He production is 4.2 appm and up to 3.8 appm for the vacuum vessel below the ELM bracket. From Table 4-4, the peak He production in the SS casing is 5.78 appm. Therefore the ELM casing, ELM stub, SS piping in the manifolds, and the vacuum vessel will not meet the re-weldability limit set for ITER. However, re-welding the ELM coil is not planned so excess He is not an issue. Additionally, re-welding the VV is not planned at this location.

To address thermal stress concerns in the VV, the nuclear heating in the front (plasma facing) 1 cm depth of the VV was calculated. The nuclear heating peaked at 1.0 W/cm3 at the front of the VV in the void region behind the manifolds and adjacent to the ELM coil. Behind the ELM coil bracket, the VV heating ranged from 0.23 W/cm3 to 0.87 W/cm3. The 10° sector average heating in the front 1 cm of the VV was 0.20 W/cm3. This results in a peaking factor of 5 which exceeds the recommended value of 4 for local heating in the VV and may require further analysis.

Table 4-4 Peak radiation damage parameters in 3-manifold poloidal ELM leg

	Current	Homogenized (2008)
Spinel Insulator		
Fast neutron fluence (n/cm^2)	2.70e20	1.05e20
Dose rate (Gy/sec)	279	177
SS casing		
He production (appm)	5.78	-
Cu conductor		
Cu dpa (dpa)	0.251	0.121
Nuclear heating (W/cm^3)	2.39	1.42

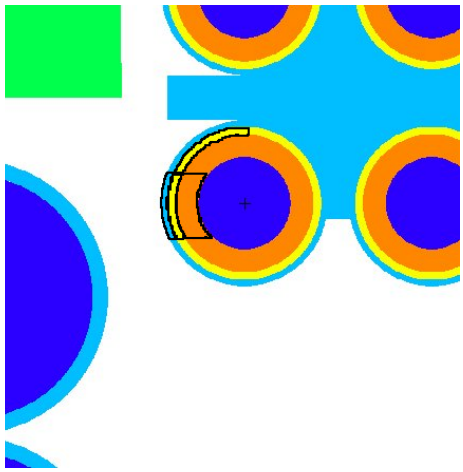

Figure 4-11 Tally volumes used for calculating peak radiation values in 3-manifold poloidal leg

4.1.3.2 2-manifold version

Figure 4-2 shows the location of the 2-manifold poloidal leg geometry that was chosen for analysis.

Figure 4-12 shows a close up 3-D view of the MCNP model of the 2-manifold poloidal leg of the 3x2 ELM coil that was developed for this work. The radial build and source were identical to that used for the 3-manifold poloidal leg model.

Figure 4-13 shows the nuclear heating (in W/cm^3) in the 2-manifold poloidal leg. The nuclear heating peaks in the Cu conductor nearest the FWS module gap at 2.41 W/cm^3. This is 4% lower than that seen in the 3-manifold poloidal leg. Figure 4-14 shows the heating profile along two sections of the ELM coil. The profiles are taken along the dotted lines as indicated in the inset

figure in the graph. Table 4-5 gives the cell (volume average) heating by component for the 2-manifold poloidal ELM. Figure 4-15 shows the corresponding cell number for each component. Looking at the values in the table, the nuclear heating is 4-17% lower in the ELM coil components for the 2-manifold poloidal leg as compared to the 3-manifold poloidal leg. This reduction in heating is due to the reduced water content in the manifold region which results in less gamma production.

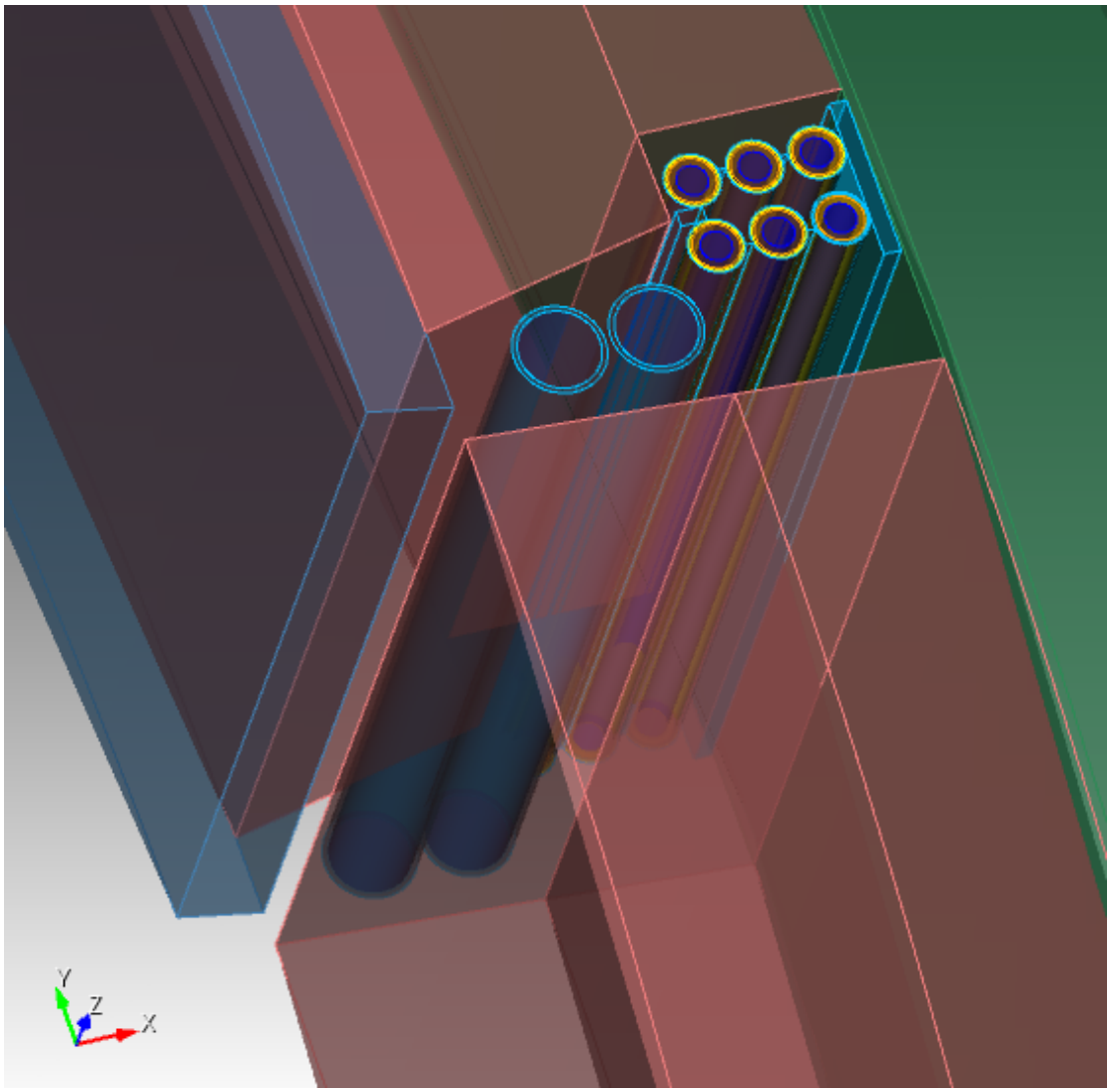

Figure 4-12 MCNP model of the 2 manifold poloidal leg of the ELM coil

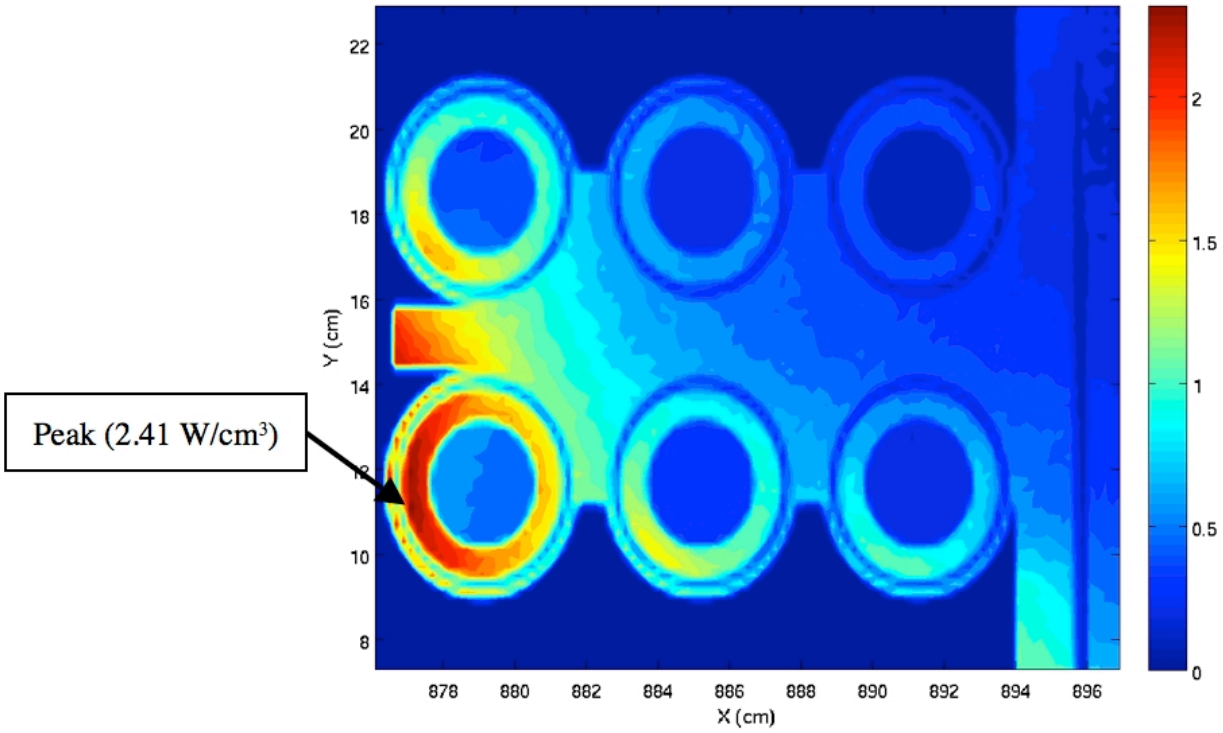

Figure 4-13 Nuclear Heating (W/cm3) in the 2-manifold poloidal leg of the ELM coil

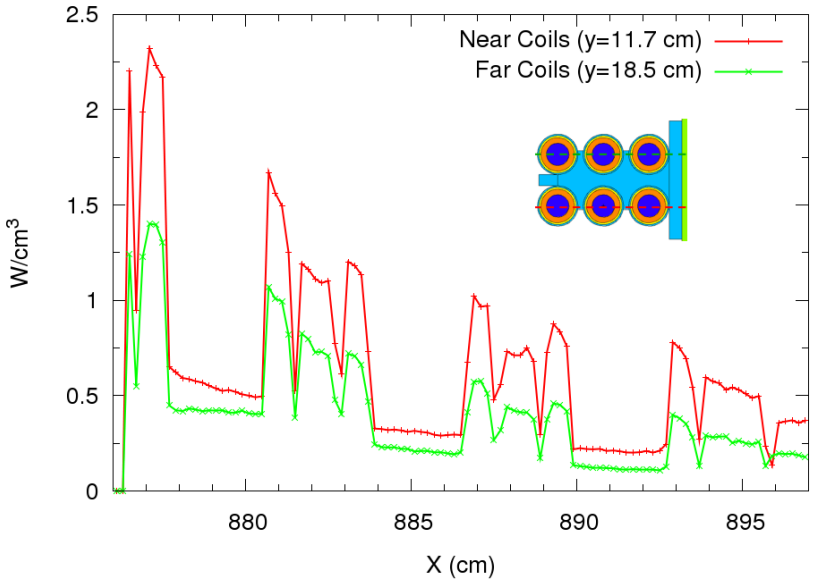

Figure 4-14 Nuclear Heating profiles in 2-manifold poloidal leg

Table 4-5 Cell (volume) averaged heating in 2-manifold poloidal ELM coil

Cell	Component	Heating (W/cm3)
101	bracket	0.454
102	spacer	0.652
103	stub	1.745
111	case1	1.049
112	case2	0.562
113	case3	0.351
114	case4	1.671
115	case5	0.957
116	case6	0.704
121	insulator1	0.479
122	insulator2	0.247
123	insulator3	0.148
124	insulator4	0.711
125	insulator5	0.401
126	insulator6	0.290
131	conductor1	1.199
132	conductor2	0.626
133	conductor3	0.400
134	conductor4	1.854
135	conductor5	1.081
136	conductor6	0.787
141	coolant1	0.423
142	coolant2	0.216
143	coolant3	0.120
144	coolant4	0.552
145	coolant5	0.311
146	coolant6	0.218

Peak radiation damage values for the 2-manifold poloidal leg in the turn nearest the FWS module gap are given in Table 4-6. Figure 4-15 shows the tally volumes where these peaks occurred. Note that fast neutron fluence, He production, and Cu dpa are slightly higher than the values seen for the 3-manifold poloidal case, while insulator dose rate and Cu conductor heating are slightly lower. This is because the reduced amount of water in the manifold region results in a harder neutron spectrum with less gamma generation. He production in SS was also calculated in the

manifold pipes, the "stub" of the Christmas tree support structure of the ELM, and at the vacuum vessel below the ELM "bracket". For the manifolds, the volume averaged He production in the SS pipe is ~23 appm for the plasma facing manifold and ~9 appm for the manifold located away from the plasma. For the "stub", the He production is 5.0 appm and up to 3.6 appm for the vacuum vessel below the ELM bracket. From Table 4-6, the peak He production in the SS casing is 6.2 appm. Therefore the ELM casing, ELM stub, SS piping in the manifolds, and the vacuum vessel will not meet the re-weldability limit set for ITER. Again however, re-welding the ELM coil is not planned and re-welding the VV is not planned at this location.

Table 4-6 Peak radiation damage parameters in 2-manifold poloidal ELM leg

	Current	**Homogenized (2008)**
Spinel Insulator		
Fast neutron fluence (n/cm^2)	2.85e20	1.05e20
Dose rate (Gy/sec)	273	177
SS casing		
He production (appm)	6.21	-
Cu conductor		
Cu dpa (dpa)	0.283	0.121
Nuclear heating (W/cm^3)	2.24	1.42

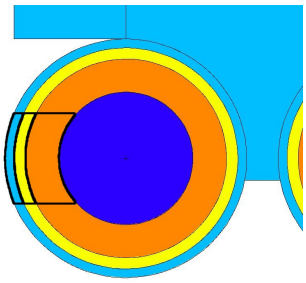

Figure 4-15 Tally volumes used for calculating peak radiation values in 2-manifold poloidal leg

4.1.4 Comparison of ELM coil Results

The poloidal leg of the mid-plane ELM is a common section for comparison of the MCNP and ATTILLA based nuclear analysis. From page 3 of the ATTILLA results[45] the nuclear heating on the SS case appears to peak along the poloidal leg at ~2.4 W/cm^3 (Figure 4-16).

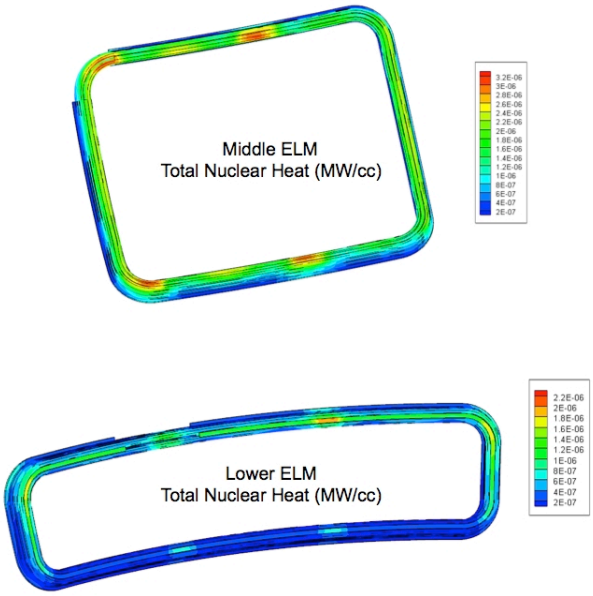

Figure 4-16 ATTILA-based ELM Coil Nuclear Heating Profiles

From Figure 4-14 which shows the nuclear heating profiles in the 2-manifold poloidal MCNP model, the heating in SS peaks at 2.25 W/cm^3. This is only 6% lower than the Attila results and is very good agreement between a Discrete Ordinates based code (ATTILA) and a Monte Carlo code (MCNP). Villari *et al*. independently performed an MCNP5 neutronics analysis[46] of the ITER IVC using the three dimensional, 40° Alite4 MCNP model. A common region for comparison is the upper ELM toroidal profiles (page 28 of the Villari document). Here Villari reports an insulator fast fluence of 1.94e20 n/cm^2 at a lifetime of 0.63 FPY. The toroidal MCNP

[45] R. Feder "ITER In Vessel Coils Neutronics-ATTILA", ITER_IVC_092510.pdf, PDF document Sep. 25, 2010.

[46] R. Villari, L. Petrizzi, G. Brolatti, "Three-Dimensional Neutronic Analysis of the ITER In-vessel Coils, ITER_D_3LCD6P, https://user.iter.org/?uid=3LCD6P, July 7, 2010.

model developed for the current work determined an insulator fast fluence of 1.84e20 n/cm^2 at 0.54 FPY and a NWL of 0.75 MW/m^2. If this number is scaled by the lifetime 0.63/0.54 and the NWL at the upper ELM (0.65/0.75) this gives a value of 1.86e20 n/cm^2 which is 4% lower than the result of Villari. At this same toroidal position, Villari reported heating in the conductor nearest the gap of 0.96 W/cm^3. The toroidal model for the current work showed heating of 1.25 W/cm^3 (from Table 4-1). If this value is scaled by the NWL ratio at the upper ELM to the peak NWL (0.65/0.75), this results in the conductor heating of 1.08 W/cm^3. This is 13% higher than Villari's results which is very good agreement.

4.1.5 **Overall Nuclear Heating Contours and ELM Peak**

Overall heating contours from the combined ELM/VS ATTILA modeling[47] is given in Figure 4-17. Peak dose to the SSMIC MgO is ~ 500Gy/s.

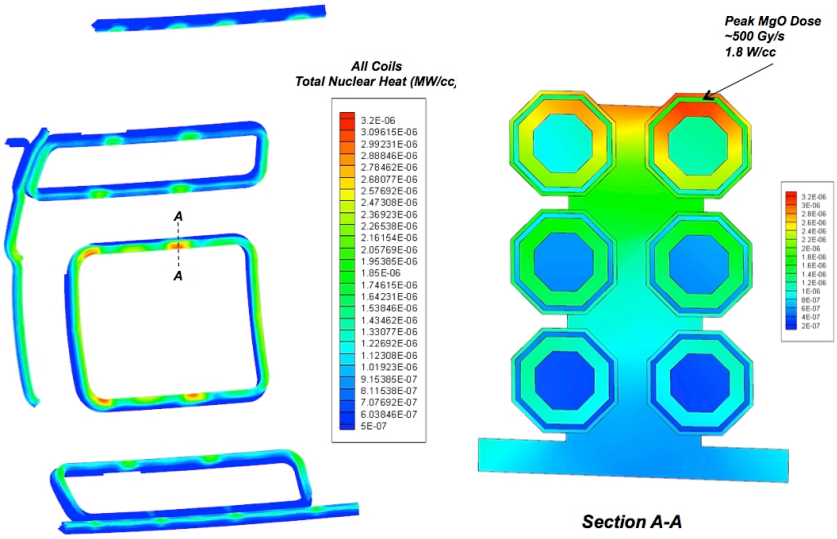

Figure 4-17 Overall ELM Contours and Local Peak

[47] "ITER In-Vessel Coils Neutronics Analysis ATTILA Discrete Ordinates Transport Code", Feder, 9/29/10

4.2 VS COIL NUCLEAR FLUX, FLUENCE AND HEATING

4.2.1 Upper and Lower VS Analysis CAD Model

Figure 4-18 and Figure 4-19 highlight features of the Upper and Lower VS analysis CAD Model. The model is a 90-degree slice of the ITER in-vacuum components. No external field coils were modeled and no port extensions were modeled. Detailed models of the shaped wall-mounted blanket modules are included around the upper and lower VS coils. All other wall mounted modules are simplified as per the A-Lite 04 model.

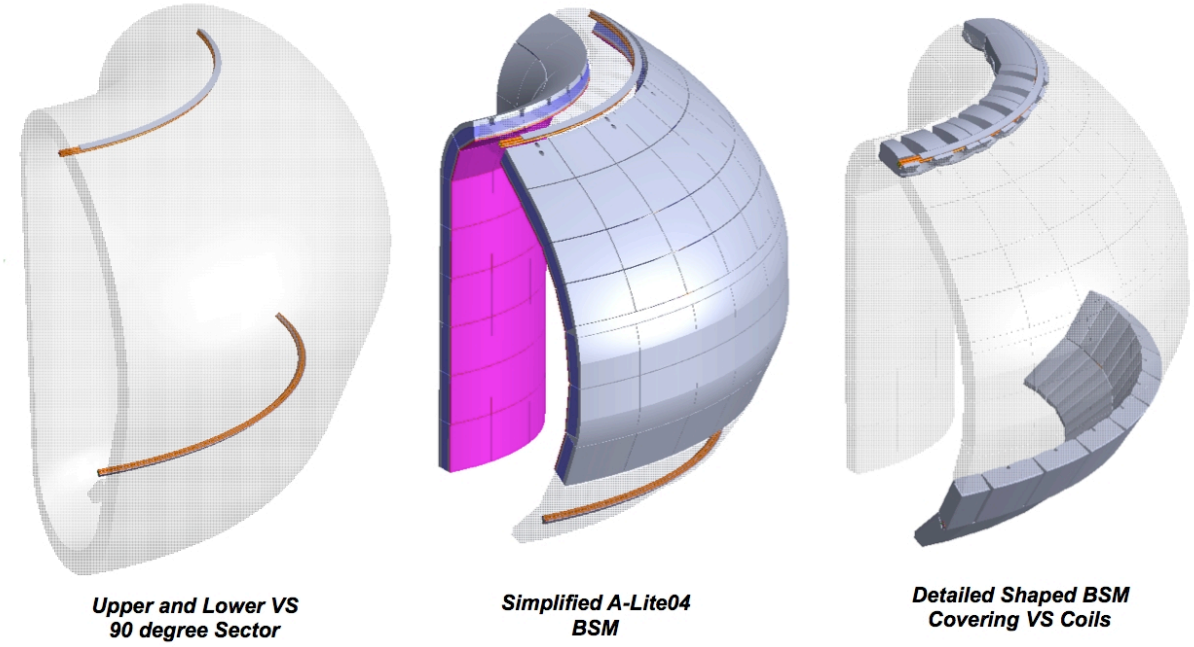

Figure 4-18 Upper and Lower VS Neutronics Analysis Model

Figure 4-19 highlights details of structures that overlap the VS coils. On the top of the machine the Upper VS coils are periodically covered by water supply and return piping. There are gaps

between the wall mounted shield that allow neutron and gamma streaming periodically on to the upper and lower VS coils. This is also shown in Figure 4-19.

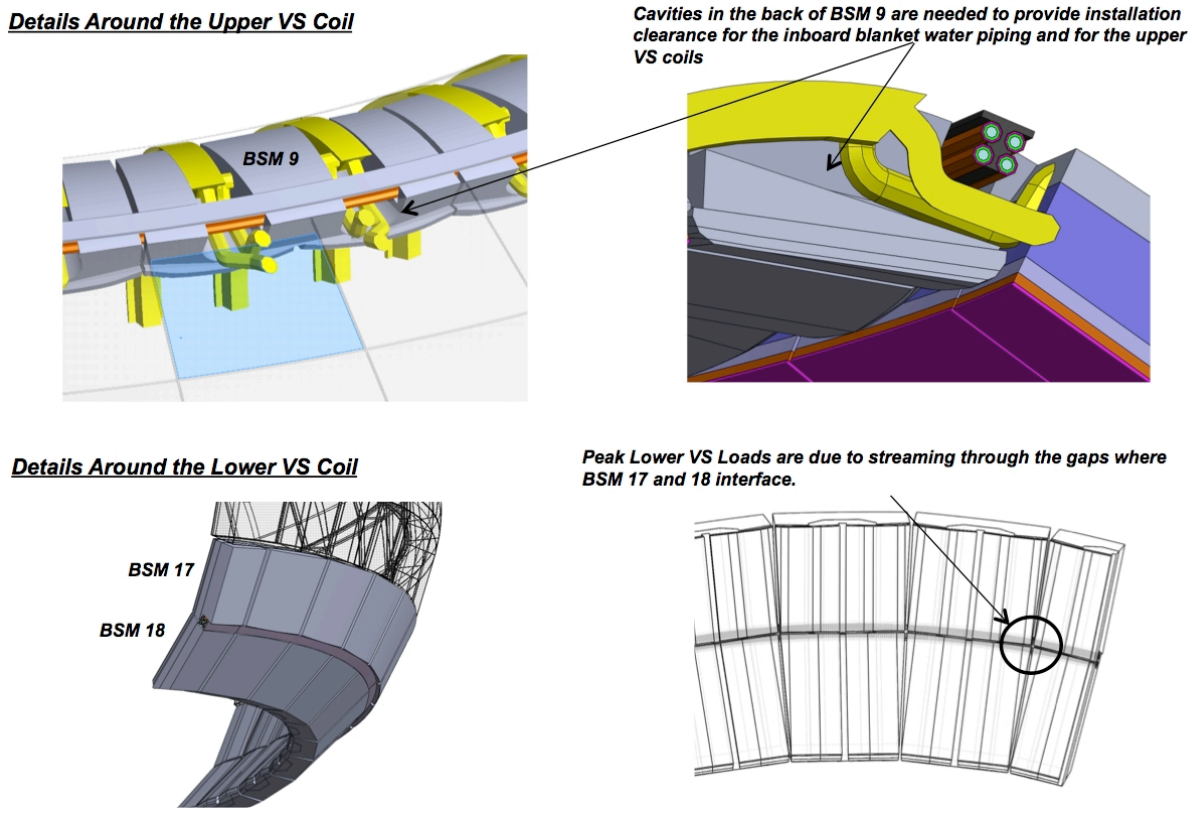

Figure 4-19 Upper and Lower VS Neutronics Analysis Model

4.2.2 **ATTILA Tetrahedral Mesh**

ATTILA applies a tetrahedral mesh to the CAD model. As shown in Figure 4-20 there were 1.6 million mesh cells in the 90-degree Upper and Lower VS model. The full 40-degree ITER IVC analysis model contained 2.1 million mesh cells. Greater mesh refinement was used for the in-vessel coils in the 40 degree model which is why there are more total cells than the 90 degree model.

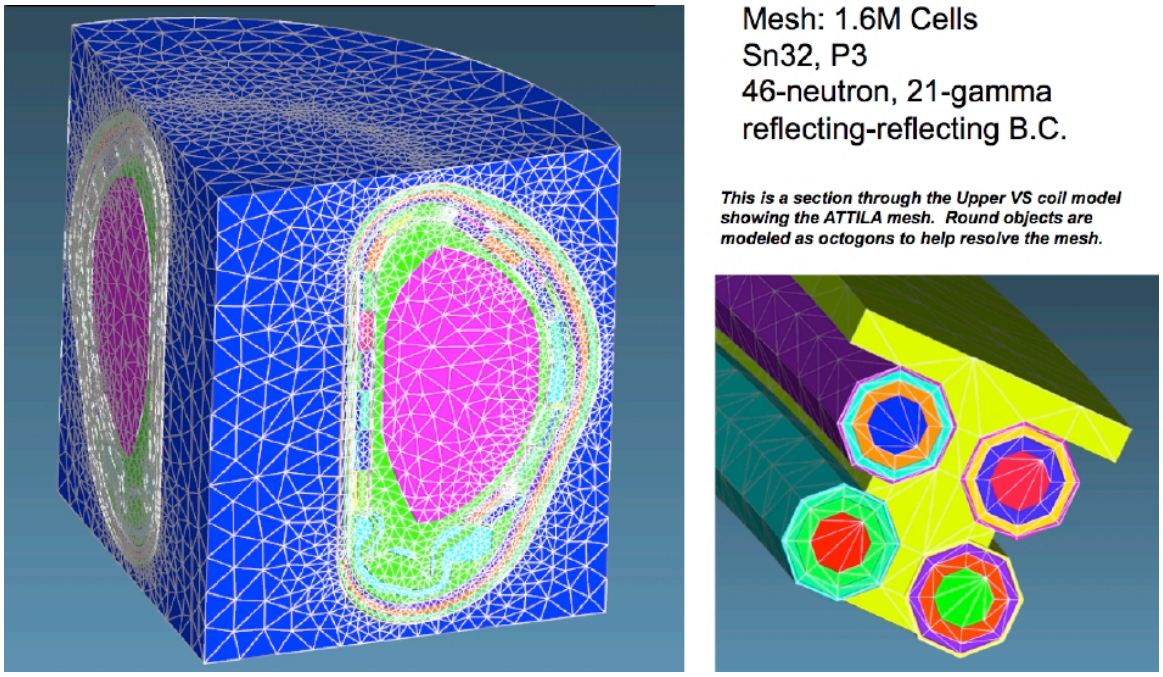

Figure 4-20 ATTILA Mesh

4.2.3 **Volume source definition**

Alite04 provides a standard 500 MW fusion neutron volume source for use with MCNP or ATTILA. 14 MeV neutrons are produced in a 40x40 R-Z grid where each cell in the grid is given a specific source strength from 1 to 0. The source is axisymmetric or uniform in the toroidal direction. Figure 4-21 illustrates the volume source model as well as a typical neutron wall loading chart for ITER.

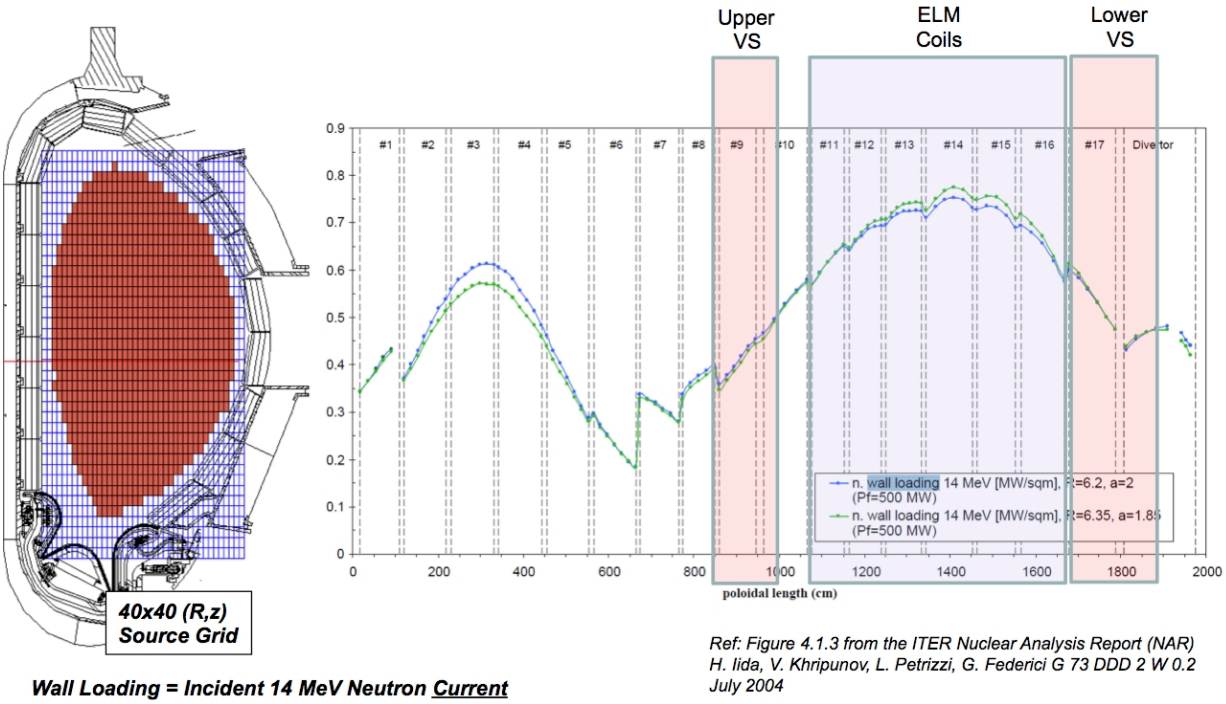

Figure 4-21 Volume Source for VS Neutronics Calculations

4.2.4 VS Neutronics Analysis Results

Figure 4-22 illustrates the total integrated neutron flux solution for the 90-degree ITER Upper and Lower VS model. Neutron streaming through local gaps in the wall mounted blankets is shown on the right side of Figure 4-22. Figure 4-23 through Figure 4-25 provide contour plots of neutron and gamma flux as well as total nuclear heating and total lifetime dose to the MgO insulator for the lower VS coil.

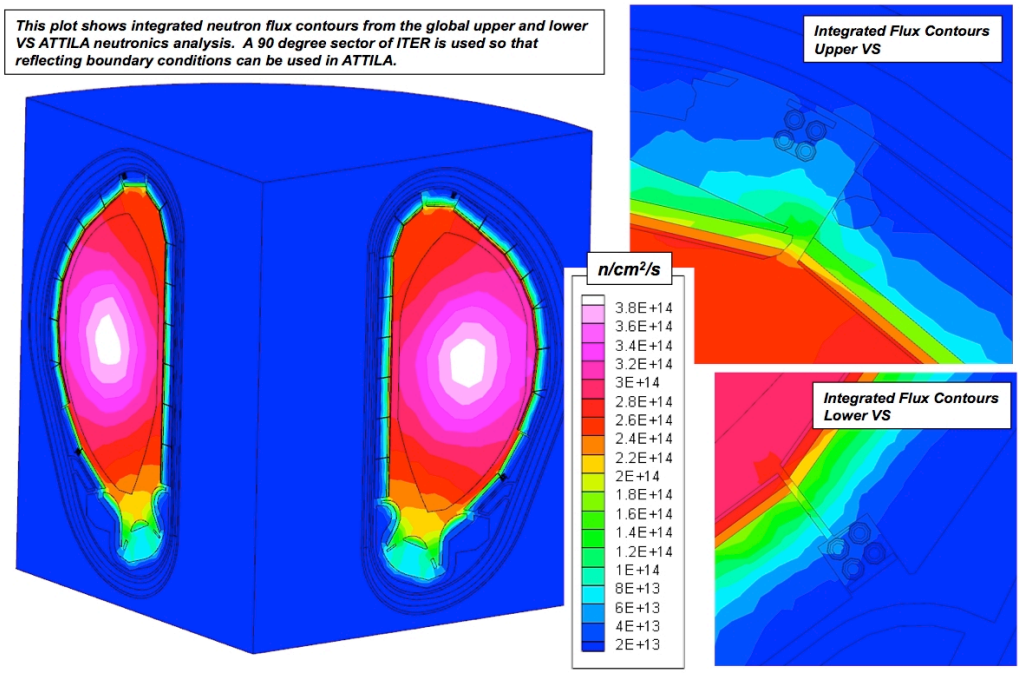

Figure 4-22 Global Upper/Lower VS Model Integrated Neutron Flux

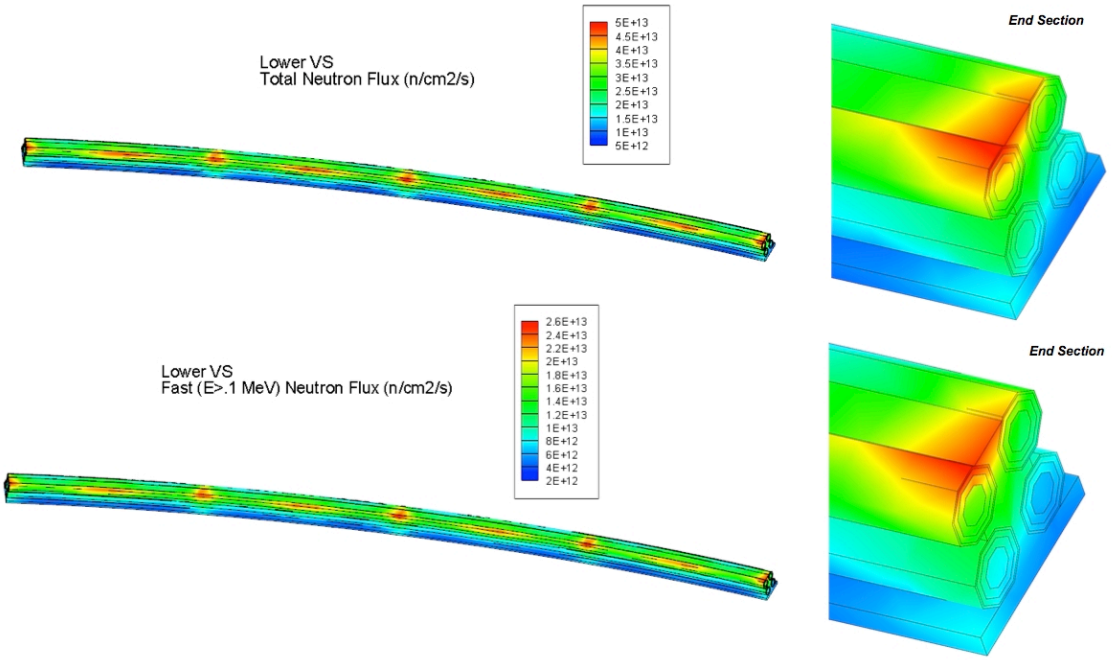

Figure 4-23 Lower VS Coil 40-deg Sector Neutronics Results – n Flux

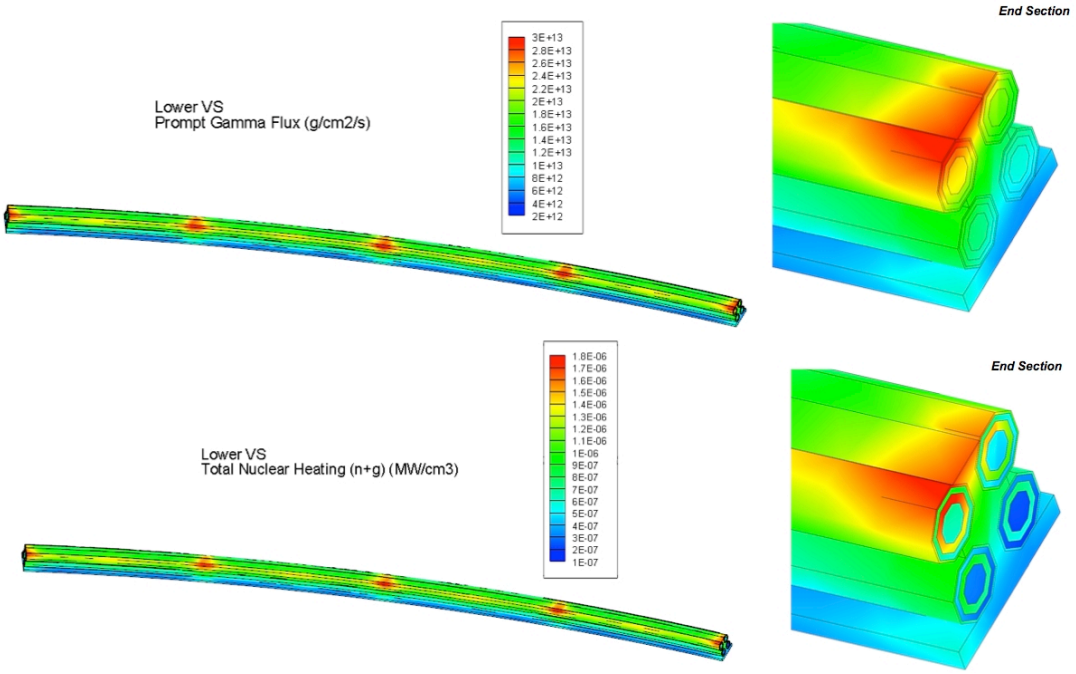

Figure 4-24 Lower VS Coil 40-deg Sector Neutronics Results – gamma flux and n heating

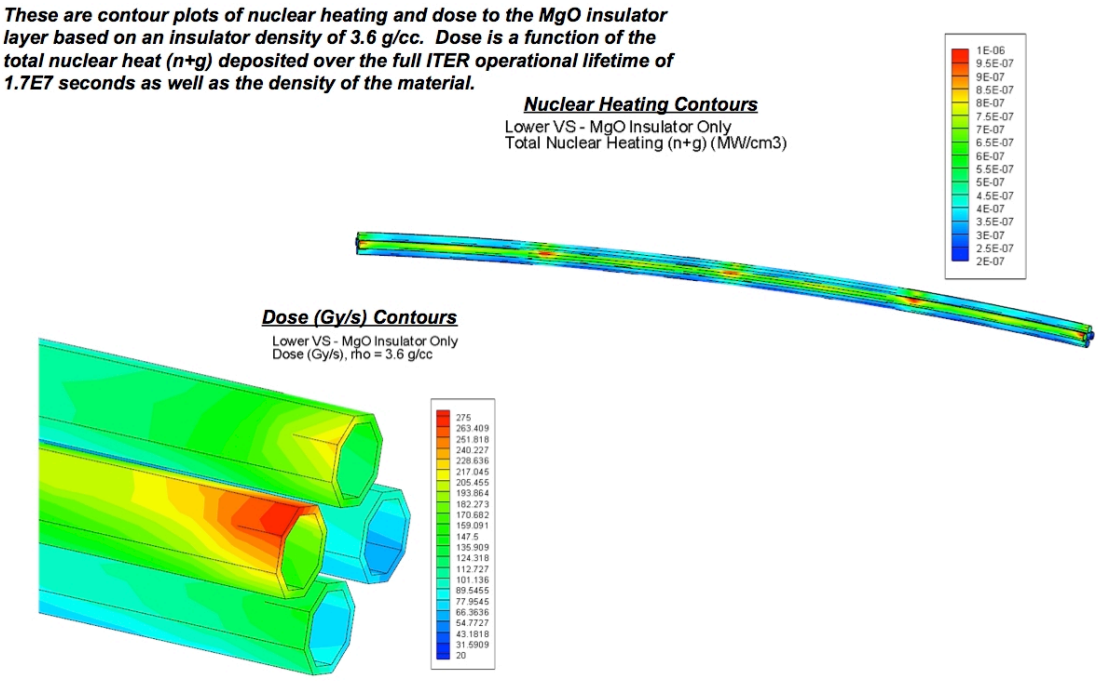

Figure 4-25 Lower VS Coil 40-deg Sector Neutronics Results – MgO Insulator

Flux and heating results for the Lower VS are always higher than for the Upper VS. This can be explained by Figure 4-21. The total neutron wall loading is higher at the Lower VS coils. Upper and Lower VS coils exhibit similar periodic peaking in all values where coils sit behind a gap in the wall mounted blanket modules. Therefore the profile plots for the Upper VS are omitted but are available in the reference.

Average flux in the individual components is summarized in Figure 4-26 and Figure 4-27

Lower VS

Coil 1	n_flux (n/cm2/s)	fast n_flux (n/cm2/s)	g_flux (g/cm2/s)	n_heat MW	n_heat MW/cc	g_heat MW	g_heat MW/cc	total heat MW	total heat MW/cc	Average Dose (Gy/s)
Case	1.96E+13	9.00E+12	1.26E+13	7.94E-05	4.01E-08	1.38E-03	6.97E-07	1.46E-03	7.37E-07	
Insulation	1.96E+13	8.87E+12	1.27E+13	3.80E-04	8.75E-08	1.15E-03	2.64E-07	1.53E-03	3.52E-07	*97.75*
Copper	1.95E+13	8.48E+12	1.25E+13	1.58E-04	3.23E-08	3.92E-03	8.02E-07	4.08E-03	8.35E-07	
Water	2.00E+13	7.44E+12	1.28E+13	7.57E-04	1.94E-07	2.99E-04	7.65E-08		2.70E-07	
Coil 2										
Case	2.76E+13	1.34E+13	1.71E+13	1.66E-04	8.46E-08	1.82E-03	9.28E-07	1.99E-03	1.01E-06	
Insulation	2.78E+13	1.34E+13	1.73E+13	8.01E-04	1.86E-07	1.53E-03	3.56E-07	2.34E-03	5.42E-07	*150.49*
Copper	2.82E+13	1.33E+13	1.74E+13	3.85E-04	7.94E-08	5.28E-03	1.09E-06	5.66E-03	1.17E-06	
Water	2.93E+13	1.22E+13	1.78E+13	1.48E-03	3.81E-07	4.05E-04	1.04E-07		4.85E-07	
Coil 3										
Case	1.10E+13	4.97E+12	6.86E+12	4.10E-05	2.06E-08	7.57E-04	3.81E-07	7.98E-04	4.01E-07	
Insulation	1.10E+13	4.88E+12	6.91E+12	1.98E-04	4.53E-08	6.30E-04	1.44E-07	8.28E-04	1.90E-07	*52.67*
Copper	1.09E+13	4.64E+12	6.83E+12	8.07E-05	1.64E-08	2.15E-03	4.38E-07	2.23E-03	4.55E-07	
Water	1.12E+13	4.05E+12	6.97E+12	4.03E-04	1.03E-07	1.64E-04	4.17E-08		1.44E-07	
Coil 4										
Case	1.42E+13	6.69E+12	8.95E+12	7.49E-05	3.79E-08	9.68E-04	4.90E-07	1.04E-03	5.28E-07	
Insulation	1.42E+13	6.62E+12	9.04E+12	3.56E-04	8.22E-08	8.10E-04	1.87E-07	1.17E-03	2.69E-07	*74.75*
Copper	1.41E+13	6.40E+12	8.99E+12	1.61E-04	3.30E-08	2.77E-03	5.67E-07	2.93E-03	6.00E-07	
Water	1.46E+13	5.73E+12	9.17E+12	6.55E-04	1.68E-07	2.12E-04	5.43E-08		2.22E-07	
T-Bar	1.30E+13	6.33E+12	7.71E+12	9.90E-04	2.84E-08	1.46E-02	4.19E-07	1.56E-02	4.47E-07	

Lower VS insulator Peak dose is ~275 Gy/s

Total nuclear heat for 360 degree Lower VS → 378 kW

Total Nuclear Heating (kW)	*41.65*

Figure 4-26 Lower VS Coil 40-deg Sector Neutronics Results – Lower VS Average Dose Summary

Upper VS

Coil 1	n_flux (n/cm2/s)	fast n_flux (n/cm2/s)	g_flux (g/cm2/s)	n_heat MW	n_heat MW/cc	g_heat MW	g_heat MW/cc	total heat MW	total heat MW/cc	Average Dose (Gy/s)
Case	1.63E+13	7.74E+12	1.20E+13	7.04E-05	4.62E-08	1.02E-03	6.69E-07	1.09E-03	7.15E-07	
Insulation	1.63E+13	7.69E+12	1.22E+13	3.29E-04	9.86E-08	8.48E-04	2.54E-07	1.18E-03	3.53E-07	**98.03**
Copper	1.63E+13	7.46E+12	1.20E+13	1.46E-04	3.90E-08	2.88E-03	7.67E-07	3.03E-03	8.06E-07	
Water	1.68E+13	6.68E+12	1.23E+13	5.91E-04	1.97E-07	2.20E-04	7.34E-08		2.70E-07	
Coil 2										
Case	2.05E+13	9.79E+12	1.48E+13	1.03E-04	6.69E-08	1.26E-03	8.17E-07	1.36E-03	8.84E-07	
Insulation	2.04E+13	9.68E+12	1.50E+13	4.69E-04	1.39E-07	1.05E-03	3.11E-07	1.52E-03	4.50E-07	**124.89**
Copper	2.03E+13	9.38E+12	1.48E+13	2.10E-04	5.53E-08	3.56E-03	9.38E-07	3.77E-03	9.93E-07	
Water	2.09E+13	8.42E+12	1.51E+13	7.87E-04	2.59E-07	2.72E-04	8.95E-08		3.49E-07	
Coil 3										
Case	1.09E+13	5.04E+12	7.21E+12	3.58E-05	2.34E-08	6.07E-04	3.98E-07	6.43E-04	4.21E-07	
Insulation	1.09E+13	4.95E+12	7.26E+12	1.69E-04	5.05E-08	5.05E-04	1.51E-07	6.75E-04	2.01E-07	**55.89**
Copper	1.08E+13	4.71E+12	7.15E+12	7.06E-05	1.87E-08	1.72E-03	4.56E-07	1.79E-03	4.74E-07	
Water	1.11E+13	4.12E+12	7.30E+12	3.28E-04	1.09E-07	1.31E-04	4.34E-08		1.52E-07	
Coil 4										
Case	1.40E+13	6.56E+12	9.22E+12	5.97E-05	3.86E-08	7.80E-04	5.05E-07	8.39E-04	5.43E-07	
Insulation	1.39E+13	6.46E+12	9.30E+12	2.77E-04	8.18E-08	6.51E-04	1.92E-07	9.29E-04	2.74E-07	**76.02**
Copper	1.38E+13	6.19E+12	9.18E+12	1.20E-04	3.16E-08	2.21E-03	5.80E-07	2.33E-03	6.12E-07	
Water	1.42E+13	5.47E+12	9.36E+12	4.83E-04	1.58E-07	1.69E-04	5.54E-08		2.14E-07	
T-Bar	1.25E+13	6.12E+12	7.89E+12	8.10E-04	3.00E-08	1.15E-02	4.26E-07	1.23E-02	4.56E-07	

Upper VS insulator Peak dose is ~220 Gy/s

Total nuclear heat for 360 degree Upper VS → 284 kW

Total Nuclear Heating (kW) 31.48

Figure 4-27 Lower VS Coil 40-deg Sector Neutronics Results – Upper VS Average Dose Summary

4.3 MATERIAL DEGRADATION

The IVCs are normal Cu conductors cooled by water and utilize ceramic compacted powder insulators (MgO or spinel). The peak nuclear parameters calculated in the detailed 3-D analysis are utilized to assess the expected radiation effects in the copper conductor and ceramic insulator. Radiation limits for such components are not defined for ITER. However, previous reviews of radiation limits for normal conducting magnets in fusion environment are available and are used here as guidance to determine the expected radiation effects[48,49].

---

[48] L.J. Perkins, "Materials Considerations for Highly Irradiated Normal-Conducting Magnets in Fusion Reactor Applications," J. of Nuclear Materials, vol. 122&123, pp. 1371-1375 (1984).

[49] M. Sawan, H. Khater, and S. Zinkle, "Nuclear Features of the Fusion Ignition Research Experiment (FIRE),"

4.2.1 Radiation effects on ceramic insulator

Candidate ceramic insulator materials are MgO, and spinel ($MgAl_2O_4$). In a nuclear environment, degradation of electrical and mechanical properties of the insulator is the main concern. The degradation of mechanical and structural performance under long-term neutron fluence is an issue. Swelling in solid ceramics with cubic structure (e.g. MgO and $MgAl_2O_4$) is isotropic under neutron irradiation. Fracture toughness increases at elevated fluences for such ceramics. The fluence limit is determined only by the maximum swelling that can be tolerated. A maximum swelling of 3% corresponds to fast neutron (E>0.1 MeV) fluences of $1.1x10^{22}$ and $4x10^{22}$ n/cm2 for polycrystalline solid MgO and spinel, respectively. This corresponds to ~10^5 MGy of cumulative absorbed dose. Neutron damage has no effect on the strength of the compacted powder ceramics since each grain is affected individually. The peak cumulative end-of-life (0.3 MWa/m2) fast neutron fluence is only ~$3x10^{20}$ n/cm2 which is about two orders of magnitude lower than the limit for 3% swelling in polycrystalline solid ceramic insulators. The cumulative dose is only ~5000 MGy. Hence, no degradation is expected in mechanical and structural performance. Under large instantaneous neutron and gamma dose rates, ceramic insulators exhibit a significant and instantaneous decrease in their electrical resistivity. Such degradation in resistivity can lead to thermal runaway. This effect is lower in solid ceramics and is only important for very high dose rates. Peak dose rates of ~300 Gy/s were calculated and the impact on increasing the conductivity of the insulator in addressed in detail in Section 4.3.

4.2.2 Radiation induced resistivity in the copper conductor

The candidates for the copper conductor include OFHC copper and the CuCrZr alloy. A concern with Cu magnet conductors is the increased electrical resistivity that impacts the performance of the coils through increasing the I^2R heating and re-distributing the current across the coil. The increase in electrical resistivity results from solute transmutation products and displacement damage (production of defects and dislocations). At high doses, the displacement damage

---

Fusion Engineering & Design, vol. 63-64, pp 547 - 557 (2002).

component approaches rapidly a constant saturation value due to displacement cascade overlap effects with a saturation value of 1-4 nΩm depending on purity and Cu alloy used. Periodic annealing of the copper components at temperatures well above recovery Stage V (~ 425 K, corresponding to thermal dissociation of vacancy clusters would cause a significant additional reduction in the displacement damage component of the resistivity increase beyond that already achieved at room temperature. It is speculated that up to ~ 90% of the displacement damage component of the resistivity increase present in Cu irradiated near room temperature could be recovered by annealing near 300°C. Hence, with bake-out of the coils, we expect the resistivity increase due to atomic displacements to be 0.1-0.4 nΩm.

The solute transmutation component of resistivity increase is directly proportional to the solute content that in turn scales with the dpa damage level according to Table 4.2-1. This increase does not anneal out. The transmutation products are dominated by Ni, Zn, and Co that build up as impurities with time resulting in changing the conductor resistivity. The peak Cu cumulative end-of-life dpa is as high as ~0.3 dpa. We used this dpa level to determine the solute transmutation component of Cu resistivity increase. The results in Table 4-7 that the maximum resistivity increase due to transmutations is only 85 pΩm. This modest increase along with the small contribution from atomic displacements is very small compared to the un-irradiated resistivity of ~ 16 nΩ-m at room temperature. Hence, for the fluence level at the IVCs, radiation induced resistivity is not expected to be a concern.

Table 4-7 Peak Cu resistivity increase due to transmutations

Solute	Transmutation rate (appm/dpa)	Solute resistivity (μΩm/at. Frac.)	Resistivity increase for peak 0.3 dpa (pΩm)
Ni	190	1.12	63.8
Zn	90	0.3	8.1
Co	7	6.4	13.4
Total			85.3

4.2.3 Radiation effects on mechanical and structural properties of the copper conductor

Although the damage levels are very low, significant effects on physical and mechanical properties might occur. These effects are strongly dependent on irradiation temperature and have been the subject of numerous studies as part of the ITER R&D program. Notice that the damage level at the conductors of the IVCs is about an order of magnitude lower than that in the CuCrZr FW heat sink. Two issues are of concern; the low temperature embrittlement and thermal creep at high temperatures. For the water cooled IVCs, high temperature creep might not be an issue. However, low-temperature radiation embrittlement at T < 150°C is a concern for Cu alloys with reductions in tensile ductility (uniform elongation) below 5% being observed for damage levels on the order of 0.01 dpa. However, the fracture toughness is typically maintained at a sufficiently high level, at least in precipitation-hardened alloys such as CuCrZr and CuNiBe. It is possible to maintain the high tensile ductility by periodically annealing the Cu at ~ 300°C for ~ 50 hr. The dpa levels determined from the 3-D neutronics calculations will help along with the operating temperatures (determined using the calculated nuclear heating) to assess the expected degradation in mechanical and structural properties of the copper conductor.

4.4 RADIATION INDUCED CONDUCTIVITY (RIC)

RIC is a well-known phenomenon[50] resulting from the excitation of valence electrons into the conduction band, and has been observed during X-ray, gamma ray, electron, proton, and neutron irradiation. A well-developed database exists, documenting the instantaneous increase in the electrical conductivity of insulating ceramics induced by exposure to ionizing radiation. Although the behavior varies considerably depending on the material and impurity content there is a database on MgO[51,52] which is applicable to the SSMIC including some results for tests DT neutron irradiation[53].

Electrical conductivity in ceramics can be modeled considering three contributing terms, one (base) intrinsic, one due to temperature, and one due to radiation.

$$\sigma = \sigma_{base} + \sigma_{thermal} + \sigma_{radiation}$$

For base conductivity we use a value[54] of 1 x 10^{-14} S/m. For the thermal term we use the following expression[55]:

---

[50] "Radiation-induced changes in the physical properties of ceramic materials", Zinkle, Journal of Nuclear Materials 191-194 (1992) 58-66

[51] "Estimated Readout Errors Produced by Radiation and Temperature Effects in Coaxial Signal Cables for FFTF", Stringer, BNWL-1025

[52] "Dose Rate Dependence of the Radiation-Induced Electrical Conductivity in MgO", Hodgson, Journal of Nuclear Materials 155-157 (1988) 357-360

[53] "Electrical properties of mineral-insulated cable under fusion neutron irradiation", Tanaka, Fusion Engineering and Design 66/68 (2003) 837/841

[54] "Radiation-Resistant Magnets", CERN-82-05, 1982

$$\sigma_{thermal} = A\varepsilon^{-B/(T+273)}$$

where A = 1.829, B= 16300 and T = temperature in degrees C.

For the radiation term we use the following expression[56]:

$$\sigma_{radiation} = KR^{d}$$

where K = 3.37 x 10^{-10}, d= 1.02 and R = radiation flux in Gy/s.

To put these results in perspective, consider a case (typical for the IVCs) where the operating temperature is 150ºC and the radiation flux is 100 Gy/s:

$$\sigma_{base} = 1x10^{-14}\,S/m$$
$$\sigma_{thermal} = 3x10^{-17}\,S/m$$
$$\sigma_{radiation} = 4x10^{-8}\,S/m$$

This shows that the RIC completely dominates the conductivity of the insulation. Note that in many applications where the operating temperature is in the 100's of degrees the thermal term would be much more significant, but is not so in the range of operation of the IVCs. The implication of RIC in terms of ohmic losses in the insulation and the circuit leakage impedance to ground will be discussed in subsequent sections.

---

[55] "Electrical Conductivity of Magnesia Insulation For Heat-Resistant Cables In The Presence Of Intense Radiation And High Temperature", Emelyanov, Atomnaya Energiya, Vol.50, No. 1, pp. 25-29, January,1981

[56] "Dose Rate Dependence of the Radiation-Induced Electrical Conductivity in MgO", E. Hodgson et al, Journal of Nuclear Materials 155-157 (1988) 357-360, curve fit to data

5 ELECTRICAL PERFORMANCE

5.1 CIRCUIT PARAMETERS

The circuit resistance and inductance calculations are performed on the DP XL spreadsheets "ELM_Design_Point_YYMMDD.xls" and "VS_Design_Point_YYMMDD.xls". These are published on the web site http://www.pppl.gov/~neumeyer/ITER_IVC/Design_Point.html and summarized in the appendices of this report.

5.1.1 Resistance

Resistances are calculated for the coils, feeders, and bus bars and then added together.

For the coils, the conductor length is taken as the maximum of the three types of coils (upper, equatorial, lower) for ELM and as the maximum of the two types (upper, lower) for VS.

For the coils and feeders an average resistivity is used which corresponds to the average conductor temperature from start to finish of the winding.

For 100% IACS Cu the 20°C resistivity is taken to be 1.7241 x 10-8 Ω-m and the "temperature coefficient of resistance" (TCR) equal to 0.0041. For CuCrZr (used on the ELM coils and feeders) a resistivity of 80% IACS is assumed with TCR = 0.0031. This is consistent with the ITER data[57] on CuCrZr. See ELM_Design_Point_YYMMDD.xls, worksheet "CuCrZr_Resistivity" for more.

[57] ITER Material Properties Handbook, Ref. ITER Document No. G 74 MA 16

5.1.2 Inductance

For ELM the coil self-inductance (based on the largest of the three coils) is computed on ELM_Design_Point_YYMMDD.xls, worksheet "Inductances" using a formula from Grover[58] for a rectangular coil. The full mutual inductance matrix was also calculated[59] but for the spreadsheet calculations it is omitted for simplicity. Later it is confirmed that the mutual effect on the impedance does not result in a significant extra voltage demand.

For VS the self-inductance is computed on VS_Design_Point_YYMMDD.xls, worksheet "Inductances" using a formula from Grover[60] for a circular ring. Separate calculations are performed for the upper and lower VS since they have different geometries. The mutual inductance is computed using Maxwell's coaxial filament formula along with the solution of complete elliptic integrals of the 1st and 2nd kind within the spreadsheet using approximate solutions[61].

For all coil inductances, agreement between the spreadsheet and the separate mutual inductance computation was confirmed.

The DC bus bar inductances were computed using a formula from Grover[62] for a return circuit of parallel conductors.

---

[58] "Inductance Calculations", Grover, 1973, eq. 58, p. 60

[59] R. Pillsbury spreadsheet "100510 L R and V for ITER IVCs.xlsx"

[60] "Inductance Calculations", Grover, 1973, eq. 119b, p. 143

[61] "Approximations for Digital Computers", Hastings sh. 48 and 51

[62] "Inductance Calculations", Grover, 1973, eq. 16, p. 39

5.2 POWER SUPPLY CONFIGURATION AND CIRCUIT BEHAVIOR

5.2.1 Normal operation

5.2.1.1 Normal operation of ELM Circuits

With a 6 turn coil the 90kA-turn requirement amounts to 15kA per turn which must be driven at 5Hz. Neglecting the mutual inductances (which actually reduce the net impedance) the minimum required power supply voltage is calculated on ELM_Design_Point_YYMMDD.xls, worksheet "Circuit":

$$V = IZ$$
$$I = 15kA$$
$$Z = R + j\omega L$$
$$\omega = 2\pi f$$
$$f = 5Hz$$
$$V = 127volt$$

In order to provide margin over the minimum viable value of 127V a power supply voltage rating of 180V has been selected. Conventional thyristor rectifier technology can easily drive the 5Hz waveform and is therefore applicable to the ELM requirements. The most likely power supply implementation would be a 4-quadrant, 12-pulse thyristor converter. More details about the electrical circuit behavior including the total ELM power supply loading of the AC distribution system are computed in "ELM_Design_Point_YYMMDD.xls", published on the web site and summarized in the appendices of this report.

5.2.1.2 Normal operation of VS circuit

As described in 2.2.2.2 the VS voltage requirement of 575 volts per turn (2.3kV for four turns) is specified directly by the physics analysis which was performed assuming the same coil configuration as the present design point but a slightly different DC bus bar design. We choose a 2.4kV voltage considering the latest bus bar design along with some margin.

An additional requirement imposed on the power supply by the physics analysis is a time response of 1mS or less. This requirement rules out a conventional thyristor rectifier design

solution and calls for a "switched mode" or "chopper" power supply solution shown conceptually in Figure 5-1. In additional to fast time response another advantage of the chopper approach is that it involves a capacitive energy storage element which buffers the transient load of the VS coil so that it is not imposed directly on the AC distribution system. A charging power supply is deployed to maintain the charge on the capacitor bank but the variations in its input power are much less transient than the VS load itself. A study of a chopper power supply[63] was performed on a prior revision of the VS coil design and needs to be updated but is still representative of the approach which will be taken.

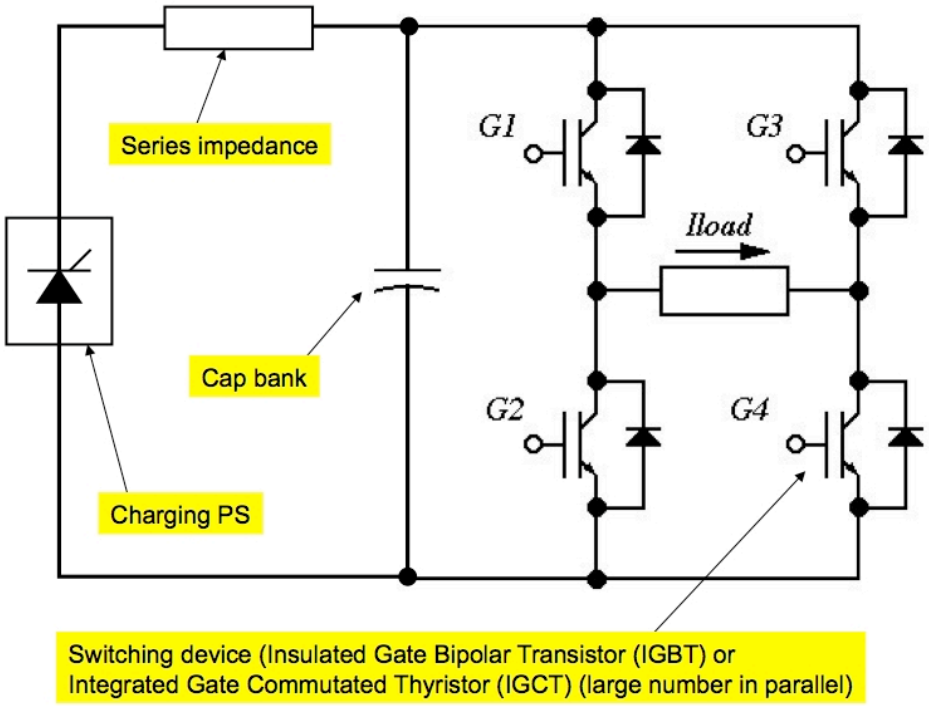

Figure 5-1 VS H-Bridge Chopper Concept

Calculations related to design of the chopper power supply (e.g. the sizing of the charging power supplies and capacitor bank. Etc.) are performed on the DP XL spreadsheet "VS_Design_Point_YYMMDD.xls", based on the earlier developed concept. These are

[63] "Pre-Conceptual Design Study of a Chopper Power Supply for the ITER In-Vessel Vertical Stabilization Coils", ITER_D_2X4HY9

published on the web site http://www.pppl.gov/~neumeyer/ITER_IVC/Design_Point.html and summarized in the Appendix II of this report.

One significant departure from the prior power supply concept is the likely need to subdivide the power supply into two parts interleaved in series with the upper and lower coils. As shown in Figure 5-2 this serves to reduce the maximum circuit voltage to ground by a factor of two, the need for which is discussed in section 5.3. This is common practice but does complicate the power supply and increase its cost. An open issue is what strategy should be used to control the two choppers and how their "Pulse Width Modulation" (PWM) should be synchronized with respect to one another.

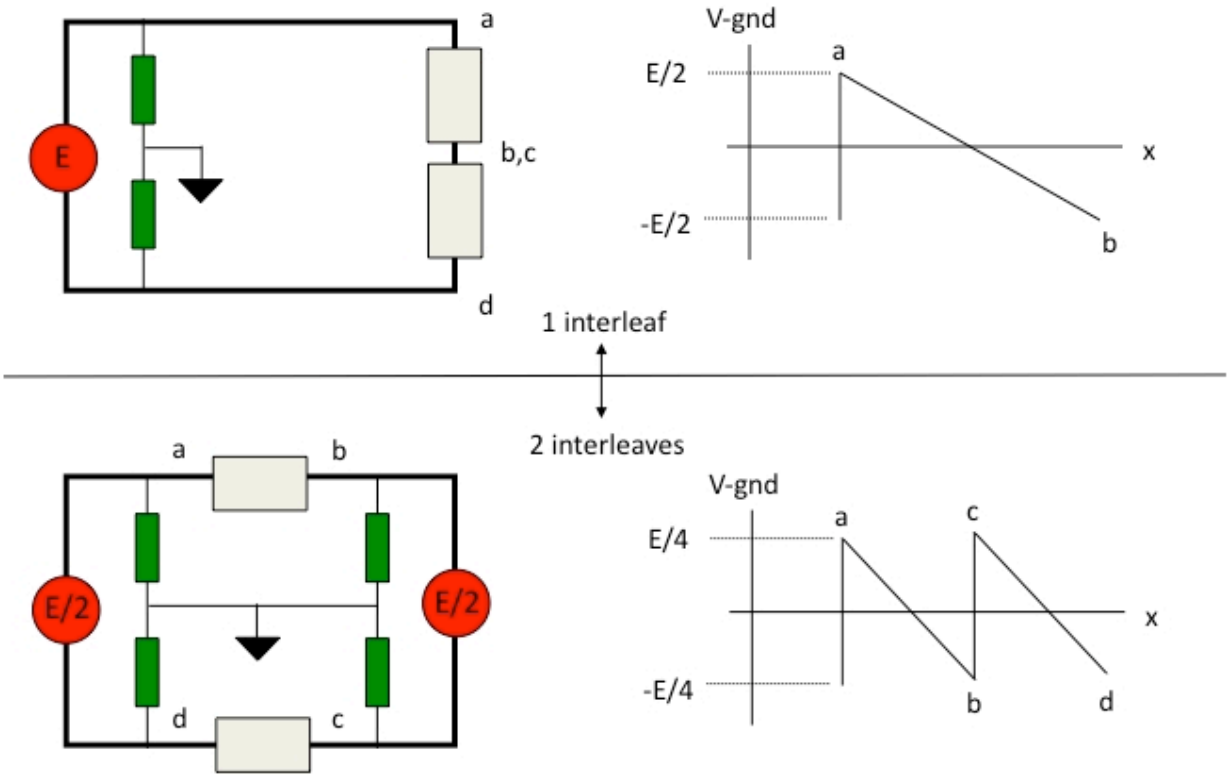

Figure 5-2 Subdivision of VS Power Supply in Two Interleaves to Reduce Voltage to Ground

5.2.2 **Plasma VDE and disruption**

5.2.2.1 ELM Behavior During Disruption

During normal operation in a thyristor AC/DC converter power supply, at least two thyristors in each 6-pulse bridge are in a conducting state and the AC source voltage is applied to the load impedance according to the firing pattern. The load impedance consists of the coil and DC bus bar plus an additional contribution due to the thyristor AC/DC converters. Typically the coil impedance is dominant. The contribution of each AC/DC converter arises from the impedance of two phases of the three phase AC source, as the current enters one phase and exits another according to the conduction pattern. When a disruption occurs, the circuit remains closed and the voltage coupled into the circuit due to mutual inductance with the decaying plasma current will add or subtract to the power supply voltage causing the current to change. Depending on the time scale of the disruption, the initial condition of the current, and the type of feedback control acting on the power supply, the power supply will try to regulate the current as long as it stays within the rated current. If the disruption effect is strong enough to cause an over current, beyond the rated current, then the power supply will go into a bypass mode in which case the thyristors will be controlled in such a way that the current is shunted from the AC source and the power supply resembles a short circuit. The power supply must be designed to carry the transient overcurrent through its bypass under these circumstances. Maximum prospective currents are given in section 6.

5.2.2.2 VS Behavior During Disruption

The VS behavior is similar to ELM but different because of the type of power supply. During normal operation the H-bridge chopper conduction pattern results in three possible states, namely 1) capacitor bank connected across the load with (+) polarity, 2) capacitor bank connected across the load with (-) polarity, or 3) capacitor bank bypassed. In any case a conduction path across the load is maintained at all times. The load impedance consists of the coil and DC bus bar plus an additional contribution due to the chopper. Typically the coil impedance is dominant. When a disruption occurs, the circuit remains closed and the voltage coupled into the circuit due to mutual inductance with the decaying plasma current will add or subtract to the power supply

voltage causing the current to change. Depending on the time scale of the disruption, the initial condition of the current, and the type of feedback control acting on the power supply, the power supply will try to regulate the current as long as it stays within the rated current. If the disruption effect is strong enough to cause an over current, beyond the rated current, then the power supply will go into a bypass mode in which case the H-bridge will be bypassed and the power supply will resemble a short circuit. The power supply must be designed to carry the transient overcurrent through its bypass under these circumstances. Maximum prospective currents are given in section 6.

5.3 CIRCUIT PARAMETER SUMMARY

Circuit parameters are summarized in Table 5-1.

Table 5-1 Summary of Coil Electrical Parameters

		VS	ELM
Coil resistance	ohm	1.46E-02	2.50E-03
Coil inductance	henry	1.22E-03	2.32E-04
Bus bar resistance	ohm	1.50E-03	1.22E-04
Bus bar inductance	henry	7.39E-05	6.01E-06
Total circuit resistance	ohm	1.61E-02	2.62E-03
Total circuit inductance	henry	1.30E-03	2.38E-04
Peak current per turn	kA peak	60	15
RMS current per turn	kA rms	9	11
Total circuit voltage	kV peak	2.4	1.8

Notes:

1) Resistances at operating temperature

2) For VS, “coil” values include upper and lower coils in anti-series for the 4-turn condition

3) For ELM, “coil” values are maximum of upper, equatorial, and lower coils

5.4 ELECTRICAL INSULATION STRESS

As mentioned in section 3.1.2, the insulation thickness is a key design parameter. For ELM, the thickness chosen is the same as that used in the largest commercially available MIC cable from the worlds largest manufacturer of same (Tyco Industries) which is a 500MCM, 600V ac power cable. For the VS, considering that the voltage is substantially higher than ELM, twice the ELM thickness has been chosen.

Until data is obtained for the actual SSMIC conductor geometry and insulation (including MgO composition and compaction) the breakdown voltage is not known with confidence, even for room temperature, non-irradiated conditions. However, information provided by Tyco can be used as a guide. According to their application engineering guide[64] their commercial MIC cables rated at 600VAC have a breakdown voltage of 5kVAC rms. Using this information, along with the dimensions of their largest cable (500MCM) we can derive the electric field at breakdown and assess the breakdown voltage of the IVC SSMIC with chosen dimensions.

Based on Gauss's Law the potential difference between the inner (Cu pipe) and outer (SS jacket) conductors of the SSMIC is:

$$V = \frac{\lambda}{2\pi\varepsilon}\ln\left(\frac{r_{outer}}{r_{inner}}\right)$$

where λ is the surface charge density in coulomb/m, ε is the dielectric permittivity equal to $\varepsilon_r\varepsilon_0$ with ε_r the relative permittivity and ε_0 the permittivity constant, and r_{inner} and r_{outer} are the radii of the annulus containing the mineral insulation. The electric field E in volts/m at any radius in the annulus is:

$$E = \frac{\lambda}{2\pi r\varepsilon}$$

The electric field is maximum at the surface of the conductor, which is the inner radius of the annulus r_{inner}.

[64] "Pyrotenax Engineering Data Manual", 1994

On this basis we compute the field at breakdown for the Tyco cable and apply the result to the SSMIC conductors in Table 5-2.

Table 5-2 Calculation of Electric Field in SSMIC

	Tyco Pyrotenax 500MCM	ELM (2.5 mm insul)	VS (5mm insul)	VS (two interleaves, 5mm insul)	
V_op	600				volt rms
V_op	849	180	2400	1200	volt
V_hipot	2697	1360	5800	3400	volt
V_breakdown	7071	7227	13765	13765	volt
V_breakdown/V_hipot	2.62	5.31	2.37	4.05	
V_breakdown/V_op	8.33	40.15	5.74	11.47	
Insulation thickness	2.645	2.500	5.000	5.000	mm
Insulation thickness	104.1	98.4	196.9	196.9	mil
R_inner	9.015	25	22.5	22.5	mm
R_outer	11.66	27.5	27.5	27.5	mm
λ_breakdown	1.53E-06	4.22E-06	3.81E-06	3.81E-06	Coulomb/m
E_average_breakdown	2.7	2.9	2.8	2.8	kV/mm
E_average_breakdown	67.9	73.4	69.9	69.9	volt/mil
E_max_breakdown	3.0	3.0	3.0	3.0	kv/mm
E_max (Max operating)	0.366	0.076	0.532	0.266	kv/mm
E_max (Nom operating)	0.366	0.038	0.266	0.133	kv/mm

According to the Tyco Pyrotenax data the breakdown electric field is about 3kV/mm or 68 volt/mil. Elsewhere in the Tyco literature a dielectric strength of 80 volt/mil is mentioned, so perhaps this result is conservative. The breakdown voltages of the ELM and VS conductors based on this data are 7.2kV and 13.7kV, respectively. The "safety margin", or ratio of breakdown to operating voltage is noted to be quite high for ELM (~40) but not so for VS (~6) unless two interleaves are used (~11). Here we use take the operating voltage to be equal to the full power supply voltage, even though the symmetric grounding scheme will result in a nominal maximum of ½ the power supply voltage. But transients and faults can upset the balance. Typically the safety margin should always be 10 or more, and considering the extreme environment of the IVCs including high temperature and radiation field, the use of two interleaves is strongly advised.

Summarizing, the max insulation stress is <100V/mm for ELM and 266V/mm for VS (one interleaf), <150V/mm (two interleaves). It is noteworthy that the overall stresses on insulation are close to but generally above the guidelines suggested by Vayakis et al[65] for mineral insulated cables used for ITER diagnostics:

- < 100 Gy/sec (peak for IVC ~ 280 Gy/s)
- < 200ºC (peak for IVC ~ 150 ºC during operations, ~ 240ºC during bakeout)
- < 150V/mm (peak for IVC ~ 133kV/mm under symmetric conditions, 266 kV/mm under asymmetric conditions)

Note that above are peak values and most of the coil conductor sees less radiation flux and less voltage.

Future R&D testing of prototype conductors will provide more data concerning the dielectric strength of the SSMIC so these findings can be refined. In addition, endurance tests will be performed with AC voltage at frequencies representative of the ELM and VS power supply waveforms so that the insulation power factor and dissipation with capacitive displacement currents can be characterized.

5.5 GROUNDING

5.5.1 General Considerations

The purpose of the grounding system is to control the circuit voltage to ground and to provide a means of ground fault detection. Following typical practice a high impedance, center point grounding scheme is recommended as depicted in Figure 5-3. Features of this scheme are as follows:

- the nominal voltage at each coil terminal is ½ of the power supply voltage per interleaf
- the occurrence of a single ground fault results in a limited fault current

[65] "Generic Diagnostic Issues for a Burning Plasma Experiment", Vayakis, Fusion Science and Technology Vol. 53 Feb. 2008

- the ground fault current can be detected by measuring the current in the ground connection which is normally zero

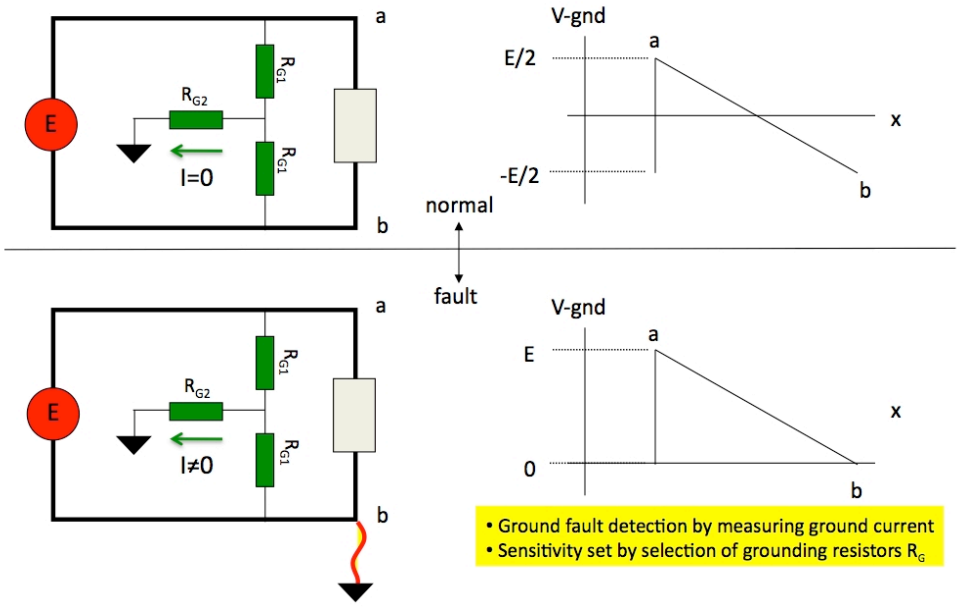

Figure 5-3 Grounding and Ground Fault Detection Scheme

However, any real system exhibits stray impedance to ground including resistive and capacitive components as shown in Figure 5-4 which, together with the grounding resistors, influence the voltage distribution to ground and the ground current.

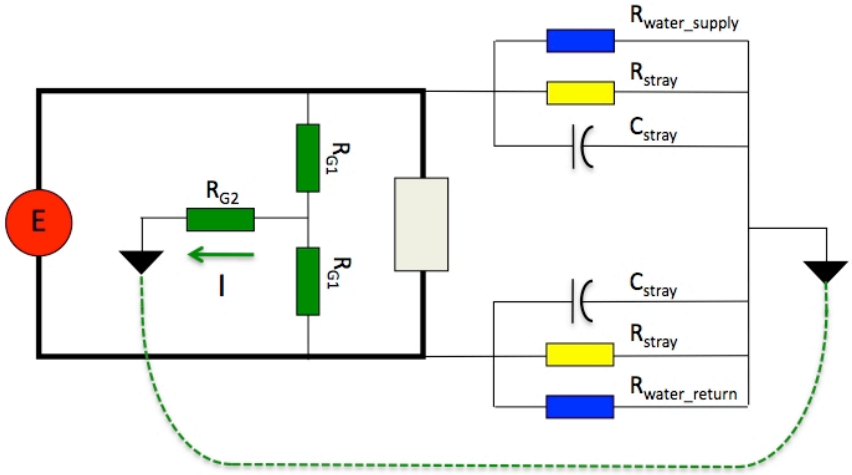

Figure 5-4 Inclusion of Stray Leakage Impedances to Ground

The stray resistance and capacitance of the SSMIC are unusual compared to traditional coils because the stainless steel jacket encompasses the conductor over the entire winding length like a coaxial cable, whereas on traditional coils a ground plane encompasses the overall winding pack. In addition, the mineral insulation conductivity varies more than traditional insulating materials with temperature and radiation flux (RIC) as described in section 4.4. An equivalent circuit of the SSMIC is given in .

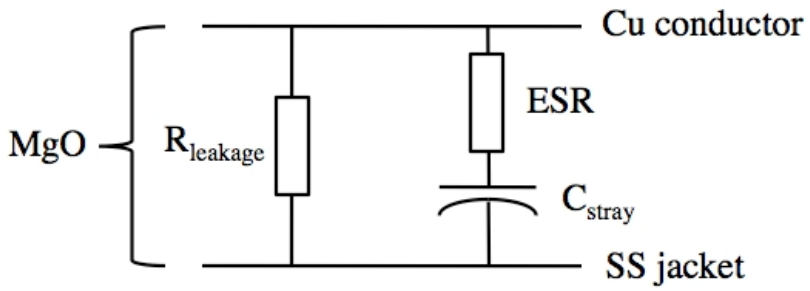

Figure 5-5 Equivalent Circuit of MgO Insulation

The stray capacitance is computed as follows:

$$C = \frac{2\pi\varepsilon_r\varepsilon_0}{\ln\left(\frac{D_{outer}}{D_{inner}}\right)}$$

where D_{outer} and D_{inner} refer to the annulus between the conductor and jacket which contains the insulation. Based on the Tyco Pyrotenax data the relative permittivity of compacted MgO power is $\varepsilon_r = 4$ such that the stray capacitance is 2.3nF/m for the ELM conductor and 1.1nF/m for the VS conductor. An "Equivalent Series Resistance" (ESR) can be used to model the frequency dependent dielectric losses due to the capacitive displacement current associated with the "insulation power factor". According to Tyco Pyrotenax "The power factor of magnesium oxide insulation is very low compared to that of most electrical cable insulations. When measured at room temperature, 60 Hz and 40 volts per mil, it is approximately 0.1%. This value increases with temperature to approximately 1.0% at 250°C". Based on this information one can estimate the dielectric losses in the insulation as shown in Table 5-3 where a 1% insulation power factor is conservatively assumed.

Table 5-3 Insulation Power Factor and Dielectric Loss Calculation

	ELM	VS	
p.f.	1.00	1.00	%
f	60	60	Hz
D_inner	0.05	0.045	m
D_outer	0.055	0.055	m
Er	4	4	
C	2.33E-09	1.10E-09	F/m
Xc_60	1.14E+06	2.41E+06	ohm-m
R_esr	11367	24116	ohm-m
V	90	600	volt
f	600	1000	Hz
Xc_f	113665	144686	ohm-m
Ic_f	5.57E-04	2.89E-03	amp/m
P_esr	3.53E-03	2.02E-01	watt/m
P_esr	8.56E-06	2.57E-04	watt/cc

The ESR is estimated based on the 60Hz data. Then it is assumed that the power supply voltage is applied in a manner balanced with respect to ground, and with two interleaves in VS with a frequency equal to that of a 12-pulse rectifier for ELM and a 1kHz chopper for VS. On this basis the dielectric losses attributable to ESR can be estimated for comparison with other losses in the insulation.

As described in section 4.4 the DC conductivity of the MgO insulation which results in its leakage resistance arises from three terms, one (base) intrinsic, one due to temperature, and one due to radiation.

$$\sigma = \sigma_{base} + \sigma_{thermal} + \sigma_{radiation}$$

Then the leakage resistance of a section of conductor of length L is as follows:

$$R = \frac{1}{2\pi\sigma L}\ln\left(\frac{R_{outer}}{R_{inner}}\right)$$

The leakage resistance along the water supply and return lines must also be considered. It is calculated according to:

$$R = \rho \frac{l}{A}$$

where ρ is the water resistivity and l and A are the length and cross section of the cooling line. In fact, the water resistivity is a function of water chemistry and temperature. We assume that the resistivity at 25°C = 5 MegOhm-cm which should be a practical, achievable level which allows the pH to go somewhat above neutral (see Figure 5-6).

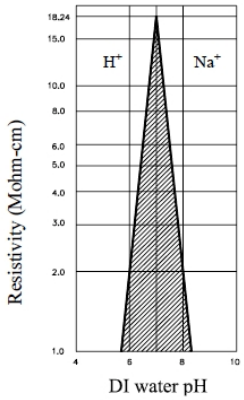

Figure 5-6 Resistivity of De-Ionized Water vs. pH[66]

Concerning the temperature effect we model the theoretical resistivity vs. temperature for pure water over the range 50-150°C as follows[67]:

$$\rho(T) = C_6 * T^6 + C_5 * T^5 + C_4 * T^4 + C_3 * T^3 + C_2 * T^2 + C_1 * T + C_0$$

where:

C_6 = 5.252E-12 C_5 = -4.36997E-09 C_4 = 1.50417E-06 C_3 = -0.000276029

C_2 = 0.028834395 C_1 = -1.662661455 C_0 = 43.30568834

---

[66] "Low Conductivity Water Systems for Accelerators", Dortwet, Proceedings of the 2003 Particle Accelerator Conference

[67] "The Fundamental Conductivity and Resistivity of Water", Light, Electrochemical and Solid-State Letters, 8 (1) E16-E19 (2005)

The resistivity of pure water at 25ºC is 18.15 MegOhm-cm. For the IVC water we assume that the resistivity at elevated temperature is proportional to that of pure water by the ratio of the 25ºC resistivities, namely 5/18.15 as shown in Figure 5-7.

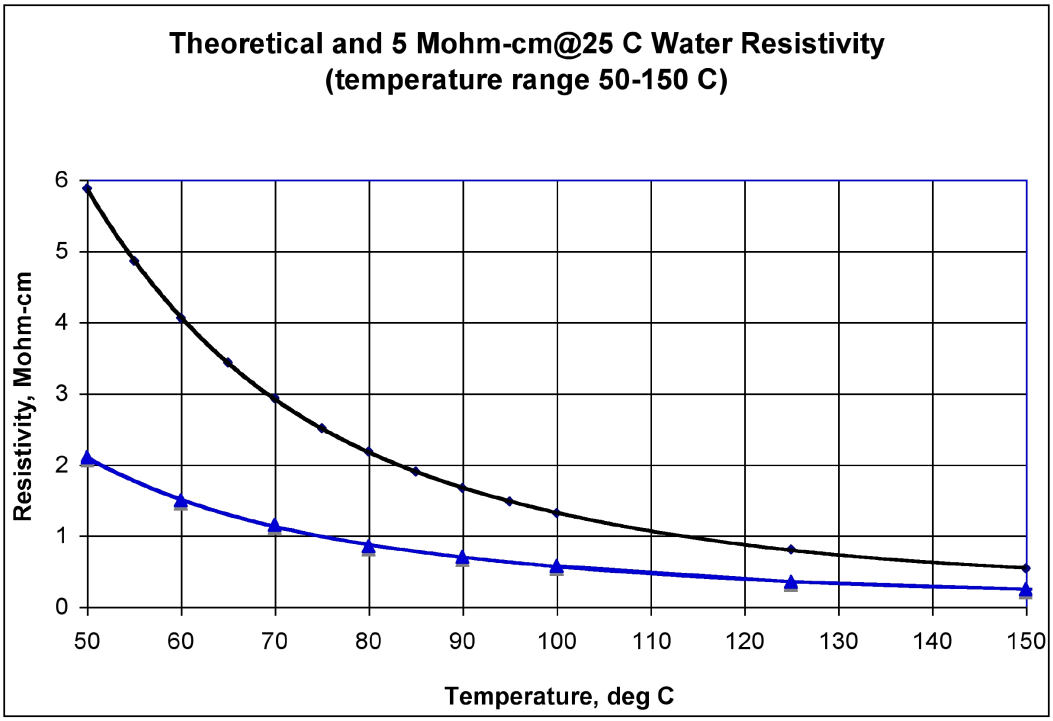

Figure 5-7 Cooling Water Resistivity vs. Temperature

Based on the above analysis the typical cooling water connection resistance will be as indicated in Table 5-4.

Table 5-4 Cooling Water Connection Resistance vs. Temperature

Water temperature	25	100	125	150	degC
Water resistivity	5	0.575	0.35	0.25	Mohm-cm
Water passage diameter	30	30	30	30	mm
Water column resistance	70.7	8.1	5.0	3.5	Mohm/m
Water column length	50	50	50	50	cm
Water column resistance	35.4	4.1	2.5	1.8	Mohm

The inlet water to both ELM and VS is 100ºC. The outlet of ELM is ~ 150ºC and of VS ~ 125ºC so the hot/cold resistance ratios (based on identical cooling line geometry on inlet and outlet) is 4.1/1.8=2.3 for ELM and 2.5/1.8=1.6 for VS.

5.5.2 ELM Grounding

The average radiation flux on the ELM turns[68] is shown in Figure 5-8. This result is based on the average of the toroidal and poloidal legs of the upper ELM coil, taking average of the average nuclear heating rates on each limb in watt/cc and dividing by the density of compacted MgO powder, assumed equal to 3.6 x 10^{-3} kg/cc.

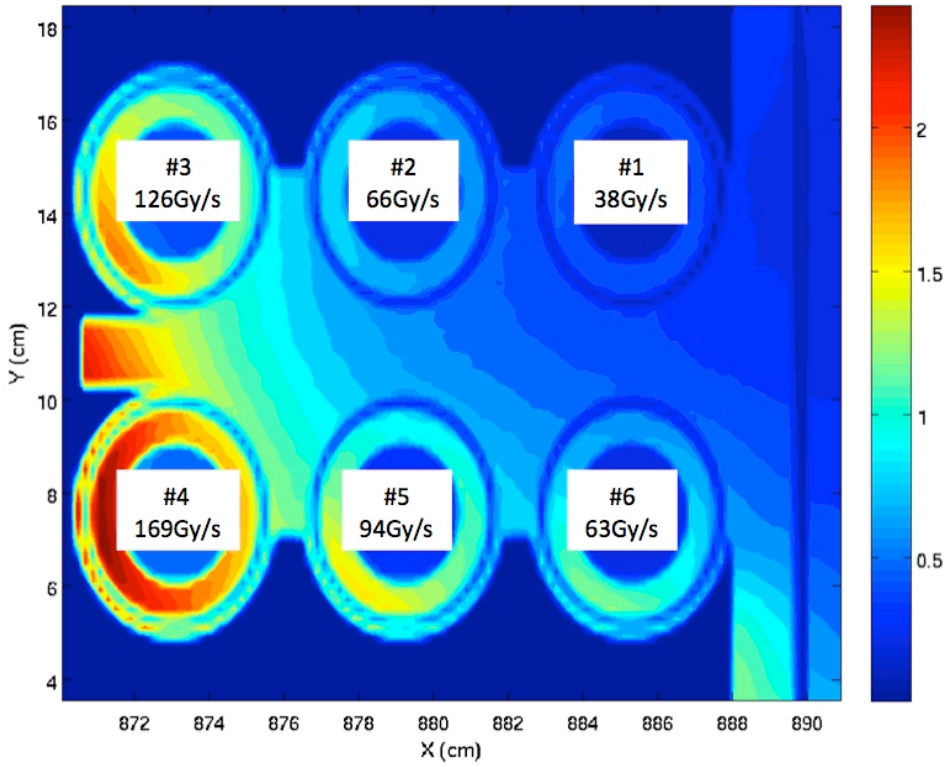

Figure 5-8 Average Radiation Flux on ELM Turns

Note that the winding pattern is chosen so that the first and last turns in the winding (turns #1 and #6), which see the highest voltage to ground, are located furthest from the plasma in the minimum flux position. This is favorable from both leakage resistance, insulation heat

[68] Estimated from "Preliminary Neutronics Analysis of 3x2 Toroidal and Poloidal Legs of ELM Coils", Bohm, ITER_D_3FZZ6T

dissipation, and electrical breakdown perspectives. A summary of the various ELM leakage resistance values is given in Table 5-5.

Table 5-5 ELM Leakage Resistance Values

Turn #	1	2	3	4	5	6	
Turn length	10.885	10.885	10.885	10.885	10.885	10.885	m
Rinner	0.033	0.033	0.033	0.033	0.033	0.033	m
Router	0.045	0.045	0.045	0.045	0.045	0.045	m
σ_base	1E-14	1E-14	1E-14	1E-14	1E-14	1E-14	S/m
Avg temp	114	122	130	137	145	153	degC
Radiation OFF							
σ_temp	9.25E-19	2.14E-18	4.77E-18	1.03E-17	2.17E-17	4.45E-17	S/m
Avg rad	0	0	0	0	0	0	Gy/s
σ_rad	0.00E+00	0.00E+00	0.00E+00	0.00E+00	0.00E+00	0.00E+00	S/m
σ_total	1.00E-14	1.00E-14	1.00E-14	1.00E-14	1.00E-14	1.00E-14	S/m
ρ_total	1.00E+14	1.00E+14	1.00E+14	9.99E+13	9.98E+13	9.96E+13	ohm-m
R_leakage	4.53E+11	4.53E+11	4.53E+11	4.53E+11	4.53E+11	4.51E+11	ohm
Radiation ON							
σ_temp	9.25E-19	2.14E-18	4.77E-18	1.03E-17	2.17E-17	4.45E-17	S/m
Avg rad	38	66	126	169	94	63	Gy/s
σ_ rad	1.38E-08	2.42E-08	4.68E-08	6.31E-08	3.47E-08	2.31E-08	S/m
σ_total	1.38E-08	2.42E-08	4.68E-08	6.31E-08	3.47E-08	2.31E-08	S/m
ρ_total	7.26E+07	4.14E+07	2.14E+07	1.59E+07	2.88E+07	4.34E+07	ohm-m
R_leakage	3.29E+05	1.88E+05	9.70E+04	7.19E+04	1.31E+05	1.97E+05	ohm
E	38000	25333	12667	12667	25333	38000	volt/m
Ohmic dissipation	1.99E-05	1.55E-05	7.50E-06	1.01E-05	2.23E-05	3.33E-05	watt/cc
Nuclear heating	0.137	0.238	0.455	0.610	0.339	0.227	watt/cc

Given the water cooling line resistance and the highly variable coil leakage resistance, the situation is rather complex, and further work via circuit analysis is needed to quantify the flow of ground current under normal and fault conditions based vs. choice of grounding resistance for the cases with and without radiation. However, the following conclusions can be drawn:

- the water line resistance will dominate the leakage when radiation is not present, and the imbalance between leakage at the water inlet (cold) end and the water outlet (hot) end will result in some amount of ground current flow TBD, depending on the choice of grounding resistance. This situation can be mitigated to some degree by utilizing different

cooling line lengths and/or diameters on the inlet and outlet ends but there since the temperature can vary there is no choice which results in symmetry under all conditions;

- The coil stray resistance will dominate the leakage when radiation is present but the winding pattern is such that asymmetries between the two halves of the winding (first three turns vs. second three turns) is minimized;
- The ohmic dissipation in the mineral insulation, due both to leakage resistance and frequency-dependent dielectric loss, is very small, much less than the nuclear heating.

5.5.3 VS Grounding

As described in prior sections the VS will most likely be divided in two interleaves in order to reduce the voltage to ground as shown in Figure 5-9. Each turn has its leads individually brought outside of the vacuum vessel and routed to the power supply building, and each turn will have a dedicated cooling water circuit. Therefore the leakage resistance of each turn will arise from the water lines and the stray resistance of the conductor as shown.

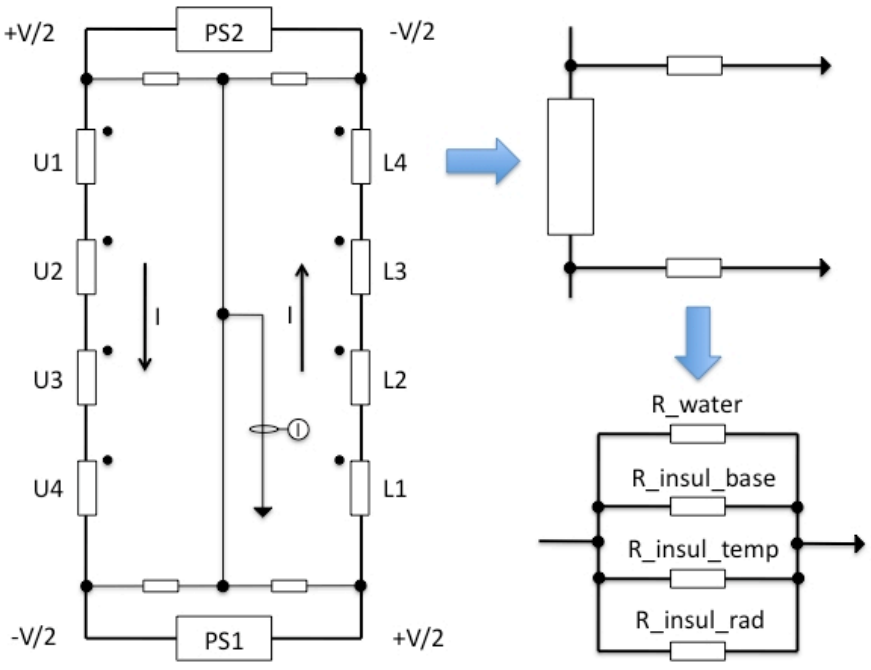

Figure 5-9 VS Circuit

Since the RIC will dominate the stray leakage of the SSMIC and the radiation flux will tend to reduce dielectric strength, it makes sense to arrange the turns such that the leakage is symmetric along the series connection of turns in each interleaf and that the high flux turns are exposed to the lowest voltage.

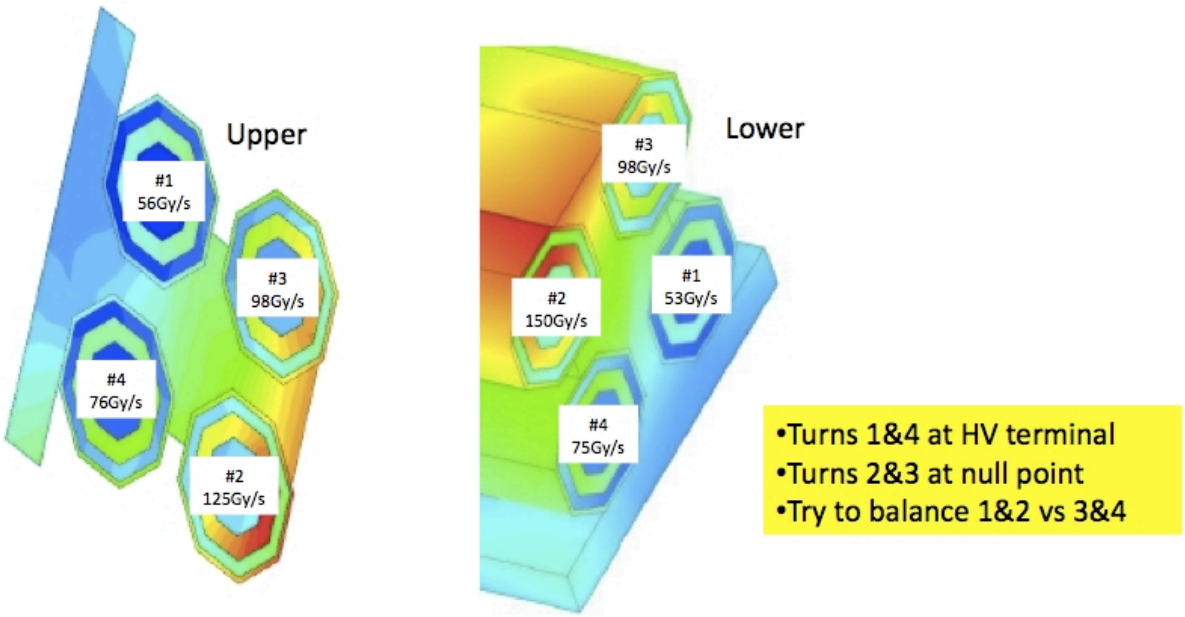

Figure 5-10 Average Radiation Flux on VS Turns

A summary of the various ELM leakage resistance values is given in Table 5-6.

Table 5-6 VS Leakage Resistance Summary

Turn #	U1	U2	U3	U4	L1	L2	L3	L4	
Turn length	36.283	36.283	36.283	36.283	47.091	47.091	47.091	47.091	m
Rinner	0.03	0.030	0.030	0.030	0.030	0.030	0.030	0.030	m
Router	0.045	0.045	0.045	0.045	0.045	0.045	0.045	0.045	m
σ_base	1.00E-14	1.00E-14	1.00E-14	1.00E-14	1.00E-14	1.00E-14	1.00E-14	1.00E-14	S/m
Avg temp	116	116	116	116	116	116	116	116	degC
Radiation OFF									
σ_temp	1.10E-18	1.10E-18	1.10E-18	1.10E-18	1.10E-18	1.10E-18	1.10E-18	1.10E-18	S/m
Avg rad	0	0	0	0	0	0	0	0	Gy/s
σ_rad	0.00E+00	0.00E+00	0.00E+00	0.00E+00	0.00E+00	0.00E+00	0.00E+00	0.00E+00	S/m
σ_total	1.00E-14	1.00E-14	1.00E-14	1.00E-14	1.00E-14	1.00E-14	1.00E-14	1.00E-14	S/m
ρ_total	1.00E+14	1.00E+14	1.00E+14	1.00E+14	1.00E+14	1.00E+14	1.00E+14	1.00E+14	ohm-m
R_leakage	1.78E+11	1.78E+11	1.78E+11	1.78E+11	1.37E+11	1.37E+11	1.37E+11	1.37E+11	ohm
Radiation ON									
σ_temp	1.10E-18	1.10E-18	1.10E-18	1.10E-18	1.10E-18	1.10E-18	1.10E-18	1.10E-18	S/m
Avg rad	56	125	98	76	53	150	98	75	Gy/s
σ_rad	2.04E-08	4.64E-08	3.62E-08	2.79E-08	1.93E-08	5.59E-08	3.62E-08	2.75E-08	S/m
σ_total	2.04E-08	4.64E-08	3.62E-08	2.79E-08	1.93E-08	5.59E-08	3.62E-08	2.75E-08	S/m
ρ_total	4.89E+07	2.16E+07	2.76E+07	3.58E+07	5.17E+07	1.79E+07	2.76E+07	3.63E+07	ohm-m
R_leakage	8.70E+04	3.84E+04	4.92E+04	6.37E+04	7.09E+04	2.45E+04	3.79E+04	4.98E+04	ohm
E	133000	66500	66500	133000	133000	66500	66500	133000	volt/m
Ohmic dissipation	3.62E-04	2.05E-04	1.60E-04	4.94E-04	3.42E-04	2.47E-04	1.60E-04	4.87E-04	watt/cc
Nuclear heating	0.202	0.451	0.354	0.274	0.191	0.542	0.354	0.271	watt/cc

For VS, the problem of cooling water supply line imbalance is less that ELM because the water temperature rise is less, but there is an option available to eliminate the issue all together. If the water flow direction is the same in all turns then the pattern of cooling supply line leakage resistance is shown in Figure 5-11 and the distribution of temperature across the turns is shown in Figure 5-12.

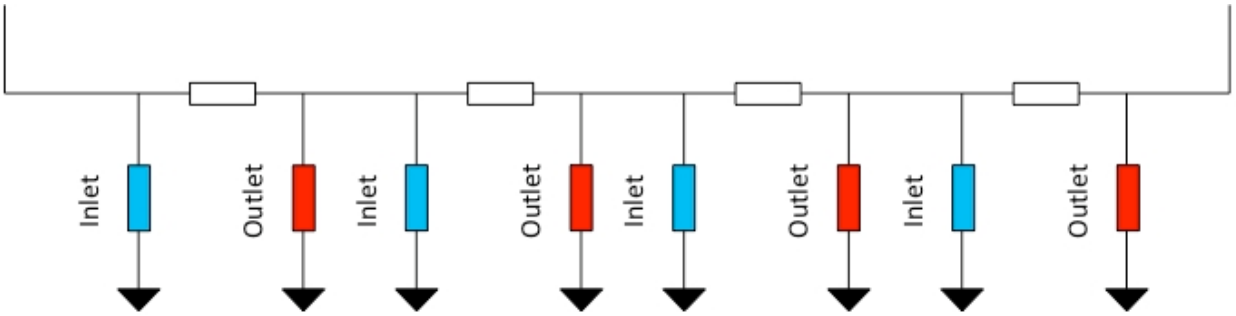

Figure 5-11 VS Water Line Pattern

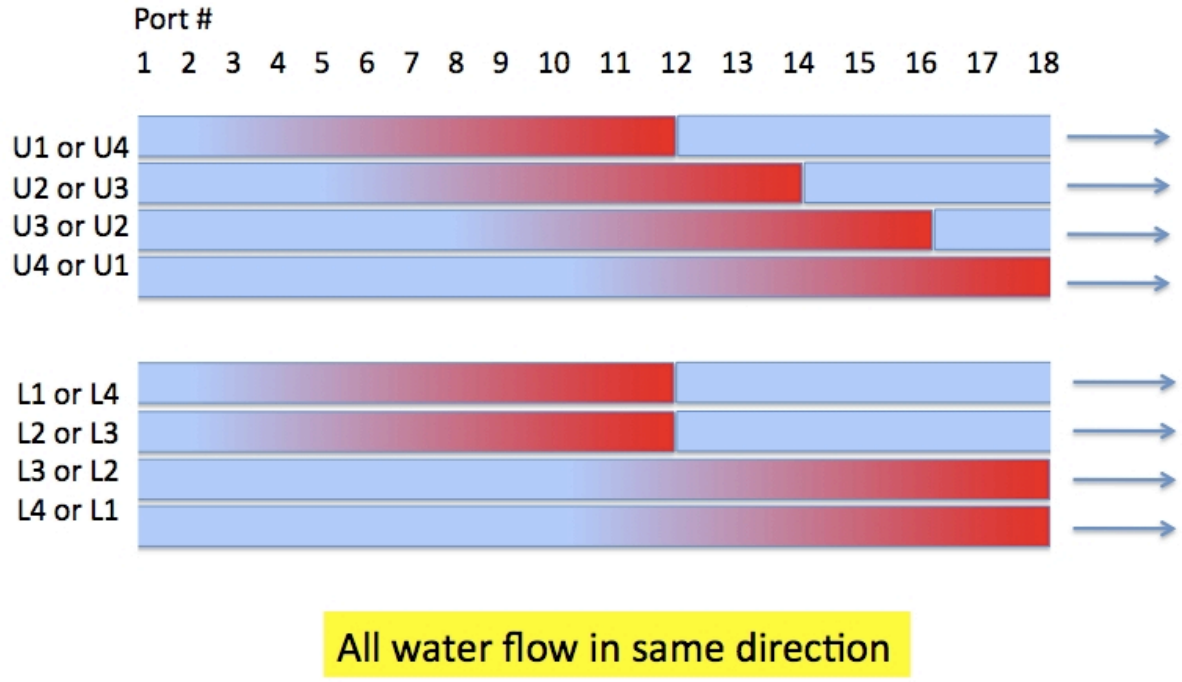

Figure 5-12 Toroidal Temperature Distribution In Turns With All Water Flow in Same Direction

Two options for alternate cooling patterns can restore the symmetry to the leakage resistance[69] as shown in Figure 5-13 through Figure 5-15.

[69] "Grounding Network Study for Vertical Stabilization of Plasmas", C. Bovet, Summer Intern Report, 2010

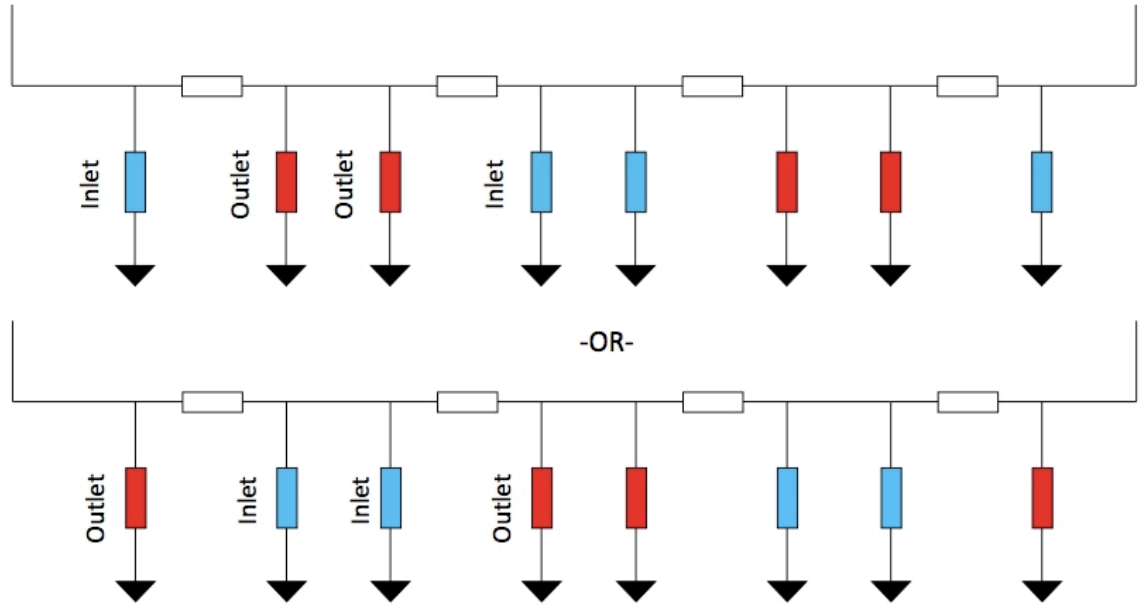

Figure 5-13 Alternate Cooling Water Patterns With Symmetry

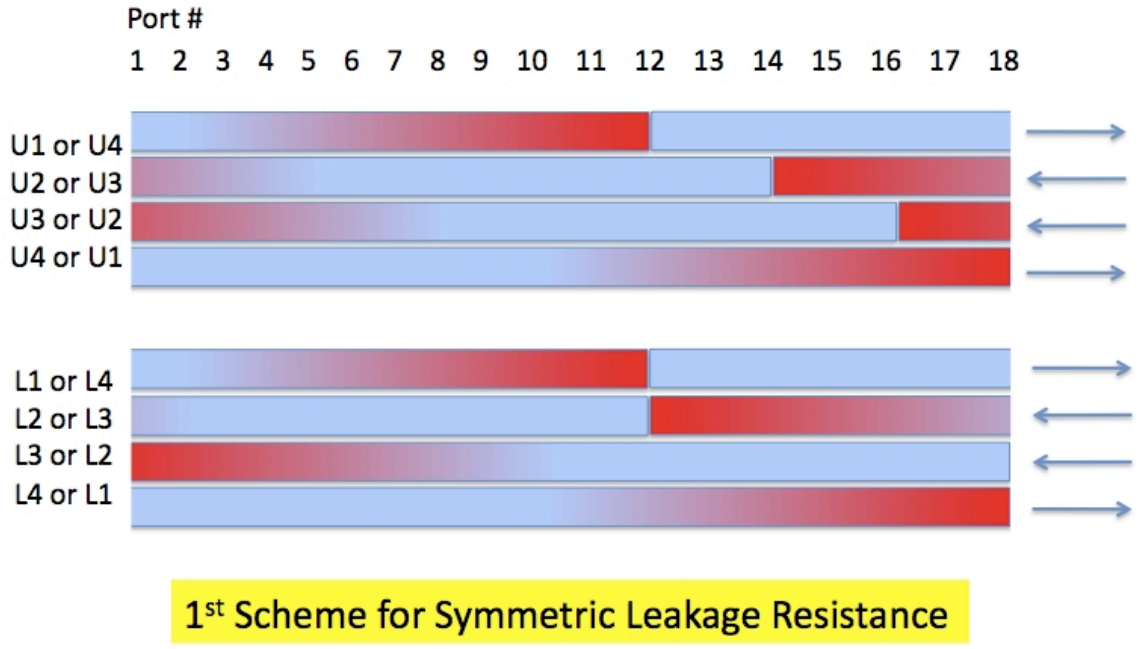

Figure 5-14 Temperature Pattern With 1st Scheme

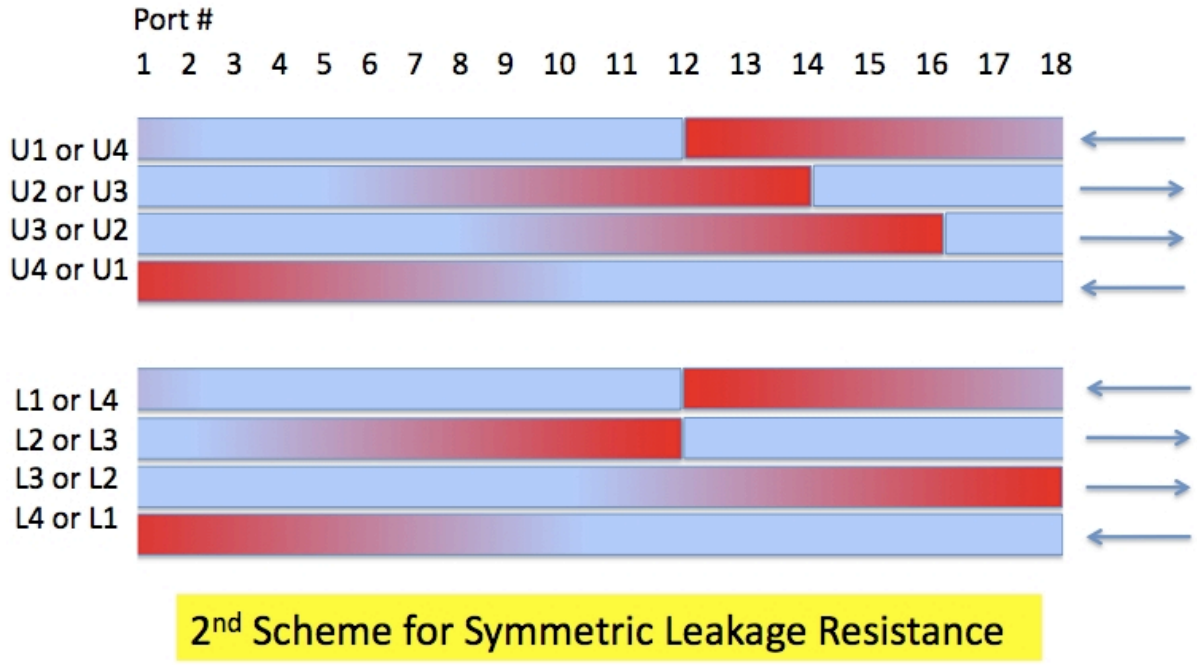

Figure 5-15 Temperature Pattern With 2nd Scheme

Given the water cooling line resistance and the highly variable coil leakage resistance, the situation is rather complex, and further work via circuit analysis is needed to quantify the flow of ground current under normal and fault conditions based vs. choice of grounding resistance for the cases with and without radiation. However, the following conclusions can be drawn:

- the water line resistance will dominate the leakage when radiation is not present. If all water flow paths are in the same toroidal direction an inherent asymmetry will exist. However by altering the water flow pattern the symmetry can be eliminated. The temperature profiles across the turns, already complex because of the different port feed locations, will be altered, which may or may not be significant;

- The coil stray resistance will dominate the leakage when radiation is present but with an appropriate turn connection pattern the asymmetries between the two halves each interleaf is minimized;

- The ohmic dissipation in the mineral insulation, due both to leakage resistance and frequency-dependent dielectric loss, is very small, much less than the nuclear heating.

5.5.4 **Ground Fault Detection**

As previously mentioned, ground fault detection can be implemented using the traditional means of measurement of ground current and annunciation of fault conditions when the magnitude exceeds a particular level. By suitable arrangement of turns and cooling lines as described the asymmetries introduced by temperature and radiation can be minimized. A circuit analysis is required to study this problem and determine an suitable value of grounding resistance which maximizes sensitivity while avoiding false trips due to electrical transients under the full range of cooling water temperature and radiation flux.

Because of the unusual nature of the coils which experience RIC and operate at high temperature, the sensitivity may be limited. Other schemes can be deployed which may provide an advantage in this application. An example would be the placement of a common mode AC voltage in the ground connection which would elevate the potential of the entire winding. A notch filter could monitor the ground current at the frequency of the AC source. In this case the effects of asymmetry previously discussed would be filtered out. This should be investigated.

6 ELECTROMAGNETIC PERFORMANCE

6.1 EM PERFORMANCE SUMMARY

The IVCs must be designed to withstand both normal operating conditions and excursions such as plasma disruptions. For normal operation, the VS coils provide up to 60 kA for vertical stabilization of the plasma. The ELM coils provide +/- 15 kA for ELM and RWM control. As mentioned in Section 2.2.1.1, these currents will oscillate on a 5 Hz time scale. During a plasma disruption, the IVCs are assumed to be short-circuited. Therefore, the current in the coils will increase or decrease depending on the scenario. Figure 6-1 shows the maximum current amplitude during normal operation and across three, 2007 disruption scenarios. All loads presented in this document are for a single 40° sector of the machine.

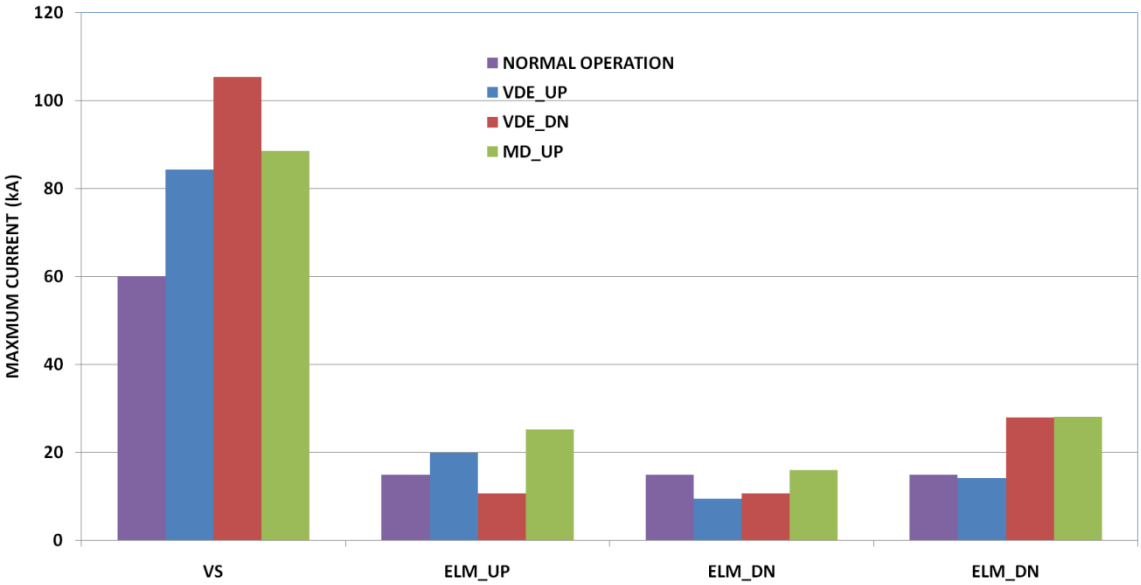

Figure 6-1 Maximum Current in IVCs for Normal Operation and Three 2007 Plasma Disruption Scenarios

The maximum current in the VS coils is 105 kA. The maximum current in ELM_UP, ELM_MD, and ELM_DN is 25, 16, and 28 kA, respectively. The currents in the passive

structure and other coils produce fields that when crossed with the IVC currents produce forces that are quantified in Figure 6-2.

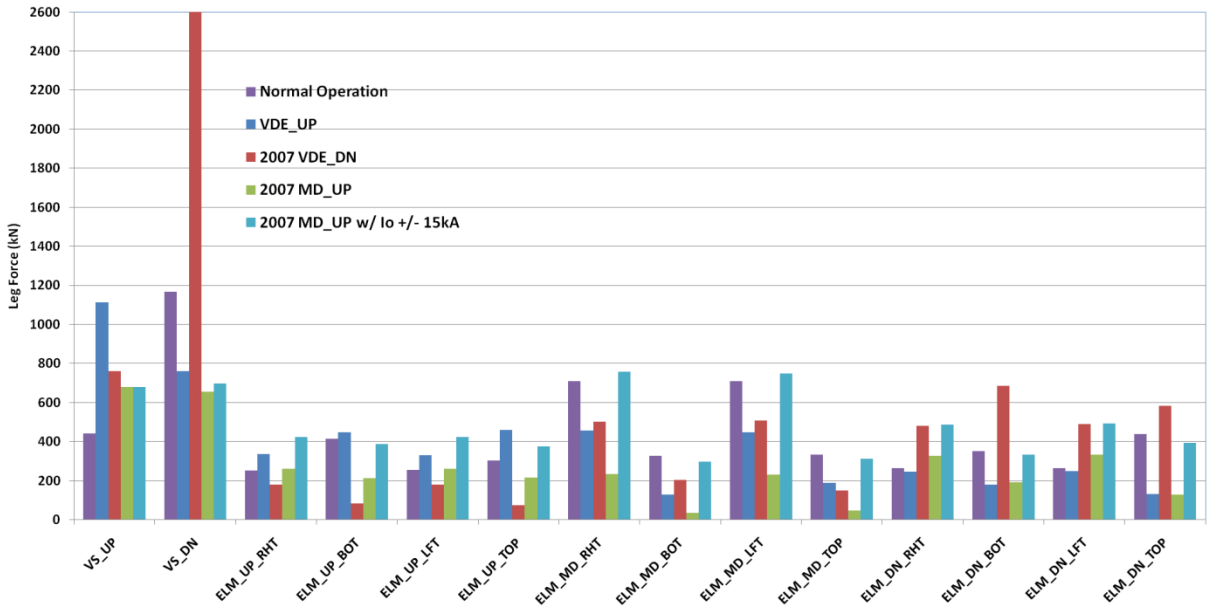

Figure 6-2 Maximum Forces on IVCs Legs for Normal Operation and Three 2007 Plasma Disruption Scenarios

The force magnitude on the VS is driven by the disruption scenarios – specifically VDEs. The forces on the upper and lower ELM coil legs are driven by the associated VDE. That is, the upper ELM coil has higher forces on the top and bottom legs for VDE_UP and the left and right legs have a higher force for the MD_UP with non-zero initial currents. The lower ELM has maximum forces during a VDE_DN. The middle ELM coil top and bottom leg forces, on the other hand, are driven by normal operation. The left and right leg forces are slightly higher (7%) for the MD_UP with non-zero initial currents.

The maximum leg forces are tabulated in Table 6-1. The for each coil leg, the cartesian components and magnitude of the force is given along with the scenario in which the maximum occurs and the time within the scenario. NO implies normal operation and no time is given. Finally, the ration of the maximum force magnitude to the maximum during normal operation is given.

Table 6-1 Maximum Force Magnitudes on IVC Legs for Normal Operation and Three 2007 Plasma Disruption Scenarios

COIL LEG	Scenario	Time (s)	Fx (kN)	Fy (kN)	Fz(kN)	|F|(kN)	ratio to normal operation
VS_UP	VDE_UP	0.845	487	169	986	1,113	2.52
VS_DN	VDE_DN	0.654	2108	769	-1482	2,689	2.30
ELM_UP_RHT	MD_UP	0.034	342	60	244	336	1.70
ELM_UP_BOT	VDE_UP	0.830	-399	-164	-124	449	1.08
ELM_UP_LFT	MD_UP	0.034	-289	-191	-241	331	1.66
ELM_UP_TOP	VDE_UP	0.830	373	119	239	459	1.52
ELM_MD_RHT	MD_UP	0.028	749	106	19	710	1.07
ELM_MD_BOT	NO	N/A	276	157	-72	326	1.00
ELM_MD_LFT	MD_UP	0.028	-662	-351	-21	710	1.06
ELM_MD_TOP	NO	N/A	-288	-126	-110	332	1.00
ELM_DN_RHT	MD_UP	0.040	-422	-48	235	479	1.85
ELM_DN_BOT	VDE_DN	0.660	519	221	-389	685	1.96
ELM_DN_LFTT	MD_UP	0.040	357	246	-236	490	1.88
ELM_DN_TOP	VDE_DN	0.0658	-534	-162	173	584	1.33

6.2 IVC FORCES DURING NORMAL OPERATION

The forces acting on the IVCs during various 15 MA DT operating scenarios were analyzed in a quasi-static mode – i.e., no eddy currents in nearby conducting structures. For previous static calculations of the forces acting on the IVCs, a single time point from a single plasma scenario was used. For the CDR the End-of-Burn (EOB) condition was chosen from a DINA simulation scenario[70]. This time point in this scenario was also the starting point for all plasma disruption runs using OPERA.

For the PDR, it was decided to investigate other time points in the scenario for the worst case loads. In addition, there are ten scenarios presently in the IDM. The quasi-static forces on the IVCs during five of the scenarios have been examined. In addition one scenario was used to examine all 16 possible signs of the IVC currents. Except for the VS, only small differences in the magnitude of the forces acting on the IVC legs was seen. Of course, a changed sign of the current implies component reversal.

The force on upper VS coil for the single time point at EOB previously reported is about 27% lower than the new scenario-based calculation. The upper VS coil sees the highest scenario-based force at the start of burn (SOB). However, the VS peak loads are significantly higher during plasma disruption events. The forces on the other IVCs are similar to the previously reported values, only differing by a few percent.

[70] EM Analysis of ELM & VS Coils ITER_D_XXXXXX v 1.0, A. Brooks, PPPL, undated.

6.2.1 Scenarios

The scenarios chosen are from the Excel workbook entitled "Contents of PF Scenario database"[71]. Those underlined have been analyzed. The scenarios are denoted:

15MA DT-DINA2010-01	15MA DT-DINA2010-01b	15MA DT-DINA2010-01
15MA DT-DINA2010-02 (v2)	15MA DT-DINA2010-02b	15MA DT-DINA2010-03(v2)
15MA DT-DINA2010-03b	15MA DT-DINA2010-04b	15MA DT-DINA2010-04c
15MA DT-DINA2010-05b		

For this memorandum, the names are truncated to 2010_xxx – e.g., 2010_04c. The scenarios were edited to reduce the number of times at which the forces at computed. All major labeled times such as X-Point formation, Start-of-Flattop, etc. where included. In addition, times at which the plasma current reached 1 MA increments from 2 MA to 15 MA were added. During the burn, the time points were sampled approximately every 20 seconds. Finally, the plasma current ramp down was captured in 1 MA decrements.

6.2.2 Model

Figure 6-3 shows a sketch of the IVC's. The IVCs are modeled with 36, 20-node brick elements in the one 40-degree sector of the model. The forces acting over portions are summed to get "leg" forces as indicated. The Lorentz forces acting on each leg at each chosen time point in the scenario were calculated using a 1x1x16 point Gaussian integration over the IVC. PF coil definitions used in the analyses are included in Appendix III.

[71] (https://user.iter.org/?uid=34263N)

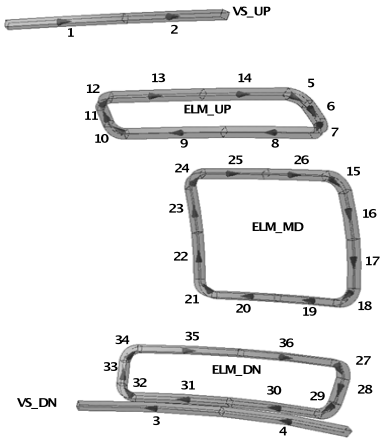

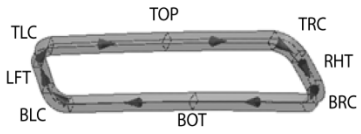

Typical ELM

The forces at the four corners are distrubted equally to the four legs. That is, half the the force on the top right corner (TRC) is added to the TOP leg and half to the RHT leg.

Figure 6-3 IVC 20-node Brick Numbering

6.2.3 **Results**

An initial scan across the five scenarios with the VS coils at 60kA and the ELM coils at -15kA showed little variation as shown in Figure 6-4. Also included (first bar in each set) is the maximum leg force for single time point (EOB) 2010_03(V2) previously used to quantify normal operating loads. The third bar shows the peak loads across all 16 combinations of signs of the VS and ELM coils.

The results for the maximum force magnitudes (and their attendant Cartesian components are shown in Table 6-2 along with the scenario and time point). Also in the last columns are the maximum leg forces for 2010_03(V2) at the EOB condition. Except for the upper VS, all the maximum forces are within a few percent of the EOB condition.

Table 6.3 shows the maximum force per unit length for scenario 2010_03(V2).

Additional plots of the leg forces versus time and forces per unit length versus time and versus length for the 2010_03(V2) scenario are shown in Appendix III.

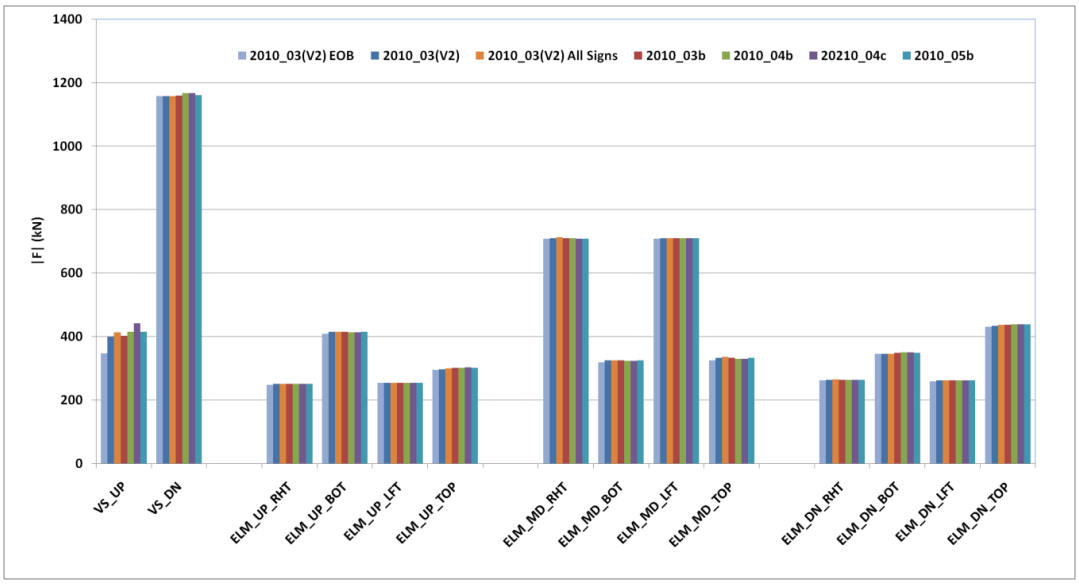

Figure 6-4 Maximum Magnitude of forces acting on the IVC legs for various plasma scenarios

Finally, Figure 6-5 compares the maximum magnitude of the normal operating forces from the PDR to those from the Reference Design and the CDR. As can be seen, with the exception of the top leg of the lower ELM coil, all loads have stayed the same or decreased. The upper VS coil has a significantly lower force due to the change in position.

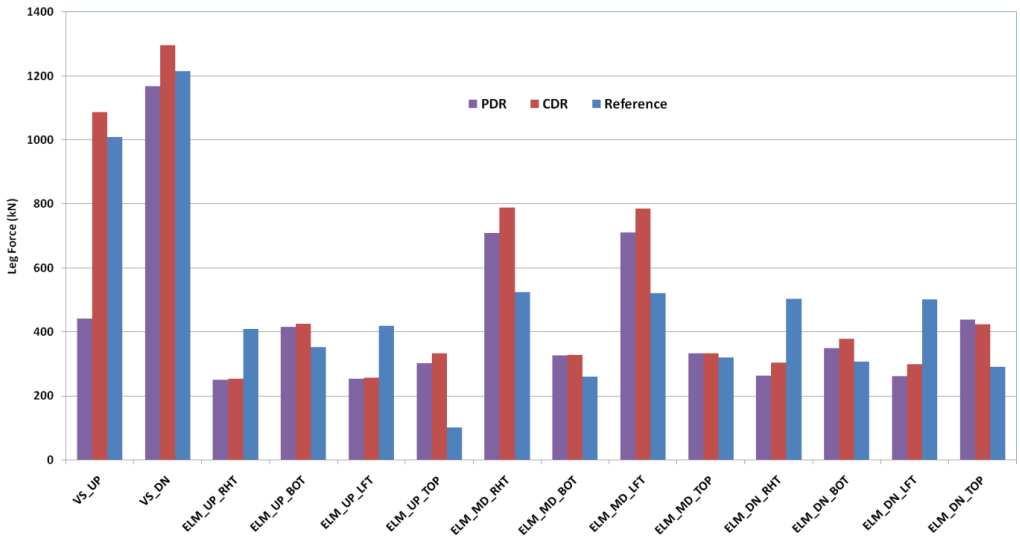

Figure 6-5 Maximum Magnitude of Forces Acting on the IVC Legs for the PDR, CDR and Reference Designs

Table 6-2 Maximum Forces across 5 scenarios (VS +60 kA, ELMs -15 kA) compared to EOB from 2010_03(V2)

	Maximum Across 5 Scenarios							EOB for 2010_03(V2)					
Coil	Time F_{max}(s)	F_x(N)	F_y(N)	F_z(N)	|F|(N)			F_x(N)	F_y(N)	F_z(N)	|F|(N)		Ratio
VS_UP	500.09	315921	176190	252466	441121	04c		253680	140255	192149	347773		126.8%
VS_DN	70.30	-756109	-437691	774922	1167809	04c		-746407	-432090	772458	1157807		100.9%
ELM_UP_RHT	1.154	-193416	-68658	-143378	250362	04c		-191452	-63779	-142962	247305		101.2%
ELM_UP_BOT	100.95	299426	191912	214302	415252	03b		291500	187336	215363	407981		101.8%
ELM_UP_LFT	250.09	154363	140662	144560	253990	03(V2)		154995	139846	144423	253848		100.1%
ELM_UP_TOP	484.89	-196834	-96862	-208185	302435	04c		-204296	-101170	-186469	294522		102.7%
ELM_MD_RHT	559.89	-677241	-211039	-16701	709557	04b		-673222	-218464	-24175	708194		100.2%
ELM_MD_BOT	100.95	276215	157103	-71679	325794	05b		269846	153907	-74216	319393		102.0%
ELM_MD_LFT	32.49	554618	443194	9309	710077	04c		559421	435060	6359	708710		100.2%
ELM_MD_TOP	170.09	-287552	-125800	-109540	332432	03(V2)		-282301	-123165	-106516	325897		102.0%
ELM_DN_RHT	50.29	-218139	-74868	126204	262920	05b		-218651	-73161	126076	262785		100.1%
ELM_DN_BOT	70.30	239832	159478	-198837	349984	04c		236379	157485	-197509	345957		101.2%
ELM_DN_LFT	559.89	160980	164528	-125690	262263	04b		156091	164902	-124505	258956		101.3%
ELM_DN_TOP	70.295	-327550	-165933	238990	438108	04c		-322702	-163134	234270	430850		101.7%

Table 6-3 Maximum Local Force per unit length for scenario 2010_03(V2)

	ELM_UP								ELM_MD								ELM_DN							
	time of max	Fu/l (kN/mm)	Fv/l (kN/mm)	Fw/l (kN/mm)					time of max	Fu/l (kN/mm)	Fv/l (kN/mm)	Fw/l (kN/mm)					time of max	Fu/l (kN/mm)	Fv/l (kN/mm)	Fw/l (kN/mm)				
RTC																								
Fumax	90.1	304.4	-34.0	-24.5	+	+	+	-	170.1	314.2	-5.9	11.7	+	-	+	+	90.1	309.8	-10.5	3.5	+	-	-	+
Fvmax	150.1	-301.3	49.2	27.0	-	-	+	+	19.1	-254.7	19.6	-10.1	-	+	-	+	70.1	-305.7	33.3	-2.3	-	+	+	-
Fwmax	170.1	-301.6	49.1	27.0	-	-	+	+	170.1	314.1	-8.9	11.8	-	+	+	-	1.2	241.5	5.8	4.0	+	-	-	+
RHT																								
	70.1	369.2	-49.5	13.4	+	+	-	-	696.5	341.3	0.9	-8.5	+	+	+	+	611.3	369.6	-25.2	0.1	-	+	+	+
	1.2	-364.3	75.3	-10.6	-	-	+	+	34.1	-339.7	16.2	8.5	+	+	+	+	611.3	-368.3	33.5	-0.1	-	+	+	-
	70.1	369.2	-49.5	13.4	+	+	-	-	696.5	-339.7	3.0	8.5	+	+	+	+	1.2	369.6	6.5	0.1	+	-	-	+
RBC																								
	1.2	237.9	-34.1	16.9	+	+	-	-	1.2	226.2	-5.0	-15.8	+	+	+	-	1.2	252.0	-10.3	6.7	-	+	+	+
	1.2	-235.7	48.9	-15.6	-	-	+	+	0.0	-221.8	18.1	15.7	-	+	-	+	611.3	-214.1	36.2	-5.8	-	+	+	-
	1.2	237.9	-34.1	16.9	+	+	-	-	1.2	-224.0	17.3	15.8	-	-	-	+	1.2	245.2	8.9	7.2	+	+	+	+
BOT																								
	170.1	106.8	-2.2	16.3	+	-	+	-	90.1	117.7	-13.5	0.0	+	+	+	+	500.1	90.6	-1.6	-0.2	+	-	-	-
	70.1	-97.9	15.8	-13.8	+	+	-	-	110.1	-115.1	22.0	0.0	+	+	+	+	611.3	50.9	28.5	-0.2	-	+	+	-
	170.1	106.5	0.5	16.5	-	-	+	+	1.2	-0.8	1.4	0.0	+	+	+	+	90.1	-89.1	8.9	0.2	+	-	-	+
LBC																								
	170.1	309.6	20.2	43.0	+	-	-	-	90.1	306.3	-2.7	20.6	-	-	-	+	500.1	309.5	-3.2	-8.5	+	-	-	-
	150.1	308.8	23.6	43.2	-	-	+	+	170.1	-302.2	16.1	-20.4	+	-	+	-	1.2	-253.7	24.6	6.9	+	-	-	+
	170.1	309.1	23.5	43.3	-	-	+	+	90.1	305.9	-6.6	20.7	+	+	-	-	90.1	-300.9	-2.6	9.2	-	-	-	+
LFT																								
	70.1	371.5	33.7	-15.1	+	-	-	-	696.5	341.3	2.2	8.5	+	-	-	-	85.1	369.6	8.1	-0.1	+	-	-	-
	1.2	369.0	51.0	-13.3	-	-	+	+	34.1	341.3	16.3	8.5	-	+	-	+	611.3	369.6	23.9	-0.1	-	+	+	-
	70.1	-371.3	-25.0	16.0	+	+	-	-	70.1	341.3	11.7	8.5	-	-	-	-	5.5	-368.3	10.9	0.1	+	+	+	+
LTC																								
	1.2	247.4	20.6	-31.8	+	+	+	+	1.2	228.8	17.7	-9.8	-	+	-	-	1.2	239.0	4.1	-3.9	-	+	+	-
	1.2	247.3	21.2	-31.7	+	+	+	+	19.1	207.1	18.3	-9.3	-	+	-	+	70.1	173.7	24.5	-4.7	-	+	+	-
	1.6	-247.0	-5.1	32.4	+	+	+	+	0.0	-225.9	-5.4	9.8	+	-	+	+	611.3	-197.9	-12.1	4.2	-	+	+	+
TOP																								
	90.1	82.3	3.5	-10.9	+	+	+	+	170.1	123.2	5.9	-0.1	+	-	+	-	90.1	106.2	-9.3	0.1	+	-	-	+
	70.1	79.6	12.4	-9.5	+	+	+	+	696.5	27.6	12.1	-0.1	+	-	+	-	70.1	-101.1	25.7	-0.1	-	+	+	-
	110.1	-81.1	5.8	11.8	+	+	+	+	170.1	-121.7	1.5	0.1	-	+	-	+	90.1	106.2	-9.3	0.1	+	-	-	+

These are maximum forces per unit length in local conductor coordinates for each of the 4 corners and 4 legs for the 2010-03(V2) scenario - with IVCs taking on all possible signs combinations. To get the row labeled RTC Fumax , the maximum Fu/l (local normal to the vacuum vessel) is found across all time points in the scenario and at each time point across all the IVC sign combinations. The Fv/l, and Fw/l at the time of the maximum Fu/l are the next two columns. The process is repeated for Fvmax and Fwmax.

The signs +,+,+ - refer to the sign of the IVC current (i.e., VS at +60 kA, ELM_UP at +15kA, ELM_MD at +15kA, and ELM_DN at -15kA)

The worst case component loads are the local diagonals i.e. the blue highlights.

6.3 VDE AND PLASMA DISRUPTION

During plasma disruption events, currents are induced in both the passive structure such as the vacuum vessel and in the IVC coils. The plasma motion, thermal quench and the current quench contribute to these currents. Once the currents have been determined, the forces acting on the IVCs are calculated across the scenario. The times and peak forces are tabulated at the beginning of Section 6.0.

6.3.1 Scenarios

The plasma disruption events analyzed were based on the 2007 DINA simulations. A single 2010 simulation was analyzed to compare the impact on IVC currents and forces. The plasma disruption events analyzed were: (a) 2007 MD_UP with a 36 ms linear current quench; (b) 2007 VDE_UP with a 36 ms linear current quench; (c) 2007 VDE_DN with a 36 ms linear current quench; and (d) the 2010 VDE_DN with a 16 ms exponential current quench. The linear current quench produces higher loads on the vacuum vessel walls[72].

[72] Load Specification for the ITER Vacuum Vessel (ITER_D_2F52JY v2.2 – sec 5.2)

Several possible sets of initial currents in the IVCs at the start of the disruption event were investigated. The initial VS coil currents were assumed to be zero for all cases since the interaction of the VS with the plasma will greatly impact the motion and nullify the physics basis of the disruption modeling. On the other hand, it is felt the ELM coils could potentially have any value of current at the time of the disruption. In these analyses, the ELM coil current chosen is the one that will provide the worst case current/force during the event.

The loss of toroidal flux during the event will induced poloidal currents in the conducting structure. One reason for including the poloidal ribs was to give additional paths for these eddy currents.

6.3.2 **Model**

Figure 6-6 shows a 40° sector of the IVCs and vacuum vessel for both the CDR and PDR designs. The PDR design includes the poloidal ribs between the inner and out vacuum vessel walls,. However, the blanket, divertor, and structural support beam are not included in this model. The poloidal ribs are shown in Figure 6-7.

All structural elements are assumed to have an electrical conductivity of 1350 Siemens/mm. The IVCs are modeled as thirty-six 20-node brick elements having a cross-section of 884 mm^2. The ELMS have a conductivity of 41,152 Siemens/mm and the VS coils 42,373 Siemens/mm.

The TF and PF coils were assumed to be held at constant current during all of the plasma disruptions. The IVCs are assumed to be shorted at the start of disruption event. The plasma is modeled as a number of stationary, co-axial, solenoids with time-varying currents to model both the motion and current quench. Figure 6-8 shows a typical model of the vacuum and coils (in red) for a downward VDE.

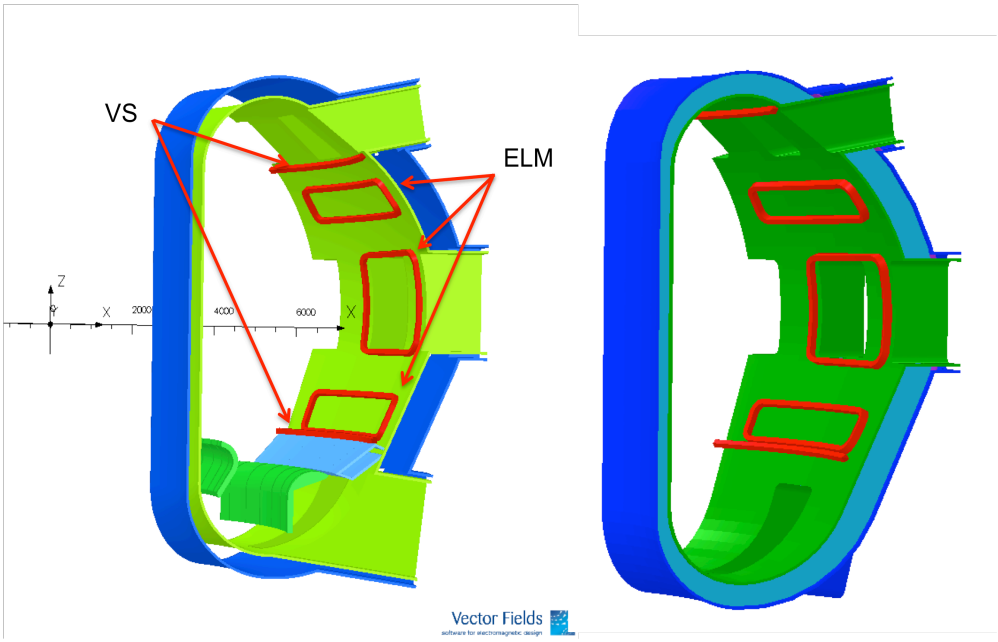

Figure 6-6 Vacuum Vessel and IVC model – CDR (left) and PDR (right) – used in plasma disruption analyses

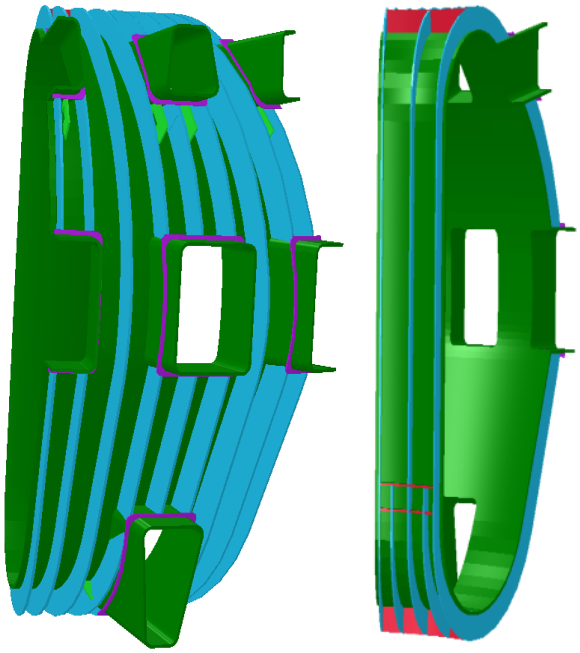

Figure 6-7 Vacuum Vessel Ribs

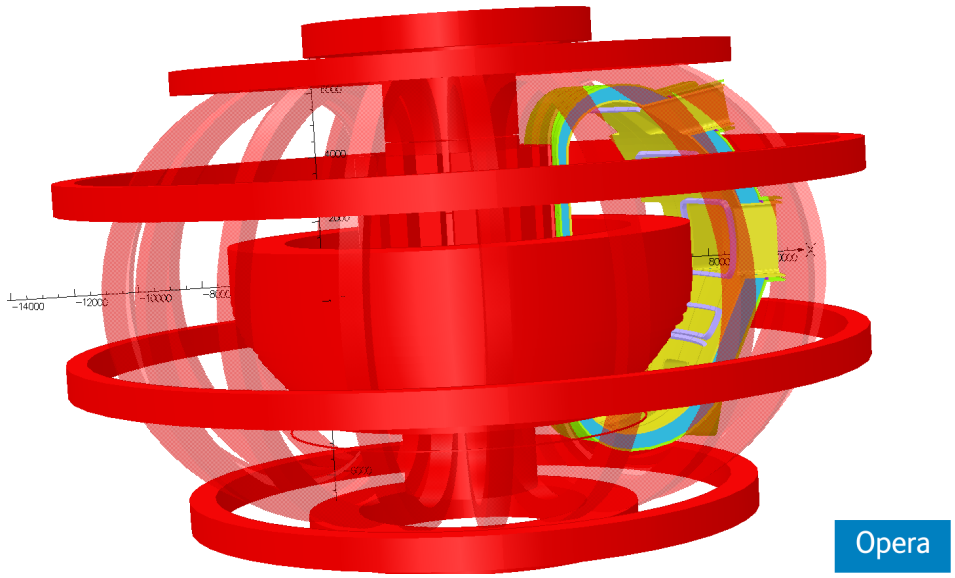

Figure 6-8 Typical Model With All Coils Shown for a VDE_DN Scenario

6.3.3 **Results**

Component Currents

The three 2007 plasma disruption scenarios with a 36 ms linear current quench were analyzed. The net toroidal current across the sector boundary versus time is shown in Figure 6-9. The total vacuum vessel current is shown along with the individual values for the inner and out vessel shells. Since the time scale of the plasma current quench is much faster than the decay time-constant of the vacuum vessel all 15 MA of the plasma current is transferred to the vessel walls.

Although a bit difficult to discern, there are open circles on each plot showing the total current for the CDR. There is little difference except in the decay rate which is slower for the present design.

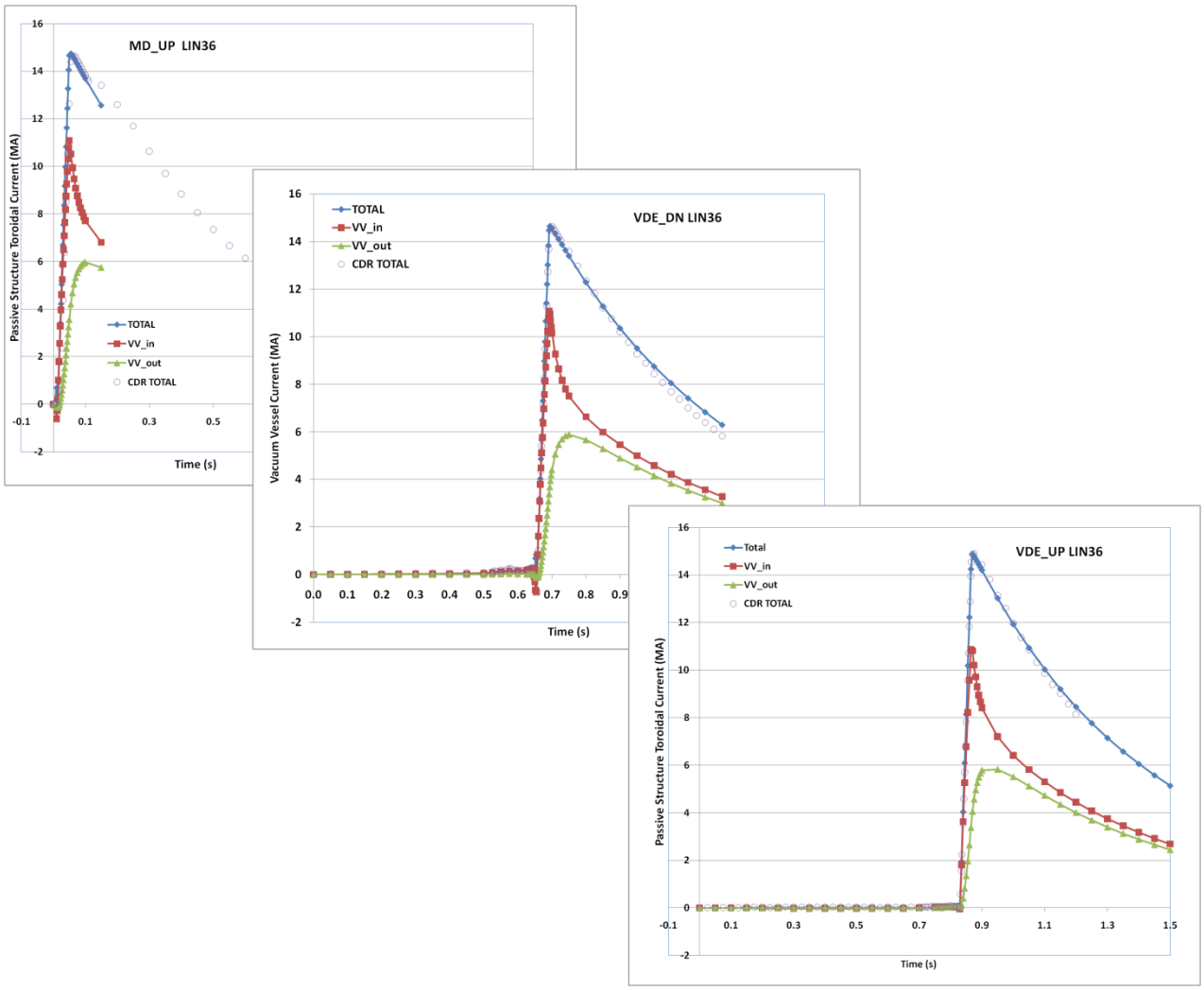

Figure 6-9 Toroidal Current in the Vacuum Vessel Walls versus Time for the Three Disruption Scenarios

The impact on the passive structure currents due to the introduction of a toroidal flux driver to capture the impact of the poloidal current decay in the plasma is shown in Figure 6-10. The two curves are the total poloidal current cross a plane at Z=0. The maximum current in the poloidal direction is approximately 120 kA per sector or about 1.1 MA for the entire tokomak.

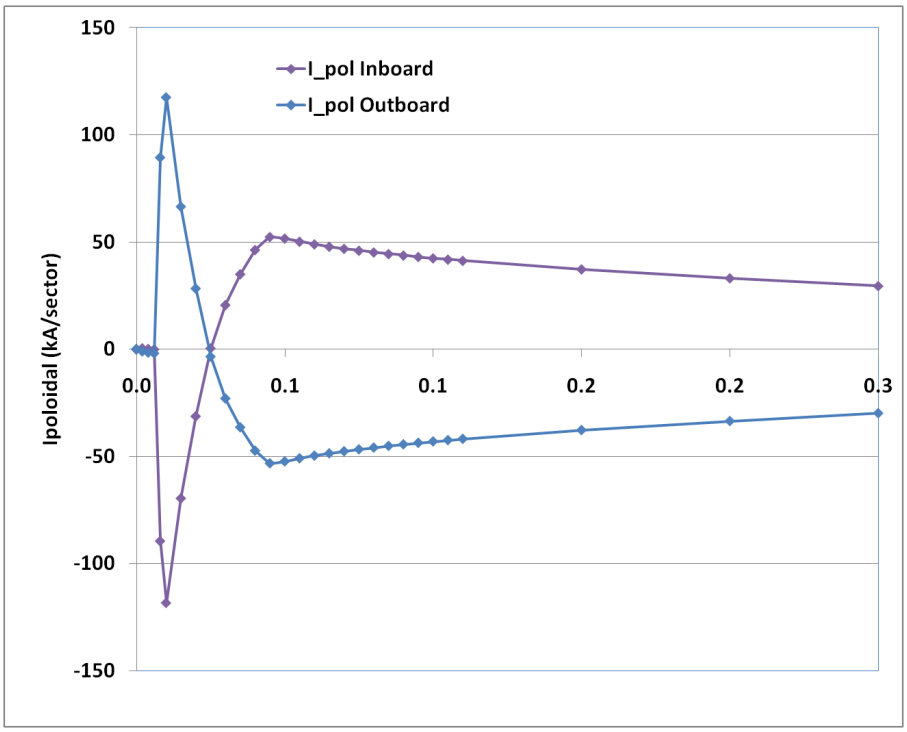

Figure 6-10 Impact of Toroidal Flux Driver on the Vacuum Vessel Currents

A single 2010 disruption scenario has been analyzed suing a new surface current model of 64 solenoids[73]. The OPERA drivers were for a 16 ms exponential plasma current decay VDE_DN scenario were provided. Although not a one-for-one comparison, Figure 6-11 shows the difference in component currents for the two scenarios. As can be seen, there is good agreement in the peak currents induced, and the actual model of the current quench does appreciably impact these currents.

[73] Riccardo Roccella, email communication.

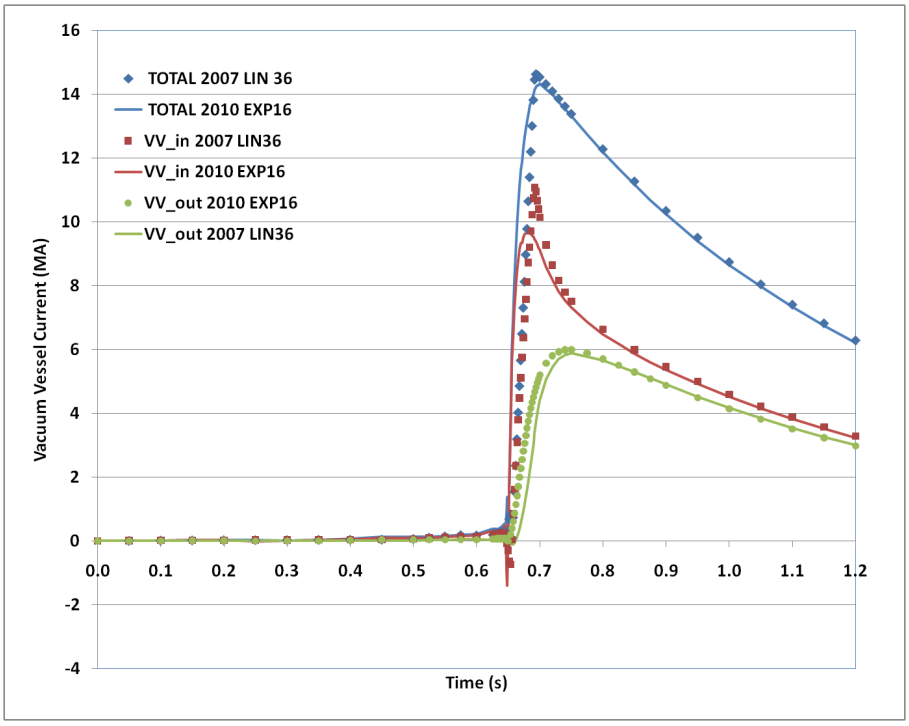

Figure 6-11 Comparison between the 2010 VDE_DN Scenario (16 ms Exponential Decay) and the 2007 VDE_DN (36 ms Linear Quench)

IVC Currents

The IVCs are assumed to be shorted at time=0 and the plasma motion and current quench induce currents in these circuit elements. Although it is possible to couple the windings to more sophisticated circuit models, these analyses had a zero resistance short across the coil leads.

One of the concerns in these analyses is to capture the worst case currents and forces. One major uncertainty is the current in the IVC at the time it is shorted. For these analyses it is assumed that initial currents of +/-15 kA in the ELM coils will not appreciably impact the plasma disruption scenario. However, it is felt that the VS coils cannot be started at +/- 60 kA since such a current would have a significant impact on the evolution of the disruption. CDR and early PDR analyses assumed the VS had an initial current of +/- 60 kA (which ever produced the higher current during the disruption), so the information is available but not deemed credible without a DINA simulation specifically addressing this point.

As will be shown below for the VDE_DN and VDE_UP, the choice of initial current has very little impact on the peak current during the plasma disruption. This is due to the relatively short decay time of the coil and the relatively long drift phase of the plasma.

The currents induced in the VS coils for the three scenarios are shown in Figure 6-12 on the same graph. In these cases, the initial current is assumed to be zero. As can be seen, the maximum current seen is 105 kA for the VDE_DN.

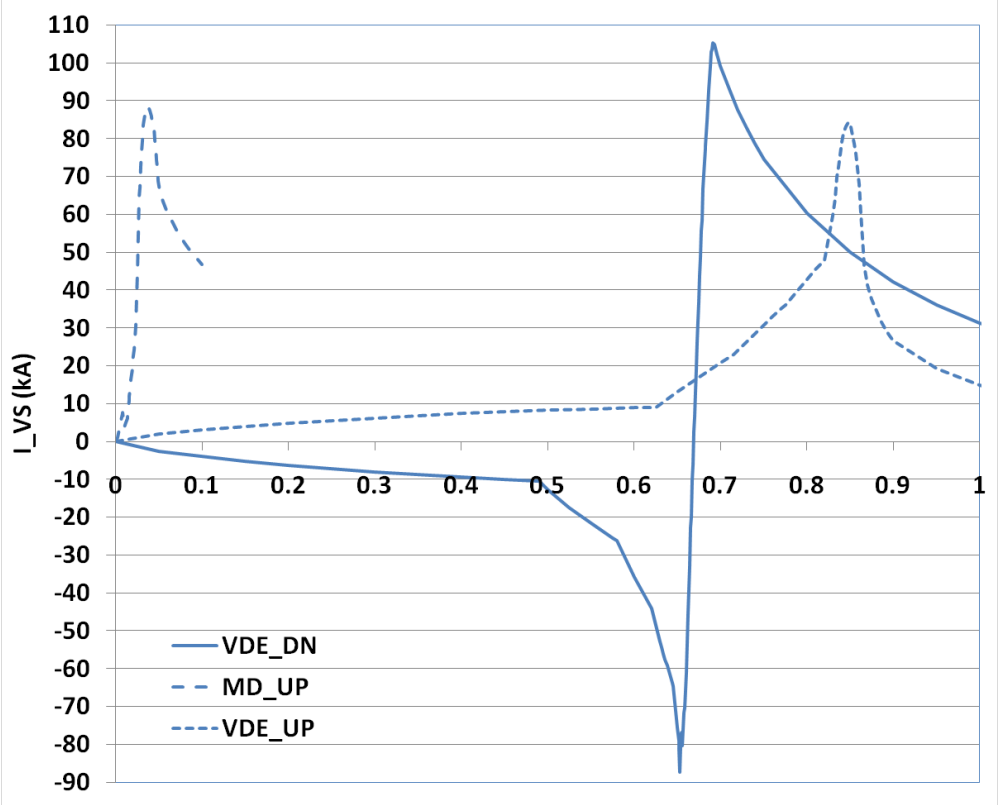

Figure 6-12 VS Current Versus Time for all three 2007 LIN36 Scenarios

Figure 6-13 through Figure 6-15 show the impact of a non-zero initial current in the ELM coils for the three scenarios. As can be seen, except for the MD_UP, the peak currents are not appreciably different from the zero initial current cases.

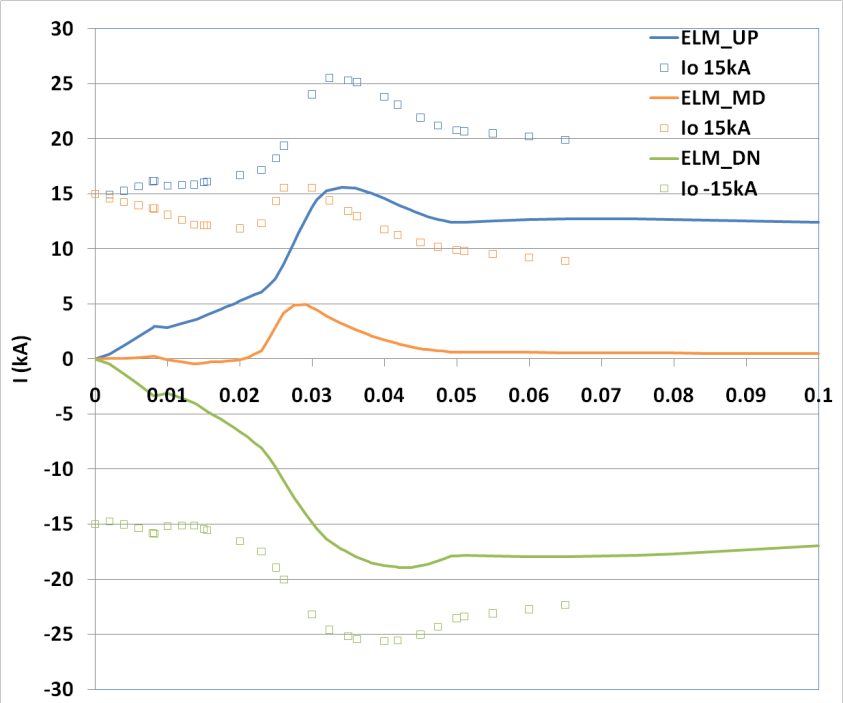

Figure 6-13 Impact of Initial Currents on ELM Coils versus time for 2007 MD_UP LIN36

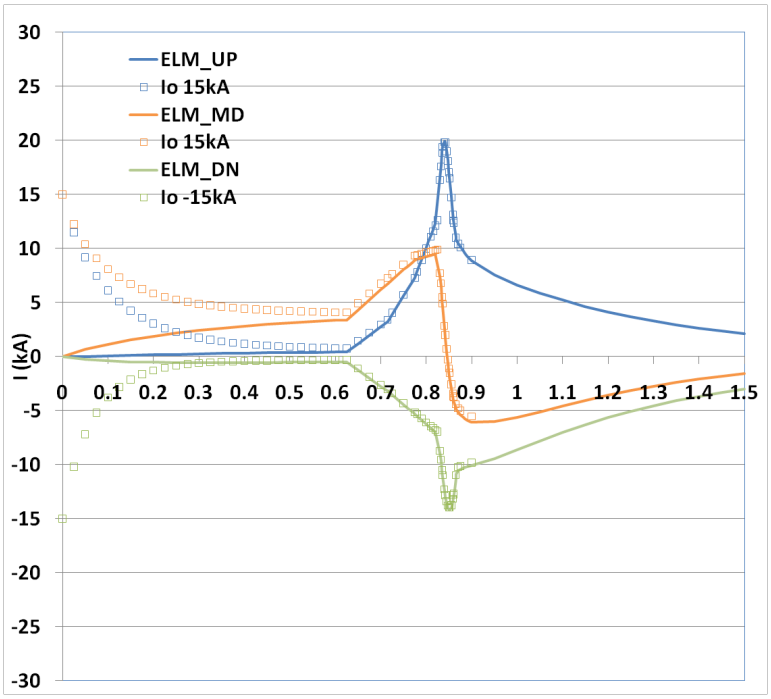

Figure 6-14 Impact of Initial Currents on ELM Coils versus time for 2007 VDE_UP LIN36

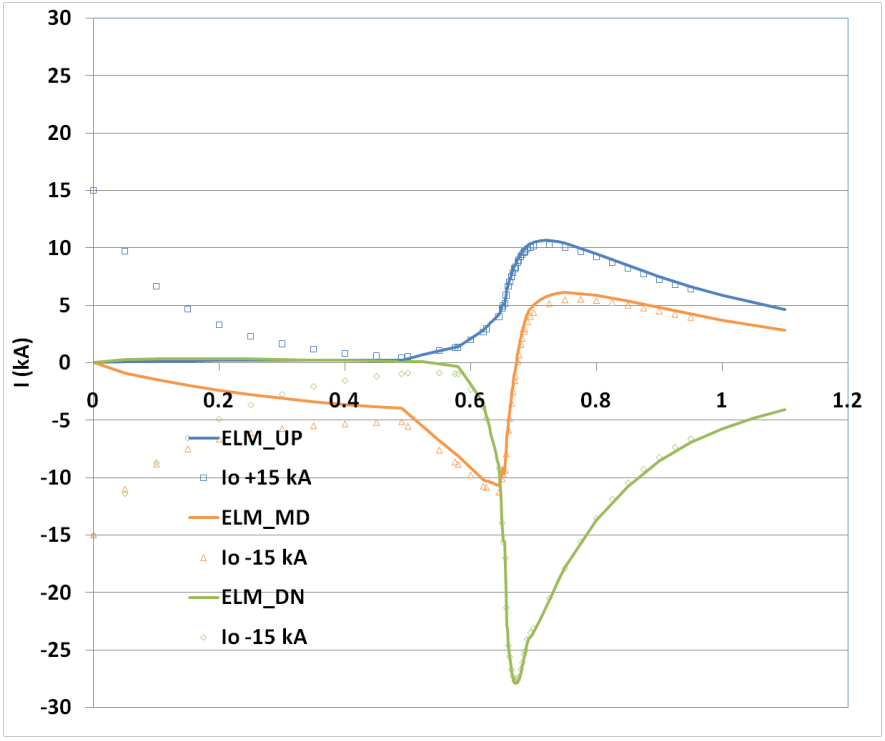

Figure 6-15 Impact of Initial Currents on ELM Coils versus time for 2007 VDE_DN LIN36

IVC Forces

At each time in the three plasma scenarios, the forces on the 20-node brick conductors of the IVCs are calculated. These are summed in the same way as the normal operating forces discussed in the previous section and are shown in Figure 6-16.

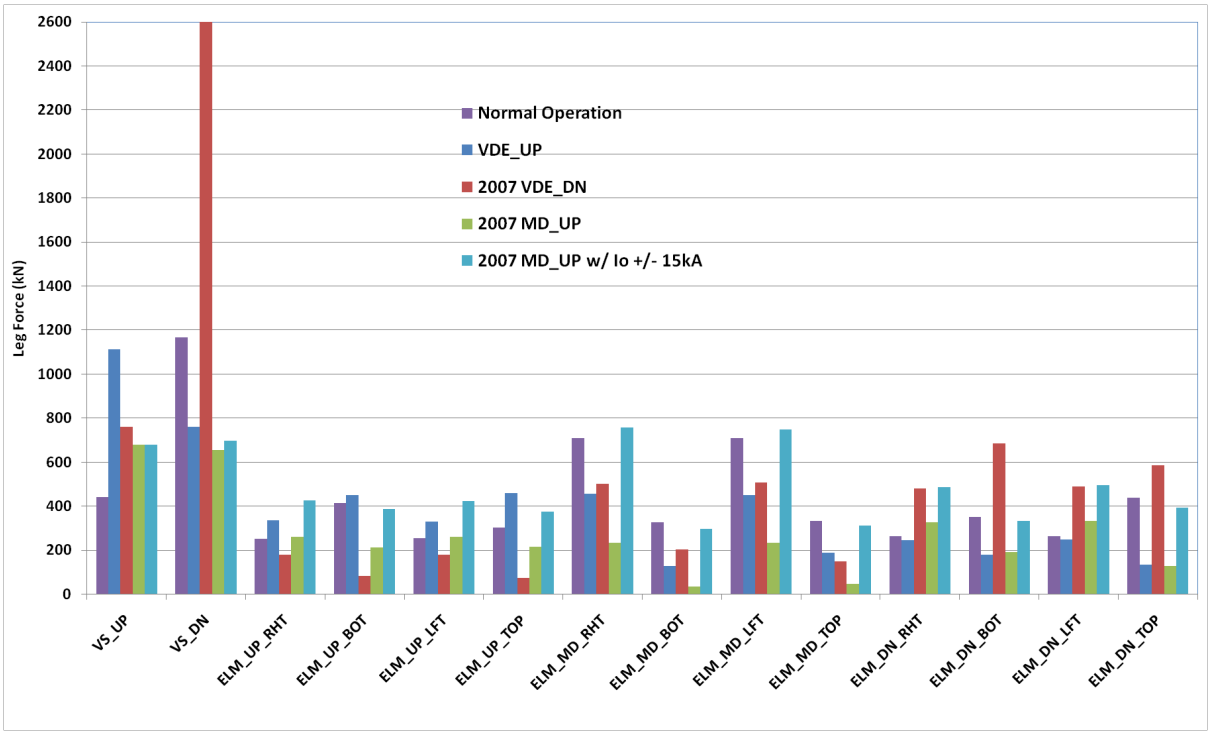

Figure 6-16 Disruption Force Summary

Two different analyses were performed for the MD_UP scenario. The first was with all ELM coils at zero initial current. The second analysis was with the upper and middle ELM coils at +15 kA and the lower ELM at -15 kA. Unlike the VDEs, the MD happens on a short time scale and the initial currents do not have time to decay.

7 THERMAL/HYDRAULIC PERFORMANCE

7.1 THERMAL PROFILES

7.1.1 Plasma operation

To determine the temperature profile of the ELM and VS coils a thermal hydraulic analysis was performed and cross checked using several different methods. First the power into the coil was determined by combining the resistive losses during a pulse with the power imparted to the coil assemblies as determined by the neutronics analysis. When in equilibrium the resistive plus nuclear power deposited into the coils is balanced by the heat rejected by the cooling water. This heat rejection is equivalent to the product of the mass flow rate, Cp, and temperature increase of the water. The power rejected by the coil must also be balanced by the ability of the water to pull the heat from the inner surface of the cooling hole. This is equivalent to the product of the heat transfer coefficient, the inner surface area of the cooling channel, and the difference in temperature from the cooling channel surface to the cooling water. For the ELM and VS Coils the heat transfer coefficients is high enough that the temperature rise from the water to the copper walls is much less significant, about an order of magnitude less than, the heat rise of the water from the inlet of the coil to the outlet of the coil. The results shown in the spread sheets attached as Appendix I and Appendix II, ELM and VS Coil Design points, used these methods to determine the outlet water temperatures.

To verify the results of the power balance calculations and to obtain time dependant plots an in house transient thermal analysis algorithm designed to solve water cooled pulse coils called FCool was run. This Fortran solver completes the picture by providing temperature vs. time plots. The transient thermal analysis uses a finite difference method breaking the coil into 500 nodes and stepping the solution from one node to the next. The heat transfer coefficient is calculated using the Sieder-Tait equation and conductor resistance as well as fluid properties are updated with respect to temperature for each time step and increasing temperature. The FCool results were bracketed by the “hand calculations” to check that the solutions were within bounds. For example the steady state maximum temperatures calculated using mass flow power balance

verified the FCool steady state maximum water temperature. For the thermal stress analysis these highest steady state temperatures were used.

For the VS Coil the temperature profile was calculated using a 10 second Pulse as described in section 2.2.2.2. The wave form was adjusted upward to include the nuclear power deposition from the neutronics analysis. The result shown in Figure 7-1 is for the Coil with both the inlet and outlet feeders. Note that while the requirement is for three pulses maximum the result shown here is for a steady state solution achieved after 7 pulses. The temperature rise used in the thermal stress analysis is based on this steady state worst case temperature. After 3 pulses the temperature is actually roughly half the steady state solution.

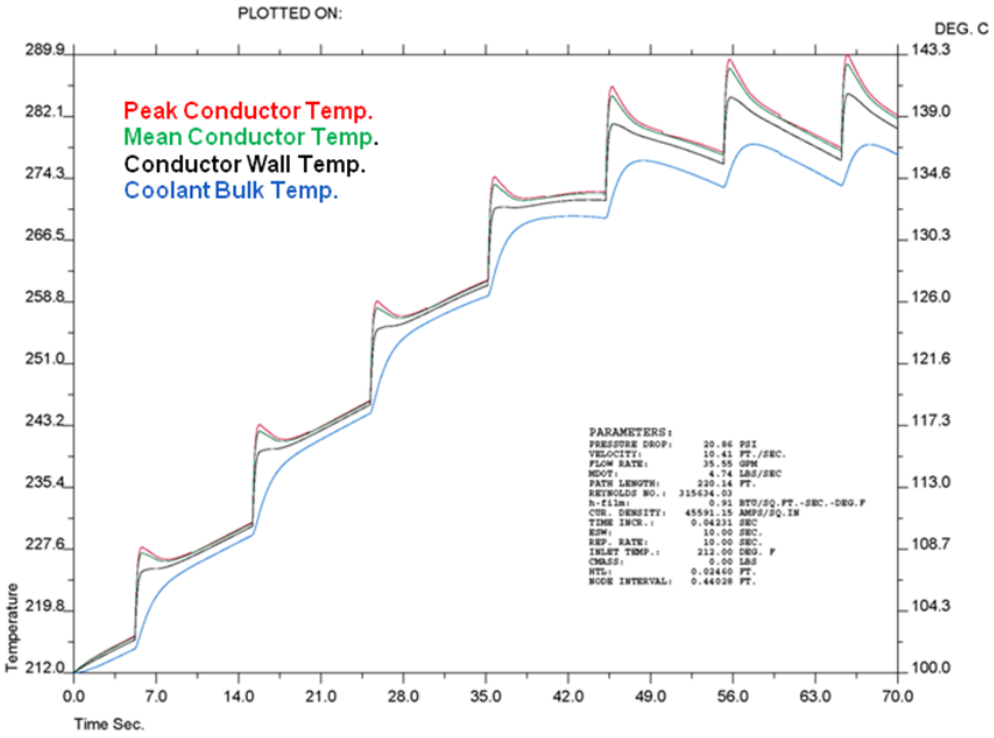

Figure 7-1 VS Coil and Feeders With Nuclear Heating

A run was also performed for the VS Coil to determine the maximum temperatures during a 1 turn fault condition. The VS coils have 4 independent turns and are design to meet their amp-turn requirement after the failure of one of those turns. The thermal profile in Figure 7-2 is the result of increasing the current by 4/3 to account for the loss of one turn. Note that the inlet temperature is 80C. This is to accommodate the FCool program which does not run above a discharge

temperature of 150C (resulting dT is must be adjusted 1 C hotter due to slightly higher resistivity of the copper at 100C). The delta T of the water inlet to outlet increased from 36C to 56C while the peak copper delta T increased from 43C to 69C for the 3 Turn failure scenario.

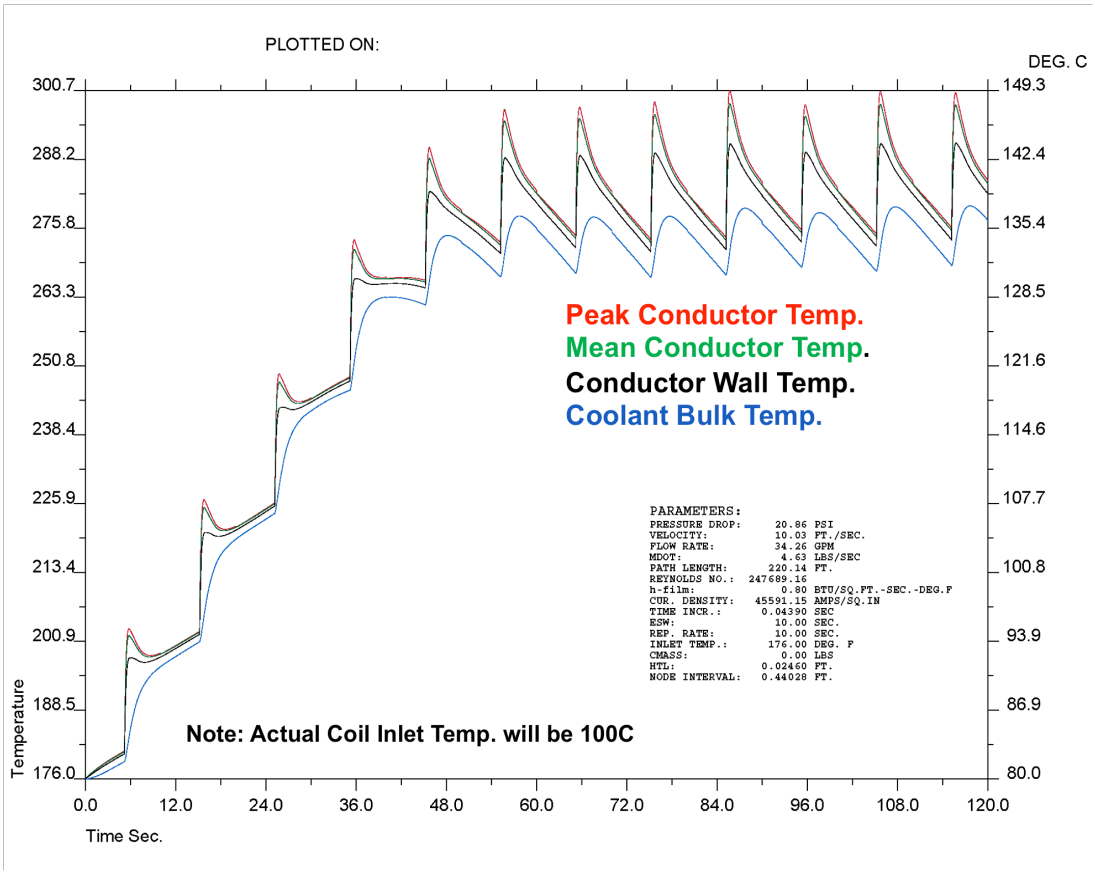

Figure 7-2 VS Coil and Feeders With Nuclear Heating 3 out of 4 Turns Operating

Finally the ELM temperature profile was calculated using the 90kA-turn equivalent pulse described in section 2.2.2.1. The wave form was adjusted to include the power deposition from the neutronics analysis. The result shown is for the Coil with both the inlet and outlet feeders. While it is unlikely that the coils will see continuous operation a 1000 second pulse length was chosen which clearly reaches a steady state solution. The temperature rise used in the thermal stress analysis is based on these steady state worst case temperatures. Note again that the result is shown in Figure 7-3 with an 80C water inlet temperature and the actual water inlet temperature

will be 100C. The maximum dT of the water for the ELM coils was 64C and the peak dT of the copper was 69C.

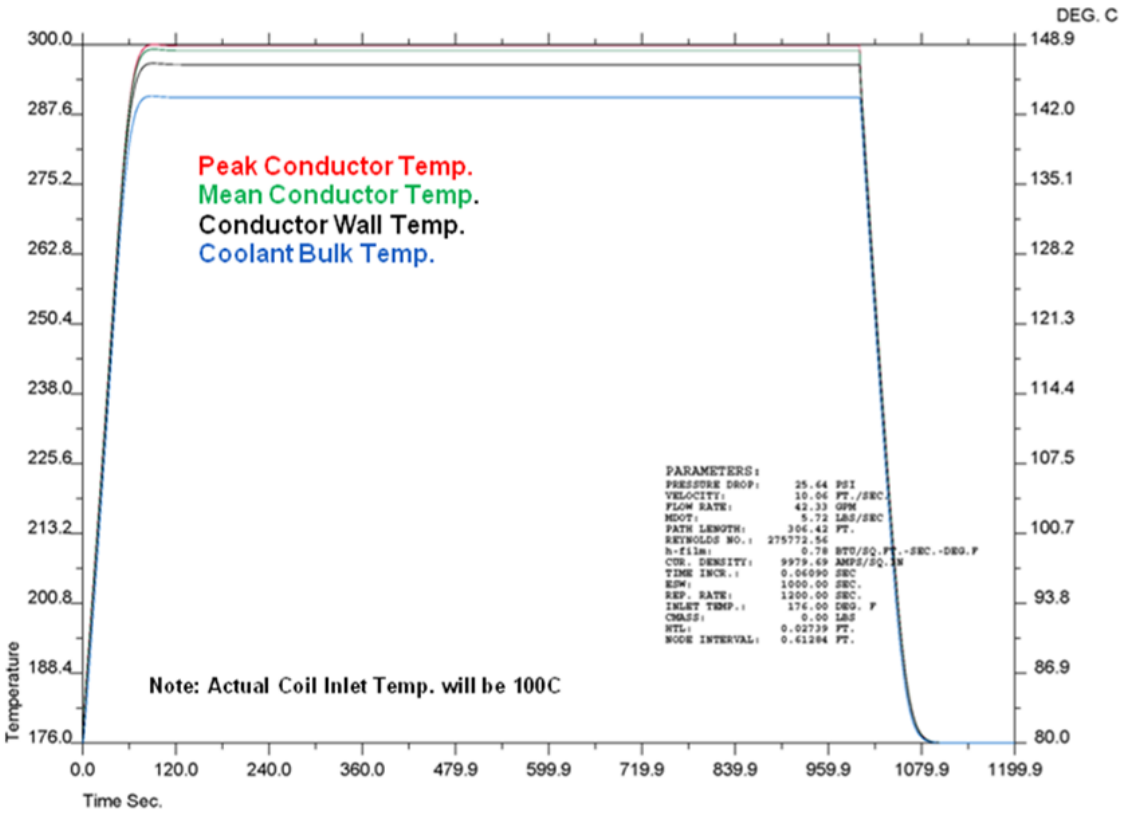

Figure 7-3 ELM Coil and Feeders with Nuclear Heating

The thermal stress analysis performed with ANSYS used the water temperatures derived from the simple steady state calculations to fix the surface temperature of the inside of the cooling hole. Then copper temperatures were determined by mapping neutronics power deposition onto the coil and coil structure and adding the bulk resistive heating. These calculations are described in section 8.

7.1.2 **Bakeout**

Bakeout operations will raise the VV temperature with water to 200C and the Blanket and In Vessel Coils to 240C. The water temperature will be increased slowly, aiming to reach the peak

temperature in 100 hours. This gradual ramp rate is designed to minimize the risk associated with thermal stresses caused by differential thermal expansion. Once complete, the water temperature will be gradually reduced to the operating temperature of 100C.

With a thermal ramp rate of 3 or 4 degrees C per hour the differential temperature from the start to the end of the coils will always be substantial less than the 67C ELM Coil or 33C VS Coil end to end differential temperatures generated during operation due to the resistive and nuclear heating. The differential temperature between the Coils and the Vacuum Vessel will at first be only a few degrees as both the vacuum vessel and the IVCs will be seeing the same temperature water and the slow increase of the water temperature will provide enough time for the heat to soak through the structure guaranteeing small temperature differences across the structure. During the final phase of the bakeout when the IVC temperatures rises from 200C to 240C the IVCs will see some thermal stress due to the coil now being 40C higher than the 200C vacuum vessel. However, during bakeout the IVCs do not incur electromagnetic loads so the only stress incurred in the coils is due to these thermal stresses. The thermal stresses incurred due to the temperature difference between the vacuum vessel and the coils will be analyzed to guarantee they are within acceptable limits.

7.2 FLOW, PRESSURE, AND EROSION ANALYSES

7.2.1 Cooling water supply flow/pressure/pressure drop

To minimize erosion the flow velocity for both the VS and ELM coils was chosen as 3 m/s. Then flow calculations were performed first calculating Reynolds Numbers and friction factors and then determining the overall pressure drop of the coil with its adjacent feeders. Calculation of the thermal response of the coils followed and the resulting temperature profile was fed into the thermal stress analysis. Below is an example of one of the pressure drop / flow calculations:

$D = 3\,cm$ $\rho = 992\,\frac{kg}{m^3}$ $p = 1.9 \times 10^5\,Pa$ $\varepsilon = 3.048 \times 10^{-3}\,mm$

$h_f := \frac{p}{\rho \cdot g}$ $\mu = 1.002 \times 10^{-3}\,\frac{N \cdot sec}{m^2}$ $L = 67.1\,m$

$$f := \left[-2 \cdot \log\left[\frac{\frac{\varepsilon}{D}}{3.7} + \frac{2.51}{\rho \cdot \frac{D}{\mu} \cdot \left(2 \cdot g \cdot h_f \cdot \frac{D}{L}\right)^{.5}} \right] \right]^{-2}$$

This equation solves for f (friction factor) when the flow rate is unknown but the head loss is known, check for laminar flow

$f = 0.019$ $\frac{\varepsilon}{D} = 1.016 \times 10^{-4}$

Solve for the Reynolds # in terms of the friction factor.

$$Re_t := \frac{9.287}{\sqrt{f}} \cdot \left(3.7 \cdot \exp\left(\frac{-1.15129}{\sqrt{f}} \right) - \frac{\varepsilon}{D} \right)^{-1}$$ $Re_t = 8.94 \times 10^4$ for turbulent flow

$Re_l := \frac{64}{f}$ $Re_l = 3.383 \times 10^3$ for laminar flow

Check that Re is turbulent if not use Re=64/f Generally turbulence begins at Re>2000

$Re := if(Re_t < 2000, Re_l, Re_t)$ $Re = 8.94 \times 10^4$ $f = 0.019$

$v := \frac{\mu \cdot Re}{D \cdot \rho}$ $v = 3.009\,\frac{m}{sec}$ The velocity of the fluid

$Q := v \cdot A$ $Q = 128\,\frac{liter}{min}$ $m := Q \cdot \rho$ $m = 2.11\,\frac{kg}{sec}$

Table 7-1 summarizes the parameters for the interface with the cooling water system.

Table 7-1 Water Supply from the TCWS and Coil requirements

	Normal Operation	**During Baking**
Inlet water temperature	100 C	240 C
Maximum outlet temperature	167 C	240 C
Inlet pressure	3.0 MPa	4.4 MPa
ELM Coil Required Pressure Drop 3m/s	0.26 MPa	N/A
VS Coil Required Pressure Drop 3m/s	0.24 MPa	N/A
ELM Coil Required Flow per Coil	2.59 kg/sec	N/A
VS Coil Required Flow per Coil	2.11 kg/sec	N/A

The available pressure provided by the TCWS is well in excess of the required pressure necessary to achieve the flow rates needed for rejecting the heat. The flow to both the ELM and VS coils will be throttled at the cooling water discharge so that the pressure drop across the coils is as stated in the table above. Restricting the flow serves two purposes. One is that the flow is reduced to a level that while high enough to provide adequate cooling it is still low enough that the flow velocity will not cause excessive erosion over the operating life of the coil. Second, restricting the flow at the discharge raises the minimum water pressure in the coil and prevents cavitation, which could otherwise increase the risk of system failure and accelerate wear. Cavitation occurs when pressure differentials create local regions with pressure below the fluid's vapor pressure, resulting in the cyclic formation and collapse of small bubbles.

For example as a fluid flows through a pipe elbow, there is not only a non-recoverable pressure drop, but also temporary radial pressure redistribution. It is important to verify that this redistribution of pressure does not result in pressures lower than the vapor pressure.

An empirical study performed by R. E. Stonemetz at NASA's Marshall Flight Center, "Liquid Cavitation Studies in Circular Pipe Bends" has previously investigated this phenomenon. A water tower was constructed, with flow passing through a removable, transparent pipe. Water velocity was increased until formation of bubbles was visually observed, and the process was repeated for various bend angles, bend radii, pipe diameter, and flow speeds. An empirical formula predicting the onset of cavitation was then developed. It should be noted that the parameter range included water speeds and pipe diameters close to those used in our coil design.

Figure 7-4 shows the minimum fluid pressure required immediately before entering the bend to avoid cavitation for the ELM Coils. It should be noted that the result, ~ 0.8MPa, is lower than the minimum pressure expected. For a flow rate of 4 m/s and the ELM Coil bend radius we note that we are operating in a regime where the curve has nearly flattened out. This means that the bend radius of the pipe is large enough with respect to the diameter of the pipe that the tendency toward cavitation is only marginally higher than in a straight pipe. This result is highly sensitive to fluid temperature, but is relatively insensitive to other parameters once the ratio of the bend radius approaches ~ 2x the pipe diameter. In conclusion for our flow regime keeping the back pressure higher than the vapor pressure at temperature will be effective in preventing cavitation and the design as is has significant margin in that respect.

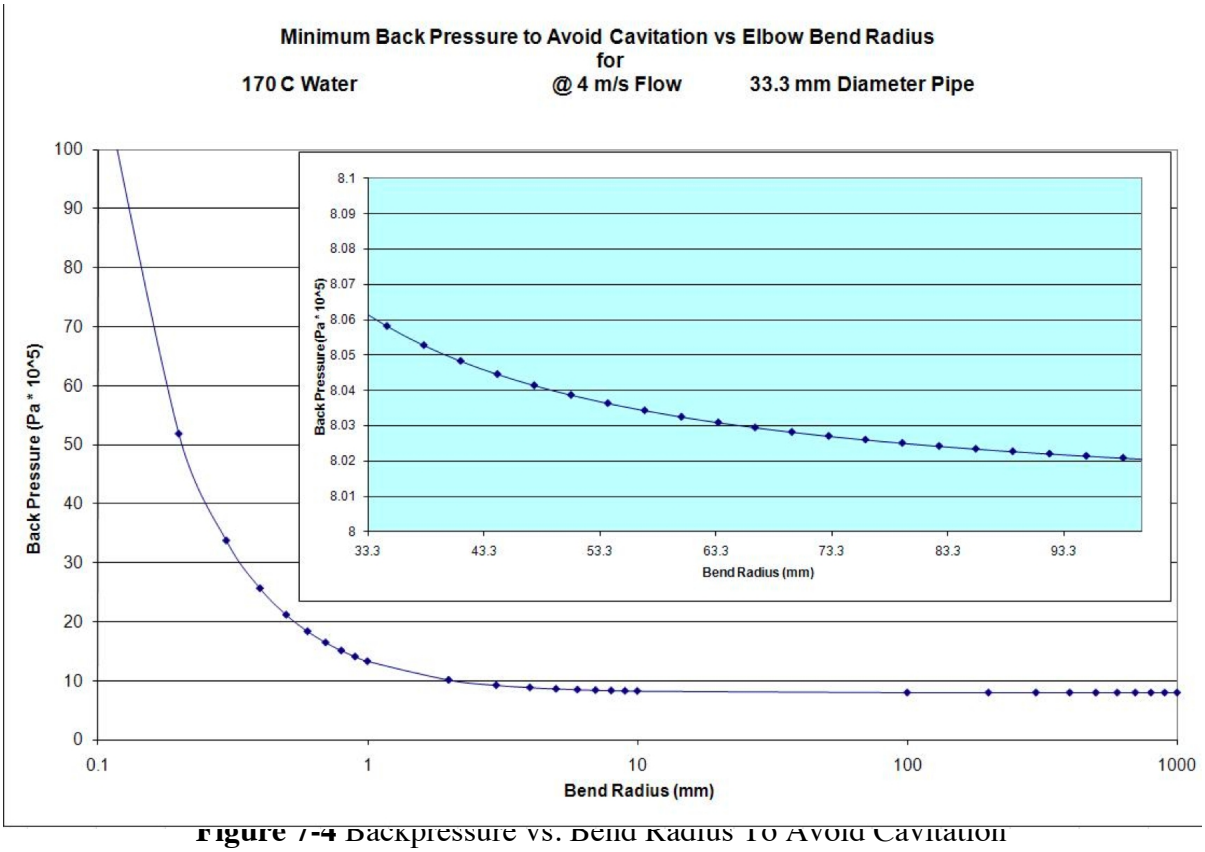

Figure 7-4 Backpressure vs. Bend Radius To Avoid Cavitation

7.2.2 **Erosion due to flow and water chemistry**

7.2.2.1 Fluid dynamics

The fluid dynamics are determined by the magnitude of the Reynolds number, $Re=\rho_w uL/\mu_w$. Here u=6 ms^{-1} is the mean flow velocity, R=15 mm is the ELM coil radius, and typical water density and viscosities are, respectively, $\rho_w \approx 1000$kg m^{-3} and $\mu_w=10^{-3}$–10^{-4} Pa s (dependent upon temperature). These values yield a Reynolds number $Re=10^4$–10^5 and indicate that the flow will be turbulent. The potential to reduce the flow velocity to 3 ms^{-1} has been proposed, which will reduce the Reynolds number by a factor of two, though the flow will still remain in the turbulent regime. To ensure maximal safety, the strategy adopted for all stages of the analysis of the erosion and corrosion process will be to consider the worst-case scenario.

7.2.2.2 Conceptual model for the pipe-wear process

Contributions to pipe wear arise from several processes. To assess the magnitude of each of these first requires a statement of the mechanism for how pipe wear occurs. Initially the pipe is corrosion-free and the flowing water contains oxygen but no corrosion products. In this state the pipe wear occurs primarily due to turbulent shear stresses generated at the walls. Corrosion of the pipe wall occurs via the reaction between oxygen dissolved in water and the copper surface, producing copper oxide (CuO and Cu_2O) layers on the pipe surface. These corrosion layers may spall off due to thermal or mechanical shock or due to flow effects.[74] Applying the worst-case-scenario approach, it is assumed that all copper oxide is released into the flow in the form of particles. The collision of these particles with the pipe walls then provides a second mechanism of erosion observed in the ELM-coil wear process. Since the subsequent release of particles via this mechanism is proportional to particulate concentration, if left unchecked this process induces an *exponential* increase in material within the flow, and consequently erosion rate with time, so must be carefully controlled. It is thus crucial both for the implementation of a filter and periodic changing of the water contained in the system to limit the erosion rate and we propose suitable operating conditions based upon these options. An ion-exchange bed is also proposed in the design set-up, which will play a key role in removing particles from the flow.

The pipe-wear process may thus be separated into the following contributions:

1) Erosion due to turbulent wall shear stresses.

2) Corrosion.

3a) Erosion due to particle collisions with the pipe wall due to turbulent flows.

3b) Erosion due to particle collisions that arise due to changes in pipe geometry, specifically pipe bends.

4) Chemical dissolution via ion-exchange filter.

[74] Molander, A., 2006 Corrosion and Water Chemistry Aspects Concerning the Tokamak Cooling Water Systems of ITER.

Of particular significance in the ELM-coil set-up is the inherent coupling of each of these processes. Specifically, processes 3 and 4 are dependent upon the concentration of particles within the flow, and are thus coupled to processes 1 and 2 (and each other) via their contribution to the release of particles.

1) Influence of turbulent shear stress on pipe wear

To assess the magnitude of the shear stress we consider a fully developed flow profile in a straight channel[75] with comparable geometry to the ELM coils (width 30 mm and a mean flow velocity of 6 ms^{-1}), depicted in Figure 7.5. Such a turbulent flow will generate a typical wall shear stress $\tau \approx 60$ Pa, which is identified with the exertion of a force of approximately 10^{-20} N on each copper molecule on the pipe surface. A typical force required to break a Cu-Cu bond is of the order of 10^{-10} N. While the presence of defects will generally induce material failure at stresses of one or two orders of magnitude lower than the bond strength, forces of ten orders of magnitude weaker than the bond strength pose no significant threat to the structural integrity of the pipe, nor can they be expected to cause any erosion.

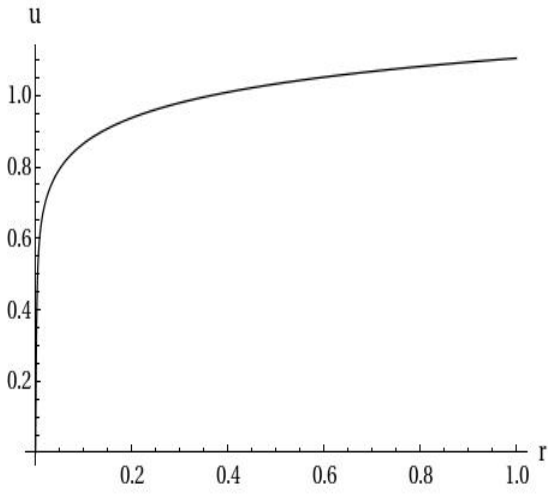

Figure 7-5 Fully developed turbulent velocity profile for water flowing at 6ms^{-1} in a channel of size 30mm scaled with mean flow velocity; *r* denotes the distance from the wall, scaled with pipe radius. The turbulent wall shear stress is approximately 60Pa.

[75] Van Driest, E.R. 2003 On turbulent flow near a wall. *AIAA Journal* **42**, 259-264.

2) Corrosion modeling

For the materials and the stated water chemistry, a typical corrosion rate is 60 μm per year.[76] Assuming that all corrosive product is released into the flow, this corresponds to a rate of mass release into the system via corrosion of K_c=0.35 kg/year. Comparison of this rate with the mean flow velocity indicates that a mass of only approximately 10^{-8} kg will be released during each cycle of the ELM-coil system. As a result, the variation in concentration of corrosive product contained in the flow between the beginning and end of a flow cycle will be minimal and so the corrosion contribution is thus significant on a timescale comparable with the total system lifetime.

3) Erosion modeling

The rate of erosion by particle collisions at the wall is dependent on the volume eroded by each collision. A particle of mass m striking a material with flow stress σ (the stress required to continuously deform the material), at a velocity v and angle β to the perpendicular is given by $V=\lambda\, m\, v^2\, f(\beta)/4\sigma$, where $f=\sin(2\beta)-3\sin^2(\beta)$ for $\beta \leq \beta^* \approx 0.32$, and $f=\cos^2(\beta)/3$ for $\beta \geq \beta^*$, and $\lambda \approx 0.5$ is a constant representing the fraction of particles that cut in an idealized manner.[77] We note that f takes its maximum value when $\beta=\beta^*$ so that β^* represents the optimal angle of strike. The resultant flux of particles off the surface is thus proportional to $v^3 f(\beta)$.

3a) Erosion due to particle collisions with the pipe wall due to turbulent flows

Collisions with the wall due to turbulent flow arise as a result of turbophoresis and Saffman lift forces. The former corresponds to the observed particle migration to regions of lower turbulence, while the latter drives particles towards the walls due to the presence of shear. Particle collision velocities generated via these two processes typically cannot exceed a maximum $v_t \approx 0.1u^*$ where

[76] Molander, A., 2006 Corrosion and Water Chemistry Aspects Concerning the Tokamak Cooling Water Systems of ITER.

[76] Finnie, I. 1995 Some reflections on the past and future of erosion. *Wear*. **186**, 1-10.

$u^* = \sqrt{\tau / \rho_w}$ is the friction velocity for the turbulent flow.[78] This indicates a maximum wall collision velocity of approximately 0.02 ms^{-1}. Assuming that all particles collide with the wall at the optimal angle of strike, β^*, this provides an estimate for the rate of supply of mass to the flow through turbulent wall collisions at a particular instant in time, $k_t m$ (kg/year) where m is the mass of particles contained within the water at that time, and k_t is the rate coefficient, given by

$$k_t = \frac{\lambda \rho_p v_t^3 f(\beta^*)}{2\sigma R} \approx 0.15/\text{year}, \qquad (7.2.2a)$$

where ρ_p is the particle density.

3b) Erosion due to particle collisions that arise due to changes in pipe geometry (pipe bends).

Particles will strike the wall due to their inertial resistance to changes in the flow direction as they encounter bends in the pipe. The particle collision velocity in this case is given by the flow velocity 6 ms^{-1} (which is much greater than those velocities induced by turbulence in 3a) upon which we recall the flux onto the surface depends cubically. The angle and position of particle strike are dependent upon the particle size, and thus the contribution to erosion via changes in pipe geometry is reliant upon the design of the filtration system. Under general operating conditions, one per cent of the total water flow is filtered, removing all particles of size exceeding 10 μm.

It is important to ascertain the relative importance of larger particles, which will cause further erosive damage due to their resistance to changes in flow direction but are also removed from the flow at a given rate by filtration, and smaller particles, which will not be filtered but cause less damage upon collision with the walls. Comparison of the rate of supply of corrosive product to the system through corrosion with the rate at which particles are filtered indicates that larger particles will be removed before they are able to offer any sizeable contribution to erosion. Thus, we address the worst-case scenario in which the particles released into the flow are the maximal

[77] Young, J. & Leeming, A. 1997 A theory of particle deposition in turbulent pipe flow. *J.Fluid Mech*. **340**, 129-159.

size to pass through the filter, which, for example we take here to be 10μm. We note that this approach assumes that all particles pass through the filter, an assumption that is dependent upon the filter positioning.

Analysis of the trajectory of particles of size 10 μm indicates that such particles are strongly influenced by the flow and, as a result, only graze the pipe walls at typical angles of approximately 0.03°, for a bend with radius of curvature 30 cm, as illustrated in Figure 7.6, which gives which $f \sim 10^{-7}$. Despite this, due to the cubic dependence on velocity, the rate of supply of material, $k_{\text{strike}} m$ (kg/year), is still significant:

$$k_{\text{strike}} = \frac{\lambda \rho u^3 f(\beta^*)}{4\sigma\pi R^2 L} \approx 1.2/\text{year}. \qquad (7.2.2b)$$

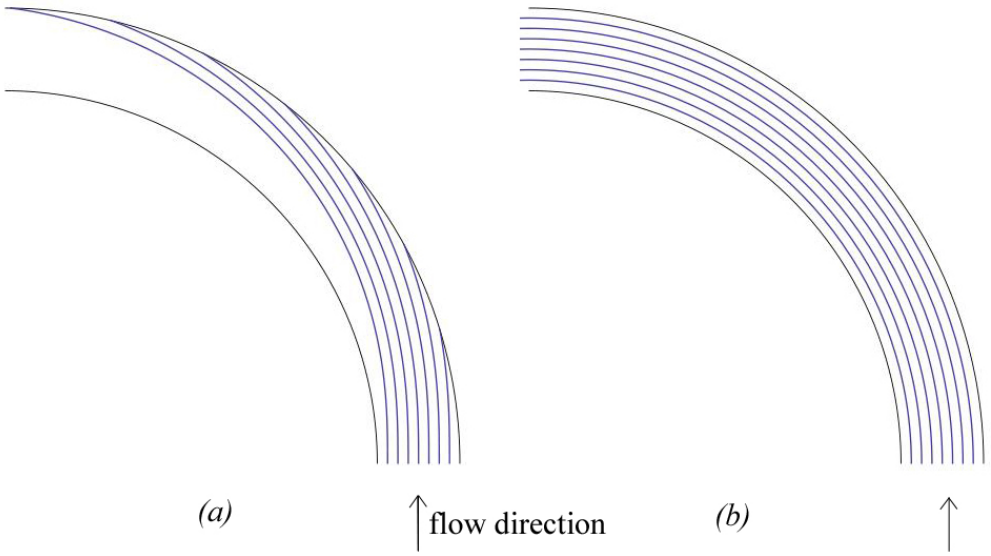

Figure 7-6 Trajectories of *(a)* 2.5 mm diameter particles (as an illustrative example), and *(b)* 10 μm in a pipe bend with radius of curvature 30 cm (which are only weakly deflected from the streamlines).

4) Chemical dissolution

The rate of removal of particles via the ion-exchange filter is given by $k_{diss}m$, where k_{diss} is the corresponding rate coefficient. However, in the absence of experimental data in this area, to maintain a worst-case-scenario approach we assume here that $k_{diss}=0$ and the ion-exchange filter removes no particles.

Cumulative pipe wear

The total particulate mass released into the flow, m, due to corrosion and particle erosion due to turbulent flow and pipe bends may be determined. The result may then be used to determine the total erosion rate due to corrosion and erosion,

$$\text{Erosion rate}\,(\text{ms}^{-1}) = \frac{K_c + (k_t + k_{\text{strike}} - k_{\text{diss}})m}{2\rho_p \pi RL}. \qquad (7.2.2c)$$

Figure 7.7 illustrates the predicted cumulative wear as a result of corrosion and erosion due to turbulence and particle collisions due to bends for the typical parameters in the ITER design.

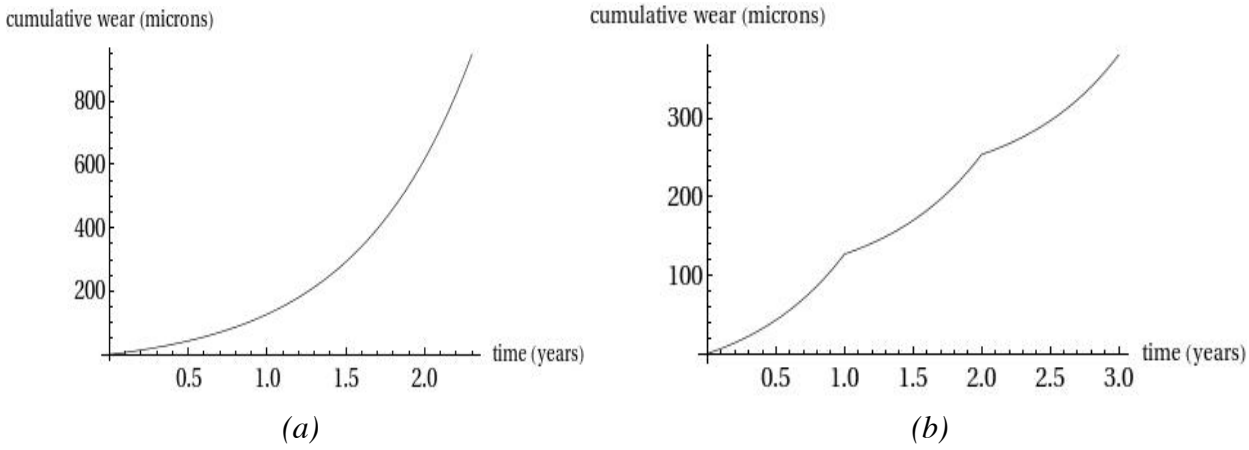

Figure 7-7 Cumulative wear versus time, accounting for wear via corrosion and erosion due particle collisions as a result of turbulence and changes in pipe geometry. In *(a)* the exponential increase in erosion in the absence of periodic water changing is illustrated. In *(b)* the water is changed each year.

7.2.2.3 Conclusions

- The erosion rate is expected to be proportional to the cube of the mean flow velocity.
- The erosion rate due to particle collisions with the walls as a result of bends in the pipe is dependent upon particle size: the smaller the particle the smaller the angle of strike relative to the surface. The most significant particles in the erosion process will thus be the largest that are able to pass through the filter.
- The number of small particles that are allowed to pass through the filter increases exponentially with a growth rate that is proportional to the cube of the mean flow velocity thus rendering periodic water changes crucial.

7.2.3 Recommendations

- Strategic periodic changing of the water within the system will be crucial in minimizing the exponential accumulation.
- The placement of the filter and effectiveness in particle capture is a crucial component in minimizing erosion through particle collisions, for example, this analysis has assumed

that all particles that exceed 10 μm in diameter are removed.

- The use of an ion-exchange filter may enable the removal of the smaller particles that are able to pass through the filter, to increase the time between necessary water changes.
- The introduction of a coagulant that aids in aggregation of particles may be advantageous in avoiding the exponential accumulation of particles that are able to pass through the filter and maximizing the effectiveness of the filter.
- An experimental set-up of the ELM-coil design that captures the key features discussed here should be constructed and compared with the predictions made. In particular, this experiment should be used to investigate the dependence of the filter efficiency on its position in the flow system, and the optimization of an ion-exchange bed in removing particles.

8 STRUCTURAL PERFORMANCE

8.1 STRUCTURAL/ THERMAL BEHAVIOR

8.1.1 ELM Structural/Thermal

8.1.1.1 The Structural Finite Element Mesh

The ANSYS finite element program is used to construct the mesh as shown in Figure 8-1. The coil structures are modeled with continuous and uniform 20 node hexahedral element type 186 to facilitate the distribution of Lorentz loads. The supporting brackets use a similar 10 node tetrahedron.

General contact element type 174 is used at the interface between all components. Most locations, including the bracket to coil interface, assume a bonded condition although there are areas defined such as gaps that allow the coil to displace a limited distance under load.

The behavior of the gap elements between the coil and the insulation and surrounding structure is critical to understanding how load is shared and reacted through the structure.

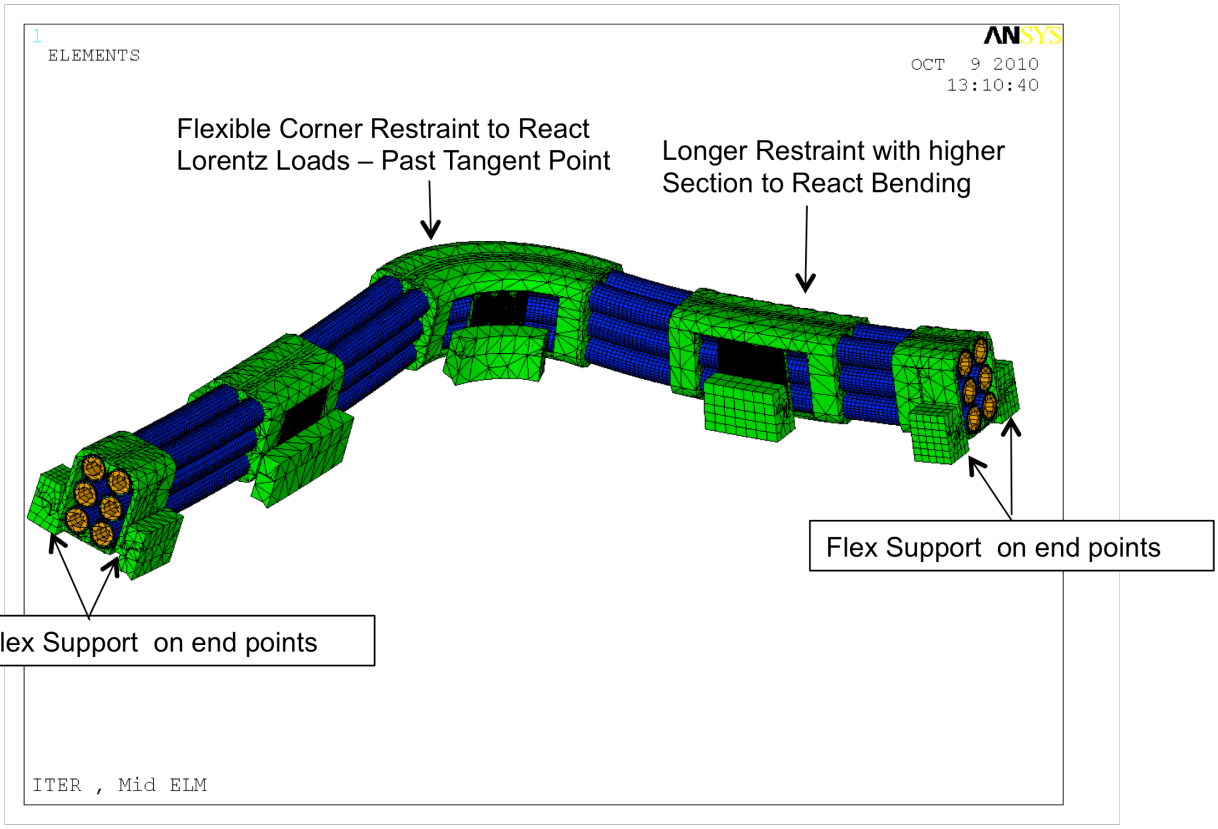

Figure 8-1 Structural Mesh

The model is not symmetric with respect to stiffness load or geometry along any normal to the reactor wall. There are, however, assumptions of symmetry at the cut boundaries on a normal that is locally parallel to the reactor wall for both ends. The symmetry is limited to stiffness along this normal. The load magnitude is not symmetric although the max values are applied and this is believed to be conservative for evaluation of stress.

The opposite side of this ELM has a number of irregular shaped coil interfaces to the feeder branch that considerably weaken the assumption of symmetry, although this is necessary in order

to keep the size of the problem computationally manageable for the specified schedule and budgetary limits.

Material properties are provided in Table 8-1 as a basis of comparison at a single temperature (200 C), however, all of the analysis applies data for all operating temperatures. The sources for the data are directly from the ITER web portal excluding the insulation MgO which is a result of an ongoing research and development project.

Table 8-1 Typical Material Properties

Component	**Young's Modulus (Pa)**	**Shear Modulus (Pa)**	**Poisson Ratio**	**Thermal Conductivity (W/mC)**	**Thermal Expansion (1/C)E**
Stainless Steel	1.85e11	7.06e10	0.31	16.98	1.78e-5
Copper	1.21e11	4.51e10	0.34	343	1.75e-5
MGO	0.96e9	2.5e6	0.42	2.363	1e-5

** All data (except for MgO) from ITER sources at 200 C

8.1.1.2 Structural Boundary Conditions

The structural boundary conditions include symmetry on the cut boundary of both ends. The foundation is rigid at the interface. Bolting of this assembly interface is evaluated as a separate sub-model.

The Structural Supports are designed and positioned along the coil length to react out the Lorentz loading and resulting bending stress across the restraint positions, as well as providing a mechanism for guided thermal displacement (Figure 8-2).

The bracket housing is extended in length specifically to provide higher section properties for the higher Poloidal leg loads. There is a tradeoff between adequate cooling by radiation with the port windows and the increased section to react the loads.

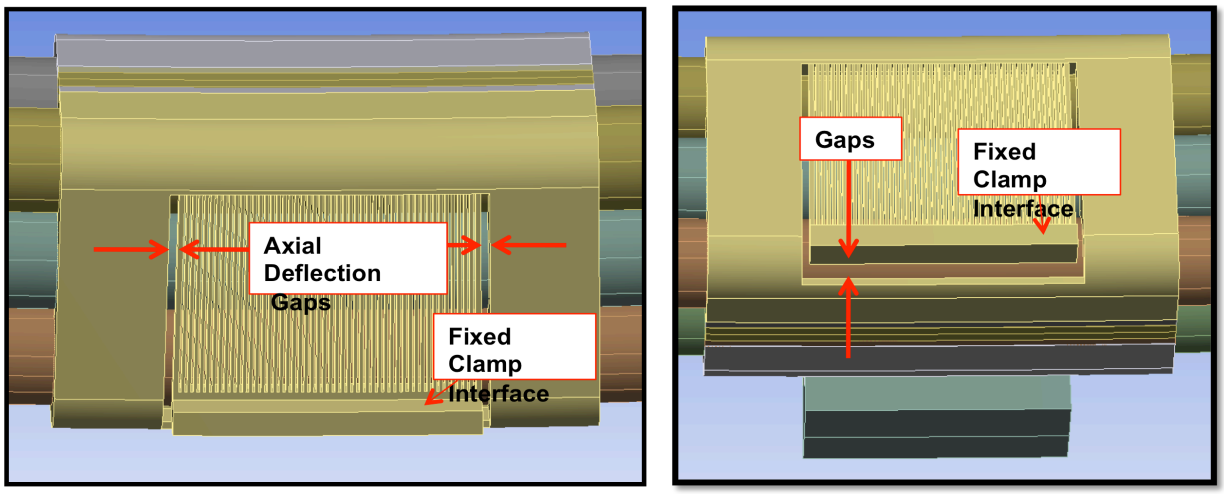

Figure 8-2 Flexible Support

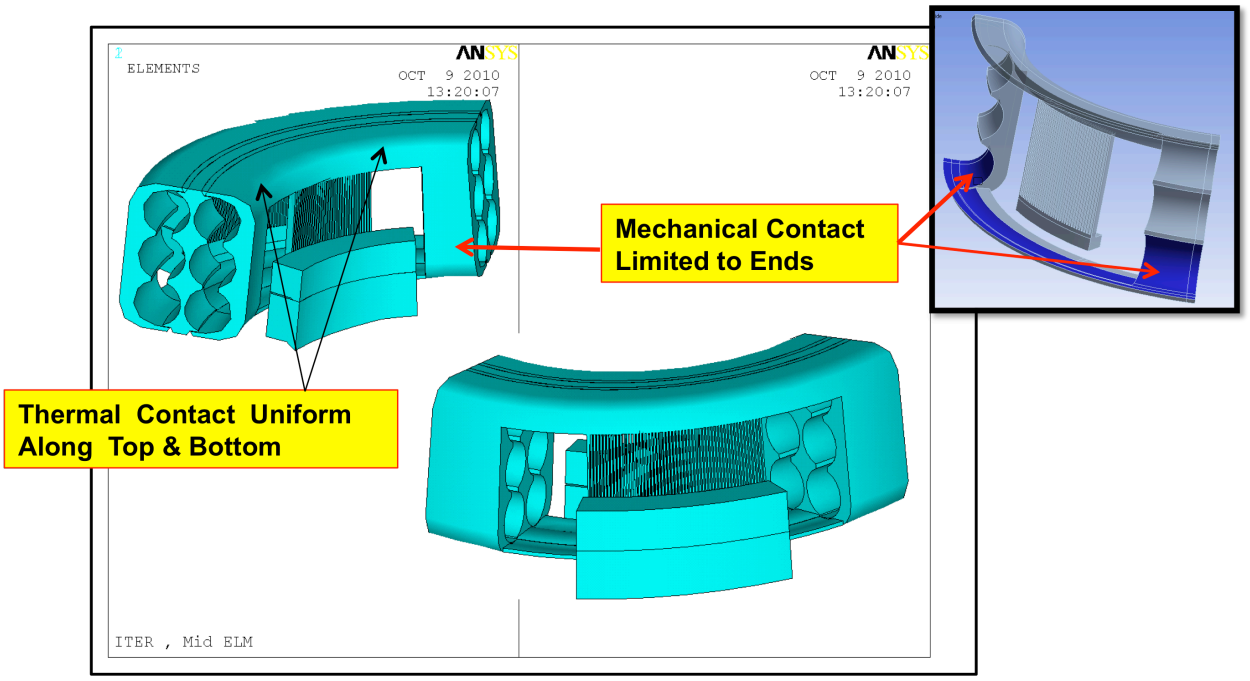

Figure 8-3 Structural Support Design Methodology

8.1.1.3 Bracket Support Optimization

All of the supports, excluding the ends have separations on the lateral flanks of the wall, which attached to the foundation clamp on either side, to reduce axial stiffness. The support of the right angle shaped corner (Figure 8-3) is supported with a similar mechanism. There are several internal features that have been iteratively shaped in order to react the load from the coil without stressing the external coil surfaces.

A detailed optimization based on stress and buckling limits of one typical support concept was completed using ANSYS parametric design language. A typical bracket support (Figure 8-4) was constructed with a variable list that included the width, depth and number of the beams (Figure

8-5). Displacement boundary conditions are extracted from the general solution and applied, (u_{axial}=1.923mm) along the coil axis and (u_{radial}=0.964mm) perpendicular to coil axis along with the Lorentz reaction load (160.53KN) perpendicular to coil axis.

One set of results using this technique is plotted (Figure 8-6) that shows the relationship of σ_{max} as a function of geometric parameters b and h (Figure 8-5). The optimum selection is based on considerations of stress and buckling. A thinner beam can reduce the stress; however, buckling would be a problem.

The final solution is a beam of 3mm width, 10.5mm depth and a total of 80 beams (40 beams per side). This resulted in a max stress in the beam of about 700MPa (101 ksi) and a max stress in the bracket of 1GPa (145ksi), which located at the corner and has a large bending component.

Results are shown (figure 8-9) with Inconel 718 which has 0.2% yield of 1124MPa (200°C), bending allowable is 1124MPa. The final design will have a fillet to reduce this peak value.

$$M_{Plastic} = \frac{1124}{700} - 1 = +\underline{\underline{0.60}}$$

The average fatigue stress for Inconel 718 is based on a stress ratio (R=0) from the Military Handbook (Figure 8-8) and shows a cyclic life of 600,000 cycles without a fillet and infinite life with a fillet. Fracture and damage tolerance studies are incomplete and additional changes may still be required. A change on the material selection from the 316 Stainless has not been fully integrated into other sections of the analysis pending a final design.

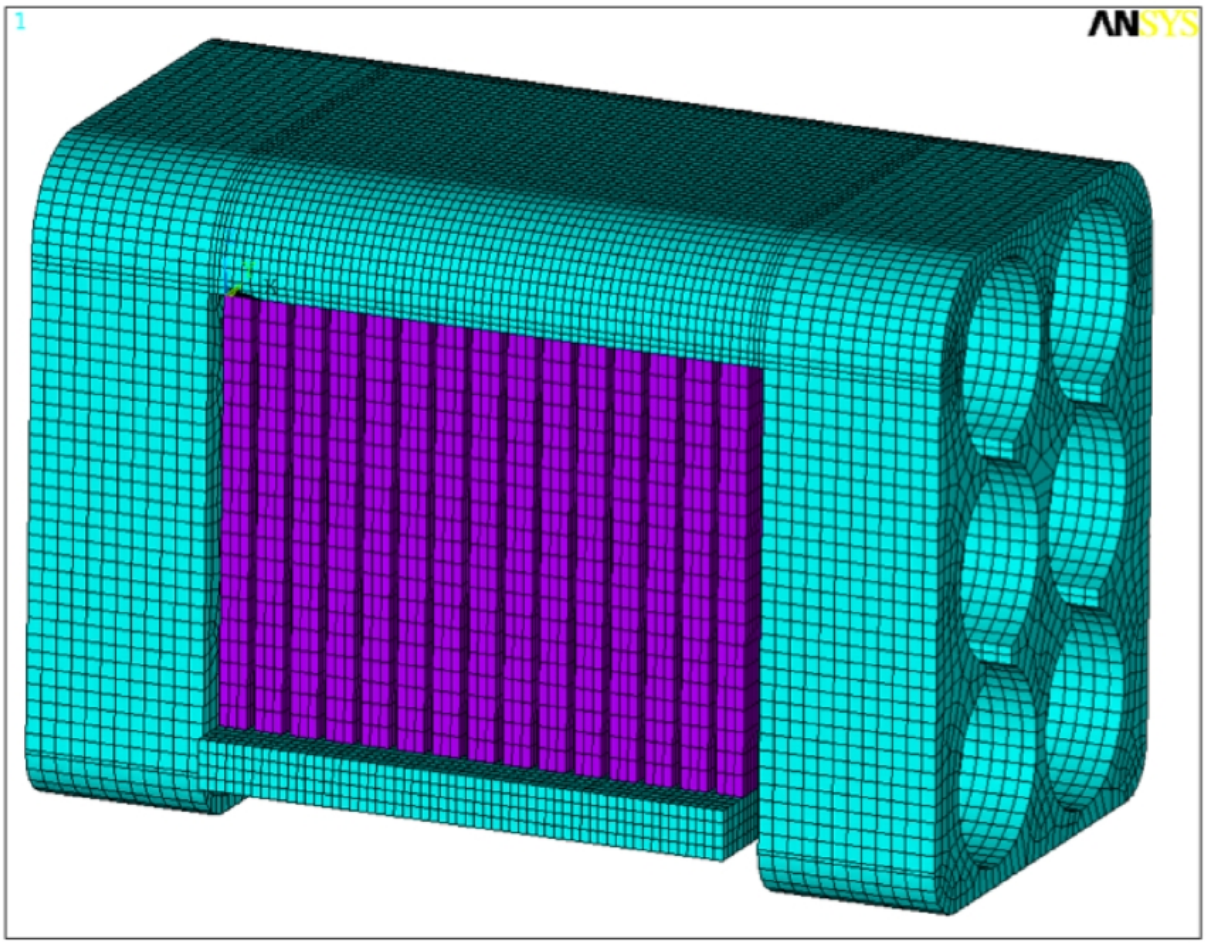

Figure 8-4 Typical Parametric Model of Coil Support

A similar line of reasoning will apply to the stress concentration on the bracket structure (Figure 8-9). The maximum value of the stress will be reduced with classical stress linearization to remove Kt and then the appropriate Kt will be applied for the most convenient radius that results in values that have infinite stress life.

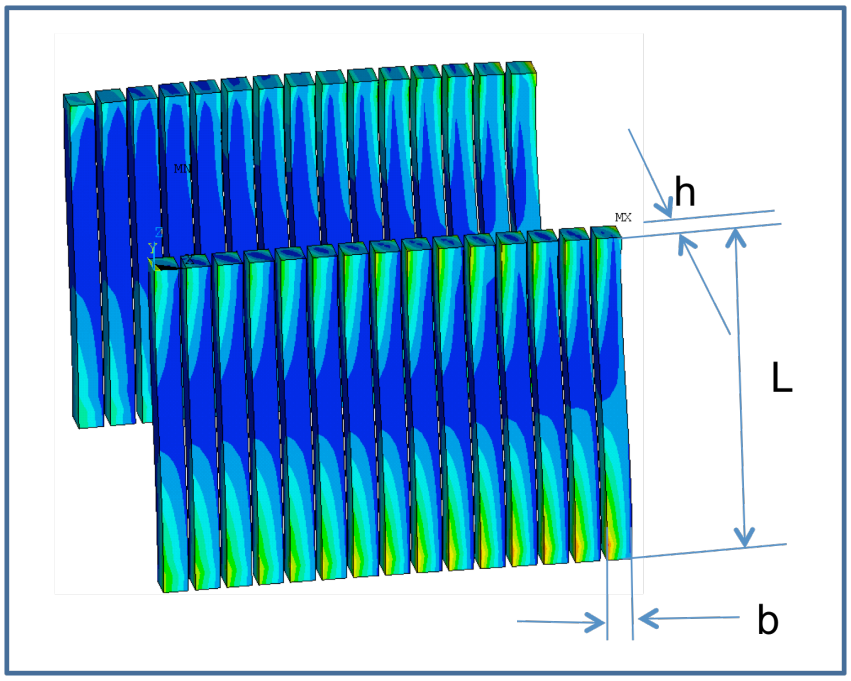

Figure 8-5 Optimization Parameters for Coil Support

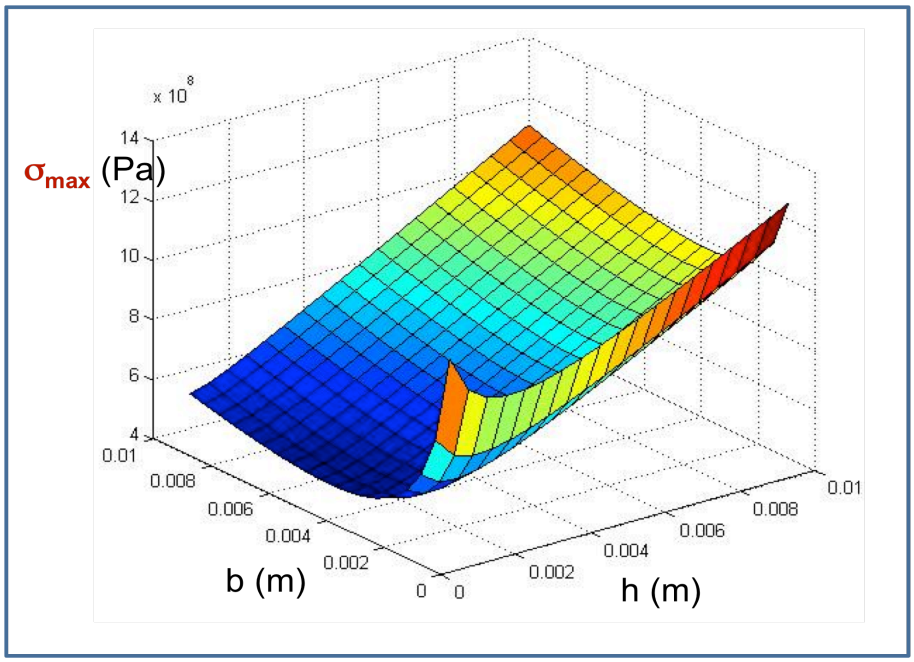

Figure 8-6 Parametric Response Envelope

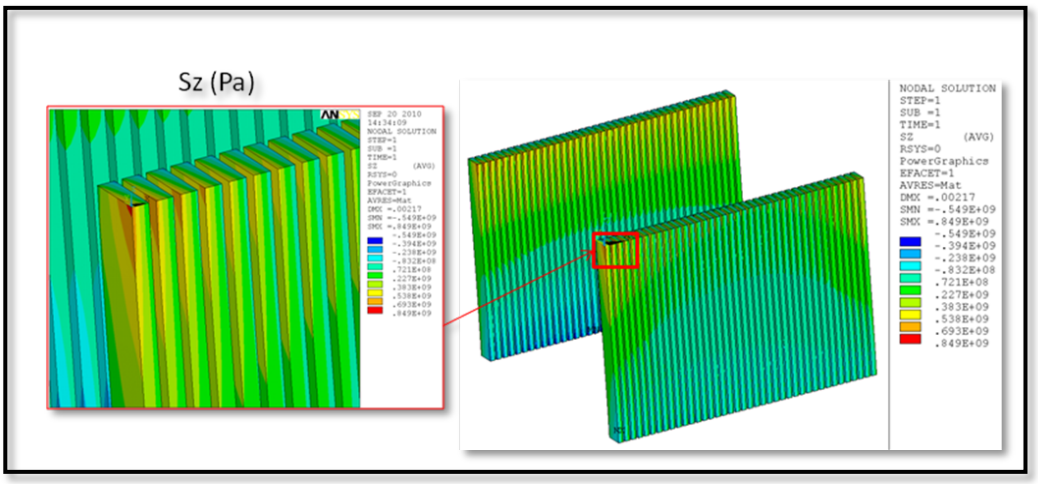

Figure 8-7 Stress Calculations in Beams

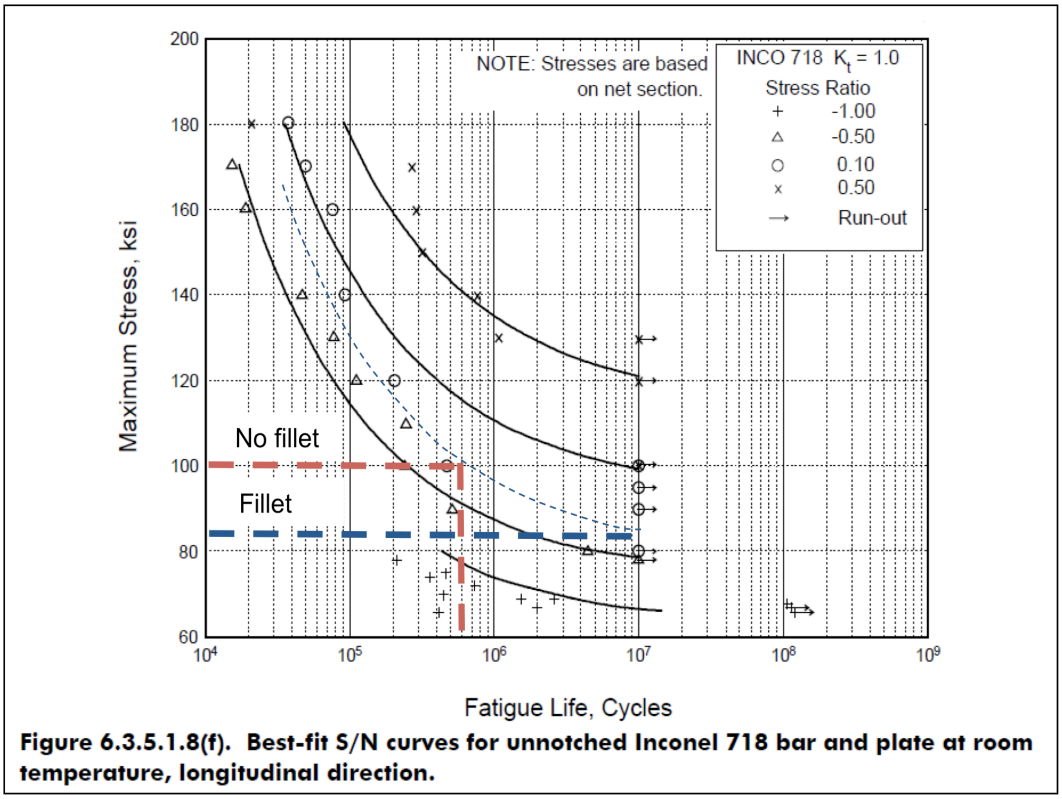

Figure 6.3.5.1.8(f). Best-fit S/N curves for unnotched Inconel 718 bar and plate at room temperature, longitudinal direction.

Figure 8-8 Beam Fatigue Prediction 718 Inconel

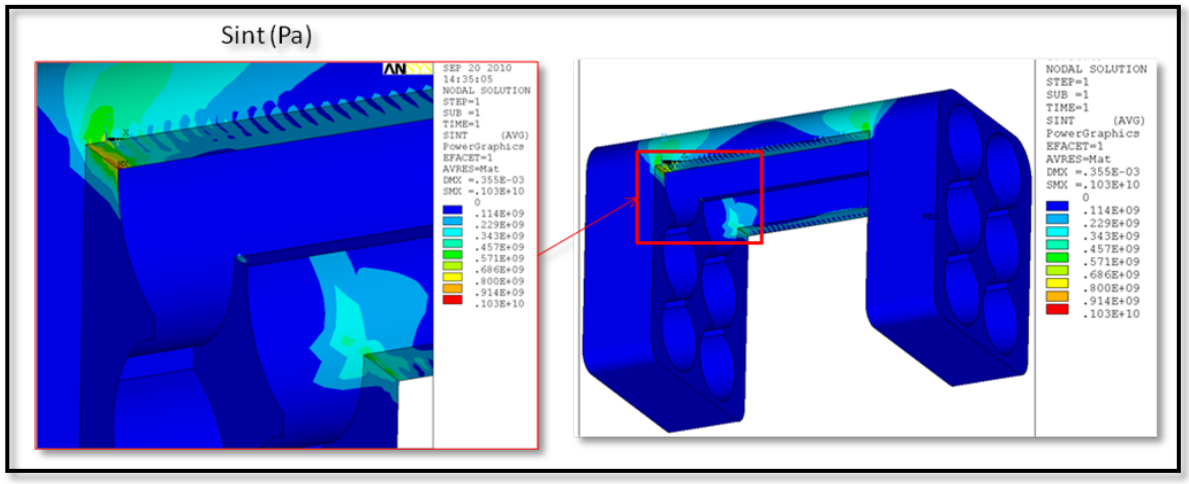

Figure 8-9 Stress Intensity in the Bracket

8.1.1.4 Buckling analysis

An Euler buckling analysis shows that buckling load on a rectangular shaped beam defined as 3mm width, 10.5mm depth above has a buckling load 400 KN which is much higher that the reaction load 160.63 KN used in the stress analysis above. The mode shape is a first order bending mode (**Error! Reference source not found.**) as expected.

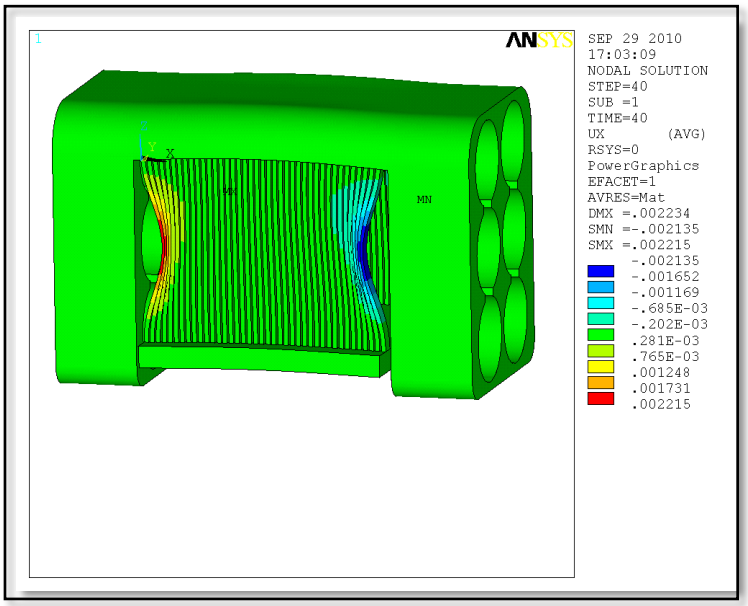

Figure 8-10 Illustration of the Buckling Load

8.1.1.4.1 Alternate beam design study

A study of alternative designs (Figure 8-11) to improve buckling load uses smooth contours positioned to accommodate displacement in axial and radial directions.

The analysis shows that using these contours on only 40 beams (20 beams per side) with dimensions of 3mm wide, beams of 7mm wide, 10mm depth for a length of 130mm length results in a max stress of 550MPa. This design separates the bending position for axial and radial displacements and thus stress concentrates at different places for independent load mechanisms.

This alternate design has a minimum (35%) improvement in buckling load (540 KN) over the rectangular design due to the fact that these beams can be much wider and thicker and the elastic parts are much shorter (**Error! Reference source not found.**).

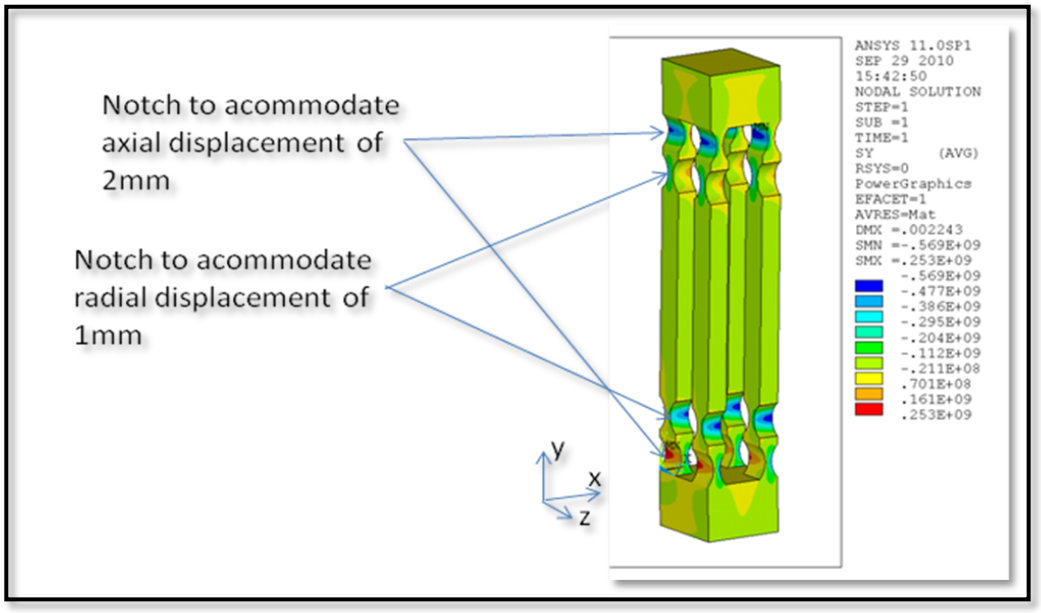

Figure 8-11 Alternate Beam Design for Buckling

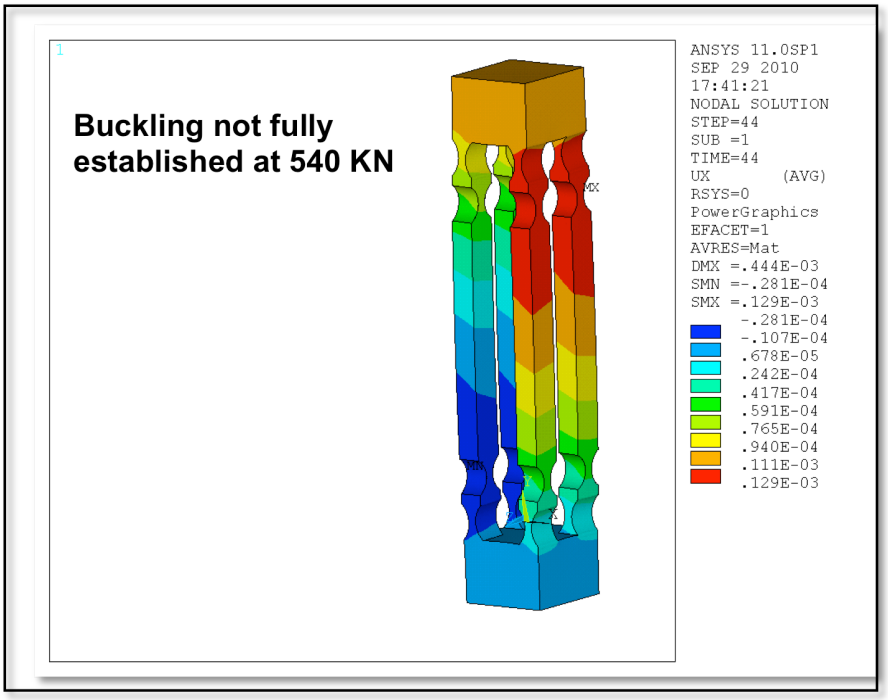

Figure 8-12 Alternate Design Buckling

8.1.1.5 Applied Loading methodology

The maximum Lorentz loads (Figure 8-13) are taken from the OPERA analysis (section 6) and applied to the structure as uniform nodal loads. The max values are plotted for several candidate sectors of the ITER reactor and compared based on a unit load basis as one moves clockwise around the coil starting with the top right corner (TRC). The area under each of these curves could be compared to delineate closer comparisons, although by inspection one can easily see that the highest loads are from sector 5 and specifically on the bottom left corner (BLC).

Theses loads are reversed in direction for a subsequent load step which is the basis for completing stress range calculations. A loading idealization (Figure 8-14 and Figure 8-15) shows how the loads are applied to the ELM coil. The thermal and fluid pressure loads are applied first followed by the two Lorentz loads since there is no vertical symmetry.

The three general classifications of loading are Inductive, Hybrid, and Non-Inductive which have 500 MW, 400MW, and 356 MW respectively (**Error! Reference source not found.**). The loads

will be applied to evaluate all combinations of power levels and cycle time. The stress results presented in this report are exclusively for Steady State Inductive operation at a power of 500 MW. The lower power levels are will be a simple ratio of the lower power to this level. The transient cases are necessary to capture the stress from gradients of temperature during the start and stop cycles.

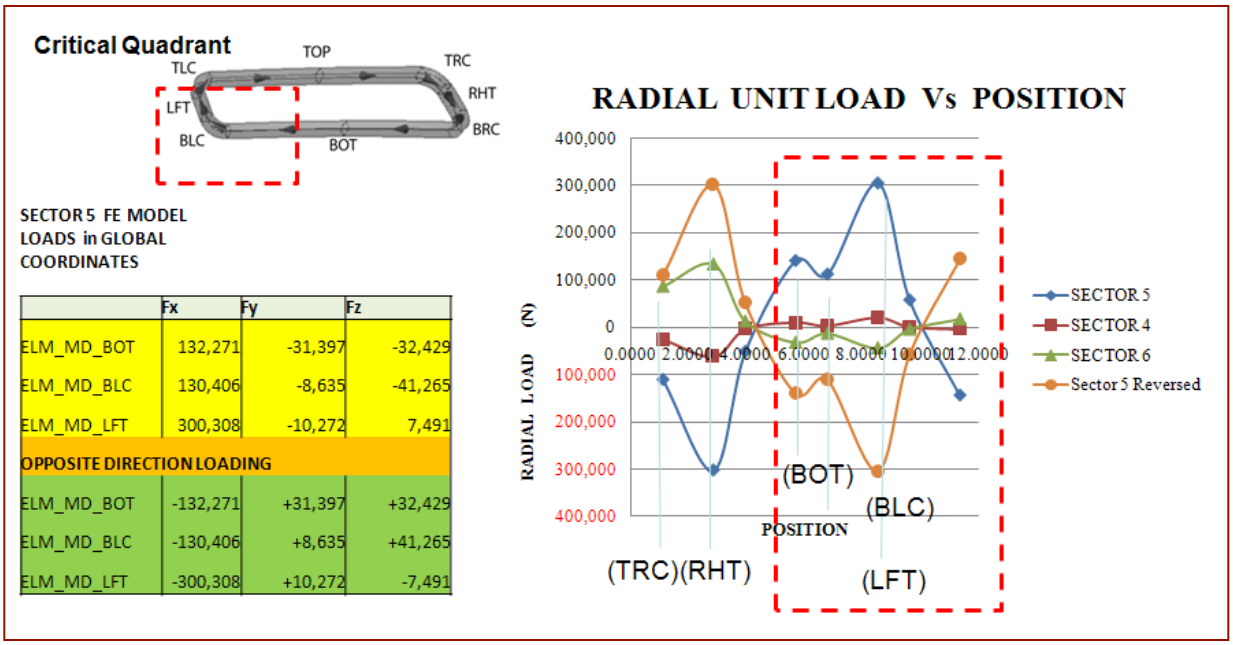

	Fx	Fy	Fz
ELM_MD_BOT	132,271	-31,397	-32,429
ELM_MD_BLC	130,406	-8,635	-41,265
ELM_MD_LFT	300,308	-10,272	7,491
OPPOSITE DIRECTION LOADING			
ELM_MD_BOT	-132,271	+31,397	+32,429
ELM_MD_BLC	-130,406	+8,635	+41,265
ELM_MD_LFT	-300,308	+10,272	-7,491

Figure 8-13 Lorentz Loads for Mid - Elm

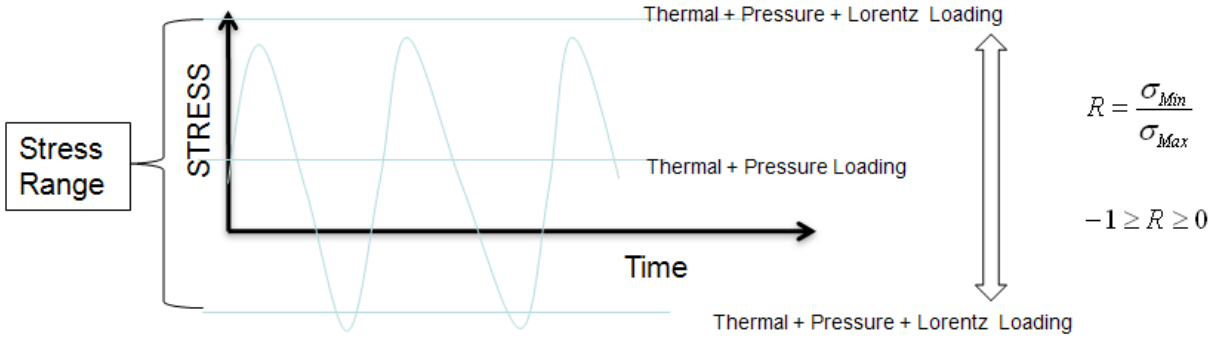

Figure 8-14 Idealized Cyclic Loading

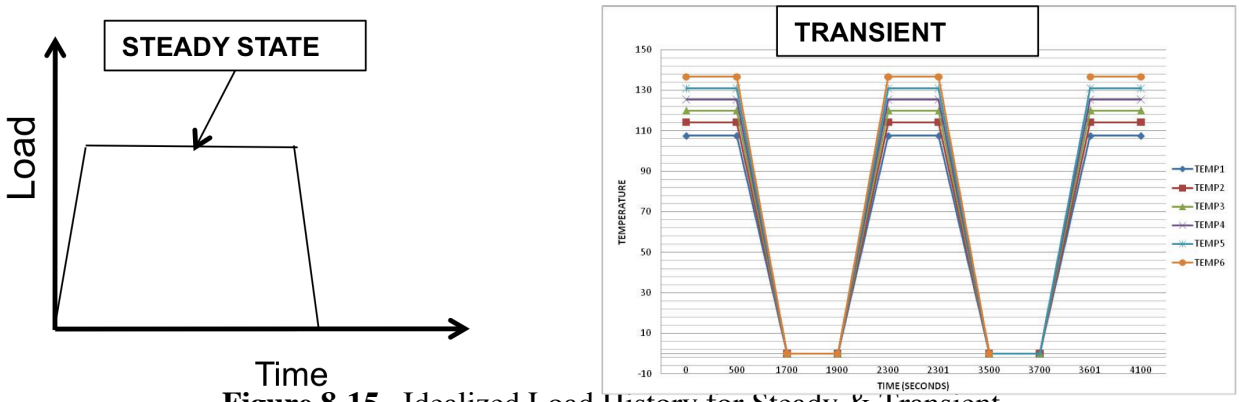

Figure 8-15 Idealized Load History for Steady & Transient

Table 8-2 Modes Nuclear Heat Operation

Parameter	Inductive Operation	Hybrid Operation	Non-inductive Operation
Fusion power (MW)	500	400	356
Burn time (sec)	300-500	1000	3000
Minimum repetition time (sec)	1800	4000	12000

8.1.1.6 Thermal Boundary Conditions

The thermal boundary conditions include conduction to the reactor wall, equivalent convection on the internal water cooled coil surfaces, and far field radiation to the surrounding blankets.

The temperature rise in the water is based on a simple energy balance between the applied nuclear and resistive heating sources and the specific heat of water around the cooling circuit.

The cooling water temperature is specified at 100C at the entrance to the coil and rises in the path around the circuit at (3 m/s). The analysis model conservatively applies the calculated exit temperature of each turn of the ELM coil to the entire length of the turn. This results in a 7.83

degree temperature rise on each turn. Details of these water cooling calculations are provided in section 7.1.

Nuclear or heat energy is calculated based on the MCNP program as a function of radius and provided by the University of Wisconsin Team. The curve fits (see Figure 8-18 and Figure 8-20) are constructed to match this cross plots of this data to represent the localized geometric trend. Separate table arrays in the ANSYS finite element code are used to map this data onto the individual components in accordance with these curve fits. The copper coil has the resistive heat generation added directly to these nuclear profiles.

Contour plots of this heat generation boundary condition are shown in Figures 8-19 and Figure 8-21 which shows close correspondence to these curve fits.

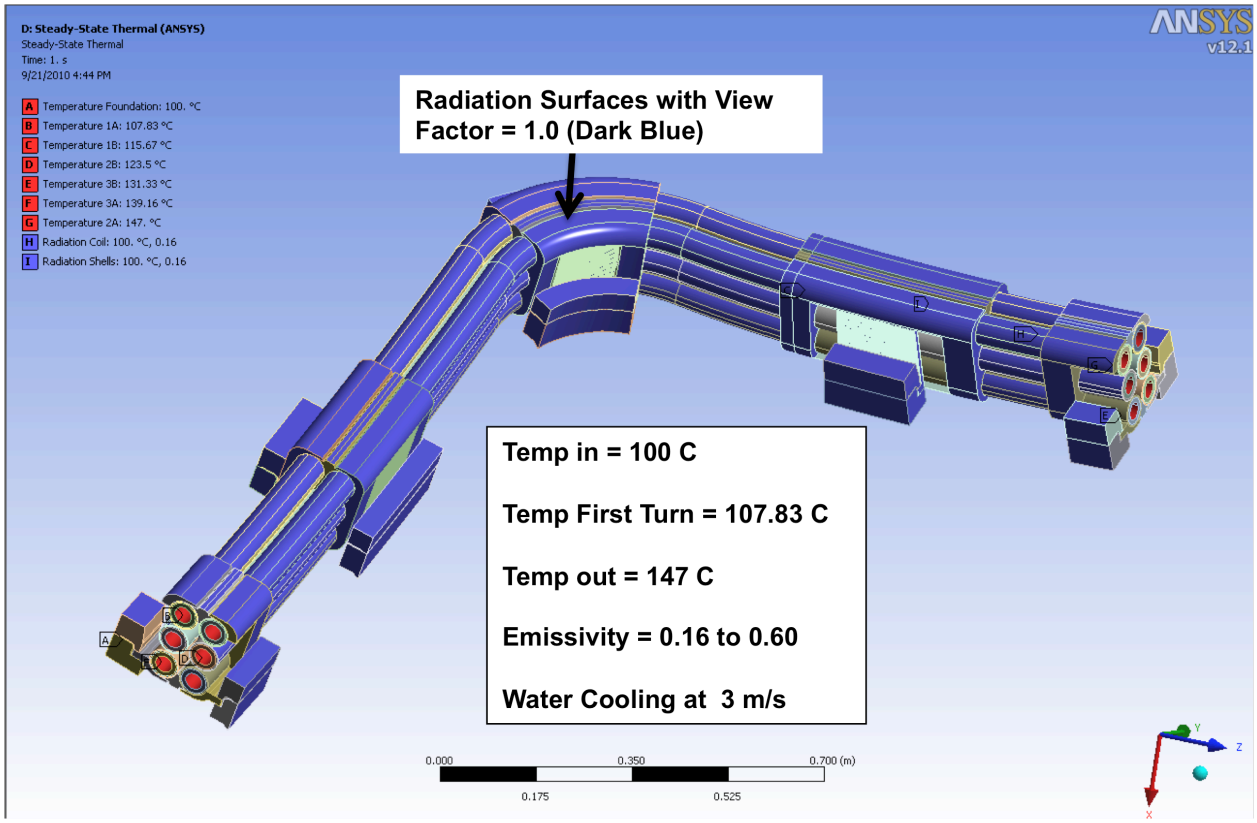

Figure 8-16 Thermal Boundary Conditions

8.1.1.7 Radiation Cooling

Radiation cooling is modeled on all exterior surfaces (Stainless Steel) of the ELM coil (Figure 8-16) that have a view factor of 1.0, to significantly simplify the analysis. All surfaces without a total view factor are conservatively assumed to not participate in any radiation.

The far field blanket structures surrounding the coil is specified to be a uniform minimum of 100C. The published surface emissivity ranges from 0.16 to 0.60 for 316 stainless steel and is assumed to be an equivalent hemispherical average across all wave lengths and directions. The target emissivity is closer to 0.60 as shown in the fault cases.

The formal definition of view factor and the terms governing radiation cooling are outlined in Figure 8-17.

Separate cases were evaluated in previous months to verify that inclusion of all surface-to-surface effects and variable view factors did show lower temperatures between the coils. The

solution time for these cases exceeded one full week and the differences obtained with the uniform far field cases demonstrated that our results were consistent and conservative.

$$Q_{i-j} = A_i F_{ij} \varepsilon \sigma (T_i^4 - T_j^4)$$

Where:

E = total emissive power

A = area of surface

ε = total, hemispheri cal emissivity of surface

σ = Stefan - Boltzmann constant

T = absolute temperature of surface

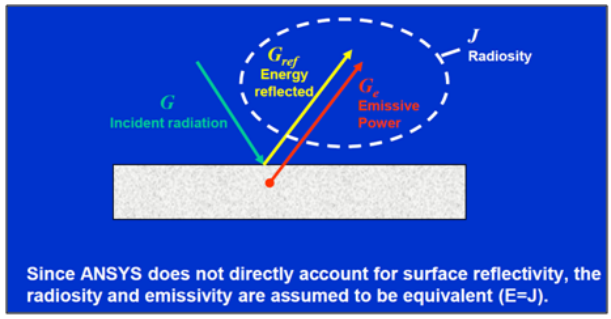

All Form / View Factors equal to 1.0

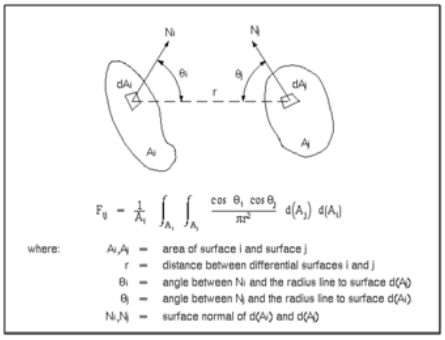

Incident Radiation is very small from 100 C Far Field

Emissivity is a Hemispherical Average
Across all wavelengths and directions

Figure 8-17 Radiation Assumptions

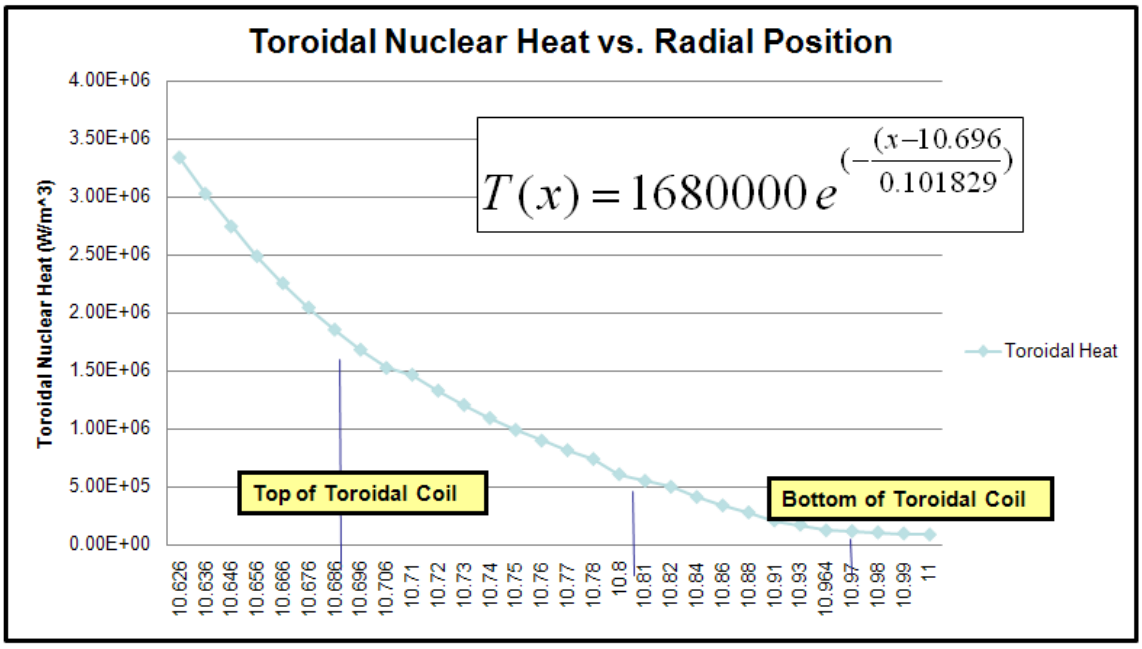

Figure 8-18 Toroidal Nuclear Heat Function

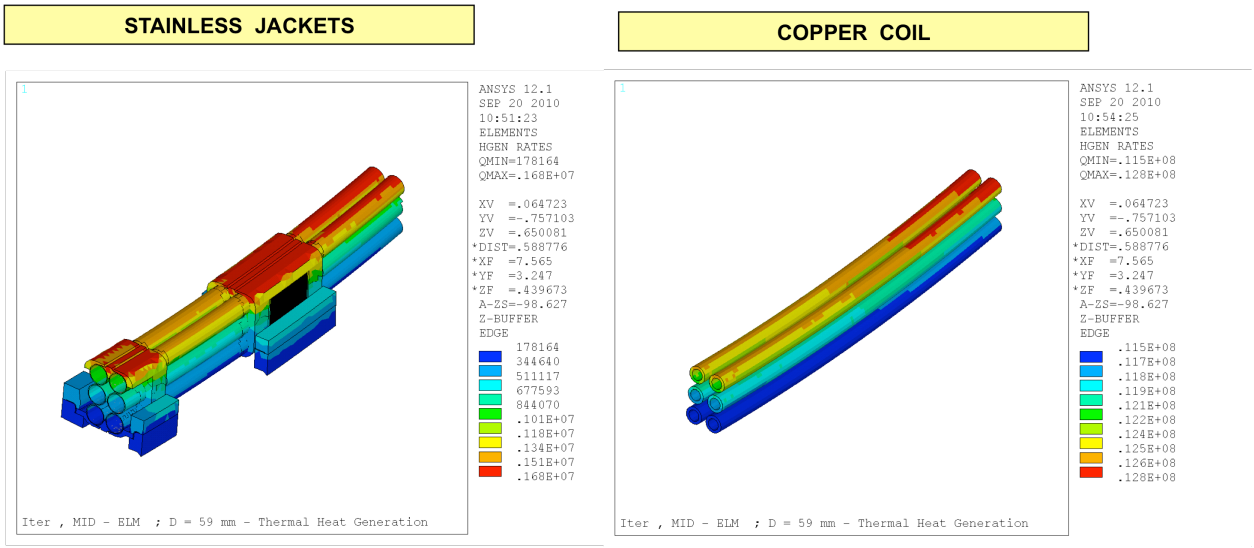

Figure 8-19 Toroidal Bracket and Coil HGEN Boundary

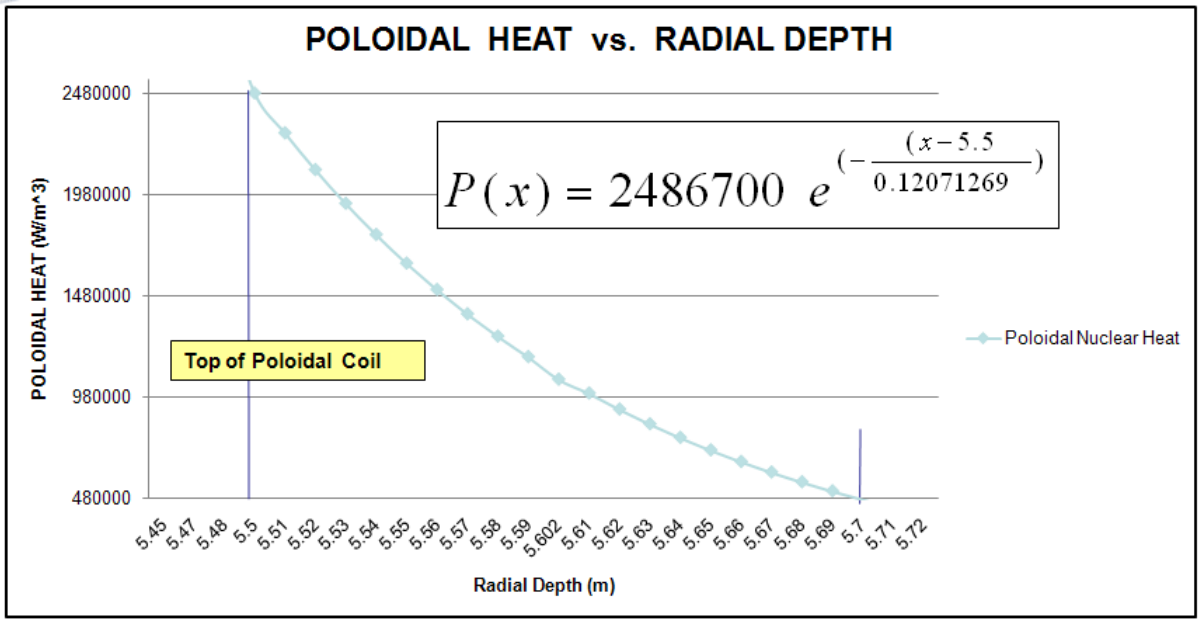

Figure 8-20 Poloidal Nuclear Heat Function

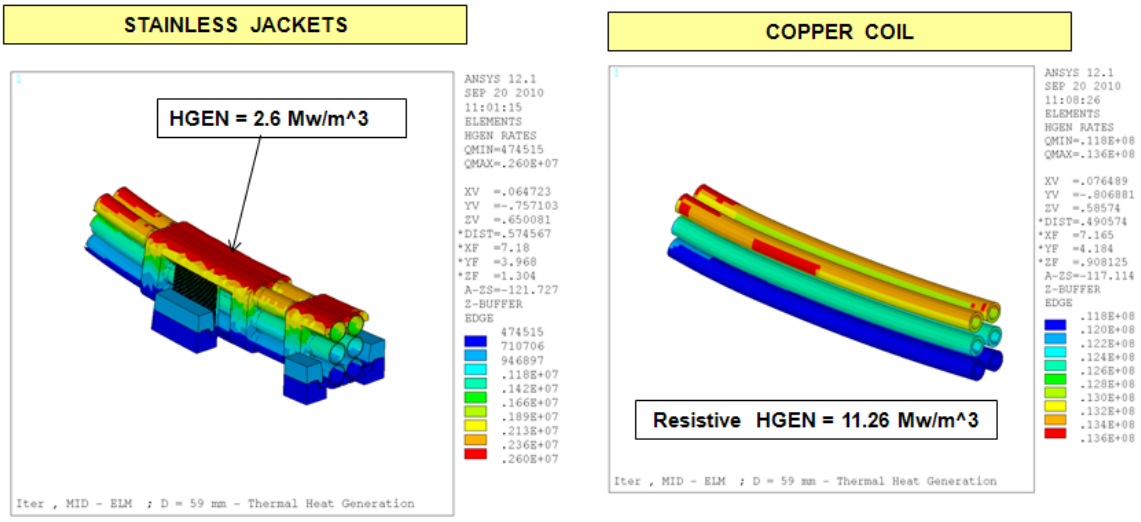

Figure 8-21 Poloidal Bracket and Coil HGEN Boundary

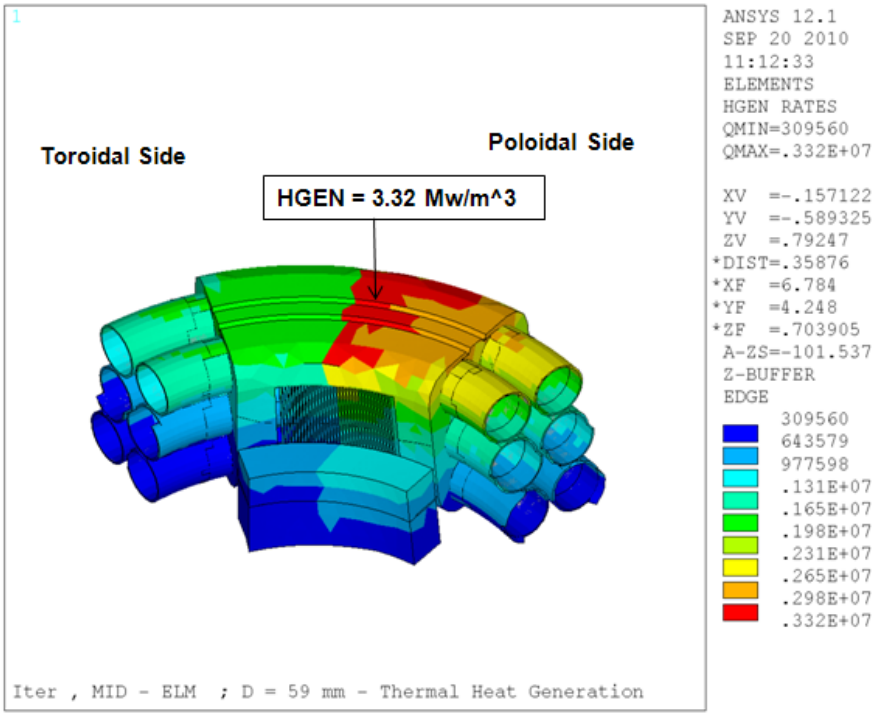

Figure 8-22 Corner Support HGEN Boundary Condition

8.1.1.8 Steady State Temperatures with Water Cooling, Normal Operation

The temperature contours for the assumptions outlined above for full steady state operation with plasma operation at 500 MW (**Error! Reference source not found.**) shows a peak temperature of 444C on the external surface of corner bracket. The asymmetrical nature of this distribution is primarily the result of applying the loads (Figure 8-22) along the mid plane with the higher Poloidal nuclear loads.

The external stainless steel jacket temperatures (Figure 8-24) shows localized areas on the Poloidal leg with higher temperatures between 200C and 328C. Although this is well below the melting temperatures of stainless, additional view ports will be added to allow radiation in these regions.

The actual copper coil temperature (Figure 8-25) shows the resulting temperatures on the coil are very close to the applied heat load boundary conditions (107.83C to 149.8C). This demonstrates that the cooling capacity to remove energy is appropriate for the applied energy.

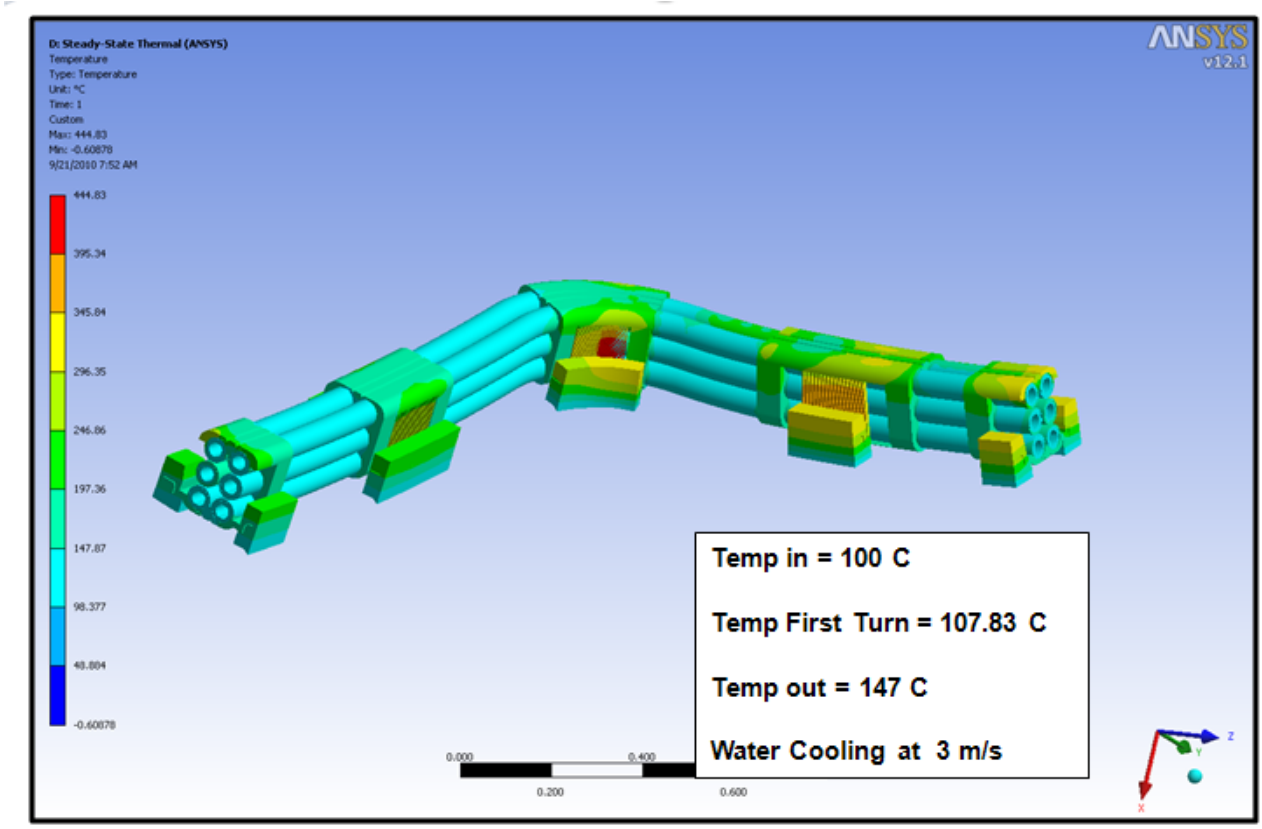

Figure 8-23 Steady State Temperatures at 500 MW

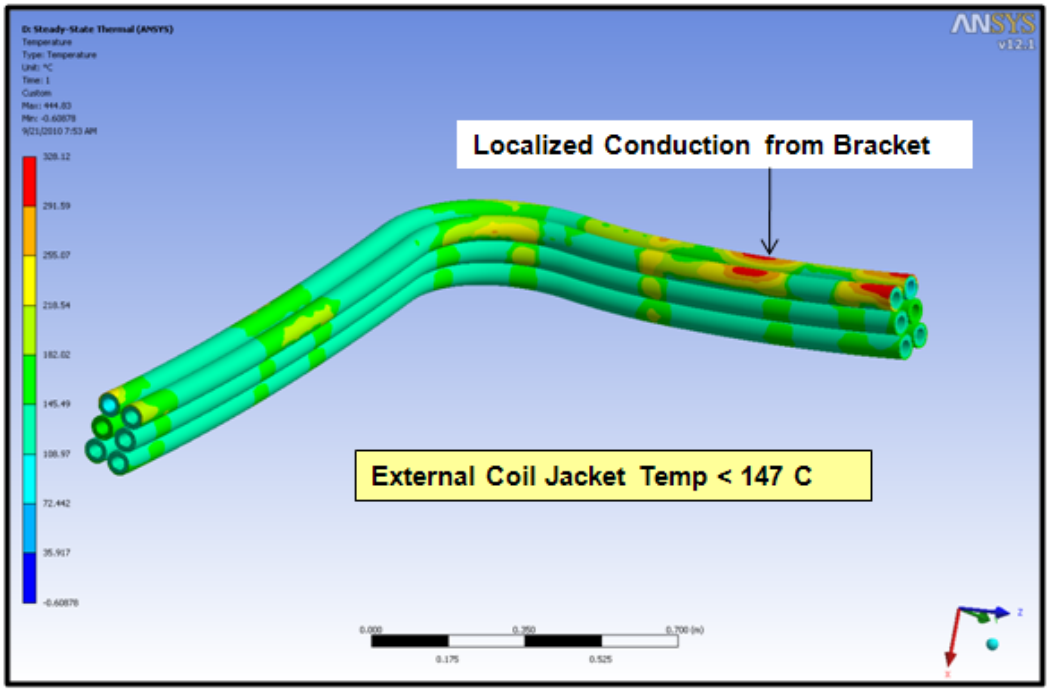

Figure 8-24 Steady State Coil Jacket Temperatures 500 MW

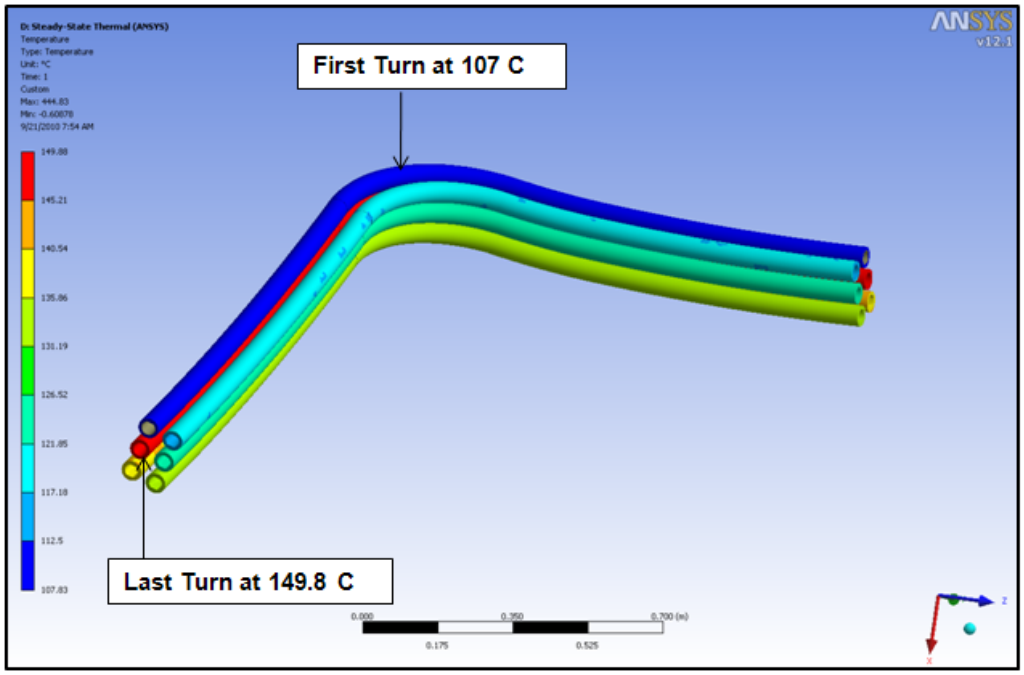

Figure 8-25 Steady State Coil Temperatures 500 MW

8.1.1.9 Steady State Bakeout Temperatures with Water Cooling

The bake out condition is without plasma operation and therefore no nuclear or resistive heat is applied to the structure.

A separate Bake out temperature distribution is not evaluated since as described in section 7.1.2 the thermal loading profile is gradual to a max value of 240 C and without significant gradients. This is insignificant in comparison to all the other cases discussed and therefore will not be evaluated further for adequacy in structural strength.

8.1.1.10 Mechanical Stress and Deflection

To understand the deflection and stress results one should refer to the load idealizations such as Figure 8-14 which illustrates the cyclic loading in the load sets. The displacement of the coil is shown (Figure 8-27) with Lorentz and thermal demonstrates a tendency of the corner to close in as a result of the thermal expansion. The largest displacement (4.139 mm) is out of the plane from these Lorentz Loads.

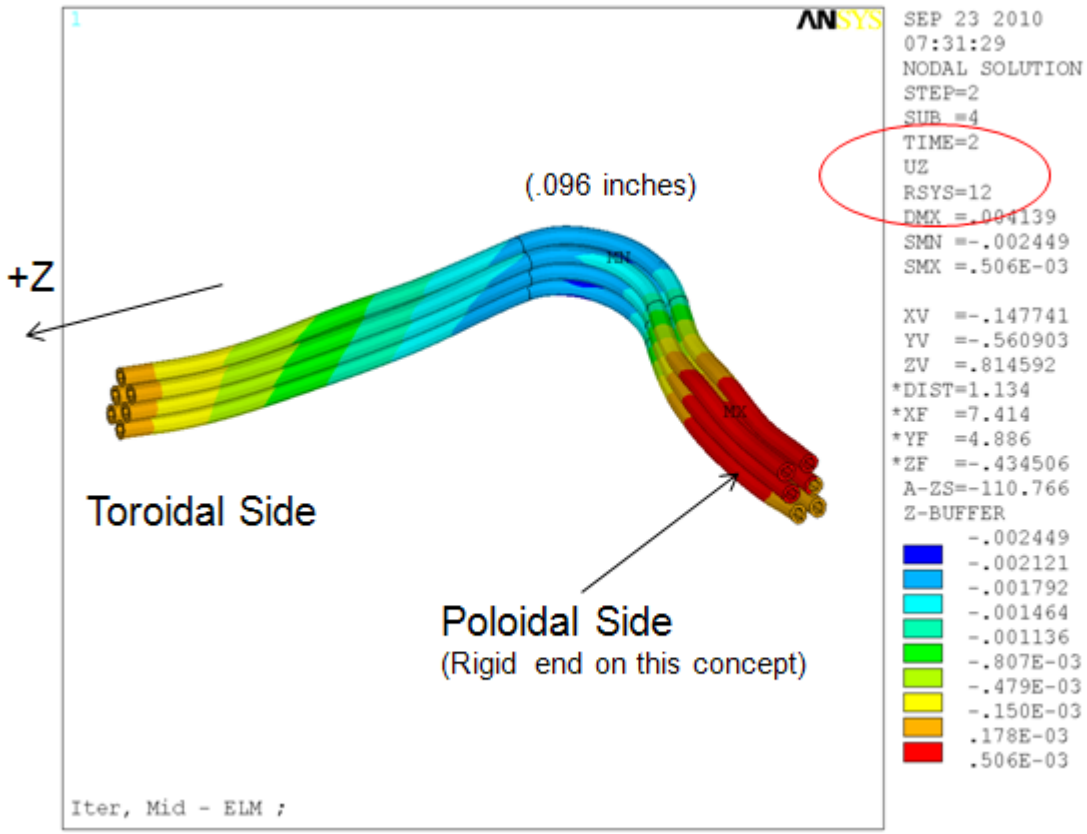

Figure 8-26 Coil Axial Displacement - Lorentz + Thermal Load

Thermal and internal fluid pressure loads produce stresses (Figure 8-28) within limit margins excluding the top turn on the corner and the ends which are unnecessarily constrained in this particular version. These localized effects have been corrected and will be available for the PDR presentation. The increased section of the supports has reduced bending stresses to around 50 MPA.

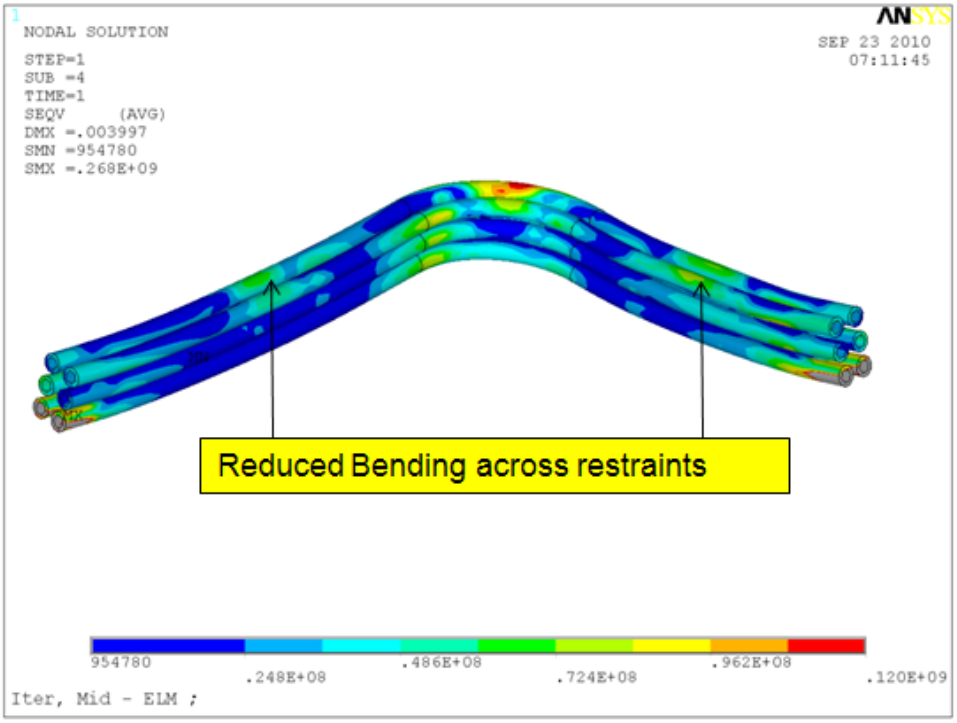

Figure 8-27 Thermal and Pressure Stress

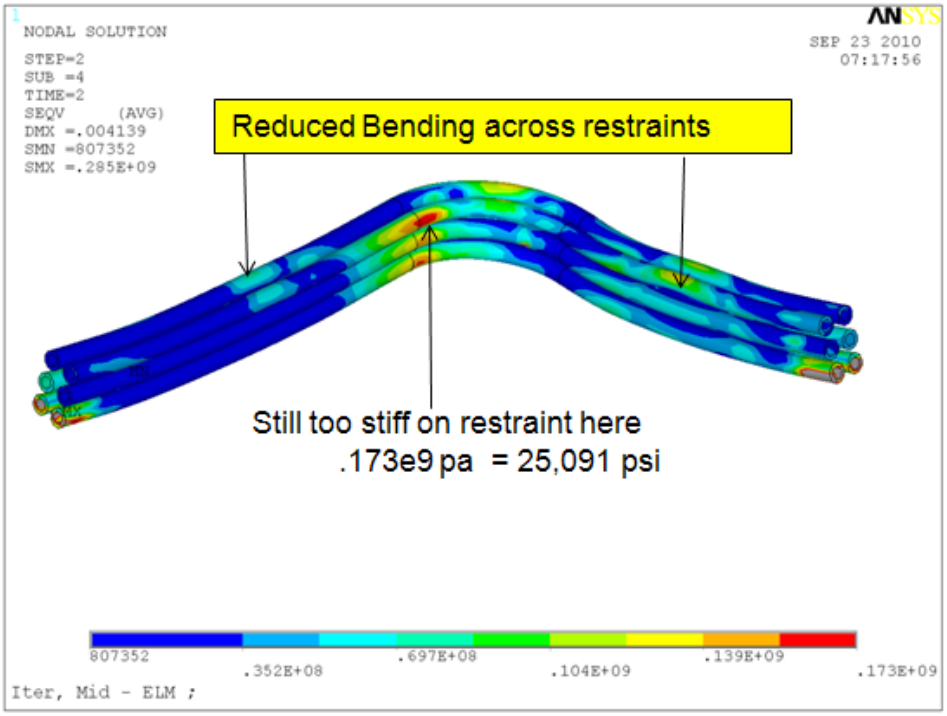

Figure 8-28 Lorentz + Thermal + Pressure Stress

Three issues that are evident on this particular design set are:

1.) The bending stress on the coil with the Lorentz load (Figure 8-29) shows a concentration.

2.) Over constraint of the support on either end due to thermal expansion (Figure 8-28)

3.) Local constraint of the internal support on the top turn of the coil (Figure 8-30)

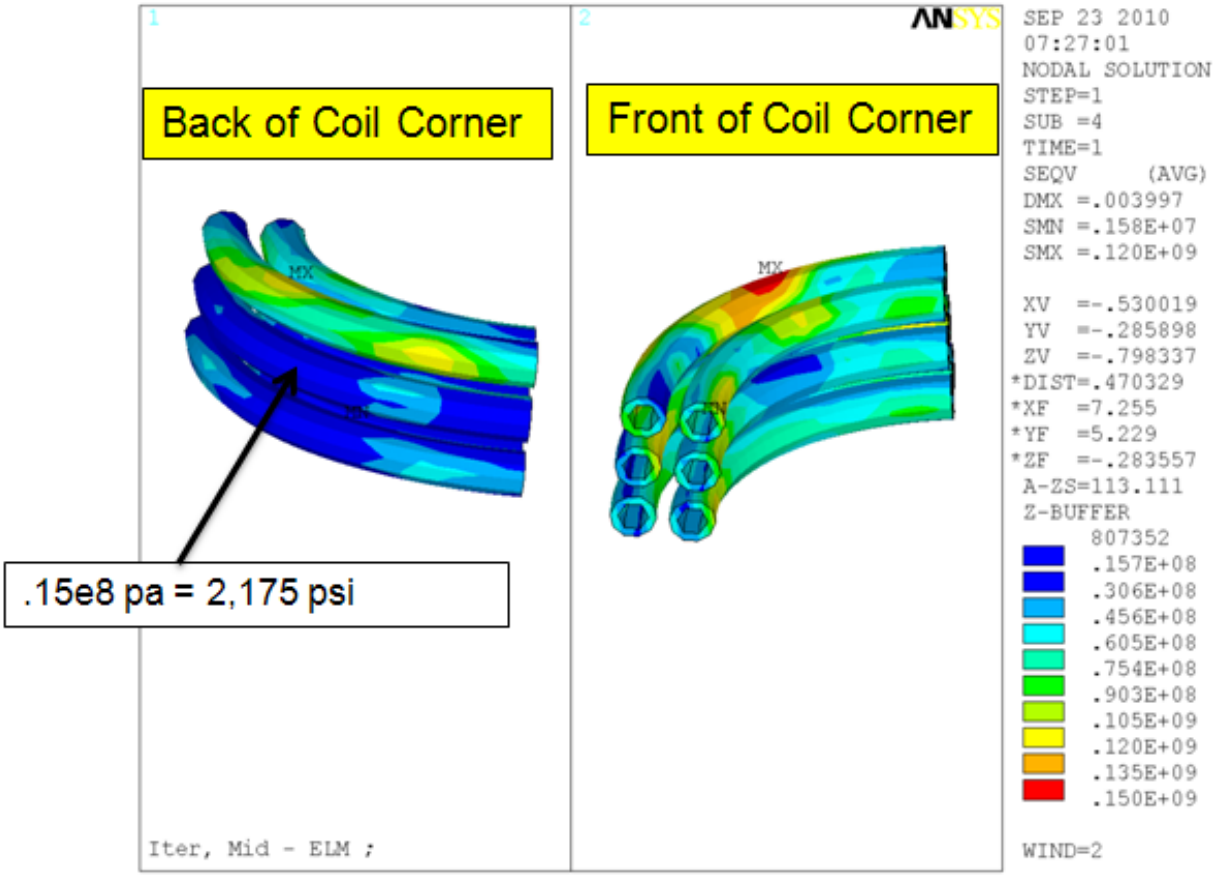

Figure 8-29 Coil Thermal + Pressure Stress

The correction of these issues is addressed by the changes shown on the revised design currently in progress (Figure 8-31). The changes are:

1.) The corner support is larger and positioned past the tangent point to limit the bending
2.) The end constraints were adjusted to allow thermal expansion
3.) The internal contact between the corner support and the coil was shaped to relieve load transfer from the support.

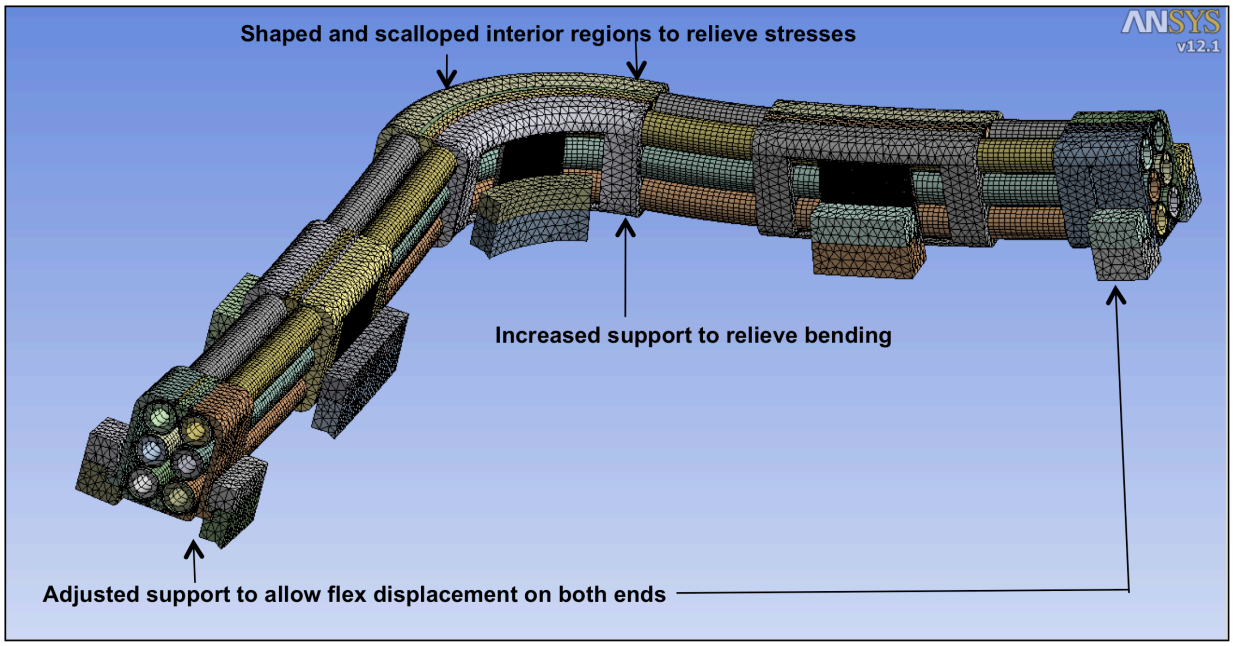

Figure 8-30 Correction Strategies in Process

The thermal contact is assumed to be bonded along the entire length of the interface between the coil and stainless steel jackets. Design is formulating various strategies to implement this requirement. The mechanical contact is only bonded on the ends of each bracket with no contact in the central region. The Design would braze these end areas directly to the stainless jacket.

8.1.1.11 Failed coil, abandoned in place

The fault case is defined to be without any circulating fluid to provide cooling to the coil, while thermally dissipating the nuclear heat energy through conduction and radiation. Several fault cases of the ELM coil were evaluated with various levels of radiation emissivity that are defined in the literature for stainless steel from 0.16 to 0.6 depending on variables such as oxidation, surface finish, and grain size.

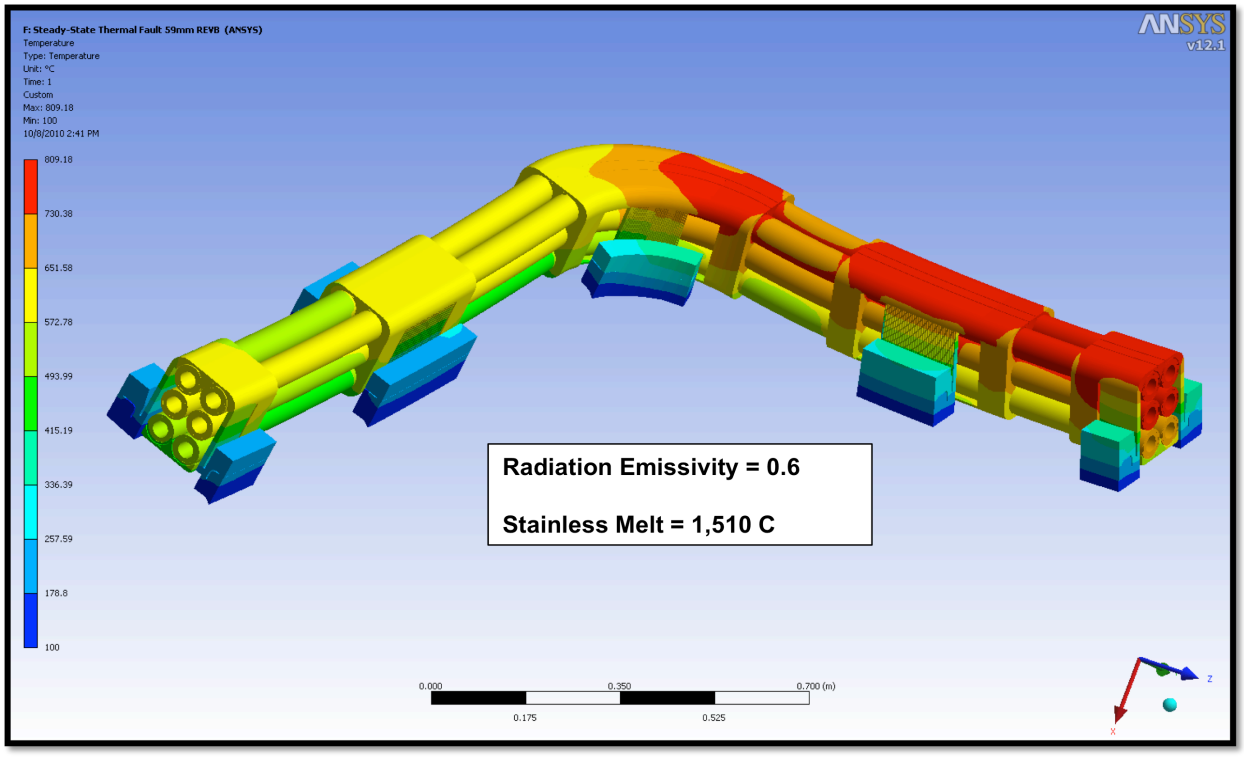

Figure 8-32 ELM Coil at Fault Conditions

The max temperatures (Figure 8-32) of 809 C are well below the melt temperature of stainless steel which is approximately 1510 C. The OFHC copper max temperatures (Figure 8-33) of 805 C are also within limits of the melt temperature of 1083 C.

These temperatures results demonstrate that we currently have an adequate design that would not be problematic in this fault scenario.

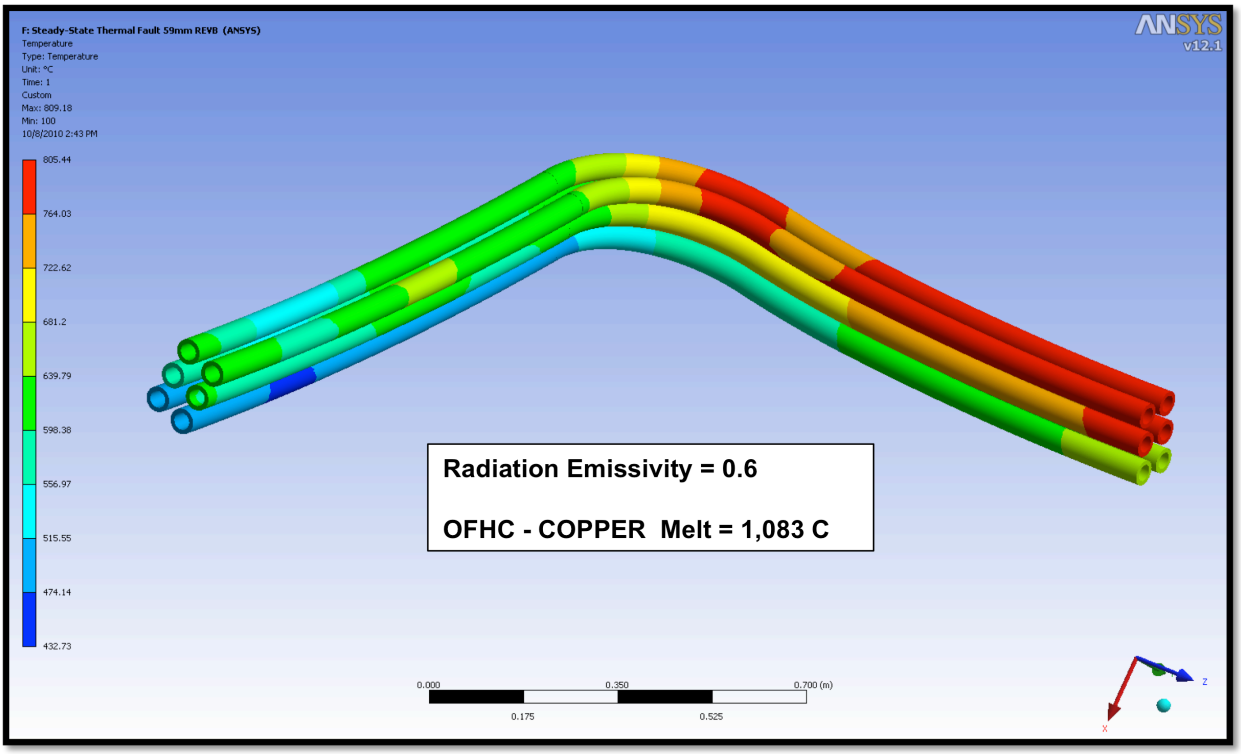

Figure 8-33 Copper Coil Temperatures at Fault Conditions

8.1.1.12 ELM Feeder Analysis

The performance of the ELM Coil Feeders during normal operation at 15 kA was analyzed using the ANSYS finite element code. The FEA model was used to calculate the thermal response from ohmic and nuclear heating, the Lorentz forces from the interaction of the feeder currents with the background field, and the structural response from the resultant temperature and force distribution as well as the internal cooling water pressure. The structural response during a plasma disruption was not modeled explicated since the OPERA EM analysis of the ELM/VS coil system showed the induced currents to be lower than the normal operating current. Also, the bake-out analysis has not yet been carried out though it is expected to be less severe since EM loads are not present and the thermal gradients, which drive the stresses, should be less by design.

The analysis assumes the MgO is bonded to the inner Copper conductor and outer SS sheath. This appears to be compatible with the preliminary test results done to assess the material MgO behavior and structural properties. It also assumes the tubes are brazed to the supports.

The discrete supports are modeled as solid elements where they support the tubes. The flexible members which tie the supports to the VV are modeled as equivalent springs in three directions with initial spring constants taken from the detailed model of a single support.

The only cooling of the feeder is assumed from the cooling water tubes. To maximize the cooling of the plasma side of the feeders where the nuclear heating is greatest, the 100C water supply temperature is fed to the upper tubes and return thought the lower tubes. The thermal-hydraulic analysis of the ELM coils yielded a 167C exit temperature which was taken as a boundary condition for the feeder return legs. Radiation to the surroundings and conduction to the VV thru the flexible supports was ignored.

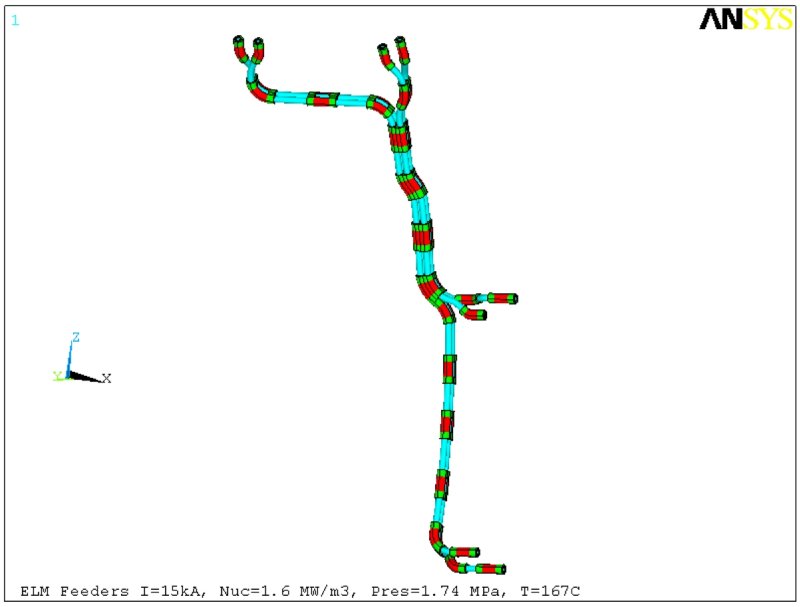

Figure 8-34 Overall Model of ELM Feeder

The overall model is shown in Figure 8-34. The material properties used are given in Table 8-1.

Table 8-3 Material Properties Used in ELM Feeder Analysis

	Material Properties at 100C						
			CuCRZr	MgO	SS		
Electrical Resitivity	rsvx	1	2.71E-08	*2.71E+01*	7.70E-07		Ohm-m
Relative Permeablity	murx	1	1	1	1		
Elastic Modulus	ex	1	125	0.96	193		GPa
Shear Modulus	gx			2.50			Mpa
Poisson's Ratio	nuxy	1	0.3	0.3	0.3		
Thermal Expansion Coef	alpx	1	1.71E-05	1.28E-05	1.65E-05		m/m-C
Density	dens	1	8854	2200	7899		kg/m3
Thermal Conductivity	kxx	1	333	2.36	15.48		w/m-C
Heat Capacitance	c	1	383	940	513		J/kg-C

The magnetic fields and Lorentz forces were calculated from the ITER PF and OH coil set shown below in Figure 8-35 and Table 8-4 and a 1/R TF field produced by a single long filament running up the machine that produced 5.3T at 6.2m. The discrete TF coils were not used since the ripple is negligible from a force standpoint at the ELM feeder location. This may not be true of the bus that penetrates the VV upper port which is outside the present scope.

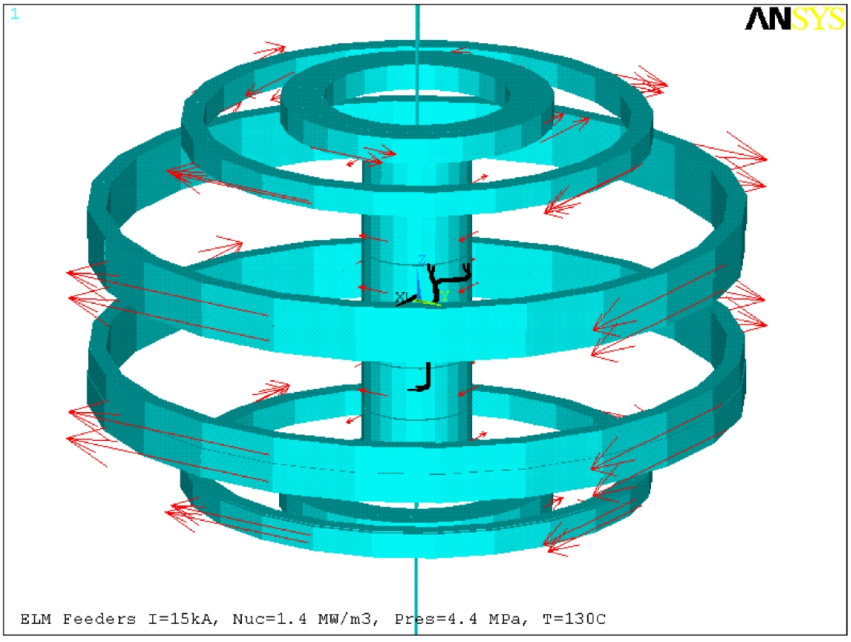

Figure 8-35 Coil Model for EM Fields

Table 8-4 Coil Set Used for EM Field Calculation

OH/PF Coil Geometry and Currents					
Coil	Rc	Zc	Dr	Dz	MA-Turns
OH1	1.688	5.071	0.749	1.979	4.03
OH2	1.688	3.043	0.749	1.979	-10.98
OH3	1.688	1.014	0.749	1.979	-18.11
OH4	1.688	-1.014	0.749	1.979	-18.24
OH5	1.688	-3.043	0.749	1.979	-8.99
OH6	1.688	-5.071	0.749	1.979	5.94
PF1	3.954	7.557	0.968	0.976	5.07
PF2	8.309	6.53	0.649	0.595	-2.22
PF3	11.935	3.265	0.708	1.125	-6.23
PF4	11.905	-2.243	0.649	1.125	-5.05
PF5	8.395	-6.73	0.82	0.945	-7.39
PF6	4.287	-7.557	1.633	0.976	17.67

The nuclear heating is assumed to be a maximum value of 1.6 MW/m2 at the surface closet to the plasma and decay in value exponentially with a decay constant of 6 cm as shown in Figure 8-36. The heating is assumed not to vary over the axial length of the feeders.

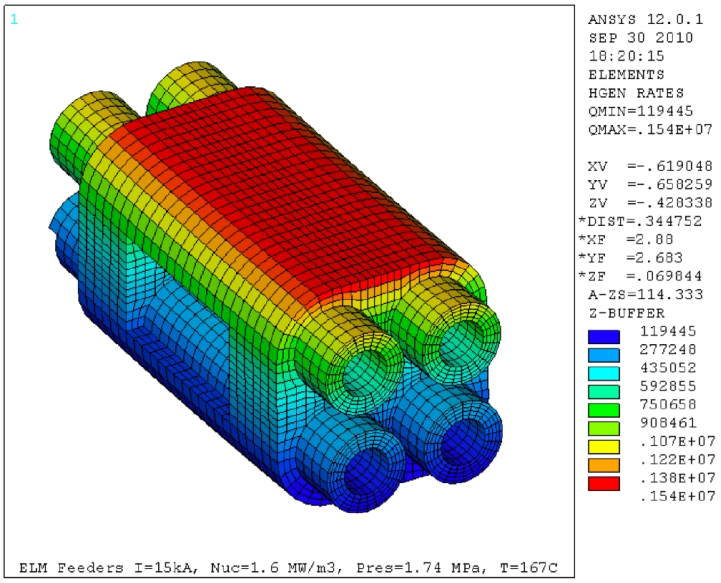

Figure 8-36 Heating Profile

The resultant temperature with the 15kA of ohmic heating is shown below in Figure 8-37. Note that in the analysis since the surface temperature of the inner wall of the conductor tube is specified (ie assumes very high heat transfer coefficient) the only effect specifing the current is to induce a gradient across the conductor from the OD to the ID. Similarly since the cooling water is the only heat sink, the nuclear heating imposes a significant gradient thru the support structures.

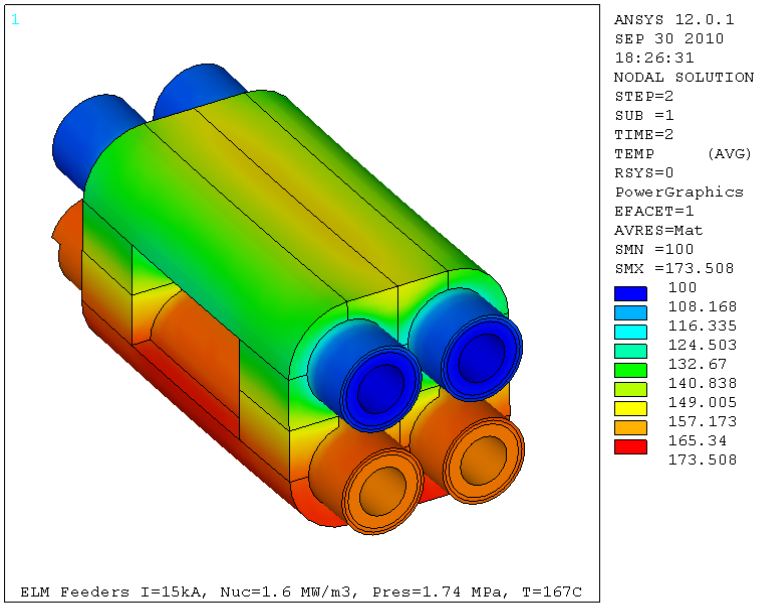

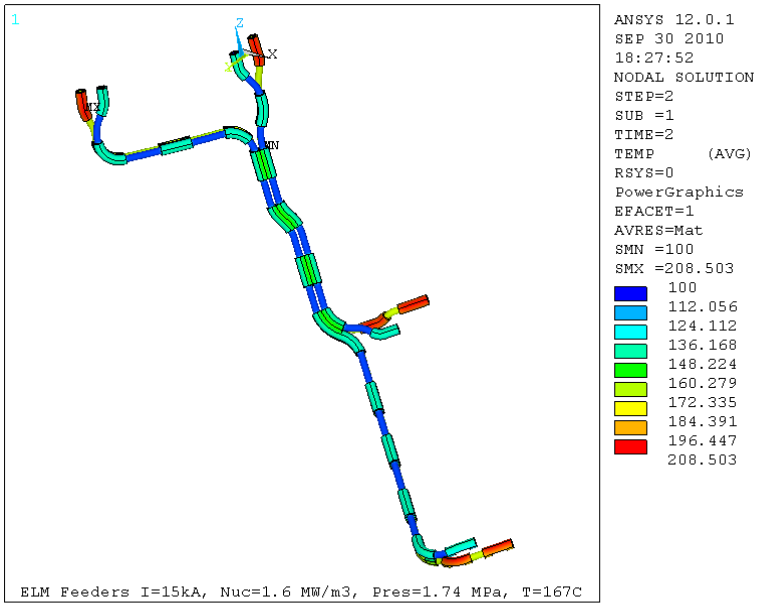

Figure 8-37 Temperature Profile With 15kA Ohmic Heating

The supports for the single tubes at the coolant exit experience a larger rise in temperature from the nuclear heating because of the warmer water.

There is very little net load on the feeder assembly since the currents flow in opposite direction produces forces equal and opposite. However, the unsupported length of conductor experiences the full 15 kA of current crossing a roughly 4 T TF field and upwards of 2 T vertical field. This limits the unsupported length the conductor can withstand to about 300 mm.

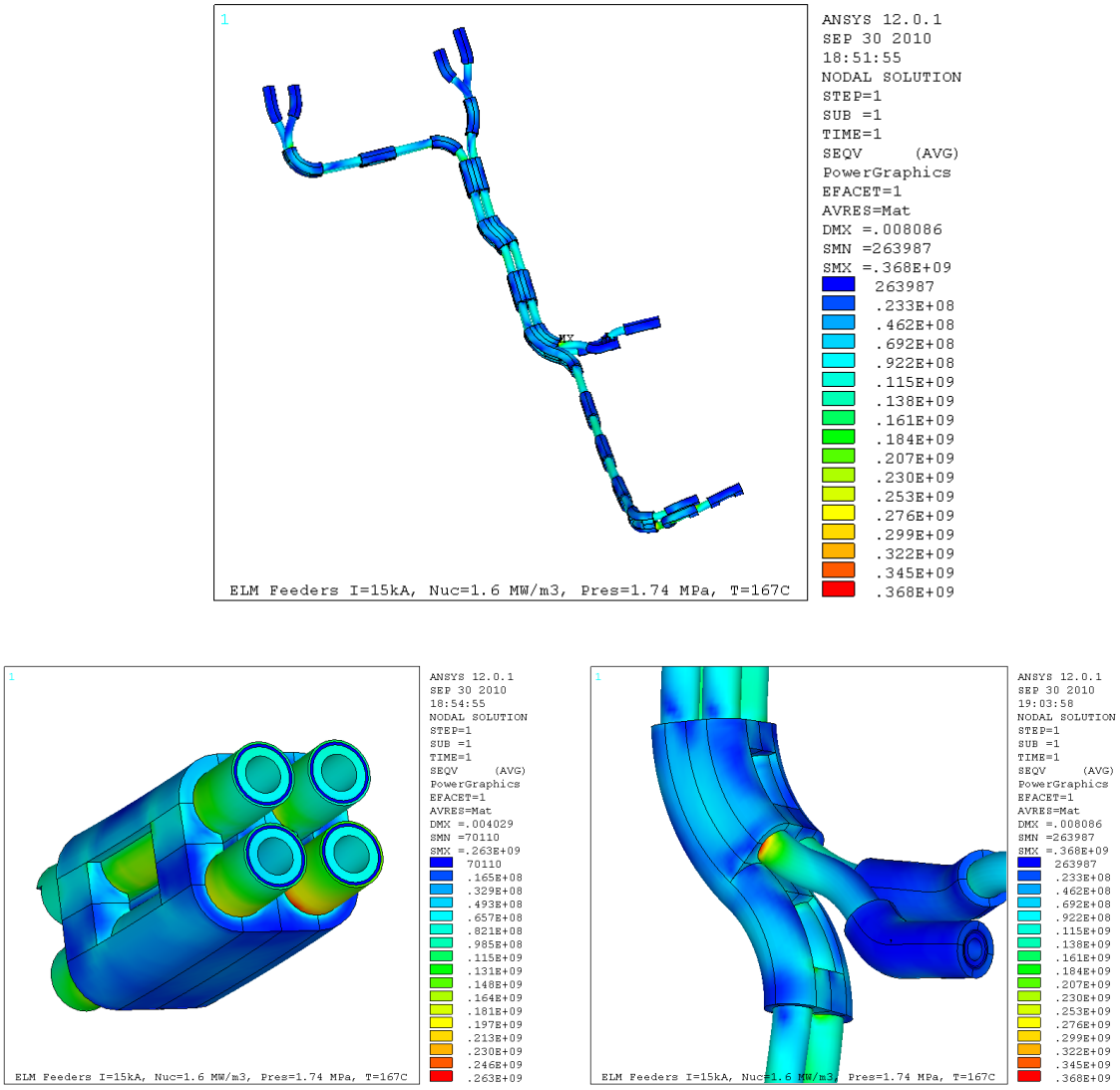

Figure 8-38 ELM Feeder Stress

The above plots in Figure 8-38 show the von mises stress for the full feeder and a closeups of the tube-support interfaces. While the top plot appears mostly ‘blue’ suggesting reasonable stress levels in most of the feeder, the lower plots reveal high bending stress at the tube-support interfaces that require further work to mitigate. Shorter spacing of the supports to minimize the free span may be needed. Based on analysis of earlier configurations, the curved sections by

themselves (as on the right above) do not offer enough flexibility to absorb the thermal expansion but instead cause kinking at the tube-support interface. For this reason, most of the bends are fully supported and rely on the flexibility of the supports to absorb the expansion.

8.1.2 VS Structural/Thermal Analysis

The inventory of in-vessel coils being provided to ITER includes the vertical stability coils. Figure 8-36 below shows the VS coils installed in EAST which are similar to the ITER VS coils. These are mounted to rails on the vessel wall with spring loaded clamps. The necessity for inclusion of the VS coils is discussed in section 1.1. The VS Coils are designed for 240 kA-t/coil (60 kA/turn) as described in 2.2.2.2. The coil is wound as 4 individual turns with separate leads and feeders as described in section 3.5. This feature:

- Allows isolation of turns, if leaks or electrical problems develop
- Keeps flow path at a reasonable length for cooling

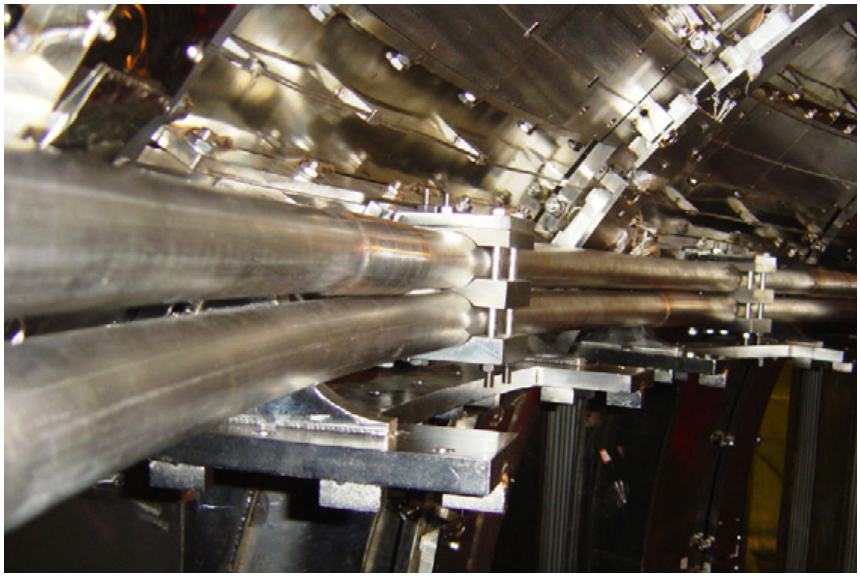

Figure 8-39 VS Coils Installed in EAST, Similar to ITER VS Coils

The ambient temperature is 100C, and the peak operating temperature of the conductor is 120C. Local temperature in the support for the coils will exceed this due to nuclear heating at regions

that are not in good thermal contact with the vessel or the actively cooled conductors. The extra temperature range due to nuclear heat is included in the analysis by imposing heat flux distribution from neutronics calculations and performing steady state heat conduction analysis of the VS conductor and support assembly as it is connected to the vessel. Figures 8-40 and 8-41 below show the VS coils and feeders and dimensions (also Table 8-5).

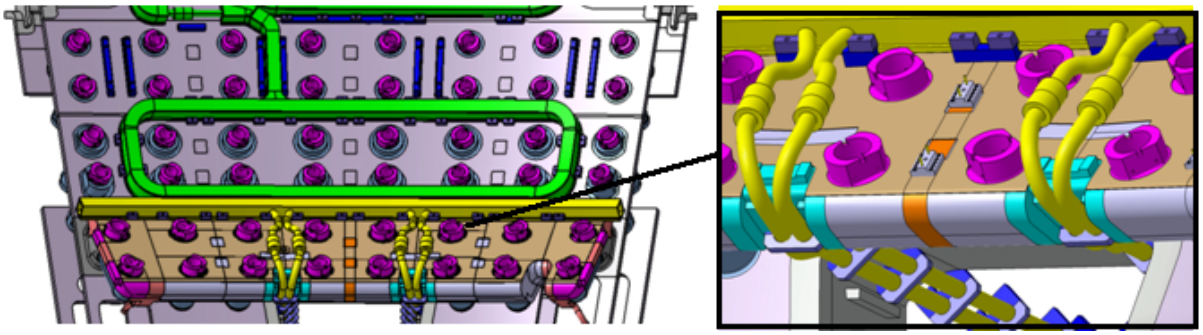

Figure 8-40 VS Coils & Feeders (Yellow)

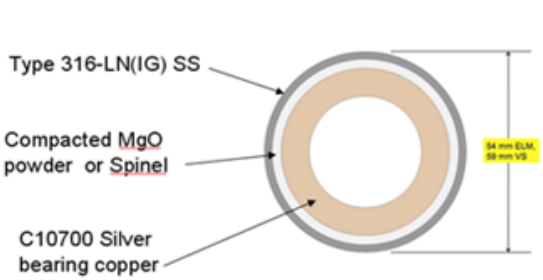

	VS
SS OD	59 mm
SS ID	55 mm
Cu OD	45 mm
Cu ID	30 mm
Mineral Insulation thickness	5.0 mm
Total length req'd.	650 m

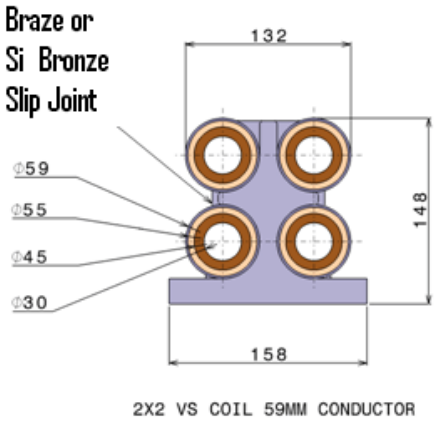

Figure 8-41 VS Conductor and 4-turn Bundle

Operational life is 20 years or 30000 Experimental pulses during which the VS will experience an average of 3 major pulses to reposition the plasma. There is a small current oscillation arising from magnetic diagnostic noise as described in section 2.2.2.2.

Criteria for Structural behavior and materials compatibility may be found in the Appendix D of the ITER In-Vessel Component Criteria Document, discussed in section **Error! Reference**

source not found.. This document implements magnet criteria based primarily on PPPL experience because the existing ITER magnet criteria is directed at superconducting coils and not water cooled normal conductors exposed to in-vessel conditions.

Table 8-5 VS Conductor Parameters

Conductor pack width	m	0.132	0.132
Conductor pack height	m	0.128	0.128
Jacket OD	mm	59.0	59.0
Jacket thickness	mm	2.0	2.0
Insulation thickness	mm	5.0	5.0
Conductor OD	mm	45.0	45.0
Conductor ID	mm	30.0	30.0
Conductor length per turn	m	47.1	47.1
Feeder length per pole	m	10.0	10.0

8.1.2.1 Summary of Analysis Results

VS coil design is in a comfortable design space to finish preliminary and go forward final design. Conductor thermal stresses are low because of the axisymmetry of the winding (no corner bends as in the ELM). Lead break-outs have bends and consequently will behave similarly to the ELM corner and thus the VS break-out supports will copy solutions decided upon for ELM coils. Support spine stresses are high under the clamp details but with some slight modifications, these will meet static and fatigue allowables. Bolt stresses during the disruption are within the allowables of high strength bolts. Pre-loading the bolts eliminates the alternating stress component. Assuming shared vessel currents during the disruption may be overly conservative. Appropriate analysis of shared current density is planned.

8.1.2.2 Analysis of the Coil and Support System

The structural performance of the coils will be governed by fatigue performance. Stress behavior is nearly axisymmetric except at the break-out and cross over for the leads. These regions share similar geometry as the ELM coil corners and the U bend test. Similar support provisions are anticipated. Analysis models of the axisymmetric area and of the cross-overs are shown in Figure 8- and Figure 8-. Failure is governed by either electrical failure or coolant leak.

Primary Loads are supported by a "spine" which is similar to the scalloped form used in the ELM coil flex support. The approach used in the support of the VS coils is to restrain the thermal growth of the conductor that results from Joule heat. This introduces compressive stresses throughout almost the entire length of the conductor. Except at the break-outs, the design does not intend to allow thermal motions as is the case with the ELM coils.

8.1.2.3 Material Allowables

The primary component of the VS coil is the stainless steel jacketed MgO insulated copper conductor. Early evaluations of fatigue showed that the compressive stress state of the restrained coil, and the frequent support spacing allowed the bulk of the conductor to be a common silver bearing copper.

Table 8-6 Preliminary Stress Allowables for Design

Material	**Sm**	**1.5 x Sm**
316 LN SST	183Mpa (26.6 ksi)	275Mpa (40ksi)
316 LN SST weld	160MPa(23.2ksi)	241MPa(35ksi)

The VS is capable of operating at full amp-turns with one turn missing. A preliminary analysis of the flow rates and cooling capability has been made (see VS design point in Appendix II). Based on 3 m/s water flow then the temperature rise for the degraded 3 turn mode is 35C as compared to the case with 4 turns and 20C.

8.1.2.4 Position of the VS in the Vacuum Vessel

CDR upper and lower coil positions were changed for the Preliminary Design activities. The CDR arrangement of the lower VS is shown in Figure 8-. The proximity of the VS and lower leg of the ELM coil added some complexity to the mounting clamps which has been improved in the PDR design. The upper VS coil was repositioned such that the Lorentz loads on the coil went down. Consequently the structural analysis is based on the more highly lower coil configuration. The orientation of the coil is shown in Figure 8-.

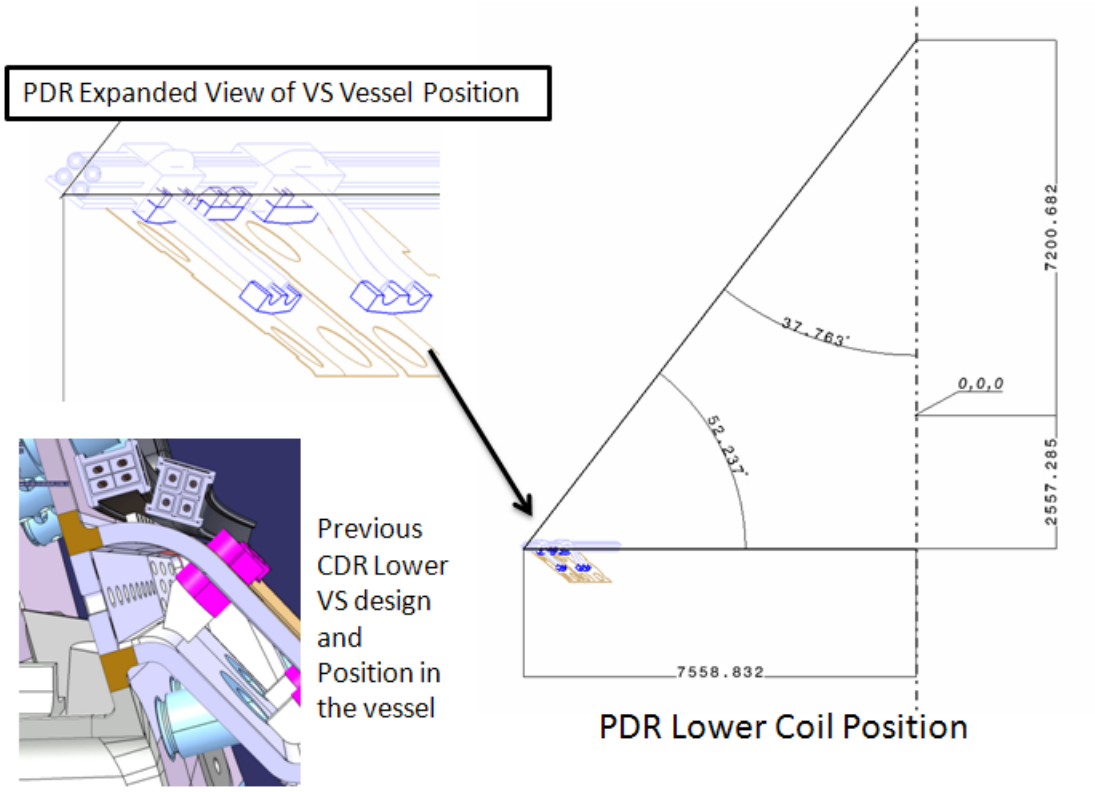

Figure 8-42 Location of the Lower VS Coil

8.1.2.5 Analysis Model

The model is a 10 degree cyclic symmetry model. The coils are supported every 5 degrees with clamps. Temperatures modeling is based on ohmic heating and nuclear heating as described in section 4.2. Radial forces are computed from SQRT(1.2) MN/40 degree sector. Vertical forces are computed from SQRT (1.2) MN/40 degree sector. Radial and vertical forces are applied concurrently. Sliding gap-friction is modeled between spine, sheath, MgO and conductor. A retainer clamp is used rather than weld or braze. The mesh is created by sweeping a 2D element section and then selecting regions for deletion.

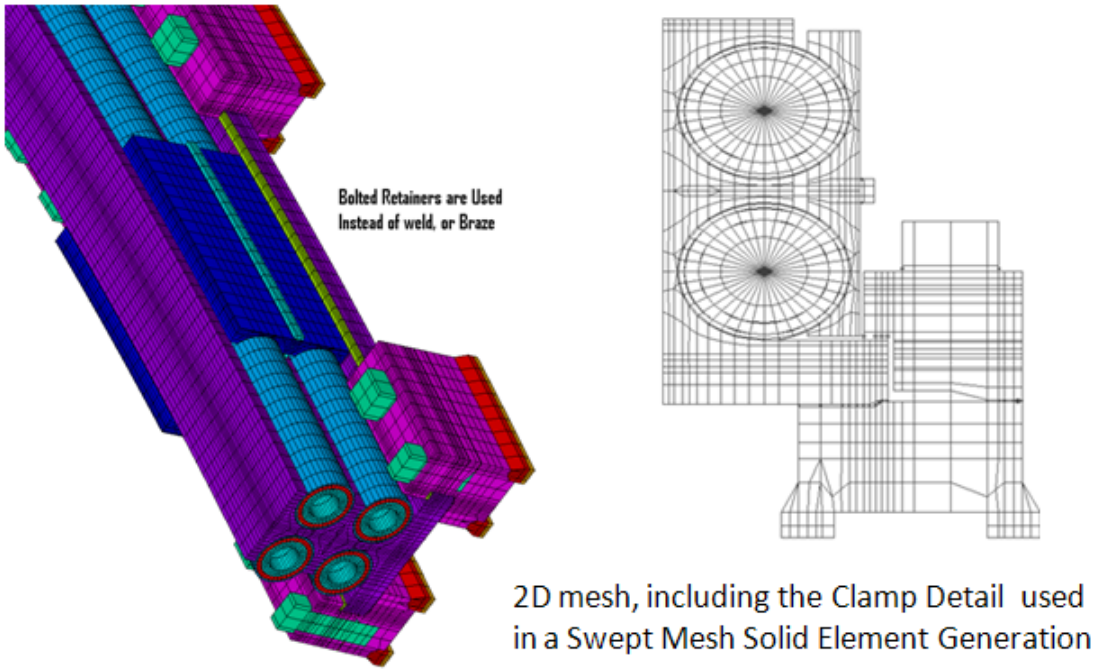

Figure 8-43 VS Analysis Models

8.1.2.6 Clamps and Rails

Clamp details as they appear in the Vessel Procurement Arrangement (PA) are shown in Figure 8-. These are simple dog-type clamps which will be provided with remote handling features as described in the ITER Remote Handling Design Practices Document.

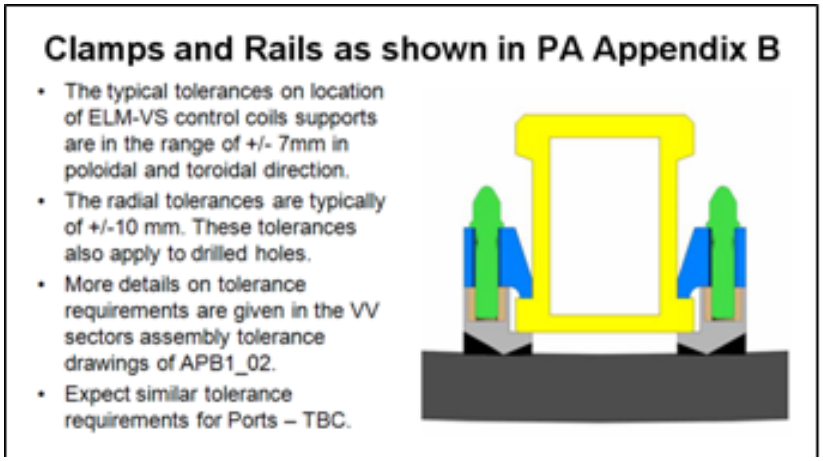

Figure 8-44 VS Clamps and Rails

Swing-away clamps were suggested in remote handling studies by Oxford Engineering, but these have not been stress analyzed and they may violate the CMM or space allocation drawing.

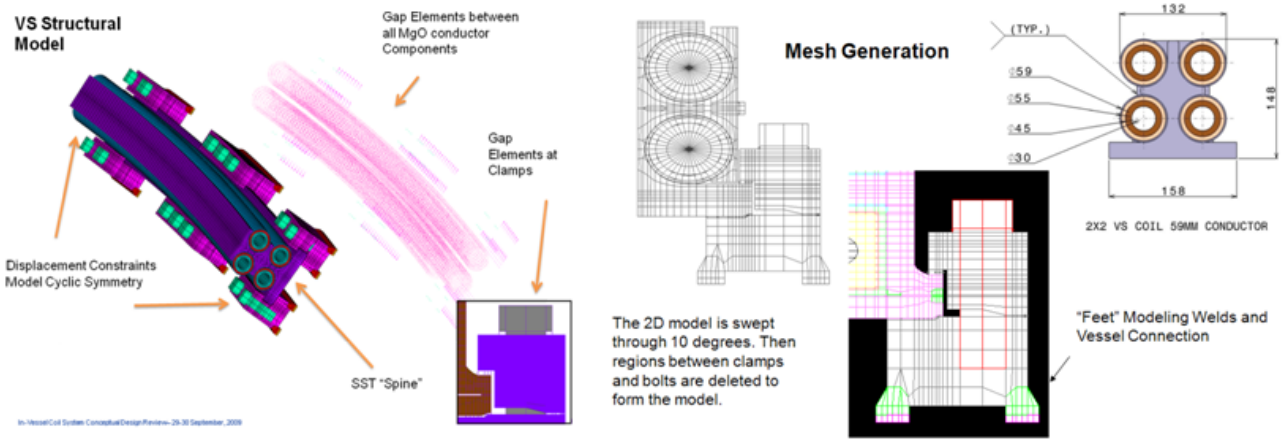

Figure 8-45 Analysis Model Details

8.1.2.7 Joule Heat Application

Joule (ohmic) heating effects are not simulated in the structural model. The temperatures of the conductors is taken from the analyses summarized in the design point, included as Appendix II

of this document which were confirmed by more detailed analyses presented in 7.1. Temperatures are applied to the structural model with a BFE command.

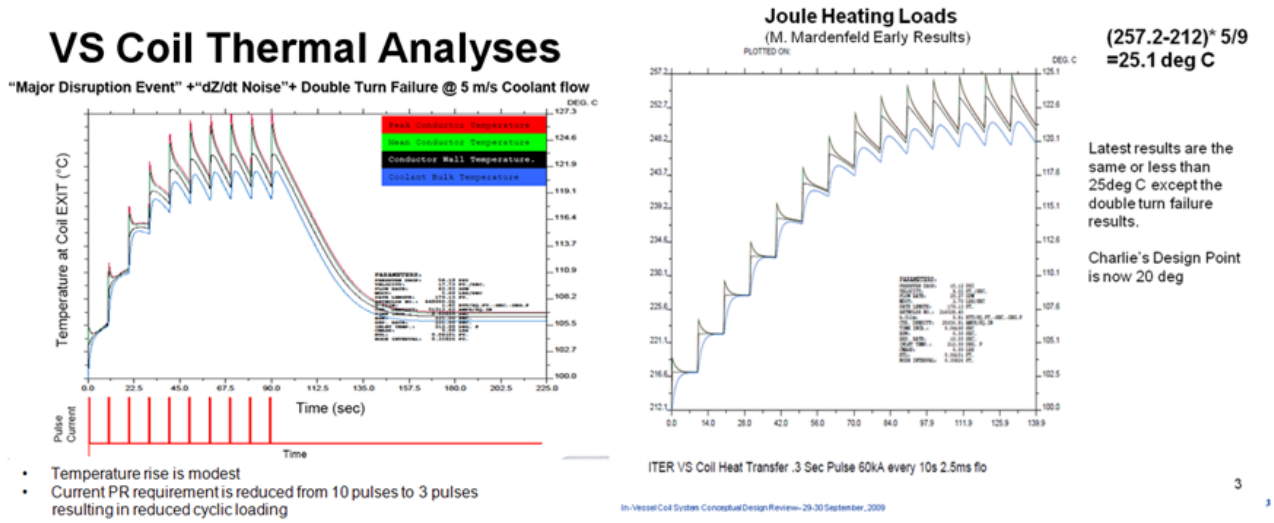

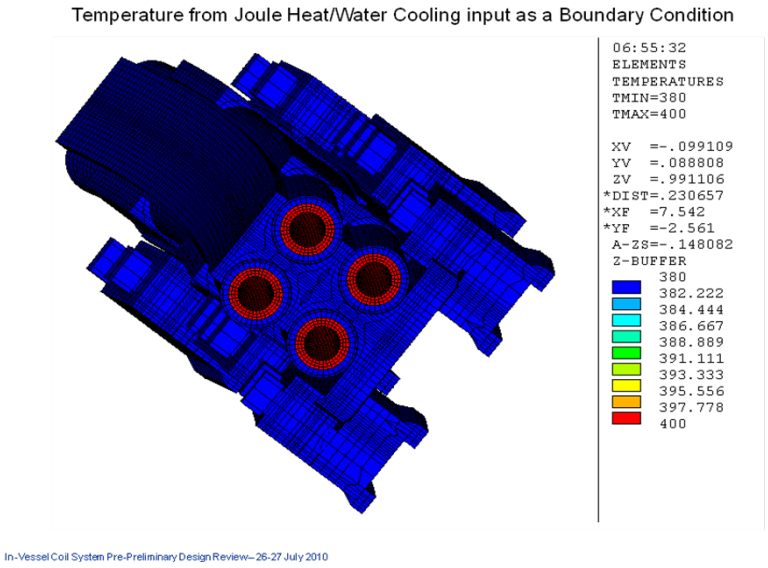

Figure 8-46 VS Joule Heating and Thermal Boundary Condition Modeling

8.1.2.8 Nuclear Heat Application

For the lower VS, the nuclear heat in watts / m^3 is 1.8e-6*100^3. The ITER recommended value for CuCrZr thermal conductivity at 100C is 333 W/mK. The nuclear heat is 1.4 MW/m^3 for the thin stainless steel sheath, and the heat generated is 1.4e6*.0019 = 2.66e3 Watts/m^2. The

thickness of the MgO is 5 mm or .005m. The thermal conductivity of the MgO is 2.5 Watts/degK/m so the delta T is 5 degrees.

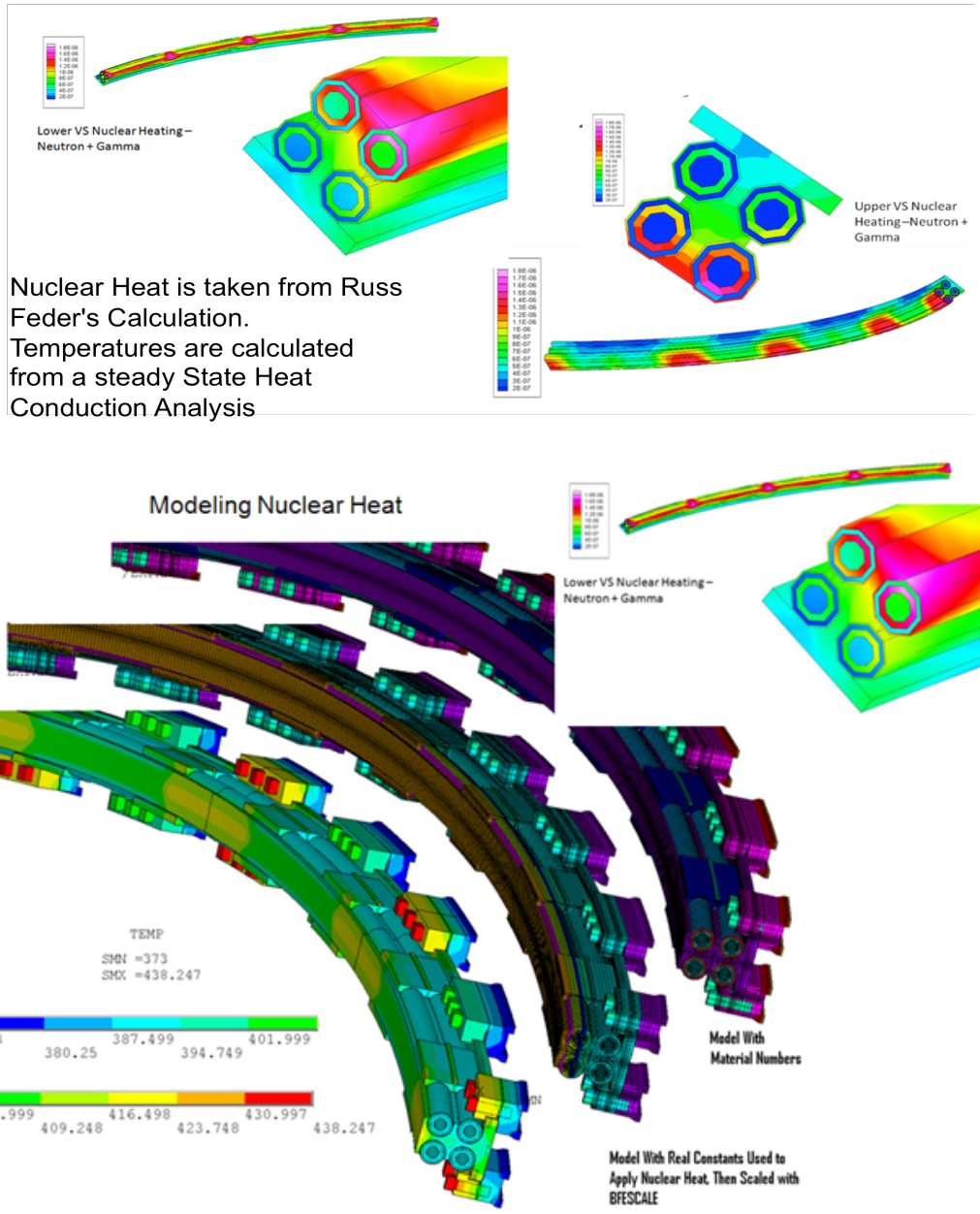

Figure 8-47 VS Analysis Model Details – Nuclear Heating

8.1.2.9 Lorentz Force Application

A load of 1.2e6 N per 40 degree sector (vector sum of radial and vertical directions) was used. LDREAD temperatures from the nuclear radiation thermal analysis. An additional 1.2e6 N (vector sum of radial and vertical directions) is applied on the case to simulate loads from shared vessel currents.

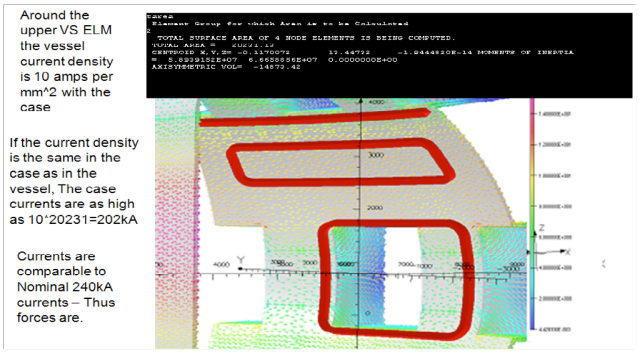

Disruption Inductively Driven Electromagnetic Loads

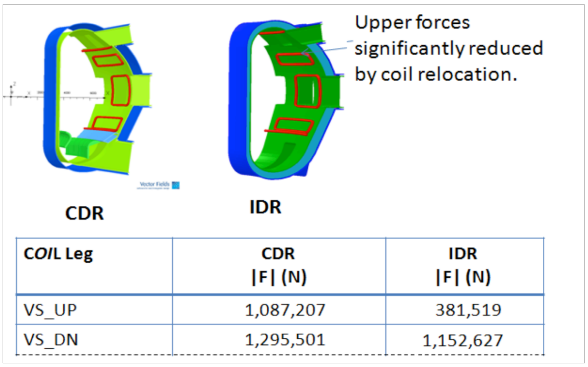

COIL Leg	CDR |F| (N)	IDR |F| (N)
VS_UP	1,087,207	381,519
VS_DN	1,295,501	1,152,627

Electromagnetic Loads VSFORCE= 1.1526e6**.5
Some Analyses Still Use the Previous 2 MN in Each Direction

```
/solu
bfe,all,temp,1,380  !100C
esel,real,11,14  $nelem
bfe,all,temp,1,400  ! Conductors 20C hotter
Nall $eall
Solve  $save
/title, Disruption + Normal Operating Loads 2e6/40deg
esel,mat,1  $nelem
f,all,fz,vsforce/4/46656 ! there are 29160 nodes in the
conductors and 2e6 is for 40 degrees
f,all,fx,-vsforce/4/46656
Nall  $eall
Solve  $save
```

```
/title, Disruption + Normal Operating Loads  +Nuclear
ldread,temp,last,,,,therm,rth
Nall  $eall
Solve  $save
/title, Lorentz+Shared Ves Disrup Current + Normal
Operating Loads 2*2e6/40deg
esel,mat,2  $nelem
f,all,fz,2*vsforce/4/52486
f,all,fx,-2*vsforce/4/52586
Nall  $eall
Solve  $save
Fini  $/exit
```

Figure 8-48 Lorentz Load Application

8.1.2.10 Results

Clamp Bolt Stress

With adequate preload (400 MPa), the bolt alternating stress is low. An EXCEL spreadsheet force and moment sum was performed and loads were resolved to the bolts. Results consistent with the finite element model were obtained.

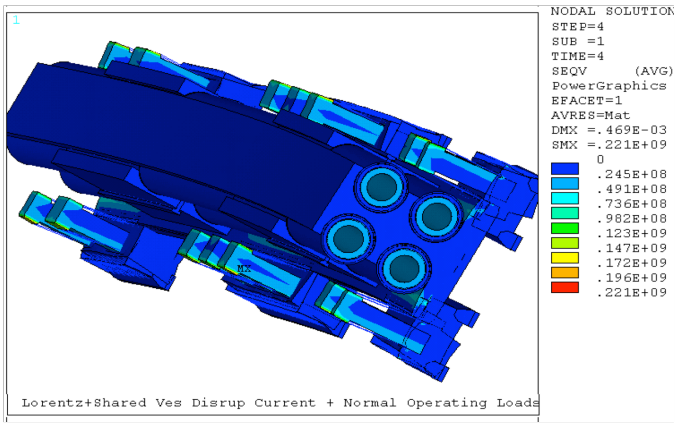

PDR Model Response, With Shared Vessel Currents
Lower Bolt Preload is Required

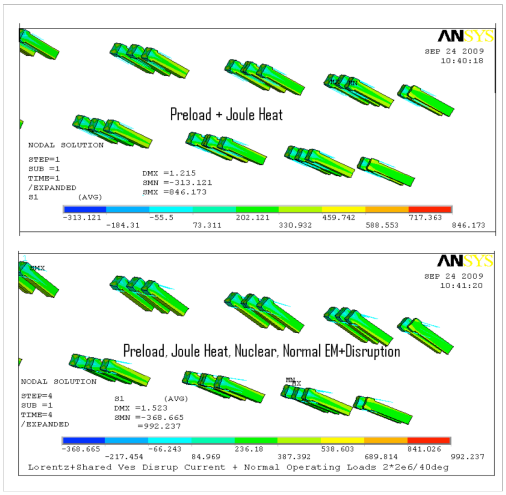

CDR Model Response, With Shared Vessel Currents

Clamp Bolt Stress

Poloidal Force Per 40 degrees sector	2.00E+06	N
Radial Force Per 40 degrees sector	2.00E+06	N
Poloidal Force Per 10 degrees sector	5.00E+05	N
Normal Force Per 10 degrees sector	5.00E+05	N
NumBolts per 10 degree Sector	12	
Conductor Centroid Height From Flange	90	mm
Case Base Width	175	mm
Diameter of Bolt	25	mm
Fing contact to Bolt CL	25	mm
Fing Contact to Clamp Edge	47	mm
Clamp Force Due to Normal Load per Bolt	4.17E+04	N
Clamp Force Due to Poloidal Load per bolt	4.29E+04	N
Total Clamp Force	8.45E+04	
Clamp Calculations		
Prying Moment	3.97E+06	N-mm
Bolt Load	180573.6	N
Bolt area	490.875	mm^2
Bolt Stress	367.8606	Mpa

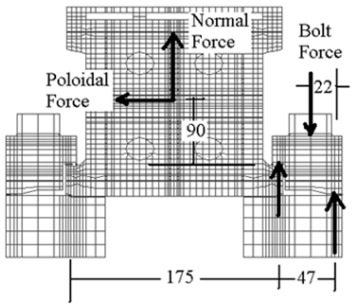

Comparable to FEA Results

Figure 8-49 EXCEL Verification of Clamp Bolt Stress

Support Spine Stress

With the full current inventory (1.2MN/40deg) in conductors and spine, stresses in the spine are acceptable.

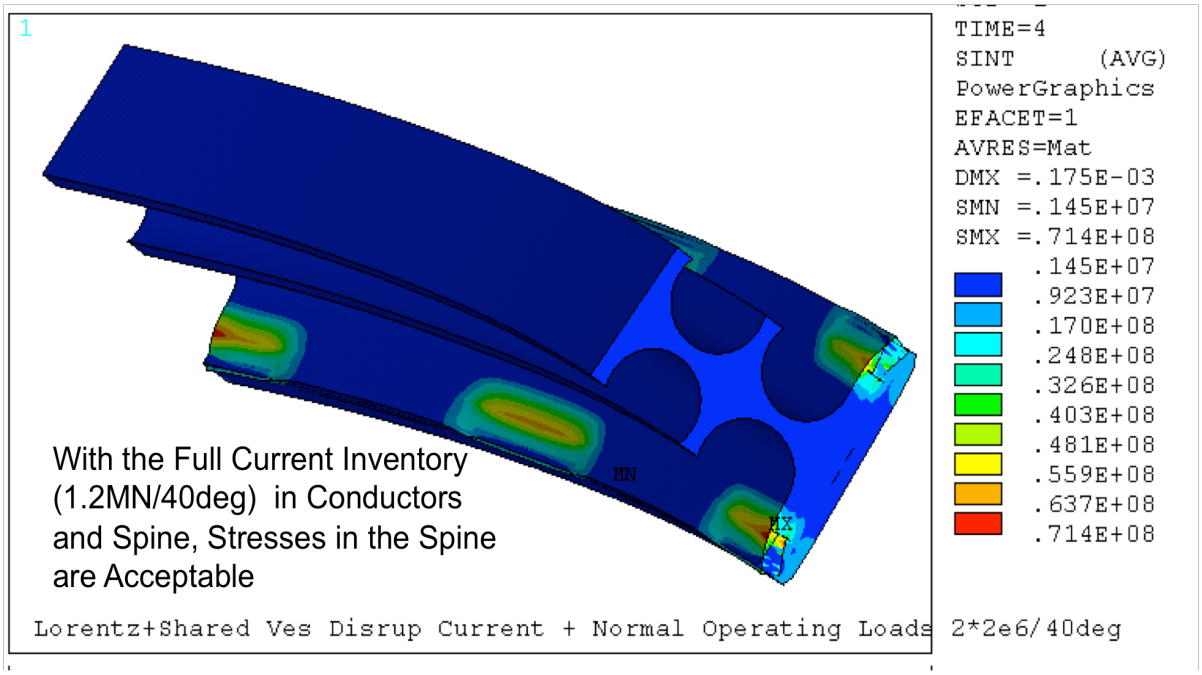

Figure 8-50 VS Spine Stresses

Conductor Stresses

The results shown in the figures are conductor stress for the CDR 2MN loading in each direction, with Joule heat and normal operating Lorentz loads. Tensile stresses are low and meet the static allowables for copper, and will be qualified by fatigue analysis

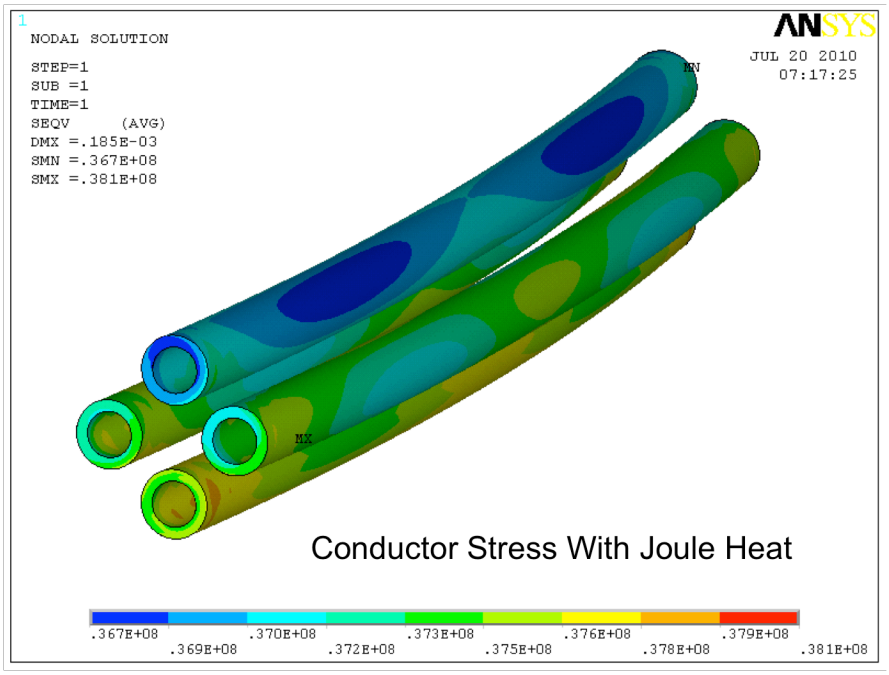

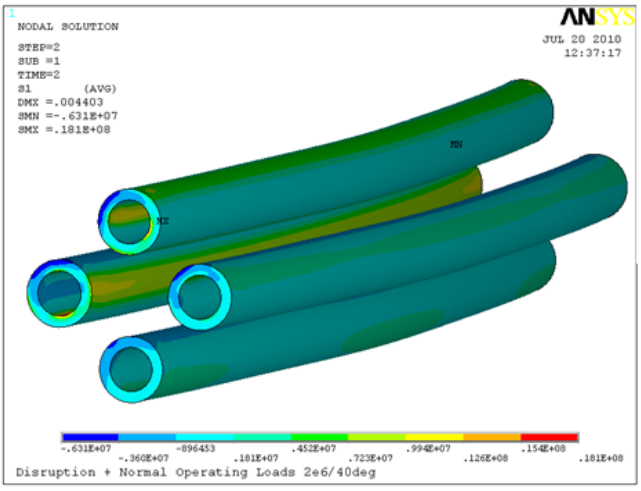

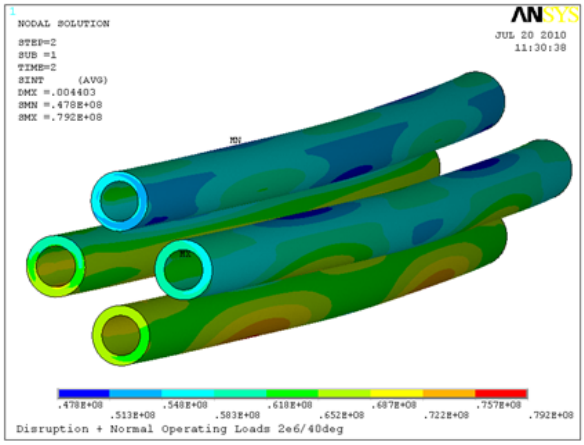

These Results are for the CDR 2MN Loading in Each Direction

Conductor Stress With Joule Heat and Normal Operating Lorentz Loads

Tensile Stresses are Low

Figure 8-51 Conductor Stresses

Weld Stresses at the Clamp Body

A more complete evaluation of the weld stress was done for the CDR. Loads have gone down, and the weld detail specified in the vessel PA is a full penetration weld vs. the bevel/fillet welds analyzed for the CDR. The peak weld stress of ~70 MPa tension is modest. It will provide some headroom for fatigue evaluations.

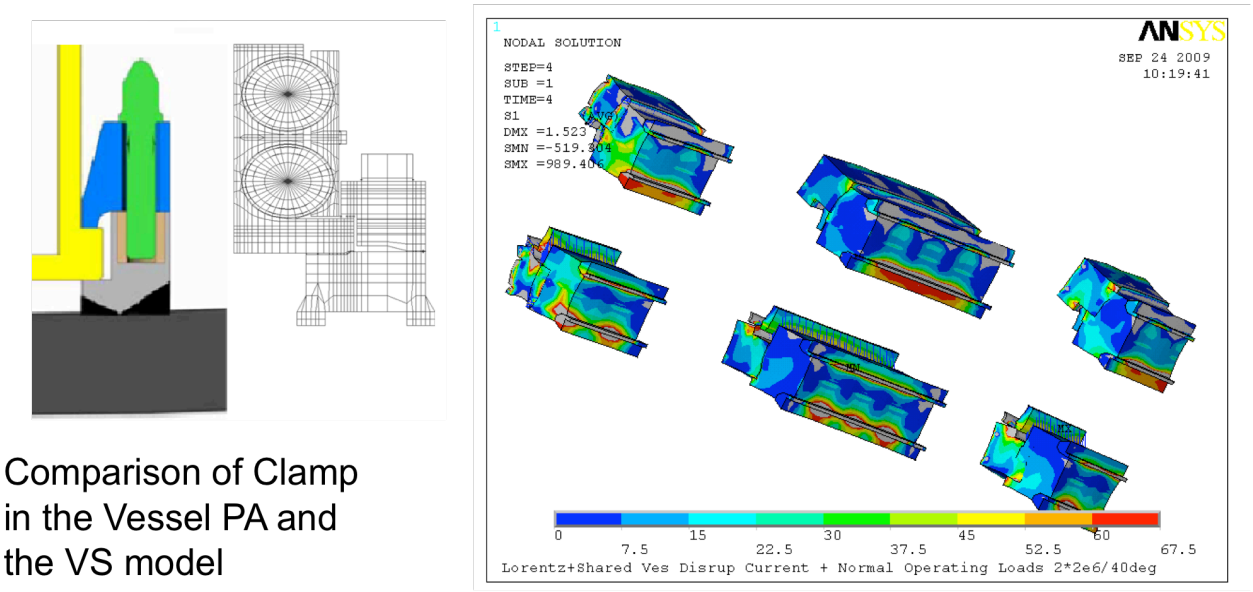

Figure 8-52 VS Clamp Modeling

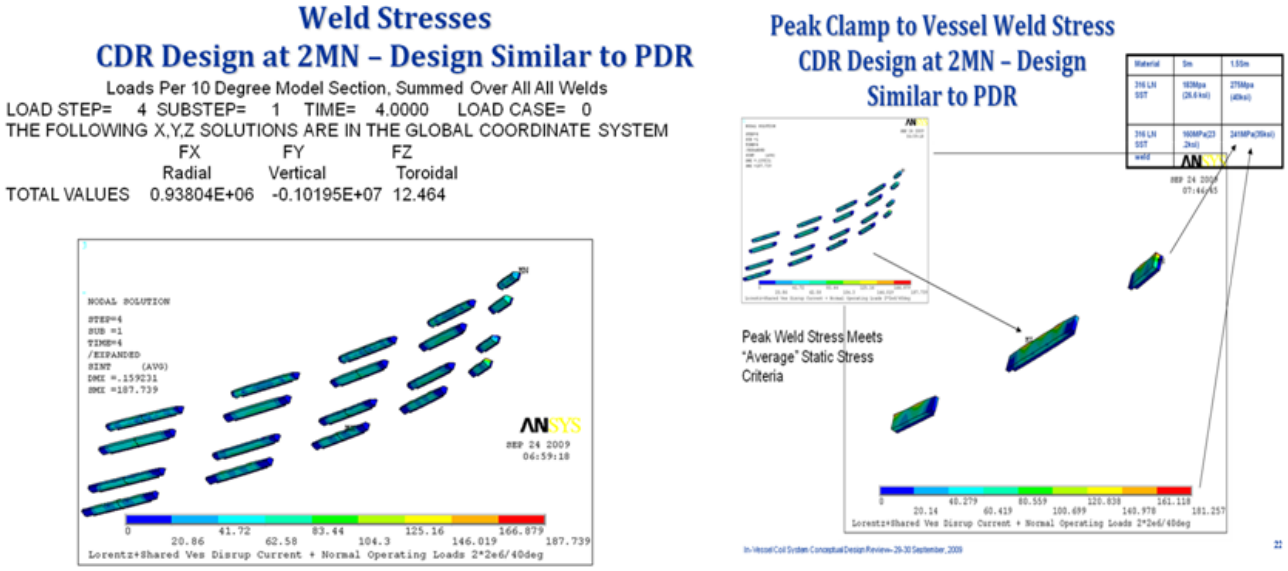

Figure 8-53 VS Clamp Weld Stresses

Break-outs and Leads

Each turn is independently connected to feeders and power supplies. This is shown schematically in Figure 3-19. Four break-outs, two with joggles to allow the turn to pass under the other turn/turns are needed for this configuration. These are shown in

Figure 8-. The bends required for the break-outs will be similar to the ELM corner configurations. Flexible supports have been developed for the ELM corners to provide thermal strain relief, but provide adequate support against the Lorentz Loads. The loads on the turns, as the current crosses the toroidal field, are oriented similarly as the loads on the ELMs. ELM support is progressing through a design optimization process and best solutions from this process will be applied to the VS coils.

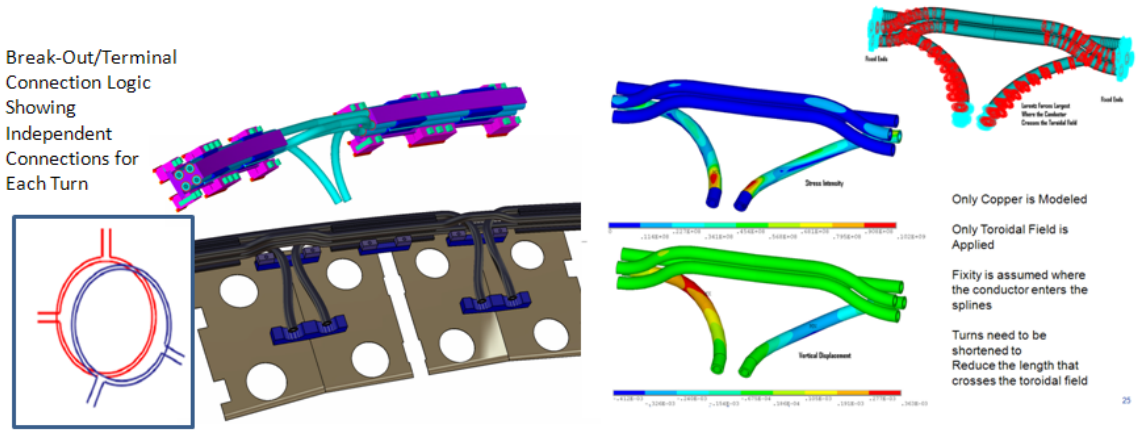

Figure 8-54 VS Individual Turn Lead Break-out Configuration

8.1.2.11 VS Feeders

As of the PDR, the feeders for the VS coils have not been analyzed. The mechanical design and analysis of these will be based on the work done to qualify the feeders for the ELM coils. Similar Lorentz forces and thermal loads will allow similar solutions as those used in the ELM feeder

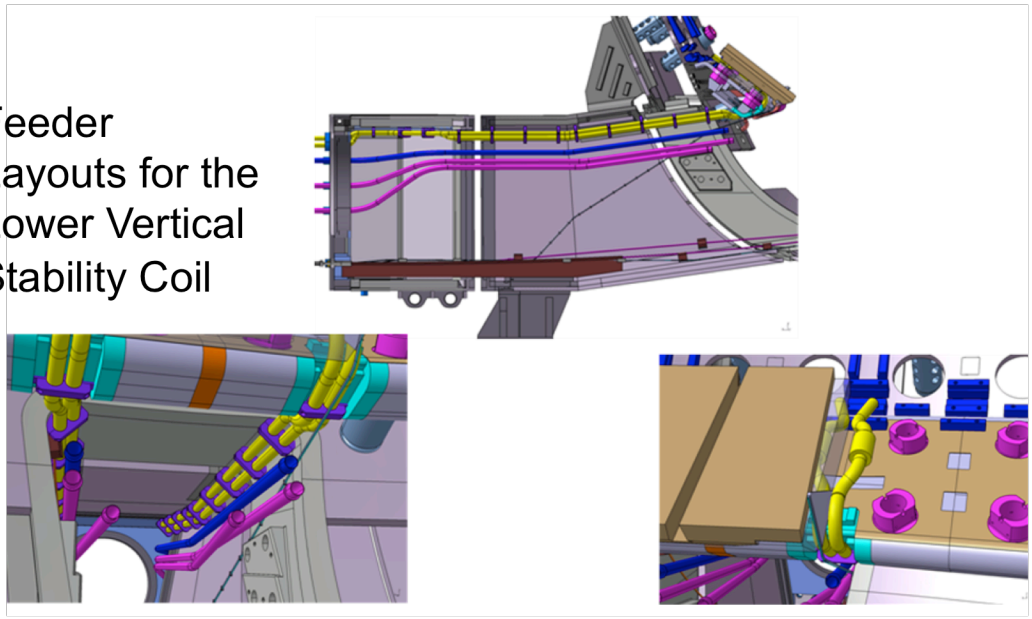

Figure 8-55 VS Feeders

8.1.2.12 Faulted Turn, Loss of Cooling Capability

The VS coils are intended to operate with one turn out and the other turns providing full amp-turns. This accounts for the Joule heat removal, but not the conduction of the nuclear heat to the vessel, or the coolant in the remaining operable coils. This analysis needs to be done. In the extreme case of complete loss of function of the coils, if ITER can operate without the vertical stability coils, the coils would be "abandoned-in-place" under these circumstances, the nuclear heat inventory must be removed via conduction or radiation. In figure _ only radiation heat removal is assumed to occur. The resulting temperatures are shown for different pulse lengths and for a few consecutive pulses up to what appears close to thermal equilibrium. For a 1500 second full power pulse length, the temperature is 1050K or 780C

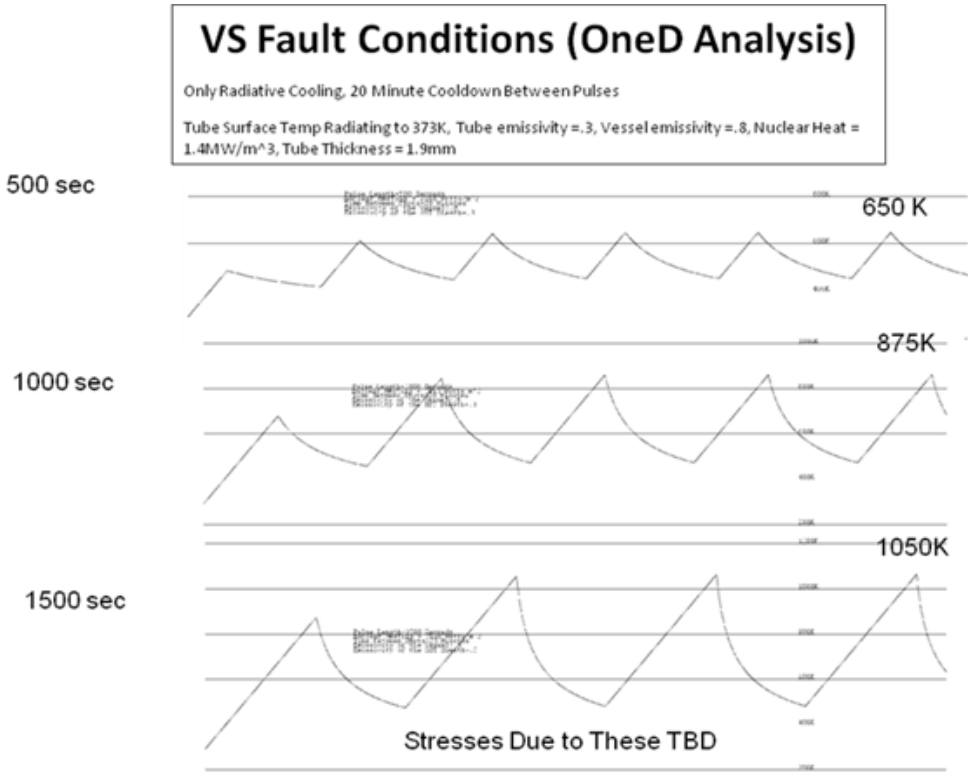

Figure 8-56 VS Coil Temperature with Abandoned, Un-cooled Turns

8.2 FATIGUE CONSIDERATIONS

The design of the VS and ELM coils for ITER[79] requires a fatigue analysis. This section reviews the material properties and applied loads, and gives estimated life for both VS and ELM coils during operation based on logical assumptions.

8.2.1 Fatigue life estimation of VS coils

8.2.1.1 Material properties[80,81]

The VS coils are designed to be made of pure copper. It's chemical composition and mechanical properties are listed in Table 8-7 through Table 8-9.

Table 8-7 General composition of pure copper

	Nominal composition (%)	**Remarks**
C10100	99.99 Cu	Oxygen-free-electronic
C10200	99.95 Cu	Oxygen-free copper
C11000	99.96 Cu, 0.04 O	Electrolytic tough-pitch

[79] P. Titus, SOW, internal memo, PPPL, 2009.

[80] N.J. Simmon and R.P. Reed, "Cryogenic properties of copper and copper alloy," NBS, DOE, 1987.

[81] N.J. Simmon, E.S. Drexier, and R.P. Reed, "Properties of copper and copper alloys at cryogenic temperature," NIST Monograph 177, 1992.

Table 8-8 Mechanical properties of pure copper

	Tensile (ksi) (MPa)	**Yield (ksi) (MPa)**	**Elongation (%)**
C10100	32-66 (221 – 455)	10-53 (69 – 365)	55-4
C10200			55-4
C11000			55-4

Note: depending on cold work, grain size, temperature etc.

Table 8-9 Fracture properties of pure copper at room temperature

Fatigue initiation (stress controlled axial fatigue)	Annealed copper $\sigma_{max}(MPa) = 271 \cdot N^{-0.074}$ @R=-1 Endurance limit is no less than 50MPa
Fatigue crack propagation (stress controlled high cyclic fatigue)	Paris parameter: C=1.32e-11 m/cycles, m=3.54 @R=0; Fracture toughness is no less than $K_{1c} = 150MPa\sqrt{m}$; Walker's coef: 0.8.

8.2.1.2 Total fatigue life estimation

The maximum principal stresses of VS coil are listed in Table 8-10 and Table 8-11 for one with thermal load and one without thermal load respectively. The case without thermal loads is more conservative, and is therefore considered in the following analysis.

Table 8-10 Max principal stresses with thermal compressive load[82]

	Max during one cycle (MPa)	**Min during one cycle (MPa)**	**Number of cycle per machine cycle**
Peak 1	-38 + 50	-38 - 50	3
Peak 2	-38 + 2.5	-38 – 2.5	33.8 x 1500

Note: Maximum operation temperature 120C

Table 8-11 Max principal stresses without thermal compressive load[83]

	Max during one cycle (MPa)	**Min during one cycle (MPa)**	**Number of cycle per machine cycle**
Peak 1	50	- 50	3
Peak 2	2.5	– 2.5	33.8 x 1500

Note: Maximum operation temperature 120C

The second peak stress is much less than the 1st stress peak as well as the endurance limit, therefore, its impact on the fatigue damage is negligible. The total fatigue life is dominated by the 1st stress peak. However, the 1st peak stress is around the endurance limit. For conservative consideration, the Coffin-Manson equation is applied to give the total fatigue life in machine cycle as 2.77e9, also much greater than the designed life 30,000 multiplied by safety factor 20, as listed in Table 8-12.

[82] P. Titus, private communication, PPPL, July 2010

[83] Ibid

Table 8-12 The equivalent full reversal fatigue stress and total fatigue life

	Amplitude (MPa)	**Fatigue life in stress cycle**	**Fatigue life in machine cycle**
Peak 1	50	8.3e9	2.77e9
Peak 2	2.5	infinite	infinite

Note: the designed machine life is 30,000 cycles

8.2.1.3 Crack propagation life

The following assumptions are made for the fatigue crack growth life estimation:

a. An elliptical sub-surface crack of aspect ratio 0.1 (equivalent surface crack of aspect ratio of 0.2) exists in the copper coil, with initial crack sizes of 0.25, 0.5, 0.75, 1.5. 3 and 4 mm^2 respectively.

b. The safety factor adopted during simulation is as follows: 2 for crack size, 1.5 for fracture toughness, and 2 for crack growth life.

c. The effect of higher temperature and radiation are included in the safety factor.

d. Any residual tension is removed by annealing.

e. The coil geometry data are: wall thickness 7.5mm, width 50mm.

The crack growth is controlled by maximum tensile principal stress, and the compression part plays no role in the crack growth except in the notch tip. The applied maximum tensile principal stress is listed in Table 8-13.

Table 8-13 Max principal stresses of VS without thermal loads [84]

	Max during one cycle (MPa)	**Min during one cycle (MPa)**	**Number of cycle per machine cycle**
Peak 1	50	< 0	3
Peak 2	2.5	< 0	33.8 x 1500

The crack growth life is obtained by the integration of Paris law, and the results are listed in Table 8-14, and shown in Figure 8-, in which the life due to combined stress is estimated by Miner's rule. It is found that the stress peak 1 is the major driver of the fatigue crack growth while the stress peak 2 is the minor. The fatigue crack growth life is greater than 60,000 machine cycles (factor 2 on the designed life) for any crack size less than 23 mm^2 (i.e., 1.7 mm in depth)

Table 8-14 Results of fatigue crack growth life

σ_{max} **(MPa)**	**Initial crack size (mm^2)**						
	20	**25**	**30**	**35**	**40**	**45**	**50**
50	3.20E+05	2.22E+05	1.59E+05	1.15E+05	8.46E+04	6.24E+04	4.62E+04
2.5	1.30E+10	9.15E+09	6.48E+09	4.66E+09	3.43E+09	2.52E+09	1.86E+09
Combined	7.53E+04	5.25E+04	3.75E+04	2.71E+04	1.99E+04	1.47E+04	1.08E+04

Note: the designed machine life is 30,000 cycles

[84] P. Titus, private communication, PPPL, July 2010.

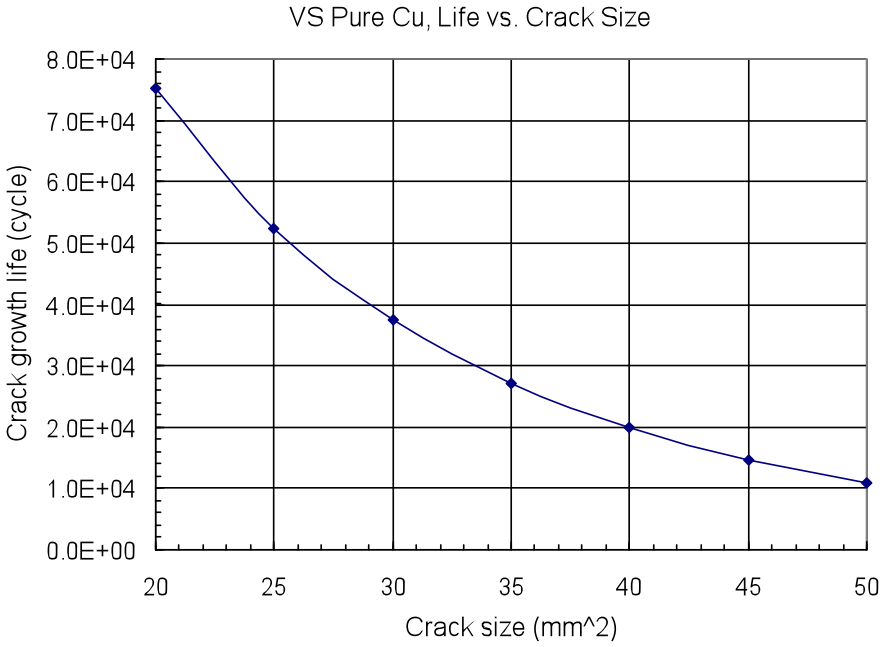

Figure 8-57 Crack growth life as a function of initial crack size

8.2.1.4 Conclusions

a. The total fatigue life of VS coil without thermal compressive loads is controlled by the 1st stress peak. The estimated total fatigue life by S-N curve is 2.77e9 machine cycles, much greater than the design life 30,000 multiplied by a safety factor 20 since the applied stress is around the endurance limits.

b. The fatigue crack growth life of VS coil without thermal compressive loads is controlled principally by the 1st peak stress. The stress peak 2 is the minor. The simulation results indicate that with any visible crack up to ~1.7 mm in depth (or crack area ~23 mm^2), the life is greater than the designed life of 30,000 multiplied by a safety factor 2.

8.2.2 Fatigue life estimation of ELM coils

8.2.2.1 Material[85]

The ELM coils are designed to be made of CuCrZr (C18150). The mechanical properties are listed in Table 8-15 through Table 8-20.

Table 8-15 Tensile Properties (average)

Material	Yield strength (MPa)	UTS (MPa)	Elongation (%)
Low strength (L)	78	248	
Intermediate strength (I)	199.4	318.6	
High strength (H)	297	405.3	
HIP heat treated CuCrZr		291	24
CuCrZr SAA	310	443	30
CuCrZr SCA	214	304	15
Elbrodur N	370		

[85] J. Feng, "Update – mechanical properties of CuCrZr alloy," internal memo, ITER-USMIT-FENG-111809-01, PSFC, MIT, Nov. 2009.

Table 8-16 Elastic modulus by assuming double slope tensile curve

Material	**E_1 (GPa)**	**$E_2 = \frac{\sigma_U - \sigma_y}{\delta_u - \frac{\sigma_y}{E_1}}$ (MPa)**
Low strength (L)	112	853
Intermediate strength (I)	112	601
High strength (H)	112	549
HIP heat treated CuCrZr	118	800

Table 8-17 S-N data (strain based): $\Delta\varepsilon = A + BN^C$

Material	**A (%)**	**B (%)**	**C**
Low strength	0.29851	103.51	-0.63213
Intermediate strength	0.2631	29.31	-0.48191
High strength	0.3183	25.48	-0.47403

Table 8-18 Endurance limit

Material	**Endurance (MPa) (%)**
Low strength (L)	~ 74 (0.2985)
Intermediate strength (I)	~ 96 (0.2631)
High strength (H)	~ 122 (0.3183)

Table 8-19 Paris parameters

Material	***C (m/cycle)***	***m***
HIP heat treated CuCrZr	6.08e-12	3.39
Non heat treated CuCrZr	6.12e-11	2.46

Walker's coefficient: 0.8.

Table 8-20 Estimated fracture toughness at room temperature

Materials	J_{1c} (kJ/m^2)	K_{1c} $(MPa\sqrt{m})$
SCA, SAA	>200	171 (~150 at 100^0C)
Elbrodur N, TL	108	112
Elbrodur N, LT	180	145

8.2.2.2 Total fatigue life

Tresca stress is the controlling factor to determine fatigue initiation life. The Tresca stress is listed in Table 8-21 for the ELM coils.

Table 8-21 Tresca stresses cycle of ELM [86]

	Max during one cycle (MPa)	**Min during one cycle (MPa)**	**Number of cycle per machine shot**
Peak 1 (thermal)	31.5	0	1
Peak 2 (thermal + Lorentz)	56	31	1500x5

Note: the maximum operation temperature is 100-150C

The equivalent reversal stress is estimated by Goodman relation, as listed in Table 8-22 for the stress peak 1 and peak 2 respectively.

Table 8-22 The equivalent full reversal fatigue stress

	Peak 1 (MPa)	**Peak 2 (Mpa)**
Low strength	16.8	15.2
Intermediate strength	16.6	14.5
High strength	16.4	14

[86] L. Bryant, private communication, PPPL, Sep. 2010.

It is found that, for all of the 3 different strength copper alloys, the stress equivalent is much less than the endurance limits. Therefore, the fatigue life due to crack initiation satisfies the required life of 600,000 machine cycles, factor 20 on designed machine cycle.

8.2.2.3 Crack propagation life

The following assumptions are made for the fatigue crack growth life estimation:

a. An elliptical sub-surface crack of aspect ratio 0.1 (equivalent surface crack of aspect ratio of 0.2) exists in the copper coil, with initial crack sizes of 0.25, 0.5, 0.75, 1.5. 3 and 4 mm^2 respectively.

b. The safety factor adopted during simulation is as the following: 2 for crack size, 1.5 for fracture toughness, and 2 for crack growth life.

c. The effect of higher temperature and radiation are included in the safety factor.

d. Any residual tension is removed by annealing.

e. The coil geometry data are: wall thickness 8.35mm, width 50mm.

The maximum principal stress is the controlling factor for crack propagation life. It is listed in Table 8-23 for the ELM coils.

Table 8-23 Max principal stresses cycle of ELM [87]

	Max during one cycle (MPa)	**Min during one cycle (MPa)**	**Number of cycle per machine shot**
Peak 1 (thermal)	17	0	1
Peak 2 (thermal + Lorentz)	56.8	24.8	1500x5

Note: Maximum operation temperature 100 – 150C

The life for single 1st stress and single 2nd stress as a function of initial crack size can be obtained by the integration of Paris law for the two different CuCrZr alloys, as listed in the first rows and 2nd rows of Tables 8-18 and 8-19. The combined life number is obtained by Miner's rule, and listed in the 3rd rows of the tables.

Table 8-24 Fatigue crack growth life for ELM coils made of HIP heat treated CuCrZr

Stress No.	**Initial crack size (mm^2)**				
	0.25	0.75	1	2	3
1	1.e9	5.81e8	4.97e8	3.33e8	2.56e8
2	7.84e7	4.63e7	3.97e7	2.65e7	2.04e7
Combined	1.05e4	6170	5290	3530	2720

[87] Ibid

Table 8-25 Fatigue crack growth life for ELM coils made of Non-heat-treated CuCrZr

Stress No.	Initial crack size (mm^2)				
	0.25	0.75	1	2	3
1	8.72e7	6.19e7	5.59e7	4.24e7	3.52e7
2	1.39e7	9.85e6	8.89e6	6.74e6	5.59e6
Combined	1853	1313	1185	899	745

It is found that, for any visible surface cracks investigated, the fatigue crack growth life does not satisfy the designed machine cycle of 30,000 multiplied by a safety factor 2. The key issue is that the stress peak 2 with 7500 cycles per machine shot is a controlling factor, and limits all over machine life. Therefore, the allowable peak 2 stress amplitude is estimated in the following section.

8.2.2.4 Allowable 2nd stress peak

Table 8-26 lists the applied principal stress range for the 1st stress (thermal) and the average mean stress for the 2nd (Lorentz).

Table 8-26 Max principal stress on ELM coil

Applied stress No.	Applied stress range (MPa)	Stress cycle per machine shot
1	0-17	1
2	Mean 40.8	1500 x 5

The life for single 1st stress as a function of initial crack size can be obtained by the integration of Paris law for the two different CuCrZr alloys, as listed in the first rows of Tables 8-21 and 8-22.

The combined life number is the designed life 30,000 multiplied by safety factor 2. Therefore, the allowed life number due to the 2nd stress can be obtained by Miner's rule, and listed in the 2nd row of Table 8-27 and Table 8-28.

Table 8-27 Fatigue crack growth life for ELM coils made of HIP heat treated CuCrZr

Stress No.	**Initial crack size (mm^2)**				
	0.25	0.75	1	2	3
1	1.e9	5.81e8	4.97e8	3.33e8	2.56e8
2	450027e3	450046e3	450054e3	450081e3	450105e3
Combined	60,000	60,000	60,000	60,000	60,000

Table 8-28 Fatigue crack growth life for ELM coils made of Non heat treated CuCrZr

Stress No.	**Initial crack size (mm^2)**				
	0.25	0.75	1	2	3
1	8.72e7	6.19e7	5.59e7	4.24e7	3.52e7
2	450310e3	450437e3	450484e3	450638e3	450768e3
Combined	60,000	60,000	60,000	60,000	60,000

The allowable 2nd stress amplitude for ELM coils is again calculated by Paris law integration for the two different CuCrZr alloys respectively, as shown in Table 8-29 and Figure 8-.

Table 8-29 Allowable stress amplitude for ELM coils made of HIP (mean =40.8 MPa)

Materials	**Initial crack size (mm^2)**				
	0.25	0.75	1	2	3
HIP heat treated CuCrZr	8.71	7.21	6.83	5.91	5.38
Non heat treated CuCrZr	2.91	2.45	2.33	2.03	1.85

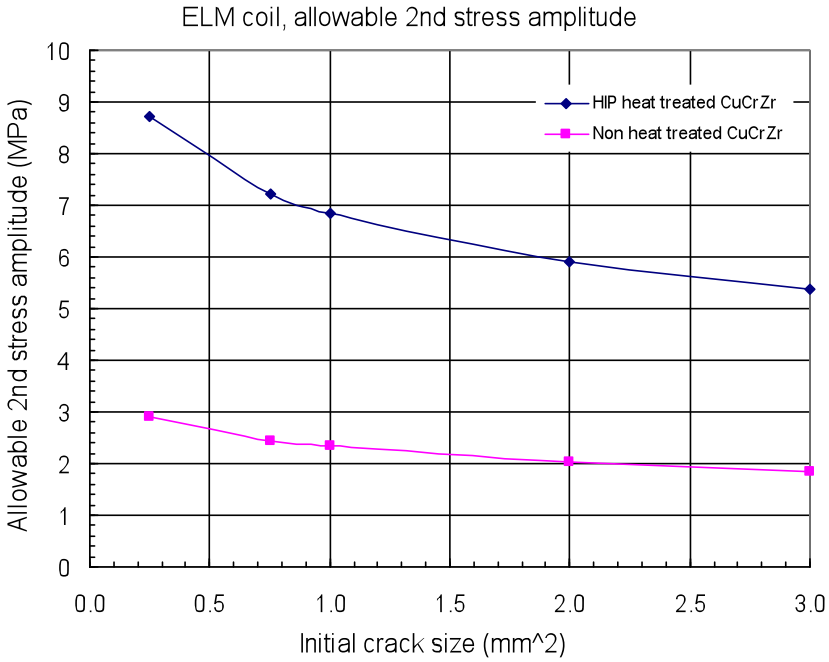

Figure 8-58 Allowable 2nd stress amplitude vs. initial crack size for ELM coil.

Conclusions

a. The ELM coil fatigue life is controlled by fatigue crack growth.

b. The 2nd stress has significant impact on the fatigue life due to its high cycle number in each plasma shot.

c. The material process and property of CuCrZr alloy have significant impact on the fatigue life.

9 SYSTEM PERFORMANCE

9.1 REMOTE HANDLING

9.1.1 Remote Handling Assessment

The previous EQ coil design included a coil casing which resulted in unacceptably small clearance within the equatorial port to allow a confident transfer into the vessel. The revised design with MI coils is smaller and has around 20-30mm clearance all around relative to the port. Whilst this is less than ideal, it should be feasible to handle the coil through the port.

The IVT cannot be deployed until the coil has been transferred to the vessel and temporarily supported on the inner wall. According to another OTL study, the use of the IVT to maneuver and install the coil in-vessel requires the deployment of the IVT rail to at least 40° past the installation location. This will inhibit the use of the MPD during the IVT operations. The IVT will need to be withdrawn after each coil installation and then redeployed to remove the End-Effector Sub-Frame from the coil.

The connection of the coils is a complex operation. The design of the joint using copper welding or brazing is not a reversible RH process. A design which segregates a bolted conductor and a welded stainless steel water pipe is favored by OTL and IO RH experts.

Further studies have demonstrated a method for installation of the coils that utilizes the MPD rather than the IVT. The alternative scenario of the ELM coil handling has been studied because the base scenario using the corporative operation of the IVT and MPD system will result in frequent exchanges of the RH equipment, which makes the operation inefficient and increases the risk.

The feasibility of the alternative scenario has been studied. Figure 9-1(a) shows the procedure to grip the ELM coil and temporary frame mounted on the hooks at the inner wall after the CMT mounted the ELM coil on the hooks. Figure 9-1(b) shows mounting procedure on

the equatorial port which is 20 degree away from the port that MPD is mounted on. The kinematic study for the sequence has been performed.

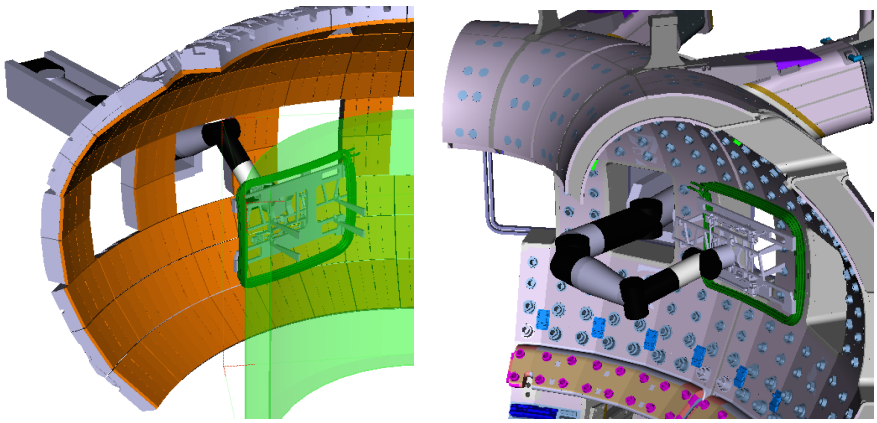

(a) (b)

Figure 9-1 Operation Sequence of the ELM Coil Handling by MPD

It has been identified that the operation for the ELM coils in the normal equatorial ports, and that in the RH port such as port #8, and #10 is different. Since the ELM coil encircles the RH port, it is impossible to remove the ELM coil at the RH port while the MPD system is located at the same port. In this case, additional equatorial port #10 has to be used for deploying the MPD system, and similar operation procedure can be used.

This alternative installation method will be compared with the proposed method to determine the most appropriate method for RH access to the ELM coils.

9.1.2 Recommendations from RH Assessment Report

- Reshape the EQ Coil connections to provide an increase in port clearance. Clearance >25mm should be achieved.
- Provide a hinged clamping system for coils and feeder that is captive to the vessel wall.
- Provide self aligning kinematic constraints to locate the coils.
- Provide wedges to provide adjustable lateral support to the coils.

- Develop a bridge connector that has bolted conductors and TIG welded stainless steel water pipe junctions.

9.2 FAILURE RECOVERY STRATEGIES

9.2.1 ELM Failure Recovery

Per the SRD the ELM coil is designed to remain in place, without water cooling, in case it suffers a fault which prevents its normal operation but does not preclude its remaining in place and exposed to the electromagnetic environment. An example would be a single ground fault caused by a water leak. In this case the coil could be drained and dried and abandoned in place with its terminals left open circuited to prevent induced currents. This is advantageous because it allows continuation of ITER operation without the need for an extended outage to remove nearby blanket shield modules and remove the fault coil, all via remote handling.

However, to take advantage of this capability it is necessary to operate ITER with a reduced ELM suppression capability. Various scenarios of single, double, and triple coil failures have been evaluated[88] in terms of the impact on ELM suppression. These scenarios are divided into two categories, namely static RMP conditions (RMP not rotating, constant current in each ELM coil) and rotating RMP conditions (rotating RMP, coil currents sinusoidal with $f \leq 5Hz$).

For single coil failures (27 possible cases) and static RMP there is no effect on the performance of the system because the toroidal phasing of the RMP can be set up such that zero current is demanded of the failed coil. For double coil failures (351 possible cases considering failures in the upper, equatorial, and lower ELM coils) and triple coil failures (2925 possible cases) and static RMP there are optimum choices for each specific failure pattern which minimize the impact on plasma operation. According to the underlying physics analysis ELM suppression at

[88] "Initial evaluation of limitations to ELM suppression in ITER associated with failure of ELM coils", A. Loarte and M. Schaffer, ITER_D_339RLD

15MA and rated B_t requires 75kA-turn capability in each ELM coil. To cover uncertainties a margin of 20% has been included in the requirement leading to a rating of 90kA-turn. Therefore, considering the probability of different combinations of two and three coil failures the impact on margin for ELM suppression is given in Figure 9-2. Similarly the level of plasma current obtainable while maintaining 20% margin is given in Figure 9-3.

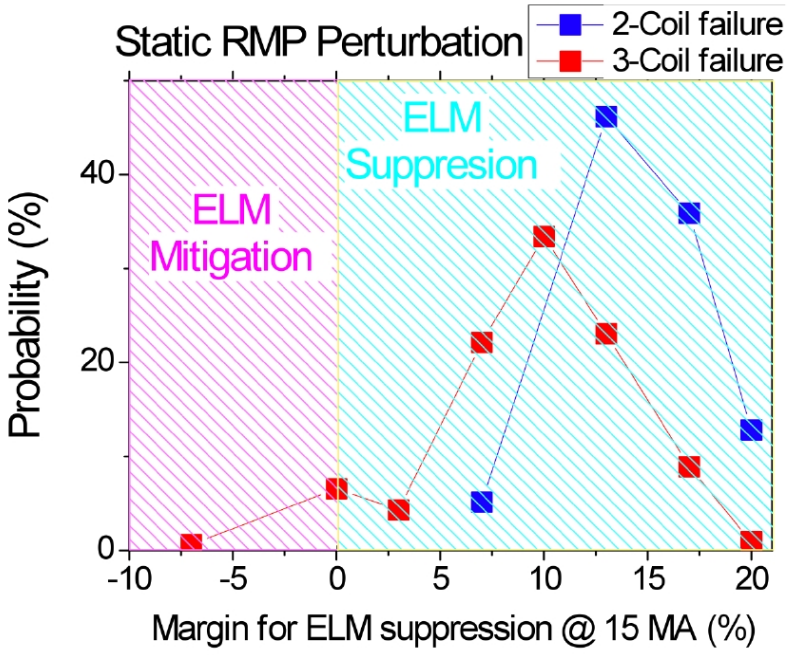

Figure 9-2 Probability Distribution of Margin for ELM Suppression at 15MA for 2-coil and 3-Coil Failure Scenarios for Static RMP

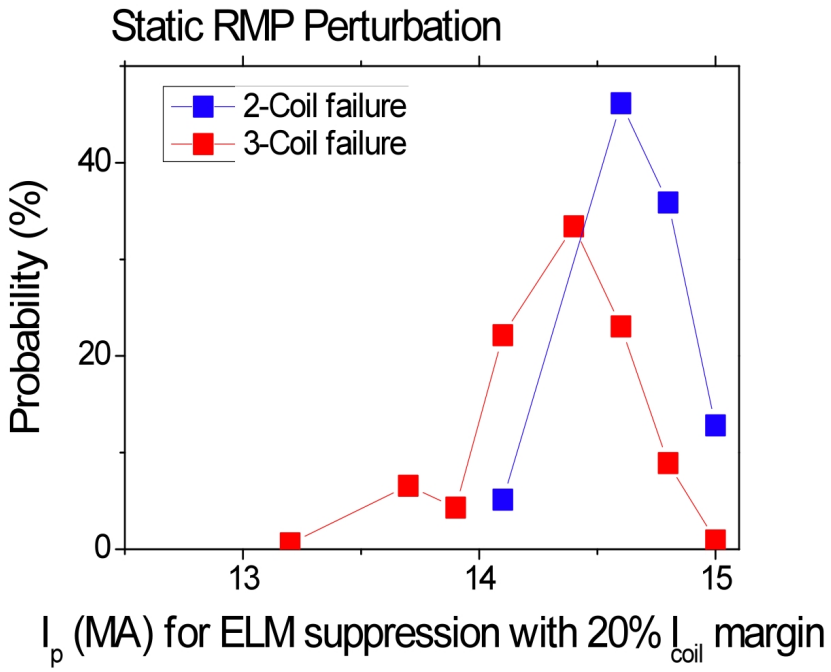

Figure 9-3 Probability Distribution of Ip Achievable with 20% Margin in ELM Suppression for 2-coil and 3-coil Failure Scenarios for Static RMP

For rotating RMPs the situation is more complex because the shortcoming in the magnetic field structure is periodic as the demand for current in the faulty coil(s) is periodic. Complete ELM suppression at 15MA cannot be achieved with rotating RMPs while maintaining the 20% margin but it can be achieved with less margin in some cases and still provide mitigation in others as indicated in Figure 9-4. Full ELM suppression with 20% margin can be achieved for rotating RMPs at reduced Ip for various failure scenarios as shown in Figure 9-5.

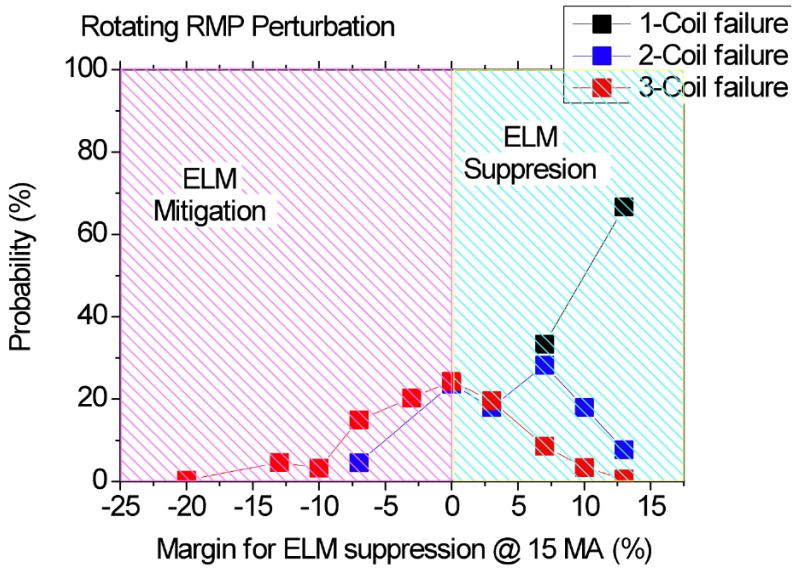

Figure 9-4 Probability Distribution of Margin for ELM Suppression at 15MA for 1-coil, 2-coil and 3-coil Failure Scenarios for Rotating RMP

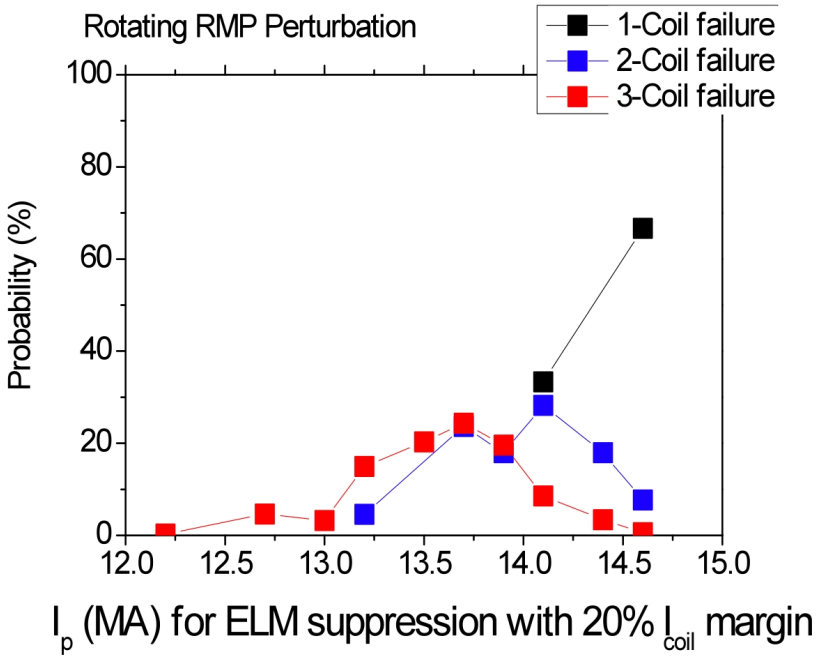

Figure 9-5 Probability Distribution of Ip Achievable with 20% Margin in ELM Suppression for 1-coil, 2-coil and 3-coil Failure Scenarios for Rotating RMP

9.2.2 VS Failure Recovery

As described in section 3.4, each VS individual turn of the 4-turn VS coil is routed outside of the vacuum vessel all the way to the power supply area. In the event of a faulted turn which can still withstand the electromagnetic environment (e.g. a coil with a single ground fault or multiple ground faults of sufficiently high impedance), it can be open circuited and the coil current can be bypassed around the faulty turn. There is ample margin in the remaining 3 turns to permit operation at full amp-turn rating. See the design point results in Appendix I where, for the VS coil, operating conditions with both 3 and 4 turns is given.

9.3 FMECA

The Failure Modes, Effects and Criticality Analysis (FMECA) methodology is not only a key component of the ITER Reliability, Availability, Maintainability and Inspectability (RAMI) Analysis Programme[89], but also a proven technique for identifying critical failure modes and proposing actions that will ultimately reduce project risk. Additionally, the results from the RAMI analyses are required as inputs to determine the RH Classification (see Figure 9-6) as described in the RH Compatibility Procedure[90]. This is very important for project planning since the development of RH tooling is tightly coupled with the specific RH classification.

89 "ITER RAMI Analysis Programme", ITER_D_28WBXD

90 "RH Compatibility Procedure", ITER_D_2NRTWR

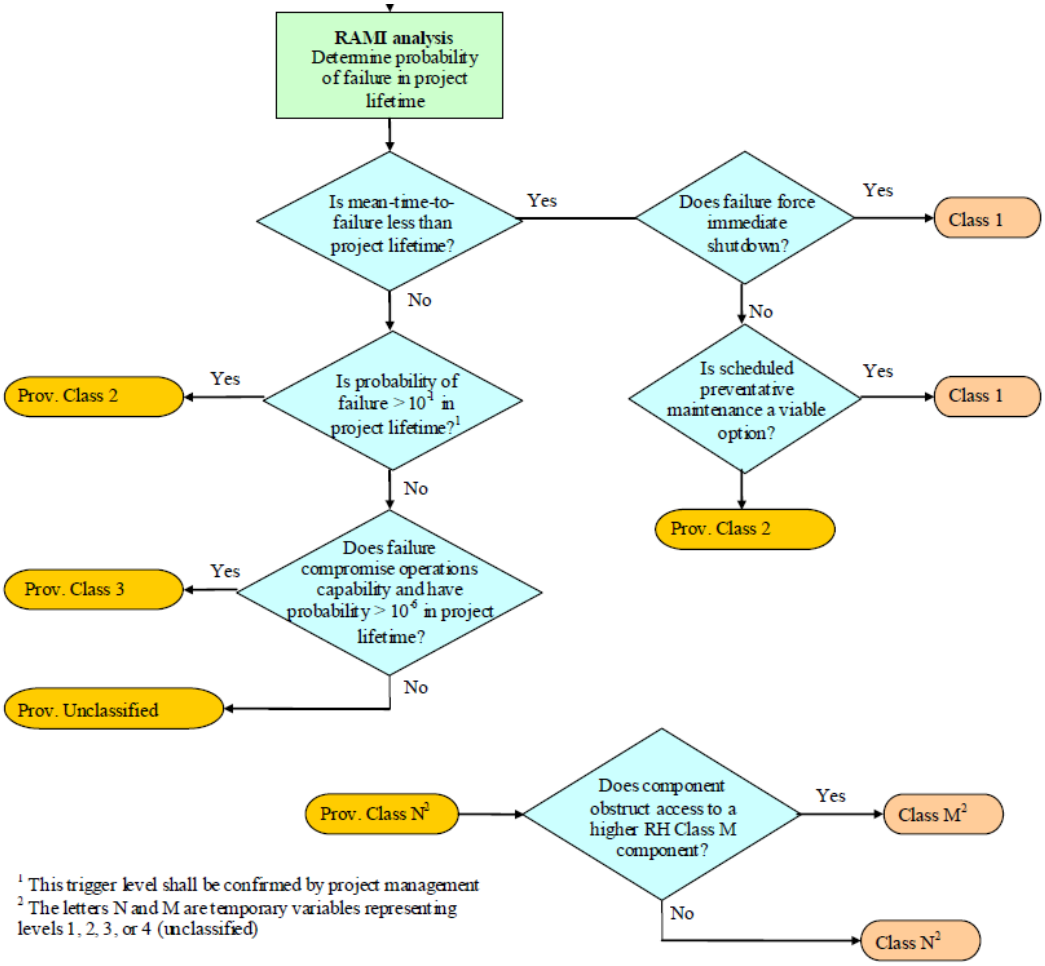

Figure 9-6 Decision Tree for RH Classification[91]

In accordance with ITER RAMI Analysis Program, a FMECA[92] was conducted for the three elements of PBS 15, namely the VV, In-vessel Coils and Blanket Manifolds. The in-depth study[93] identified 54 failure modes based on the functional model and determined applicable mitigation actions to reduce the risks, including two proposals for the ELM coils. The VS coils are not specifically mentioned in the FMECA, but it is expected that the failure modes and risk mitigations would be similar.

---

[91] "RH Compatibility Procedure", ITER_D_2NRTWR

[92] "Failure Modes, Effects and Criticality Analysis of Vacuum Vessel", ITER_D_2Y6V54, June 2009

[93] "WBS_15_Vacuum_Vessel_-_FMECA_EXCEL", ITER_D_2Y73WH

There were two causes of failure considered – a water leak from a coil into the VV interior and a failure of an individual ELM coil. The mitigation to reduce the criticality of the first failure consists of qualification testing for the non-structural elements such as manifolds and ELM coils to be performed to guarantee the reliability of these components. The mitigation to reduce the criticality of the second failure is to consider replacement of the faulted coil in a minimum time by retaining spares of each of the three coil types. The results of the FMECA classify the mitigated occurrence of risk to be less than 1 in 200 years, consistent with RH Class 3.

While these two primary causes were identified in conjunction with the VV FMECA, there are many possible modes of failure to be considered and characterized. Further detailed studies by Neumeyer[94] include a functional analysis, reliability block diagram and a detailed FMECA[95] for the entire In-Vessel Coil System. This work forms the basis of the input for a formal FMECA that will be conducted to verify the initial and expected ratings for the detailed listing of components including the coils, feeders, power supplies, bus bars and cooling water system.

Future plans include development of RAMI analysis through a formal framework contract using the FMECA as an input to confirm RH compatibility. This effort will be launched by January 2011 and expected to be completed by July 2011.

[94] C. Neumeyer, "FMECA for ITER In□VV Coils - *First attempt based on ELM Coils*", powerpoint presentation, December 2009
[95] C. Neumeyer, "FMECA for ITER In□VV Coils - *First attempt based on ELM Coils*", Excel File, December 2009

10 R&D RESULTS

10.1 PRELIMINARY TESTS

A series of mechanical and electrical tests were performed on commercially available 500 MCM copper jacketed solid copper conductors to gain an initial understanding of the behavior of mineral insulated cable. This cable has a measured jacket OD of 25.5 mm, a jacket wall thickness of 1.27 mm, solid copper core diameter of 19 mm, and a MgO insulation thickness of ~2 mm.

10.1.1 **Compressive modulus, E, determination for MgO**

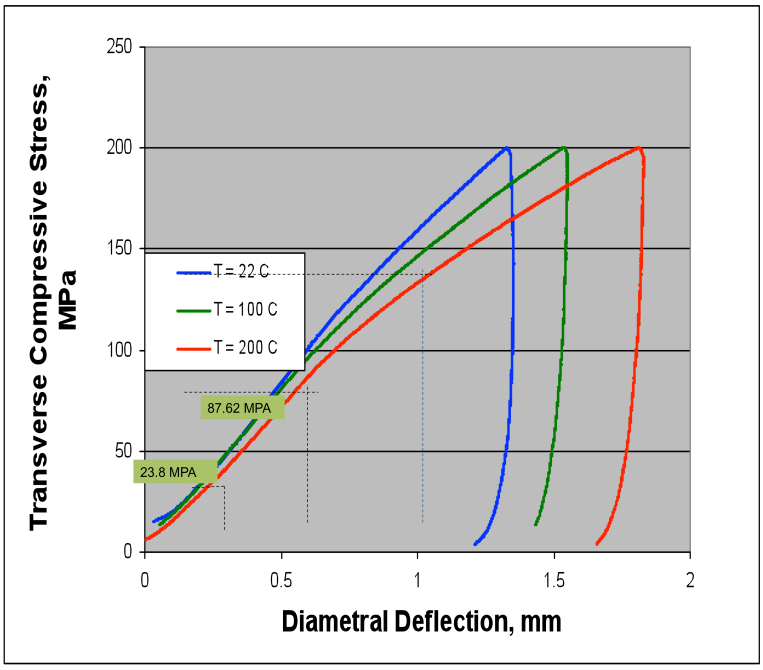

Figure10-1 Transverse Compression Test & Results

Calculation of the MgO E from test data

Find : Modulus of MgO

Given :

1.) Test Data from Compression Test and

2.) $E_{Cu} = 1.275E + 11$ Pa

3.) E_{MGO} = Unknown

Assume :

1.) Load is applied uniformly over projected area

2.) Loading is Linear Elastic

3.) Exclude Plastic or Buckled data

4) Apply a correction factor for the effective area likely participating in the transverse compression (Peter's ide

Solution :

$$\partial_T = \sum_{i=1}^{i=5} \frac{P}{A}\left(\frac{L_i}{E_i}\right) = 87.62\text{Mpa}\left(\frac{2(1.27X10^{-3}) + 19X10^{-3}}{1.275X10^{11}} + \frac{2(1.98X10^{-3})}{E_{MGO}}\right) = .5X10^{-3}\,\text{m}$$

$$E_{MGO} \approx \frac{2(1.98X10^{-3})}{\frac{.5X10^{-3}\,\text{m}}{(87.62\text{Mpa})} - \frac{2(1.27X10^{-3}) + 19X10^{-3}}{1.275X10^{11}}} = 715\text{Mpa}$$

$$E^*_{MGO} = E_{MGO}\frac{\text{A}_{\text{test}}}{\text{A}_{\text{copper}}} = 715e6\left(\frac{25.5}{19}\right) = 959.6\ \text{Mpa}$$

10.1.2 **Shear Modulus, G, Determination**

An axial shear test was performed to determine the shear modulus, G, of the magnesium oxide. In this test, the solid copper core of the sample is axially loaded with the OD of the cable supported in the test fixture, as shown in Figure 10-2 below. The load vs. displacement was plotted as a function of temperature. (see Figure 10-3)

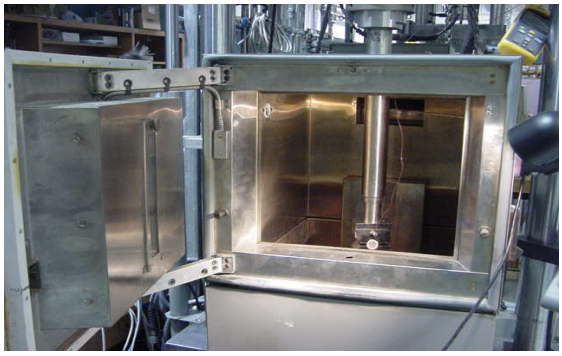

Specimen No.	Test Temp C	Max Shear Strength MPa	Total Disp at Max Shear mm
S-01	22	3.52	13.9
S-02	22	2.54	3.75
S-03	100	3.21	6.5
S-04	100	1.66	11.1
S-05	200	2.38	6.1
S-06	200	2.16	2.8

Figure 10-2. Shear Modulus Test Fixture and Data

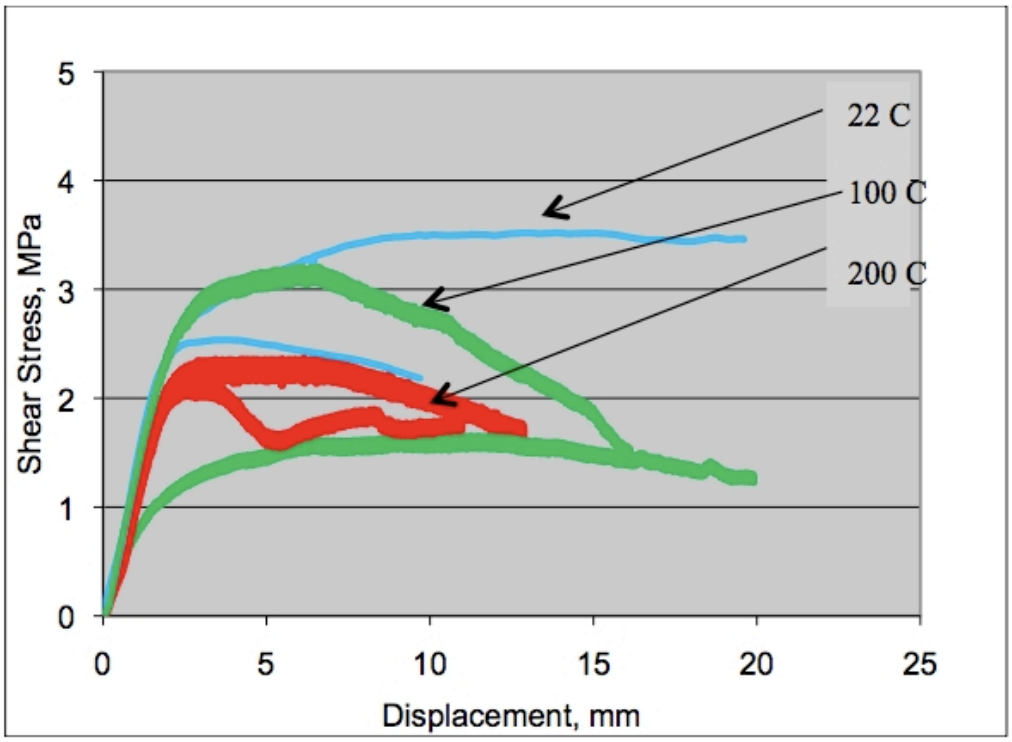

Figure 10-3 Shear Stress versus Displacement Plots

A shear modulus, G. of 2.54 MPa was calculated for the MgO insulation from this data.

10.1.3 **Cyclic loading of a bent sample**

A sample was bent 180 degrees around a 5" diameter pulley as shown in Fig. 10-4 (r/D ratio of 2.5 vs. a r/D ratio of >3 in the actual coils). A 34 kN load (representative of a thermal stress of ~33C) was applied for 30,000 cycles. The goal of this test was to determine if the electrical integrity of the insulation of a bent sample would be maintained after 30,000 fatigue cycles.

- Sample is bent 180° around a 5” minor diameter hardened steel pulley.
- Two ~ 200 mm long legs extend tangentially that are used for gripping.
- The outside sheath is stripped away and the 19 mm solid copper core is friction gripped.
- The sample is fatigue tested with an applied load of 34 kN for 30,000 cycles.
- Load vs displacement data is acquired for the first five cycles and then intermittently throughout the fatigue test to monitor the mechanical performance.

Figure 10-4 Cyclic Loading Test

The specimen is shown post-testing in Figures 10-5 and 10-6. Observations:

1. The conductors appear to survive the cyclic fatigue test well when judged by physical appearance. The samples look the same before and after testing.
2. Both samples exhibit an increase in stiffness as a function of number of fatigue cycles. This could be caused by compaction of the powder MgO insulation.
3. The load versus displacement curves shift along the positive x-axis as a function of the number of cycles, which is probably due to yielding of the ductile copper core.
4. Resistance of both samples at 250V with meg-ohm-meter (both, with and without 34 kN load applied) gave readings of approximately 1.5 G-ohm and showed no evidence of shorts.
5. Once back at PPPL, samples were cut and visually inspected. (see pictures below)

Figure 10-5 Bent Test Specimen

Figure 10-6 Cut Sections

10.1.4

lectrical Testing

A series of test specimens were fabricated and electrically tested in an oven at elevated temperatures from a 500 MCM cable length similar to the one used for the mechanical tests above. During these tests, the hygroscopic nature of MgO became obvious. Discussions with one of the full sized prototype suppliers indicated that it will be important for us to carefully specify the chemical purity of the MgO powder that will be used for production. They also cautioned that mechanical properties inferred from this commercially available cable will be significantly different than those that will be obtained from the full-scale SSMIC (Stainless Steel Mineral Insulated Cable). The full-scale prototypes will differ in materials; anneal cycles, and drawing operations – all of which could affect the mechanical and electrical properties of the compressed MgO. The electrical data presented below showed a great deal of scatter, most of which is likely due to incomplete drying of the MgO prior to testing. As a result, we have discontinued testing on the 500 MCM cable and plan to resume testing with the full-scale prototypes for which we will develop better drying procedures and end seals. The data is only presented as findings from these first initial tests, and is not indicative of the electrical performance of MgO SSMIC.

The first samples were cut from a long cable and most likely absorbed moisture while in the machine shop for several days as they were machined. The samples were baked out for 1-2 hours at 100° C prior to the application of high temperature epoxy and shrink sleeving. The electrical test results from this first batch, shown below, exhibit a great deal of scatter which is indicative of incomplete drying of the MgO.

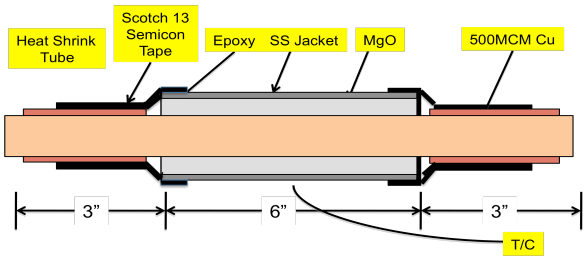

Figure 10-7 Electrical Test Specimens

Figure 10-8 Test Specimens in Oven

Table 10-1 Megger and PI Data at room and Elevated Temperatures

Date	8/3/2010	8/10/2010	8/10/2010	8/11/2010	8/11/2010
Temperature	100 C	20C	20C	128C	128 C
		Post Epoxy Seal @ Ends			
Sample No.	Bake out @ 100 C	Megger @ 500V	Megger @ 1,000V	PI @ 500V	Megger @ 500V
		Meg Ohm	Meg Ohm		Meg Ohm
					1 min / 10 min
1	1 hr	800	800	0.96	21.1 / 20.2
2	2 hr	>10K	>20K	0.87	707 / 612
3	2hr	>10K	>20K	0.98	298 / 292
4	2hr	500	560	1.05	103 / 108
5	2hr	>10K	>20K	1.05	216 / 226
6	2hr.	>10K	>20K	1.04	45.2 / 47.2

Table 10-2 Leakage Test Results (1000VDC @ 130C, Leakage Current @ 1 minute intervals)

Sample No.	0	1	2	3	4	5	6	7	8	9	10
1	12	12.2	12.3	12.4	12.5	12.8	12.9	13	13.1	13.2	13.4
2	1.7	1.73	1.73	1.73	1.75	1.77	1.79	1.81	1.83	1.85	1.88
3	3.9	3.92	3.98	4.1	4.2	4.26	4.3	4.35	4.38	4.39	4.36
4	11.8	11.8	11.8	11.8	11.8	11.8	11.8	11.8	11.8	11.7	11.8
5	2.6	2.44	2.44	2.45	2.45	2.46	2.47	2.47	2.48	2.48	2.48
6	23.5	22.3	22.3	22.9	23	22.9	22.8	22.8	22.6	22.6	20.1

A new batch of specimens, 12 inches long were fabricated. These were baked out at higher temperatures and longer durations, as indicated in the table below, and a high temperature epoxy was used to seal the ends against moisture absorption. The plots in Figure 10-9 show improved MgO insulation performance as a result of higher temperature bake-out for longer duration.

Table 10-3 Leakage Tests Data at various Temperatures

	Sample No.1	**Sample No.2**	**Sample No. 3**
Temperature (C)	Insul. Resistance Meg Ohms 2 hr bake @ 130 (C)	Insul. Resistance Meg Ohms 4 hr bake @ 200 (C)	Insul. Resistance Meg Ohms 4 hr bake @ 200 (C)
30	20,000	20,000	20,000
40	20,000	20,000	20,000
50	20,000	20,000	20,000
60	10,000	20,000	20,000
70	1,800	20,000	20,000
80	450	20,000	20,000
90		20,000	20,000
100		20,000	20,000
120		20,000	20,000
130		8,000	6,000
135		4,000	3,600
140		3,000	1,800
145		1,800	1,400
150		1,200	900
155		900	700
160		700	540

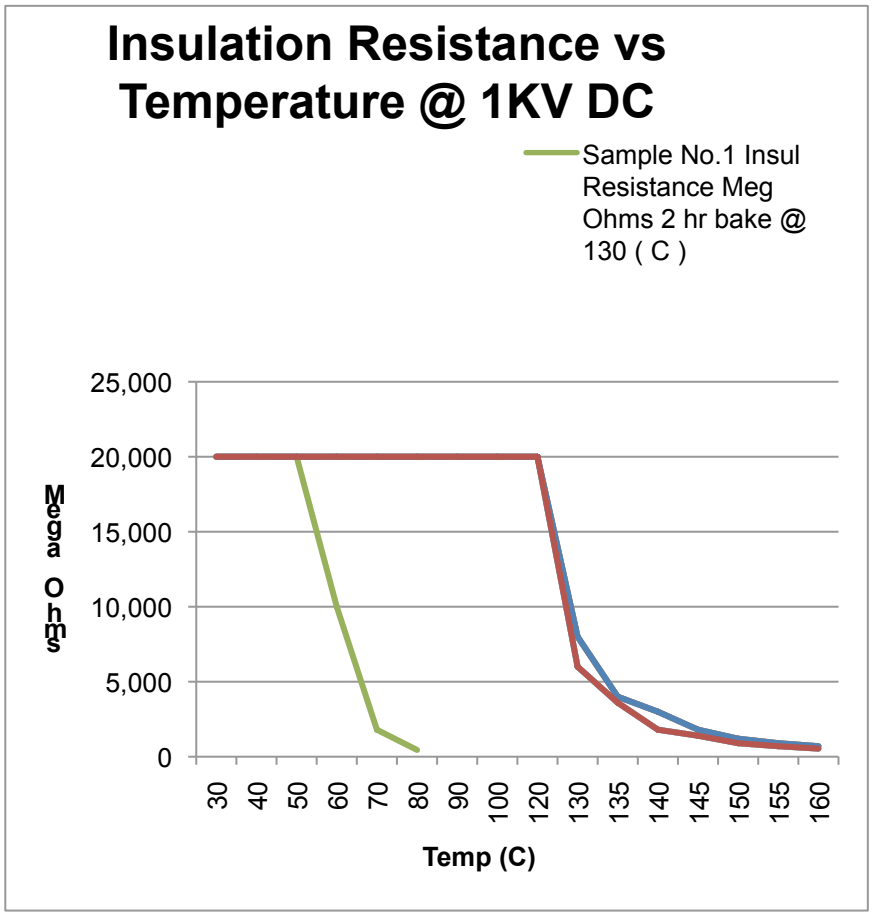

Figure 10-9 Insulation Resistance at versus Temperatures and Bake-Out Conditions

10.2 PROTOTYPE FABRICATION AND TESTING

Mineral insulated cable is routinely used for industrial (heating elements, fire resistant control wiring, etc.) and research applications (radiation resistant coils in high-energy physics, and magnetic pickup coils in fusion applications). However, the sizes needed for those applications

are considerably smaller than those required for the in vessel coils. For that reason, it was necessary to perform R&D prototype manufacturing studies to determine the feasibility of producing the SSMIC in the sizes required. Approximately full-size prototype lengths of the stainless steel jacketed mineral insulated copper conductor are being produced by two sources: ASIPP of China; and Tyco of Canada. ASIPP has produced for 5 m lengths which will be shipped to PPPL shortly. Tyco is in the processing stage and is hoping to have the prototypes finished by the time of this review.

10.2.1 **Results of tests on prototype conductors (This will be POST-PDR)**

Prototype lengths of the conductor will be tested to determine the compressive modulus, shear modulus, and thermal conductivity of the MgO as processed. These data will be fed into updates of the finite element analyses to refine the results which were obtained for this PDR based on published data and tests of commercially available copper jacketed solid copper conductor (see section 10.1)

11 IVC FABRICATION PLAN

11.1 ELM COILS

There are a total of (27) Edge Localized Mode (ELM) coils that will be manufactured and installed inside the ITER vacuum vessel. These coils will be constructed using stainless steel jacketed mineral insulated copper conductor. The coils are divided into (3) groups of (9) coils each. These are the Upper, Equatorial and Lower ELM coils.

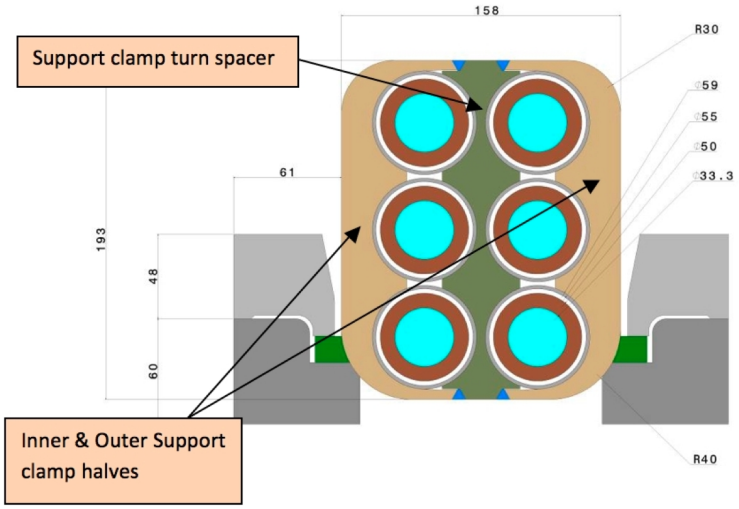

Figure 11-1 X-Section of ELM Coil

Each ELM will have the same cross-section of (6) coil turns with a single flow path (Figure 11-1). Stainless steel structural turn spacers separate the inner and outer layers of the coils at the clamp locations. The coils will be fabricated by an off-site manufacturer and delivered to the Cadarache site ready for installation.

The coils will be hydraulically formed and/or rolled into the various segments of the coil. The ends of the formed segments must remain sealed to minimize absorption of moisture into the insulation. It will be necessary to join adjacent conductors due to the maximum length conductor that industry can produce.

11.2 IVC CONDUCTOR JOINTS

Joining of IVC conductors will be necessary for both the ELMs and VS coils. Due to a maximum available length conductor, multiple conductors will be required per coil. The method described below will be used for either coil design.

Welding or induction brazing are the most likely joining processes that are being evaluated. R&D contracts have been issued investigating the most viable and reliable joining process. (Friction Stir Welding, laser, e-beam are also being considered).

Non-Destructive Testing methods will be used to verify the integrity of the joint prior to installing the stainless sleeve.

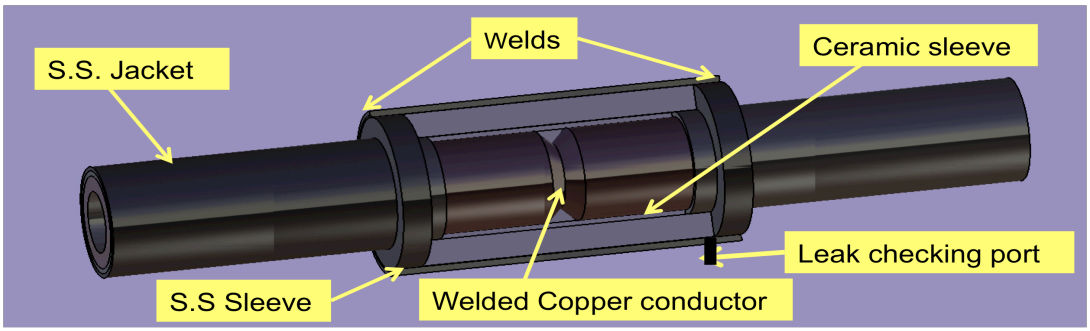

Figure 11-2 Typical Coil Joint

A stainless steel sleeve will be slid over the joint and an orbital welder will be utilized to seal the ends. The joint will then be helium leak checked. **(**Details of leak checking method; NDT of welds is being developed). See Figure 11-2. The joint will then be insulated by injection of MgO powder after installation of the stainless sleeve.

11.3 ELM FABRICATION SEQUENCE

The inner segments will be secured to a temporary winding form with adjacent segments/turns being joined together using the process described (

Figure **11-3**).

Each pre-formed segment will include one to three corner bends depending upon location. Once the inner row of turns is complete, a center stainless steel turn separator will be installed at the support clamp locations (**Error! Reference source not found.**).

The outer layer of turns will then be completed and the outer halves of the support clamps installed (Figure 11-5). The outer half of the support clamp is then welded to the center turn separator. The inner and outer turns are temporarily clamped together so that the inner winding form can be removed and the inner half of the support clamp installed. The inner clamp is then welded to the center turn spacer.

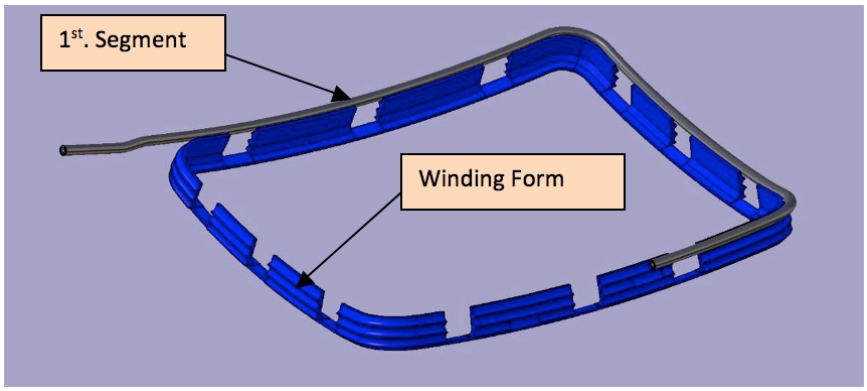

Figure 11-3 Winding Form with First Segment Positioned

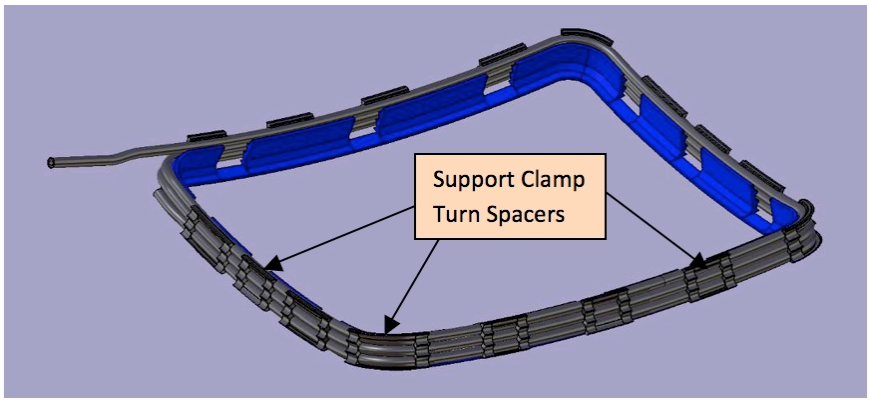

Figure 11-4 Inner Turns Complete with Support Turn Spacers Installed

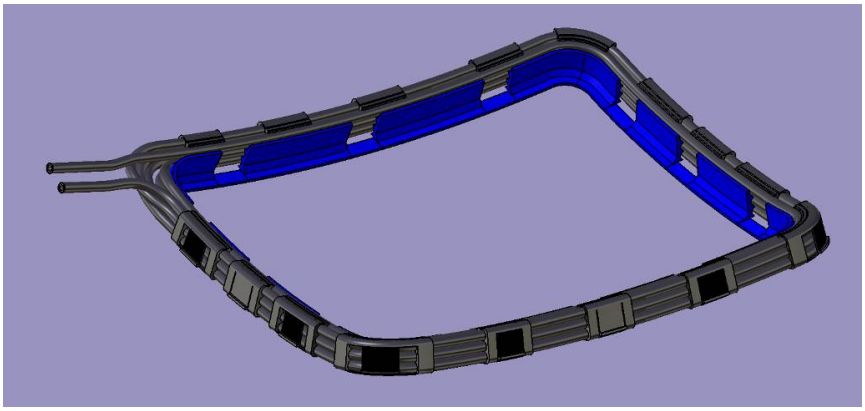

Figure 11-5 Outer Layer of Turns with Clamp Half Installed

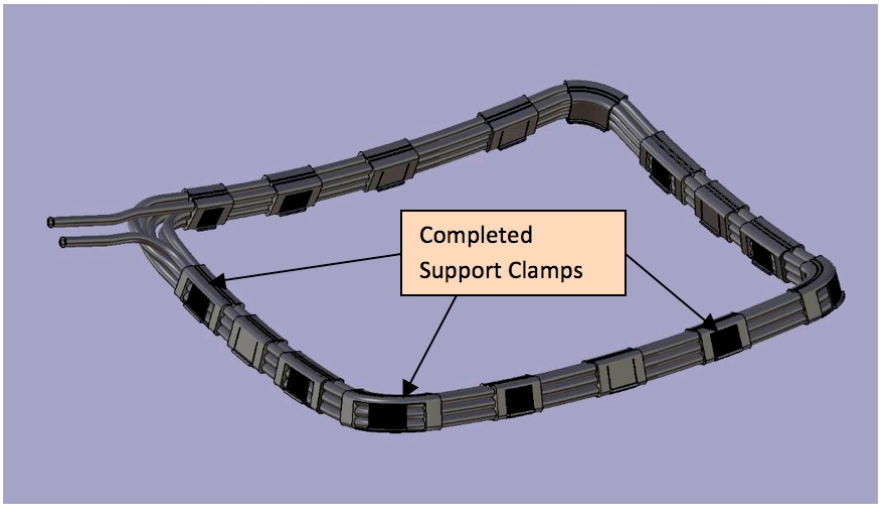

Figure 11-6 Finished Coil with Support Clamps

At each of the support clamp locations the coil turns will be brazed to the support clamps using a small localized oven. This will secure the coil turns at the clamp locations without increasing risk of damaging the conductor jacket with a welding procedure (Figure 11-6).

Final testing: The finished coil will be electrically tested and the outer jacket leak tested at the joint areas. The final sequence and type of tests needs to be developed.

11.4 VS FABRICATION

There are total of (2) Vertical Stability (VS) coils that will be manufactured, one upper and one lower VS coil. The VS coils will be constructed using stainless steel jacketed mineral insulated copper conductor, similar to the conductor being used for the ELM coils. Each VS coil will have the same cross-section of (4) coil turns with each turn individually cooled (Figure 11-7). Stainless steel turn separators are located between the inner and outer layers of the coils at the clamp locations. The coils will be fabricated off-site as individual components then packaged and delivered to the Cadarache site ready for completion of fabrication and installation.

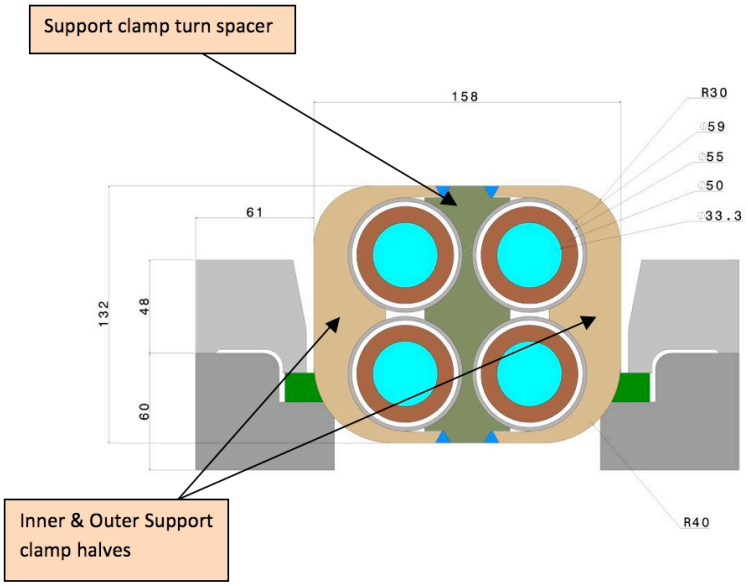

Figure 11-7 X-Section of VS Coil

Each conductor of the VS coils will be hydraulically formed and/or rolled into the various segments of the coil. The ends will be prepared for joining, and then sealed to minimize absorption of moisture into the mineral insulation. It will be necessary to join adjacent

conductors due to the maximum available length conductor that industry can produce. It is also a requirement due to their diameter to be completed in-situ of the vacuum vessel.

All conductor joining operations will occur in the vacuum vessel during the final assembly using the same process as outlined in the ELM coil section.

The VS segments will be pre-assembled at the fabricator for the purpose of a dimensional check on the full coils.

NDT of the conductors will be performed prior to packaging and shipment to the ITER site at Cadarache.

IVC FEEDERS

The IVC feeders provide the power and cooling to the VS and ELM coils. The feeders for the ELM and VS coils will be constructed using the same conductor and support clamp scheme that is being used for the IVC coils.

The feeders will be hydraulically formed using the same stainless steel jacketed mineral insulated copper conductor used for the IVC coils. Each individual conductor will be formed and conductor end prepared for joining to the coils. The end will be properly sealed to minimize moisture absorption by the mineral insulation. The Support clamps will be brazed to the conductors in the appropriate locations as defined by the design (Figure 11-9).

Final Testing: The completed feeder will be electrically tested prior to packaging and shipment to Cadarache.

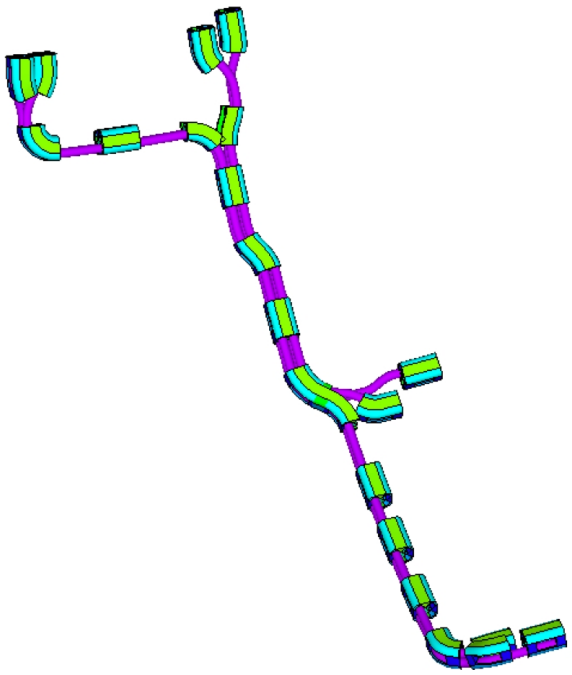

Figure 11-8 Feeder Assembly

12 IVC INSTALLATION PLAN

The ELM coils and ELM/VS feeders will be delivered to Cadarache as complete units ready for installation. The VS coils will be delivered in pre-formed components and will require assembly time inside of the vacuum vessel to complete the VS assemblies'. Figure 12-1 shows the relative position of the IVC components that will be installed in the vacuum vessel.

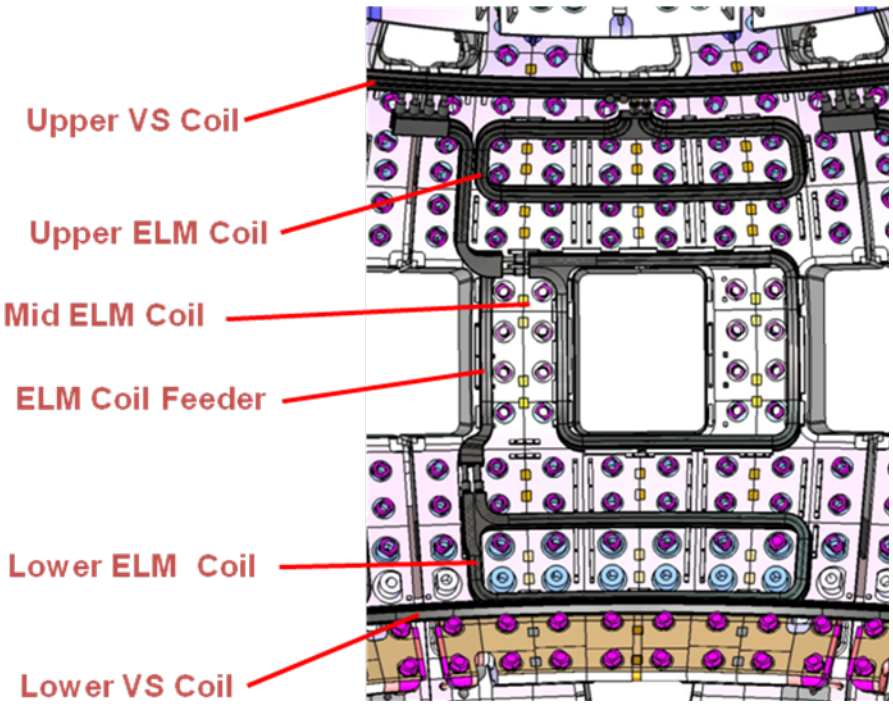

Figure 12-1 IVC In-Vessel Locations

Proposed Assembly Sequence: (Figure 12-2 shows the proposed assembly sequence for all the primary IVC components)

1 - Upper VS Coil

2 - Lower VS Coil

3 - Upper ELM coils

4 - Lower ELM coils

5 - Equatorial (mid) ELM coils

6 - Feeders

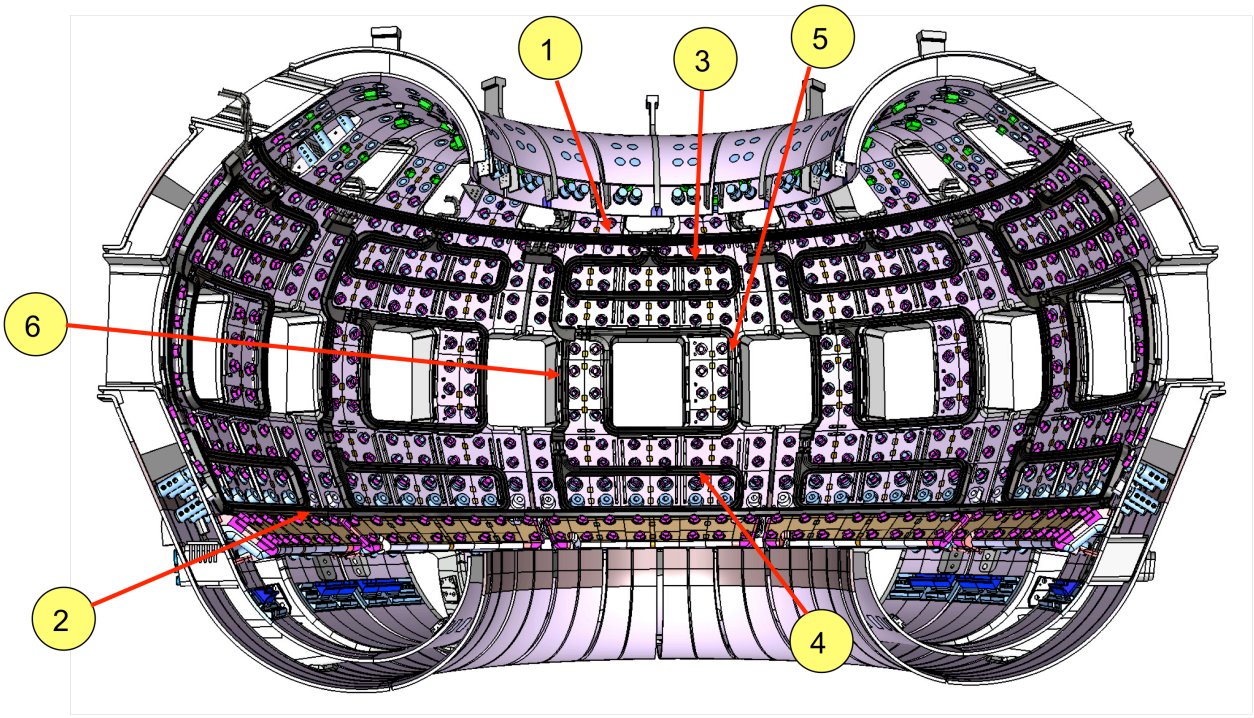

Figure 12-2 Proposed Assembly Sequence

12.1 VS COIL INSTALLATION

The VS coils will be delivered to the ITER site in 90 to 120 degree segments that will need to be completed and assembled in the vacuum vessel.

It is recommended that the components for the VS coils be pre-positioned in the vacuum vessel sectors prior to joining the vacuum vessel segments together. This will eliminate the logistics of feeding the segments through the vacuum vessel ports.

A work platform and assembly station will be installed in the vacuum vessel (Figure 12-3) to accommodate the assembly of the VS coils.

The segments for the first turn of the VS coil will be positioned in the work station and joined together using the same joining process as described in the fabrication section of this document. Each of the (4) turns of the VS coil are individually cooled and have their own coil leads.

Once the first turn has been completed, repeat the assembly process with the three remaining coil turns.

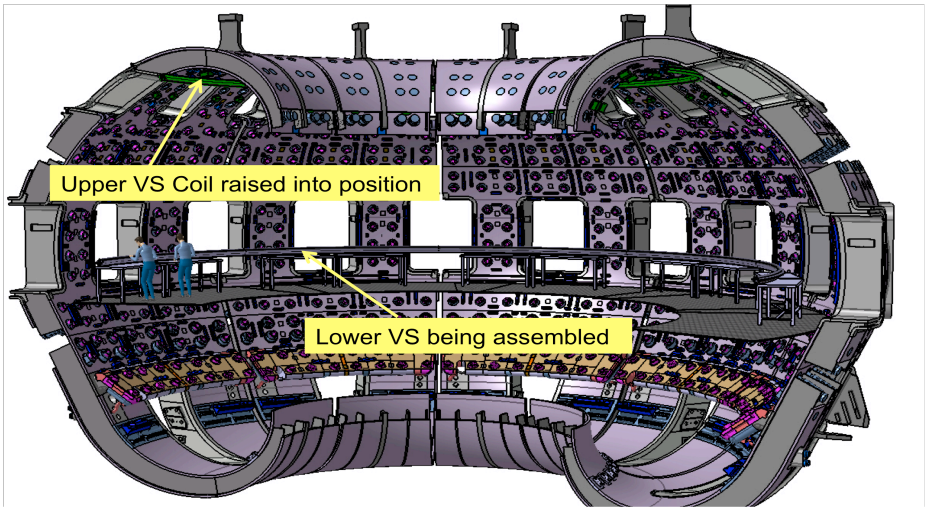

Figure 12-3 VS Coil Work Platform and Assembly Station

Once all of the VS (4) individual turns have been completed, the coil support clamps will be added. This includes the inner turn spacer and the inner and outer clamp halves. The inner and outer clamp halves are welded to the center turn spacer. (Figure 12-4) The clamp assembly and local turns are then oven brazed together using a portable braze oven.

The Upper VS coil will then be electrically tested prior to placing into its final position.

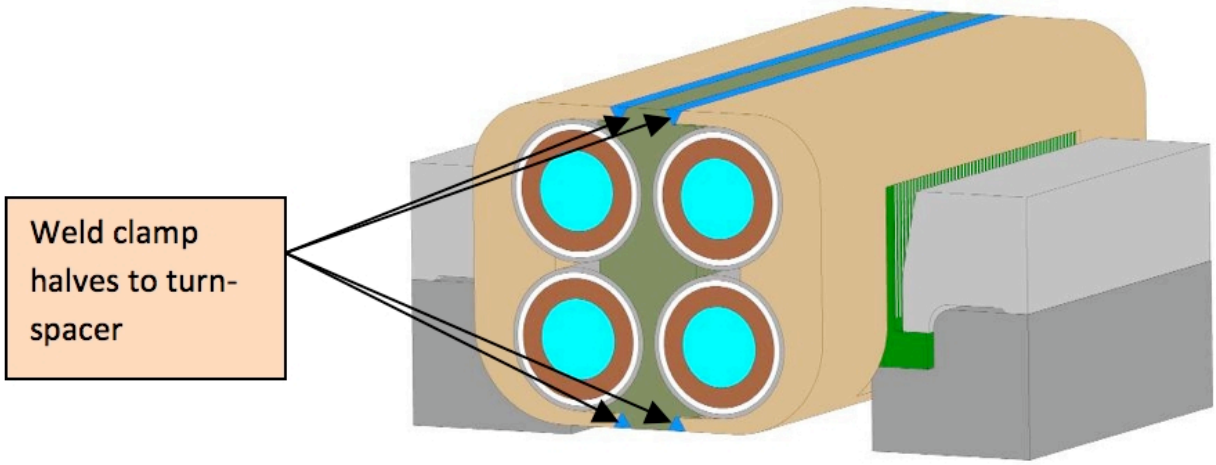

Figure 12-4 Weld Clamp Halves to Center Turn Spacer

The Upper VS coil will then be raised into its final position. The entire process will then be repeated for the Lower VS coil. Prior to installation the Lower VS coil the work station and platform will be removed.

12.2 ELM COIL INSTALLATION

The present plan is to install the ELM coils prior to 1st plasma. However there is a possibility that the ELM coils may be installed at a later date.

It is our recommendation that due to the physical size the equatorial ELMs be pre-positioned in the vessel along with the VS components prior to joining the vacuum vessel segments. This would reduce the cost and installation times associated with the ELMs.

Each ELM coil would installed into the vacuum vessel using Remote Handling (RH) tooling (

Figure **12-5**) that will introduce the coils through the ports. Each individual coil would then be raised into position and shimmed to their correct position. They will then be secured to the vacuum vessel wall with the proposed clamping scheme.

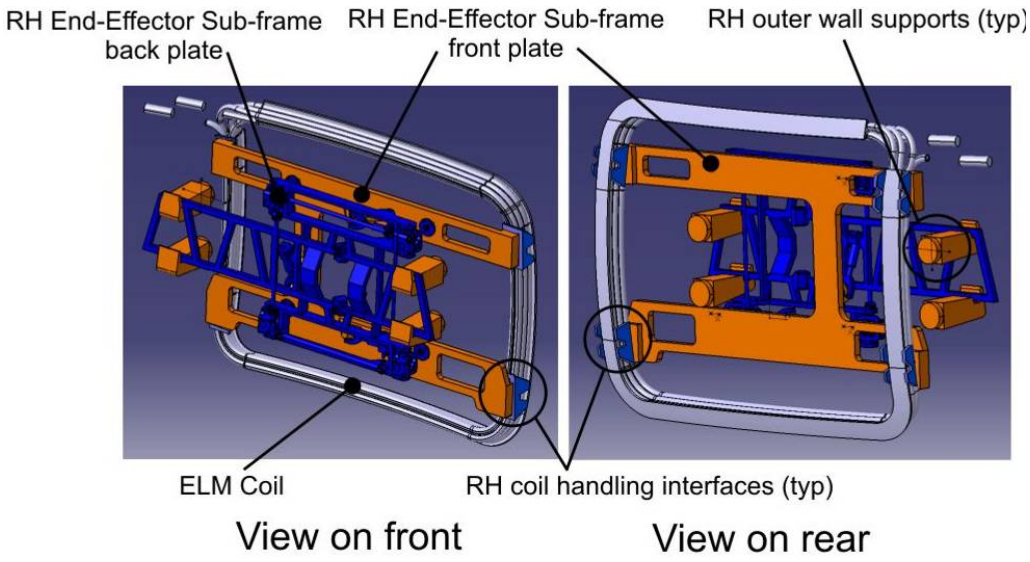

Figure 12-5 RH Tooling for ELM Coil Installation

12.3 FEEDER INSTALLATION

The IVC coil feeders will be introduced into the vacuum vessel via the vessel ports. They will be positioned and secured to the vacuum vessel wall with a similar clamping scheme that is being proposed for the IVC coils. Once the feeders have been secured the individual coil to lead connections need to be made.

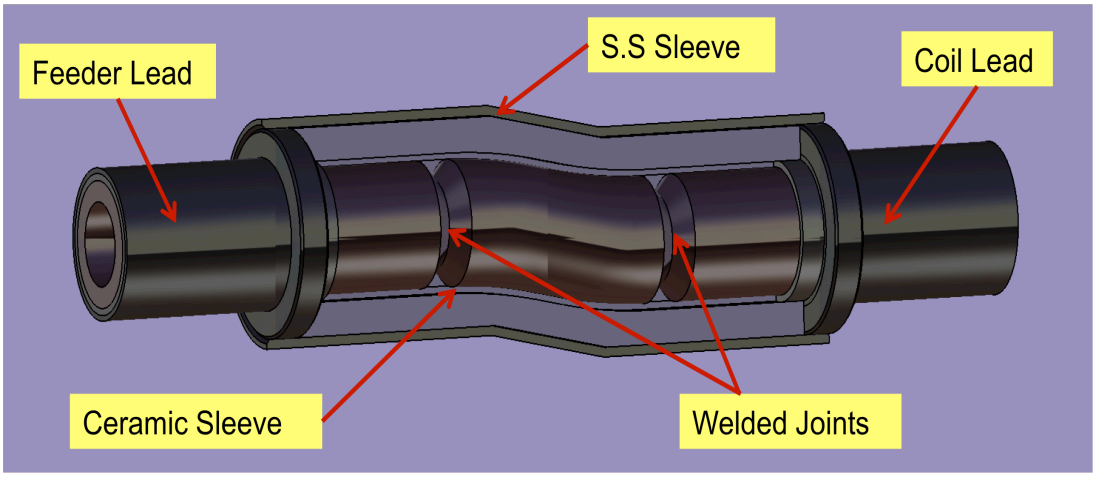

Figure 12-6 Typical IVC Coil to Lead Joint

The feeder and coil leads will already be prepared for joining. A measurement will be made at each coil to lead connection, and a custom copper jumper along with the outer can will be fabricated to accommodate misalignments. (Figure 12-6).

The plan is to use an orbital welder to join the copper jumper to the coil and leads. The (2) half stainless steel sleeve will then be positioned and welded to the adjacent jacketed components.

A pump out and fill port will be provided on the sleeve to helium leak test the welded connection. Using the same leak test port MgO will be injected into the area surrounding the copper joint. The MgO will need to be compacted to obtain maximum electrical benefits. The fill port will then be cap welded to seal the joint from the vacuum vessel environment.

Figure 12-7 thru Figure 12-8 show the upper, lower and mid (equatorial) ELM coil lead areas that will utilize the same joint process.

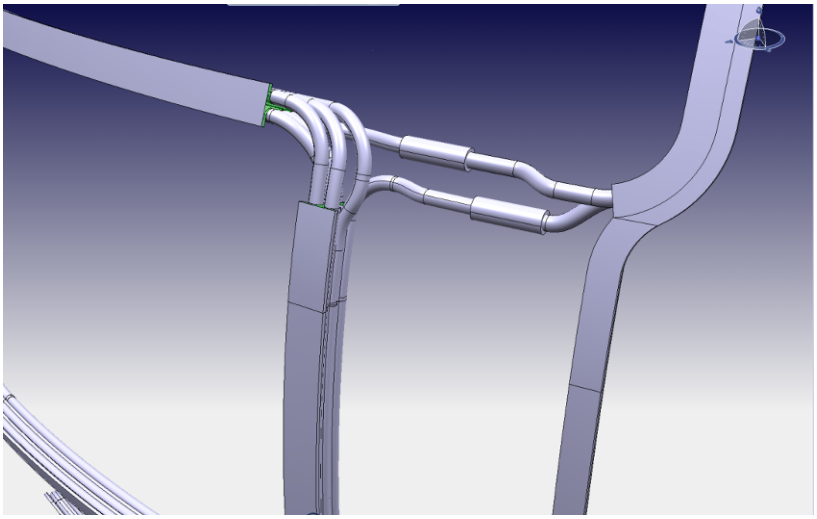

Figure 12-7 Equatorial ELM Coil Joints

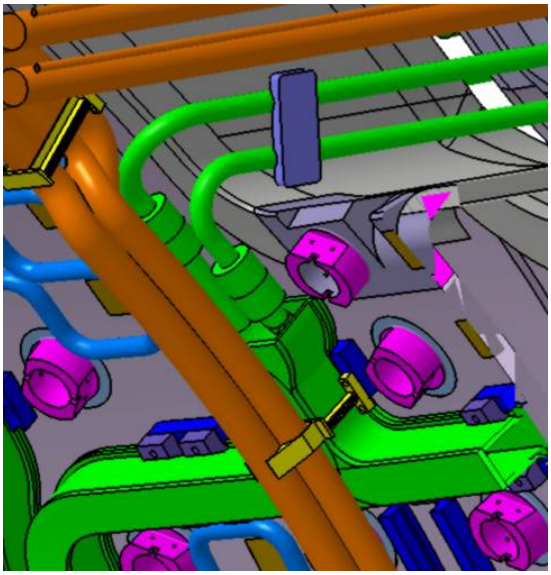

Figure 12-9 Upper ELM Coil Joints

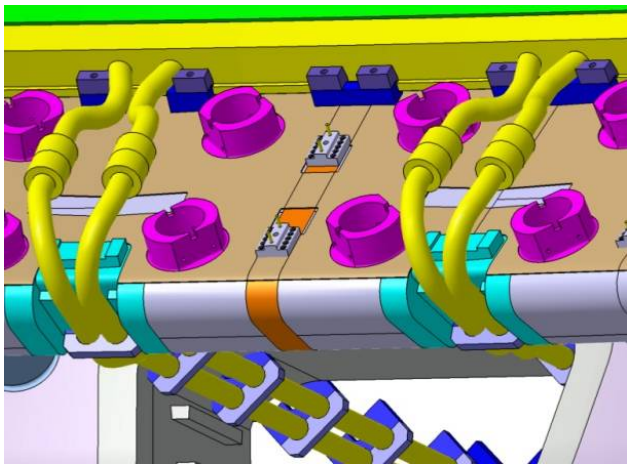

Figure 12-8 Lower ELM Coil Joints

12.4 FINAL INSPECTION AND TESTING

Once all of the IVC coils and feeders have been installed, a complete final inspection will be made of all the in-vessel IVC components. Thus will include welds, coil positions and securing of hardware.

The coil systems will individually be electrically tested. The NDT plan needs to be developed.

13 INTERFACES

The current version of the SRD (v1.5) identifies key interfaces between the In-Vessel Coils and other PBS elements. In parallel with finalizing v1.5 in May 2010, parallel discussions occurred between representatives of the IVCs and other PBS elements. See Table 13-1.

Table 13-1 Summary of Interfaces and ICD Status

Interfaces	Agreements on ICDs	Current Status (as of end of Sept 2010)
ICDs in Which IVCs Have the Lead in Developing		
15_IV & 23 (Remote Handling)	IVCs have lead to develop ICD	Draft posted in IDM (ITER_D_3MQFSV_v1.0)
15-IV & 26 (Cooling Water)	IVCs have lead to develop ICD	Draft posted in IDM (ITER_D_3QRK4Z_v0.0). Interface Sheet prepared & posted in IDM.
15-IV & 31 (Vacuum)	IVCs have lead to develop ICD	Draft posted in IDM (ITER_D_3QG22PV_v1.0)
15-IV & 41 (Coil Power Supplies)	IVCs have lead to develop ICD	Draft posted in IDM (ITER_D_3MSYPA_v1.0).
15-IV & 62-23 (Radwaste Bldg)	IVCs have lead to develop ICD	Draft posted in IDM (ITER_D_3MSYPA_v1.0).
15-IV & 66 (Radwaste Treatment & Storage	IVCs have lead to develop ICD	Draft posted in IDM (ITER_D_3MQFSV_v1.0). If PBS 67 (Hot Cell and Radwaste Facilities), collapsed into this PBS, will need an Interface Sheet to define the interfaces.
ICDs in Which Other PBS Elements Have the Lead, but IVCs will Provide Interface Sheets		
15-IV (and 15-MA) to 15-VV (Vacuum Vessel)	15-VV has the lead to develop	ICD prepared & posted in IDM (ITER_D_2WSMKHK_V1.0). This includes both the IVCs and the Blanket Modules. 4 Interface Sheets prepared and posted in IDM **(One Disapproved).** IVCs will prepare an Interface Sheet to the VV ICD to address the IVC-Blanket Modules interfaces. May have to also modify VV ICD to address both the IVCs and Blanket Manifolds interfaces better.

15-IV & 16 (Blankets)	16 has the lead to develop	ICD between Vacuum Vessel & Blanket prepared & posted in IDM (ITER_D_2NR7LR_V1.2). IVCs may have to prepare an Interface Sheet since previous attempt under VV disapproved.
15-IV & 22 (Machine Assembly)	22 has the lead to develop	ICD prepared & posted in IDM (ITER_D_32LVEM_V1.1). Interface Sheet prepared and posted in IDM.
15-IV & 24 (Cryostat)	24 has the lead to develop	ICD between Vacuum Vessel & Cryostat prepared & posted in IDM (ITER_D_2NRU42_V2.1). Interface Sheet prepared and posted in IDM.
15-IV to 55 (Diagnostics)	55 has the lead for the ICD	ICD between Vacuum Vessel & Diagnostics prepared & posted in IDM (ITER_D_2EZV2T_v6.4). 2 Interface Sheets prepared and posted in IDM.
15-IV to 62-11 (Tokamak Bldg)	62-11 has the lead for the ICD	ICD between Tokamak Building & Vacuum Vessel prepared & posted in IDM (ITER_D_2EQ8NT_V1.3). IVCs may have to prepare an Interface Sheet.
I5-IV to 62-11-BP (Bioshield Plugs)	62-11-BP has the lead for the ICD	ICD prepared & posted in IDM (ITER_D_339QGF_V1.01). Interface Sheet prepared and posted in IDM.
No Direct Interface or Possible Interface Expected to be Collapsed into Another PBS		
15-IV $ 43 (SSEPN)	Interfaces thru PBS 41 (Coil Power Supplies to IVCs	Although interfaces with PBS 43 are via PBS 41 (Coil Power Supplies), IVCs may have to prepare an IS to define local interfaces.
15-IV $ 45 (CODAC)	Interfaces thru PBS 41 (Coil Power Supplies to IVCs	Although interfaces with PBS 43 are via PBS 41 (Coil Power Supplies), IVCs may have to prepare an IS to define local interfaces.
15-IV & 46 (Central Interlocks)	Interfaces thru PBS 41 (Coil Power Supplies to IVCs	Although interfaces with PBS 43 are via PBS 41 (Coil Power Supplies), IVCs may have to prepare an IS to define local interfaces.
15-IV & 47 (Plasma Control System)	Interfaces thru PBS 41 (Coil Power Supplies to IVCs	Although interfaces with PBS 43 are via PBS 41 (Coil Power Supplies), IVCs may have to prepare an IS to define local interfaces.
15 –IV to 26 (Cooling Water)	IVCs/Cooling Water to prepare IS	One IS in IDM: IS-15-IV-26 (ITER_D_3QRK4Z_v0.0)
15-IV & 67 (Hot Cell & Radwaste Facilities)	Per discussions in May 2010, expect this PBS to be collapsed into PBS 66 (Radwaste Treatment & Storage)	Once this is done, will need an Interface Sheet for these interfaces.
Interface Sheets		
15-IV to 15-VV (Vacuum Vessel)	IVCs/VV to prepare Interface Sheets	Four Interface Sheets prepared and posted in IDM: • IS-15_VV_15-IV-001 Main Vessel (ITER_D_34MNJ8_v1.0 • IS-15_VV_15-IV-002 Upper Port

		(ITER_D_33MQQM_v1.2 • IS-15_VV_15-IV-003 Lower Port (ITER_D_34ZUY5_v1.2) • IS-15-16-006 Space for IV Coils (ITER_D_33X3P85_v1.1) – **DISAPPROVED IN IDM**.
15-IV to 22 (Machine Assembly Tooling)	IVCs/Machine Assembly Tooling to prepare Interface Sheet	One Interface Sheet posted in IDM: IS-15-IV-22 (ITER_D_3SA8WG_v1.0)
15-IV to 24 (Cryostat)	IVCs/Cryostat to prepare Interface Sheet	One Interface Sheet posted in IDM: IS-15-IV-24-01 VV Penetrations & Cryostat (ITER_D_32JR7E_v1.1)
15-IVto 26 (Cooling Water)	IVCs/Cooling Water to prepare Interface Sheet	One Interface Sheet posted in IDM: IS-15-IV-26 (ITER_D_3QRK4Z_v1.0)
15-IV to Diagnostics	IVCs/Diagnostics to prepare Interface Sheets	Two Interface Sheets prepared and posted in IDM: • IS-15-55-002 Microfission Chambers (ITER_D_2F8EE9_V5.0) • IS-15-55-010 In-Vessel Magnetics (ITER_D_2FE4R2_V3.0)
15-1V to 62-11 (Tokamak Bldg) & 62-74 (Diagnostic Bldg)	IVCs/Tokamak & Diagnostic Bldg to prepare Interface Sheet	One Interface Sheet posted in IDM: SES-KD0-06 (ITER_D_32FXR2_v1.5).
Other Interface Sheets possibly needed	IVCs will take the lead in preparing the necessary Interface Sheets	15-IV to 15-MA (Blanket Manifolds) in VV ICD;15-IV to 16 (Blankets); 15-IV to 62-11 (Tokamak Bldg); & 15-IV to 67 (Hot Cell and Radwaste Facilities); and local interfaces for 15-IV interfaces with 43 (SSEPN), 45 (CODAC), 46 (Local Interlocks) & 47 (Plasma Control System).

APPENDIX I – ELM DESIGN POINT

ELM COIL		
Conductor pack width	m	0.123
Conductor pack height	m	0.176
Jacket OD	mm	59.0
Jacket thickness	mm	2.0
Insulation thickness	mm	2.5
Conductor OD	mm	50.0
Conductor ID	mm	33.3
Conductor length per turn	m	10.9
Feeder length per pole	m	14.0
#Sub-circuits		1
#Turns per sub-circuit		6
Total conductor length per sub-circuit	m	93.3
#Sub-circuits in series hydraulically		1
#Sub-circuits in parallel hydraulically		1
#Sub-circuits in series electrically		1
#Sub-circuits in parallel electrically		1
Base total current	Amp-turn rms	90000
#Turns effective		6
Per unit current	p.u.	1.00
Current per turn effective	Amp rms	15000
Current per sub-circuit	Amp rms	15000
Net series/parallel circuit resistance at 20C	mOhm	1.850
Flow velocity	m/s	3.0
Water Inlet Temperature	deg C	100
Coil delta_T	deg C	47
Total delta_T across hydraulic circuit	deg C	67
Maximum temperature	deg C	167
Net series/parallel circuit resistance at average resistivity	mOhm	2.501
Total ohmic dissipation	kW	563
Volumetric nuclear heating rate	watt/cc	0.49
Nuclear heated volume	m3	2.16E-01
Total nuclear heating	kW	106

Total heat load	kW	669
Heat load per hydraulic circuit	kW	669
delta_T/sec (LOCW)	degC/sec	1.8
Total Pressure Drop	MPA	0.26
Boiling Pressure at Outlet Temp	MPA	0.74
Return pressure	MPA	1.48
Inlet pressure	MPA	1.74
Total Cu wetted surface to TCWS	m2	10
Total water volume in TCWS	m3	0.08

ELM BUS BAR		
Conductor width	m	0.0500
Conductor height	m	0.1000
Cooling hole diameter	m	0.0175
Current	Amp rms	15000
Avg conductor length per pole	m	30
#Conductor in parallel electrically and hydraulically per pole		2
Resistance per pole at 20C	mOhm	0.055
Flow velocity	m/s	2.8
Flow per conductor	m3/s	6.69E-04
Mass flow per conductor	kg/s	0.66
#Poles in series hydraulically		2
Hydraulic path delta_P	MPA	0.25
Return pressure	MPA	0.02
Inlet pressure	MPA	0.38
Water Inlet Temperature	deg C	45
Water delta_T	deg C	5
Resistance per pole at average temperature	mOhm	0.061
Ohmic dissipation per pole	kW	14
Ohmic dissipation per unit length	kW/m	0.45
Total # bus bar poles		2
Total ohmic dissipation, fraction of total coil + bus bar		0.05
Total flow	m3/s	2.67E-03
Total mass flow	kg/s	2.6
Total bus bar resistance at 20C	ohm	1.10E-04
Total bus bar resistance at average temperature	ohm	1.22E-04
Total bus bar inductance	henry	1.85E-03

TOTAL ELM CIRCUIT		
Coil resistance at operating temperature	ohm	2.50E-03
Coil inductance	henry	2.32E-04
Bus bar resistance at operating temperature	ohm	1.22E-04
Bus bar inductance	henry	6.01E-06
Total circuit resistance at operating temperature	ohm	2.62E-03

Total circuit inductance	henry	2.38E-04
Current per turn	amp	15000
AC Mode		
Frequency	Hz	5
Inductive reactance	ohm	7.46E-03
Complex impedance	ohm	7.91E-03
Load power factor		0.33
Phase angle		71
Voltage drop	volt	119
Current at peak voltage	amp	4974
Power supply regulation at full load		0.20
Power supply regulation at current at peak voltage		0.07
Min power supply no-load voltage		127
Selected PS voltage		180
Active power	watt	2.95E+05
Apparent power	volt-amp	2.70E+06
Reactive power	volt-amp-reactive	2.68E+06
Net power factor		0.11
DC Mode		
Voltage drop	volt	39
Active power	watt	5.90E+05
Apparent power	volt-amp	2.70E+06
Reactive power	volt-amp-reactive	2.63E+06
Net power factor		0.22

TOTAL ELM SYSTEM		
# coils		27
Simultaneity factor		0.50
Total input active power	watt	7.97E+06
Total input reactive power	volt-amp-reactive	7.25E+07
Total input apparent power	volt-amp	7.29E+07
Total ohmic + nuclear heat load from coils to TCWS	watt	1.05E+07
Total mass flow to coils from TCWS	kg/s	63
TCWS Inlet pressure	MPA	0.74
Total Coil Pressure Drop to TCWS	degC/sec	1.81
TCWS Return pressure	MPA	0.26
TCWS Water Inlet Temperature	m/s	3
TCWS Water Outlet Temperature	deg C	167
Total Cu wetted surface to TCWS	m2	264
Total water volume in TCWS	m3	2.20
Total heat load from bus bar to CCWS	watt	3.71E+05
Total mass flow to bus bar from CCWS	kg/s	71

APPENDIX II – VS DESIGN POINT

VS COIL		N Turns	N-1 Turns
Conductor pack width	m	0.132	0.132
Conductor pack height	m	0.128	0.128
Jacket OD	mm	59.0	59.0
Jacket thickness	mm	2.0	2.0
Insulation thickness	mm	5.0	5.0
Conductor OD	mm	45.0	45.0
Conductor ID	mm	30.0	30.0
Conductor length per turn	m	47.1	47.1
Feeder length per pole	m	10.0	10.0
#Sub-circuits		4	3
#Turns per sub-circuit		1	1
Total conductor length per sub-circuit	m	67.1	67.1
#Sub-circuits in series hydraulically		1	1
#Sub-circuits in parallel hydraulically		4	3
#Sub-circuits in series electrically		4	3
#Sub-circuits in parallel electrically		1	1
Base total current	Amp-turn rms	35895	35895
#Turns effective		4	3
Per unit current	p.u.	1.00	1.00
Current per turn effective	Amp rms	8974	11965
Current per sub-circuit	Amp rms	8974	11965
Net series/parallel circuit resistance at 20C	mOhm	5.237	3.927
Flow velocity	m/s	3.0	3.0
Water Inlet Temperature	deg C	100	100
Coil delta_T	deg C	21	34
Total delta_T across hydraulic circuit	deg C	31	49
Maximum temperature	deg C	121	134
Net series/parallel circuit resistance at average resistivity	mOhm	7.291	5.468
Total ohmic dissipation	kW	587	783
Volumetric nuclear heating rate	watt/cc	0.48	0.48

Nuclear heated volume	m3	8.57E-01	8.57E-01
Total nuclear heating	kW	414	414
Total heat load	kW	1001	1197
Heat load per hydraulic circuit	kW	250	399
delta_T/sec (LOCW)	degC/sec	1.2	1.9
Total Pressure Drop	MPA	0.24	0.24
Boiling Pressure at Outlet Temp	MPA	0.28	0.28
Return pressure	MPA	0.56	0.56
Inlet pressure	MPA	0.80	0.80
Total Cu wetted surface to TCWS	m2	25	19
Total water volume in TCWS	m3	0.19	0.14

VS BUS BAR			
Conductor width	m	0.0500	0.0500
Conductor height	m	0.1000	0.1000
Cooling hole diameter	m	0.0175	0.0175
Current	Amp rms	8974	8974
Avg conductor length per pole	m	47	47
#Conductor in parallel electrically and hydraulically per pole		2	2
Resistance per pole at 20C	mOhm	0.084	0.084
Flow velocity	m/s	1.2	1.2
Flow per conductor	m3/s	2.93E-04	2.93E-04
Mass flow per conductor	kg/s	0.29	0.29
#Poles in series hydraulically		1	1
Hydraulic path delta_P	MPA	0.04	0.04
Return pressure	MPA	0.02	0.02
Inlet pressure	MPA	0.17	0.17
Water Inlet Temperature	deg C	45	45
Water delta_T	deg C	3	3
Resistance per pole at average temperature	mOhm	0.094	0.094
Ohmic dissipation per pole	kW	8	8
Ohmic dissipation per unit length	kW/m	0.16	0.16
Total # bus bar poles		16	16
Total ohmic dissipation, fraction of total coil + bus bar		0.09	0.09
Total flow	m3/s	9.37E-03	9.37E-03
Total mass flow	kg/s	9.3	9.3
Total bus bar resistance at 20C	ohm	1.35E-03	1.35E-03
Total bus bar resistance at average temperature	ohm	1.50E-03	1.50E-03
Total bus bar inductance	henry	1.05E-02	1.05E-02

TOTAL VS CIRCUIT			
Coil resistance (upper + lower) at operating temperature	ohm	1.46E-02	1.09E-02
Coil inductance (upper + lower anti-series)	henry	1.22E-03	6.88E-04
Bus bar resistance at operating temperature	ohm	1.50E-03	1.50E-03
Bus bar inductance	henry	7.39E-05	7.39E-05
Total circuit resistance at operating temperature	ohm	1.61E-02	1.24E-02
Total circuit inductance	henry	1.30E-03	7.62E-04
Rated voltage	Volt	2400	2400
WAVEFORM COMPONENTS			
Transient component			
I_max	Amp per turn	60000	80000
Amplitude	Amp	7.44E+04	9.92E+04
Tau_1	sec	0.304	0.304
Tau_2	sec	0.016	0.016
Peak current	Amp per turn	60000	80000
Period	Sec	10	10
Events per plasma	Events	3	3
Noise component			
RMS Current	Amp per turn	2907	3876
Peak Current	Amp per turn	4111	5482
Fraction of max voltage driving noise		0.5	0.5
Impedance Z	Ohm	2.76E-01	2.07E-01
Reactance X	Ohm	2.75E-01	2.06E-01
Frequency	Hz	33.8	25.3
Total Current			
Min plasma duration	sec	200	200
Base period	sec	10	10

I2T over base period	Amp2-sec	8.05E+08	1.43E+09
I_rms over base & consecutive periods	Amp per turn	8974	11965
I_rms over min plasma duration	Amp per turn	2680	3728
VS Power Supply			
Rated voltage	Volt	2400	2400
Equiv series resistance of cap bank	Ohm	3.78E-03	3.78E-03
Capacitor bank	Farad	5.208	5.208
Charger rated output power	Watt	1.30E+06	1.30E+06
Equiv series resistance of charger	Ohm	0.712	0.712
Charger rated current	Amp	675	675
Charger rated apparent power	Volt-amp	1.62E+06	1.62E+06

TOTAL VS SYSTEM			
# coils		2	2
Simultaneity factor		1.00	1.00
Total input active power	watt	1.30E+06	1.30E+06
Total input reactive power	volt-amp-reactive	9.71E+05	9.71E+05
Total input apparent power	volt-amp	1.62E+06	1.62E+06
Total ohmic + nuclear heat load from coils to TCWS	watt	2.00E+06	2.39E+06
Total mass flow to coils from TCWS	kg/s	15.4	11.5
TCWS Inlet pressure	MPA	0.80	0.80
Total Coil Pressure Drop to TCWS	MPA	0.24	0.24
TCWS Return pressure	MPA	0.56	0.56
TCWS Water Inlet Temperature	deg C	100	100
TCWS Water Outlet Temperature	deg C	121	134
Total Cu wetted surface to TCWS	m2	51	38
Total water volume in TCWS	m3	0.38	0.28
Total heat load from bus bar to CCWS	watt	1.21E+05	1.21E+05
Total mass flow to bus bar from CCWS	kg/s	9	9

APPENDIX III – PLOTS OF THE LEG FORCES FOR THE 2010_03(V2) SCENARIO

The PF Coil definitions used in these analyses are shown in Table AIII-1.

Table AIII-1 PF Coil Dimensions and Turns

COIL	R (m)	Z (m)	dr(m)	dz(m)	Turns
CS3,U	1.6960	5.4350	0.7340	2.1200	553
CS2,U	1.6960	3.2650	0.7340	2.1200	553
CS1U	1.6960	1.0950	0.7340	2.1200	553
CS1,L	1.6960	-1.0750	0.7340	2.1200	553
CS2,L	1.6960	-3.2450	0.7340	2.1200	553
CS3,L	1.6960	-5.4150	0.7340	2.1200	553
PF1	3.9431	7.5737	0.9590	0.9841	248.6
PF2	8.2847	6.5398	0.5801	0.7146	115.2
PF3	11.9923	3.2752	0.6963	0.9538	185.9
PF4	11.9628	-2.2336	0.6382	0.9538	169.9
PF5	8.3910	-6.7265	0.8125	0.9538	216.8
PF6	4.3340	-7.4660	1.5990	1.1075	459.4

Figures AIII-1 through AIII-4 show the various leg force magnitudes for scenario 2010_03(V2) versus time. The maximum forces can occur at times other than the EOB, but the difference is small – with the most significant difference for the upper VS. The side legs of the various coils have almost constant forces since the fields are dominated by the TF coils.

Finally, the choice of +60 kA for the VS and -15 kA for the ELM coils was arbitrary. The scenario 2010_03(V2) was run with all 16 combinations of VS and ELM currents – i.e. +/- 60 kA in the VS and +/- 15 kA in each of the ELM coils. The most significant difference in the force magnitude came in VS_DN and ELM_DN due to their proximity. Figures AIII-5 through

AIII-9 show the force magnitude versus time for all the IVC legs for all 16 combinations of VS and ELM currents. As can be seen, there really isn't a great deal of variation with the exceptions of VS_DN and ELM_DN.

Finally, at the time point at which the maximum force magnitude occurs, all force magnitudes as a bar chart are plotted against the VS and ELM current signs. The data is presented in the order VS, ELM_UP, ELM_MD, and ELM_DN. So -1,+1,+1,-1 would be VS -60kA, ELM_UP +15 kA, ELM_MD +15 kA, and ELM_DN -15kA.

All the force components on all the 36 conductor elements at each of the time points in the 5 scenarios have been saved are available to interested individuals. These are the basis for the processing into local coordinates.

Figure AIII-10 shows the IVCs against the vacuum vessel wall with local coordinates (U,V,W) shown at the centers of the corners and legs.

LEG FORCES VERSUS TIME:

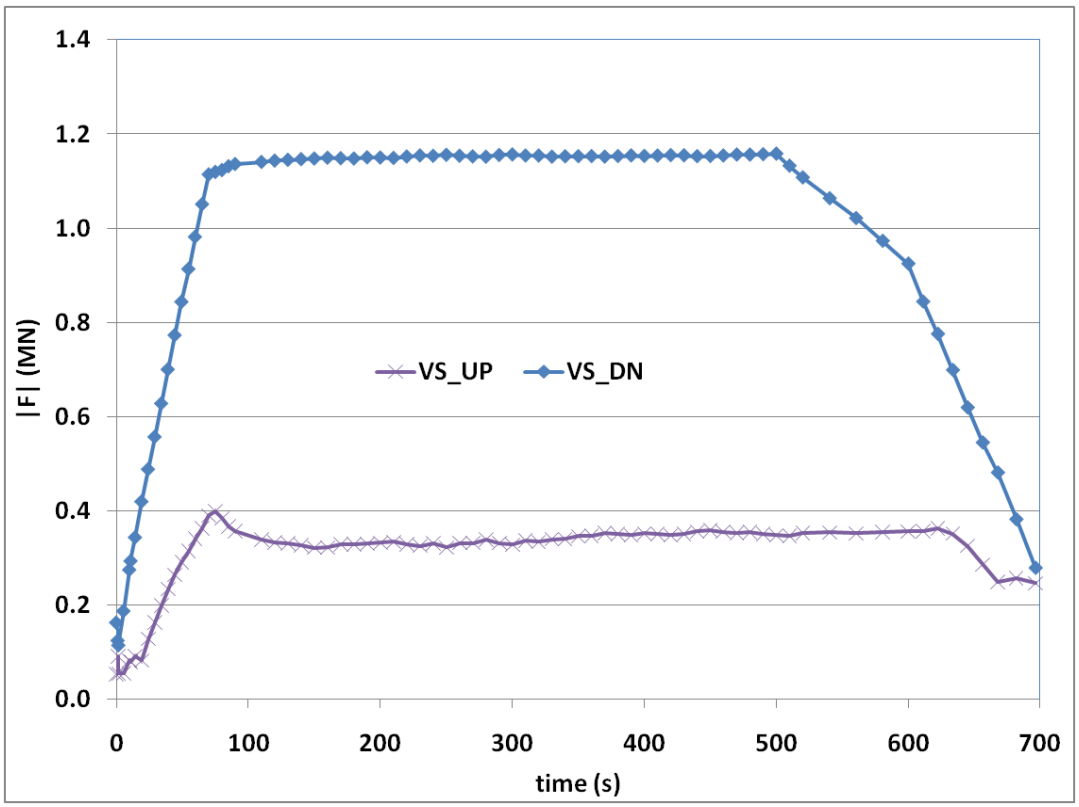

Figure AIII-1 Forces on the VS Coils as a function of time for scenario 2010_03(V2). VS at 60 kA, ELMs at -15 kA

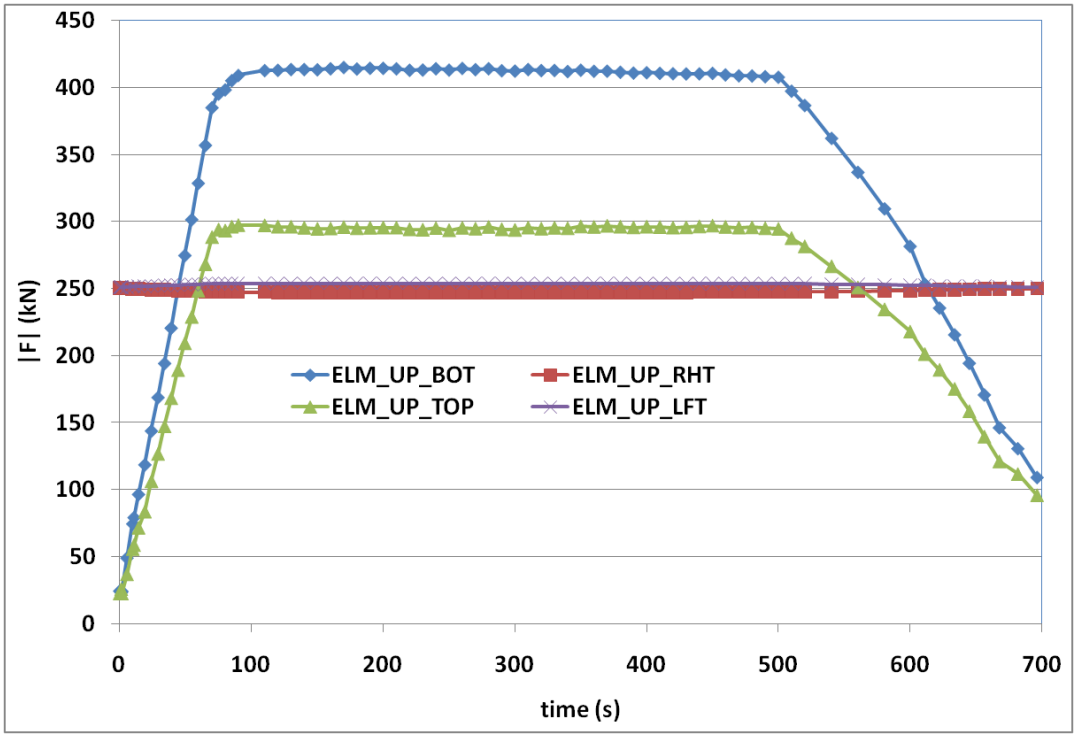

Figure AIII-2 Forces on the ELM_UP Coil as a function of time for scenario 2010_03(V2). VS at 60 kA, ELMs at -15 kA

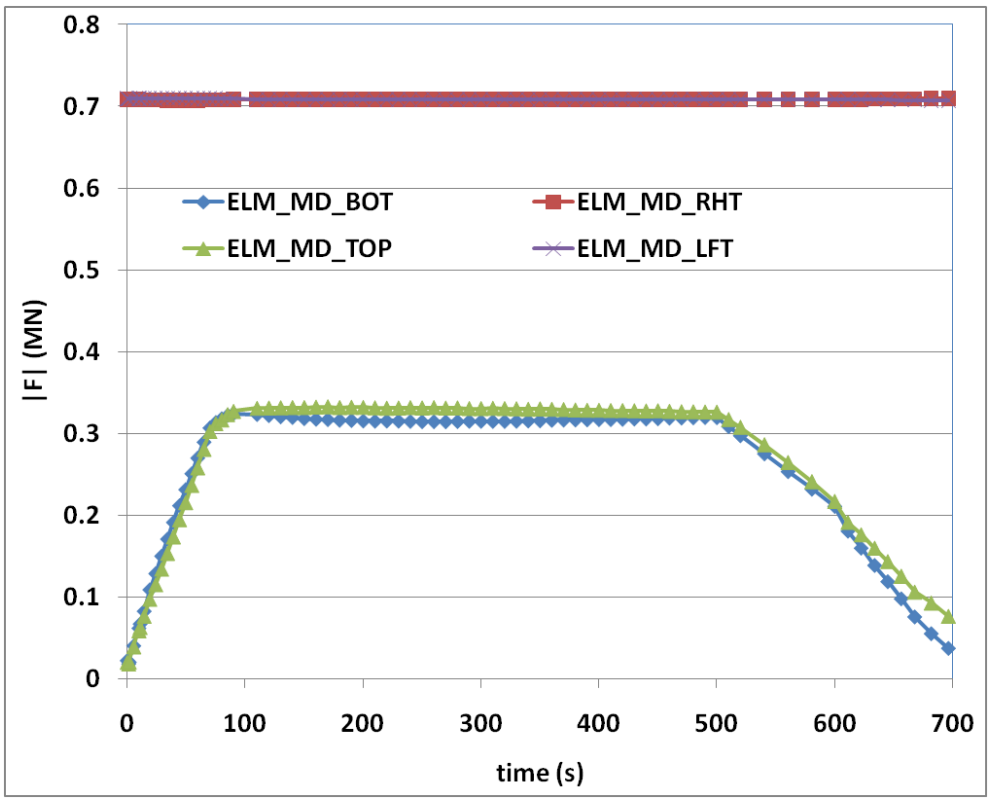

Figure AIII-3 Forces on the ELM_MD Coil as a function of time for scenario 2010_03(V2). VS at 60 kA, ELMs at -15 kA

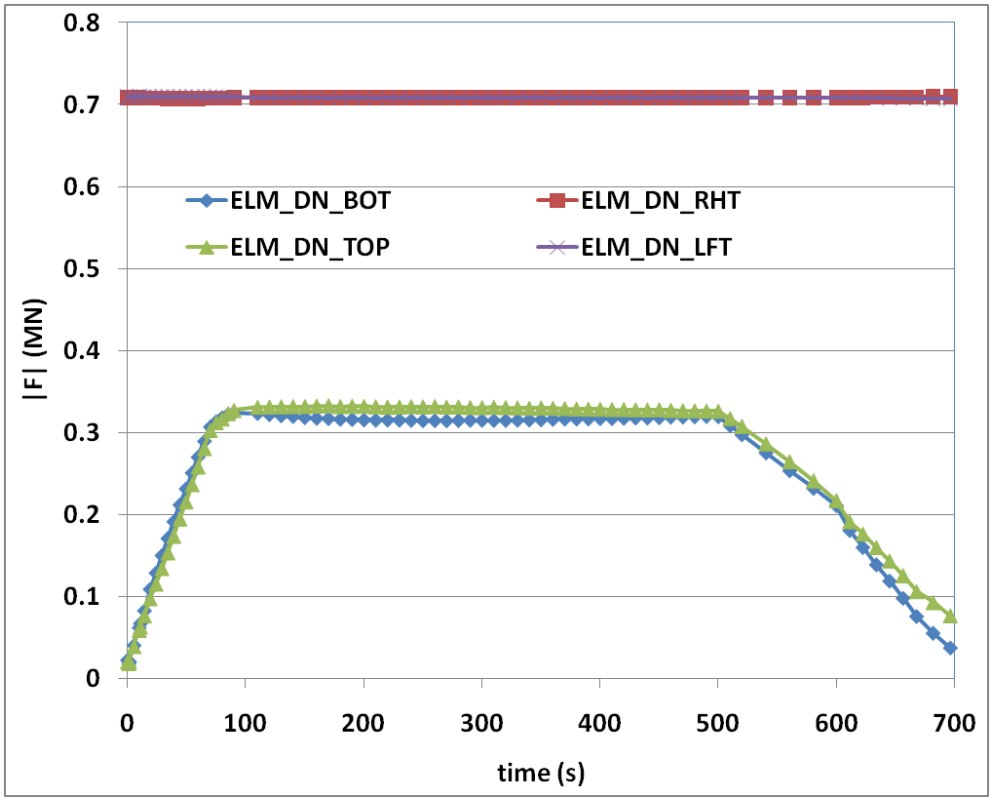

Figure AIII-4 Forces on the ELM_DN Coil as a function of time for scenario 2010_03(V2). VS at 60 kA, ELMs at -15 kA

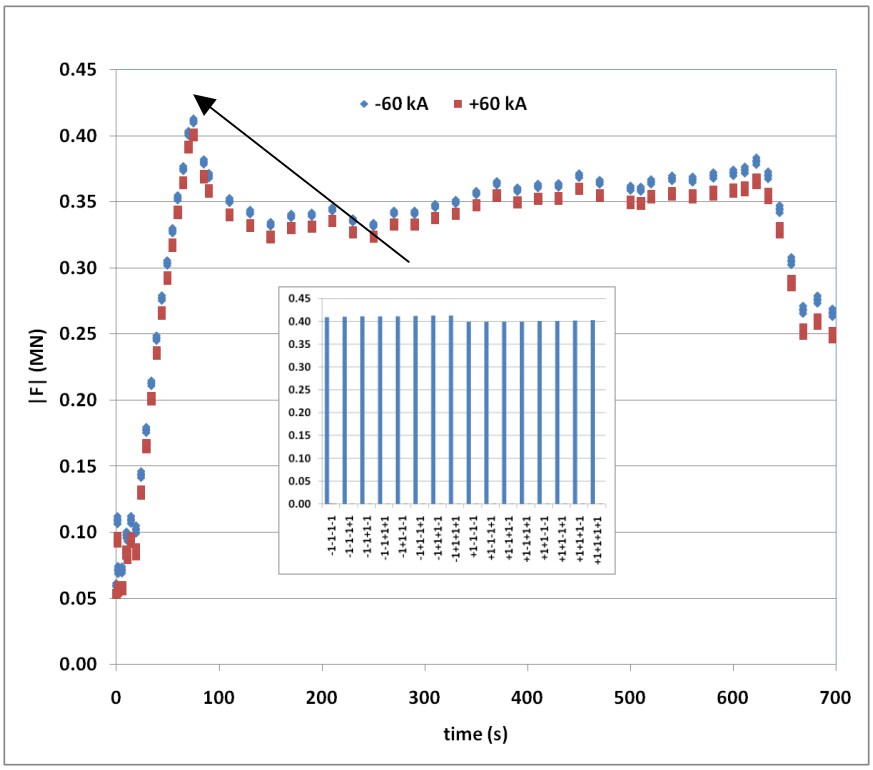

Figure AIII-5 Forces on the VS_UP Coil as a function of time for scenario 2010_03(V2) with 16 variations in sign of the VS and ELMs. Inset shows variation w/ sign of IVC currents at 75 seconds

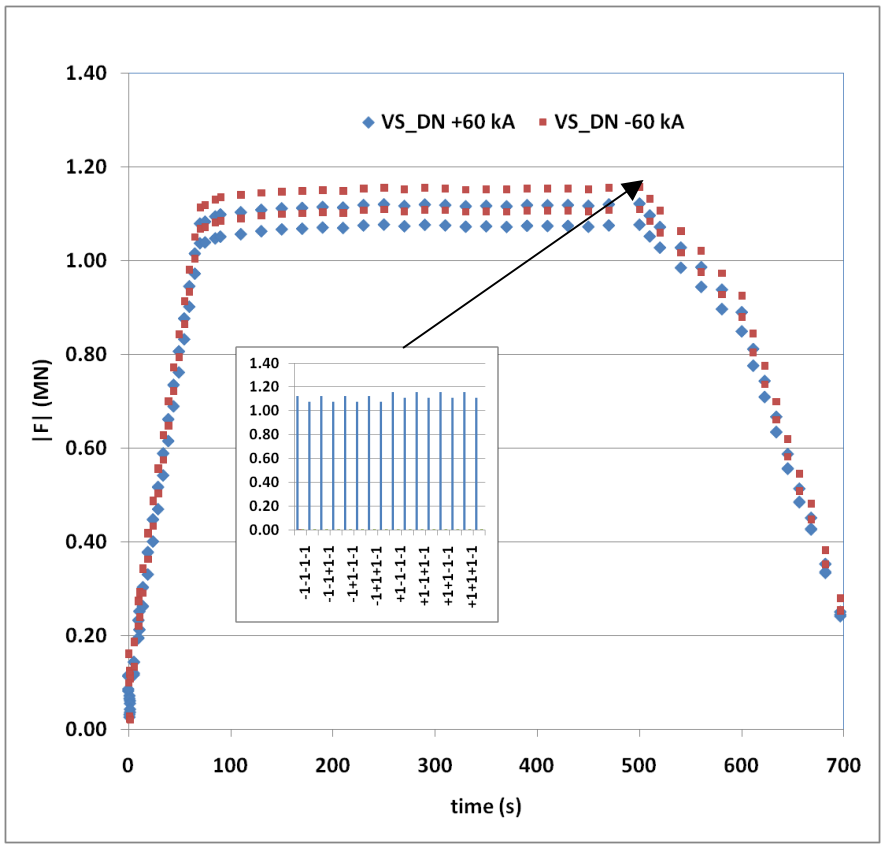

Figure AIII-6 Forces on the VS_DN Coil as a function of time for scenario 2010_03(V2) with 16 variations in sign of the VS and ELMs. Inset shows variation w/ sign of IVC currents at 500 seconds. VS at +60kA (note VS_DN would then carry -60kA as labeled) produces the higher force.

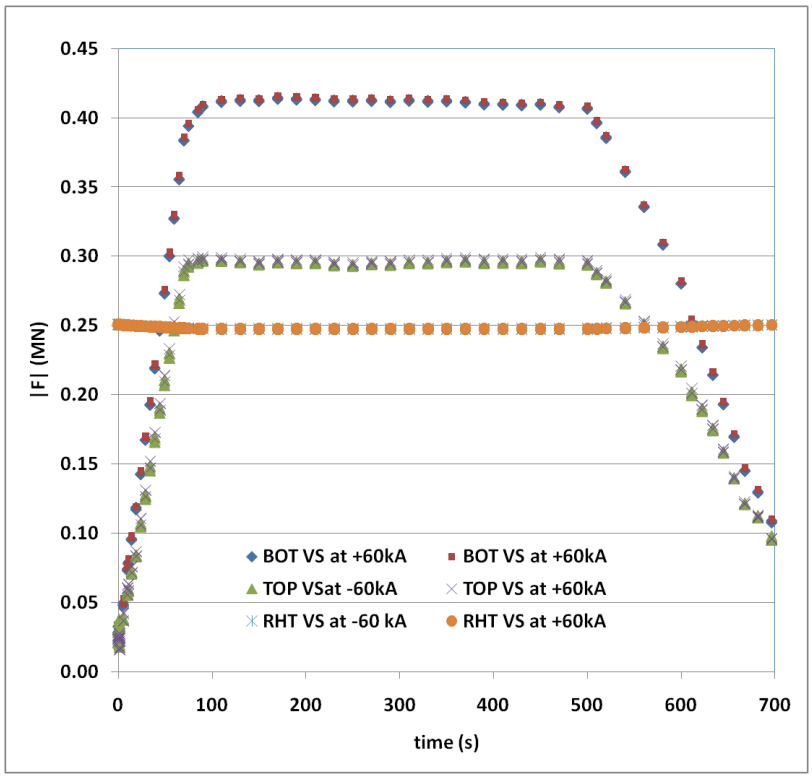

Figure AIII-7 Forces on the ELM_UP Coil as a function of time for scenario 2010_03(V2) with 16 variations in sign of the VS and ELMs. Signs of ELM current do not appreciably impact the magnitudes. VS at +60kA produces a slightly higher force.

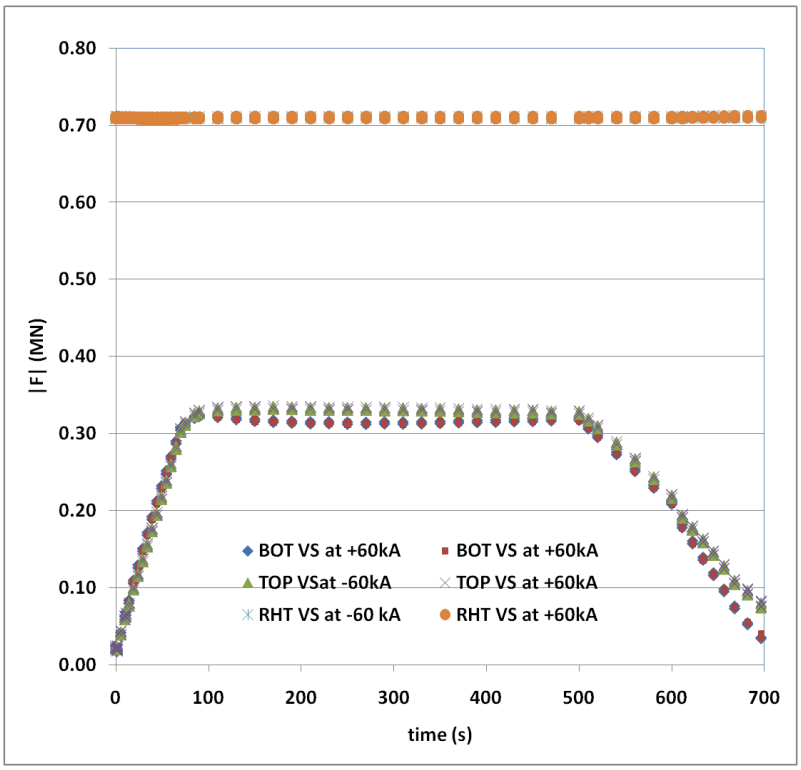

Figure AIII-8 Forces on the ELM_MD Coil as a function of time for scenario 2010_03(V2) with 16 variations in sign of the VS and ELMs. Signs of ELM current do not appreciably impact the magnitudes.

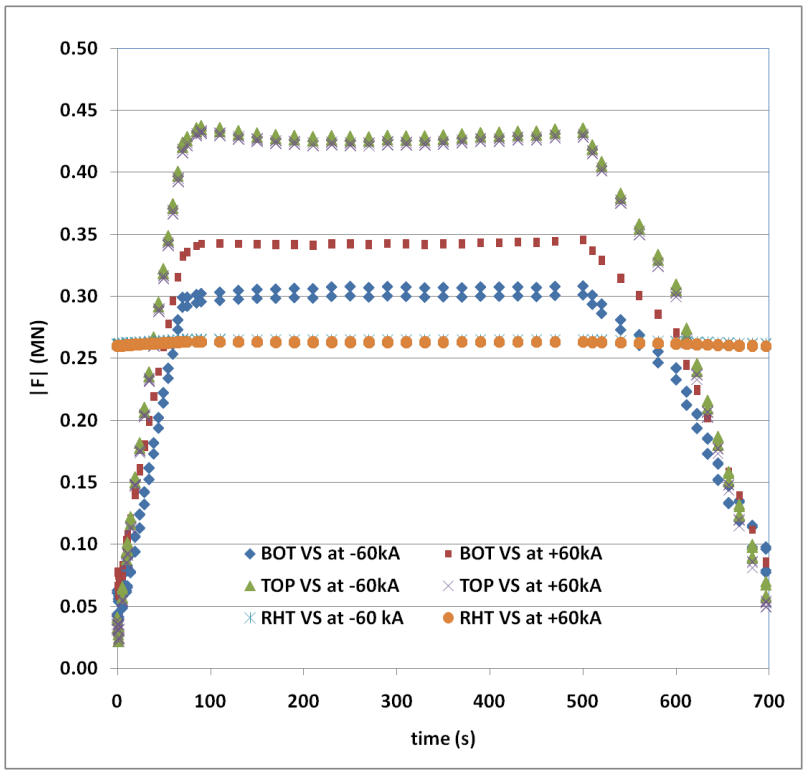

Figure AIII-9 Forces on the ELM_DN Coil as a function of time for scenario 2010_03(V2) with 16 variations in sign of the VS and ELMs. Signs of ELM current do not appreciably impact the magnitudes. VS at +60kA produces a slightly higher force. (N.B. A positive VS current in the plasma current direction in VS_UP but opposite in VS_DN).

FORCES IN LOCAL COORDINATES

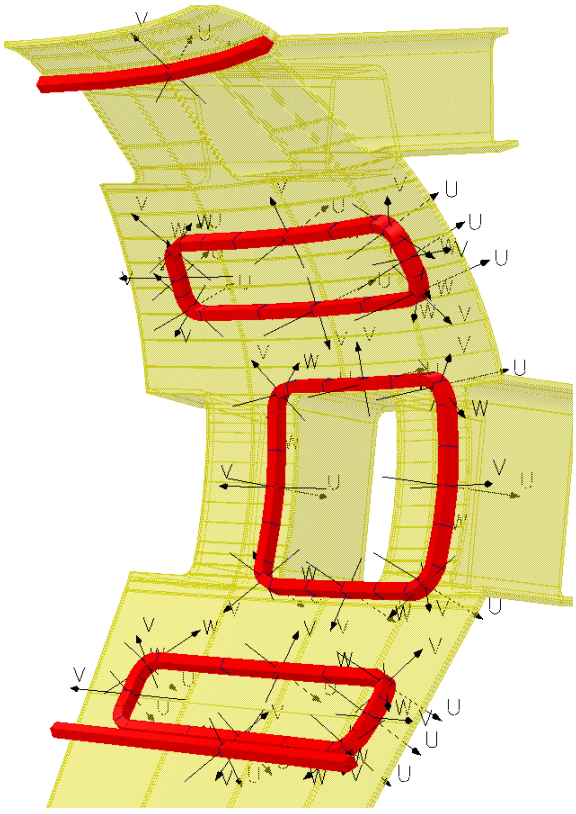

Figure AIII-10 IVC Local Coordinates

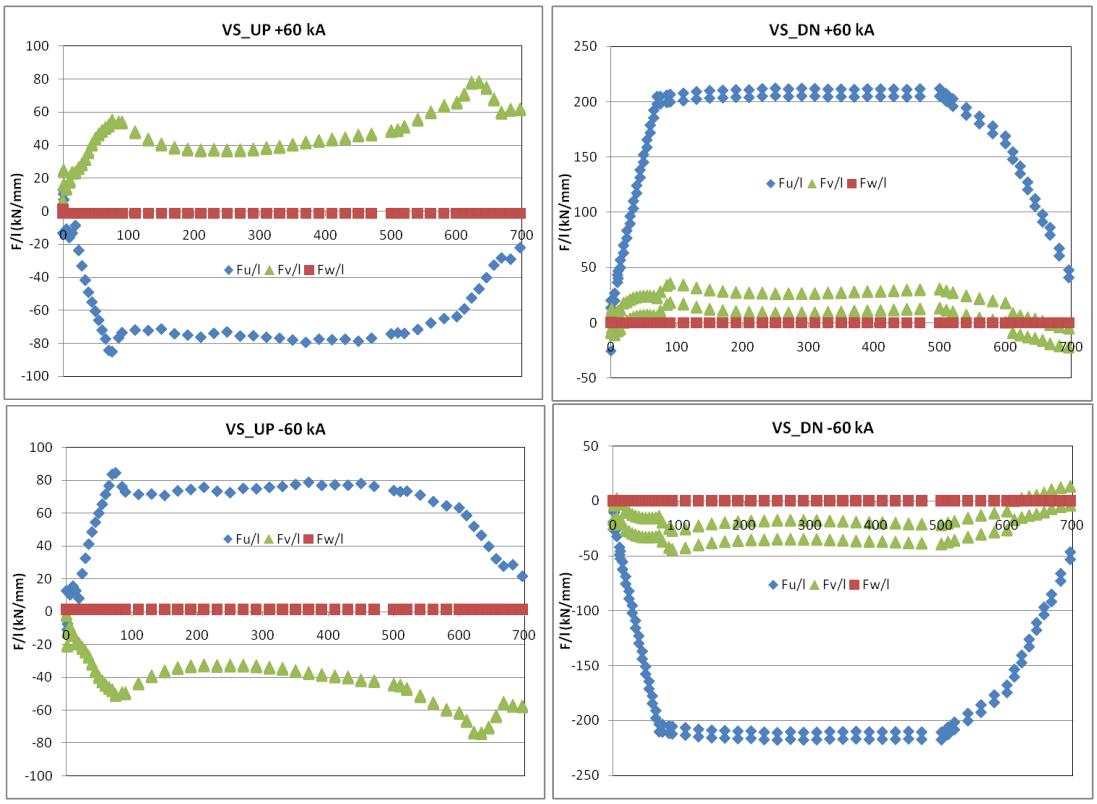

Figure AIII-11 Forces per unit length time running length for the VS coils for scenario 2010_03(V2)

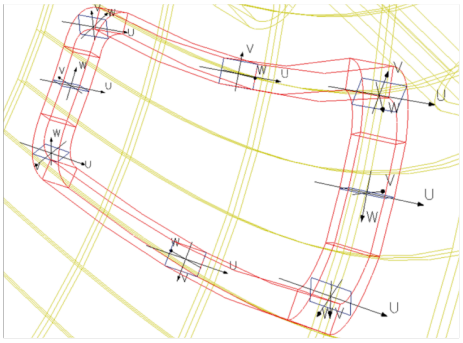

All time points in the scenario (55) and all possible signs of the IVCs (16) are shown

The line represents EOB condition previously reported

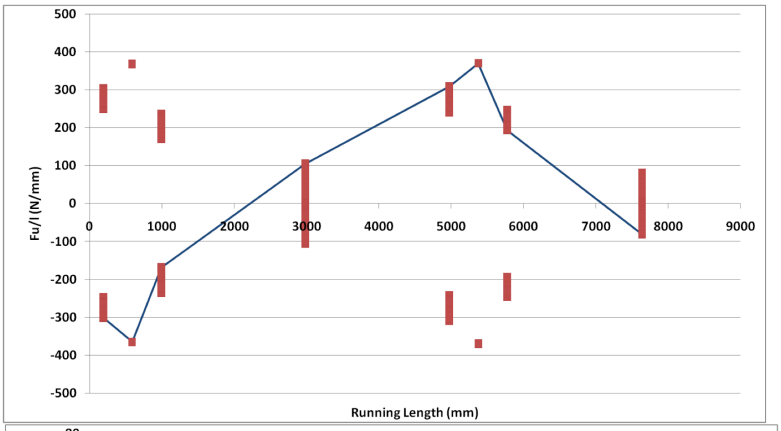

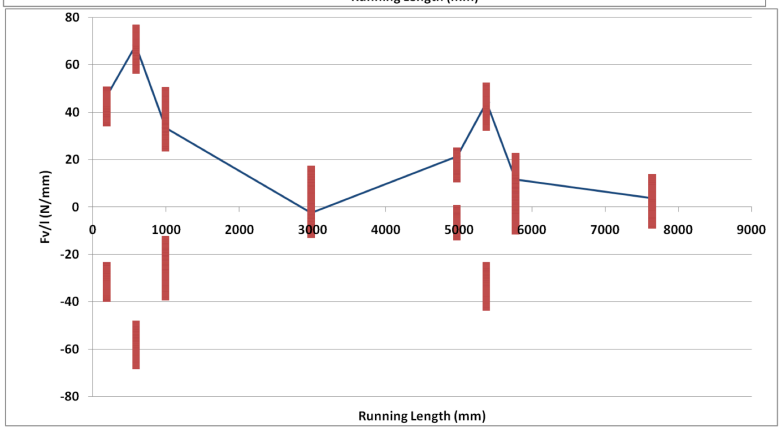

Figure AIII-12 Local force per unit length versus running length of the upper ELM for scenario 2010_03(v2)

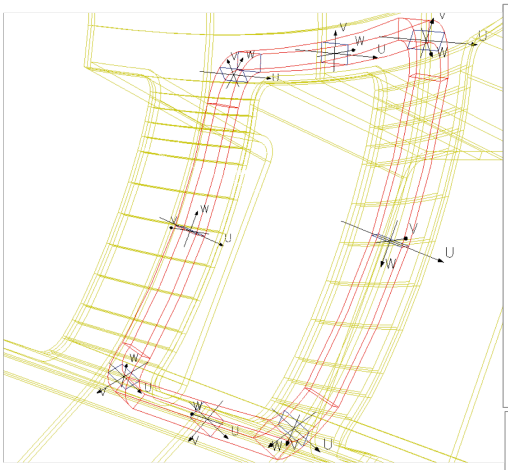

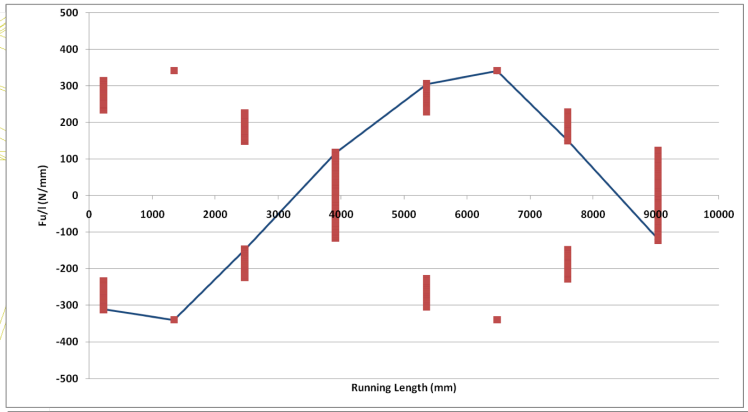

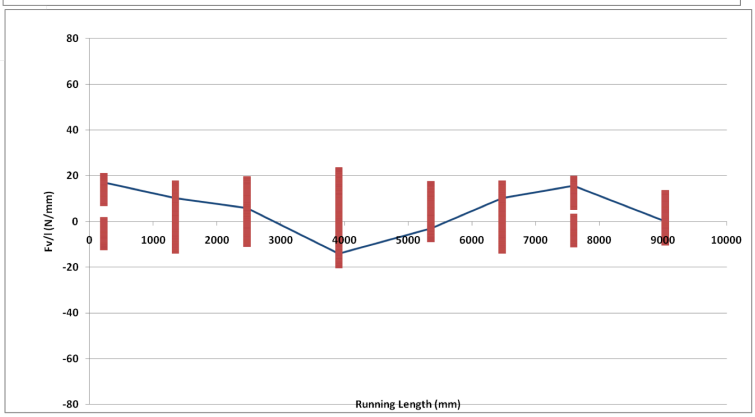

All time points in the scenario (55) and all possible signs of the IVCs (16) are shown

The line represents EOB condition previously reported

Figure AIII-13 Local force per unit length versus running length of the middle ELM for scenario 2010_03(v2)

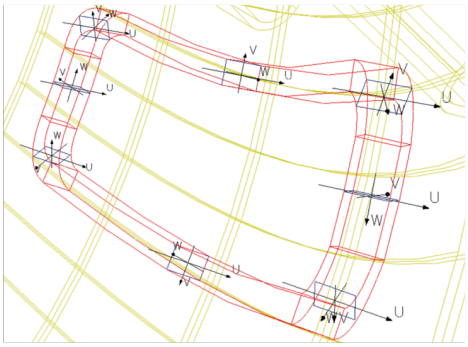

All time points in the scenario (55) and all possible signs of the IVCs (16) are shown

The line represents EOB condition previously reported

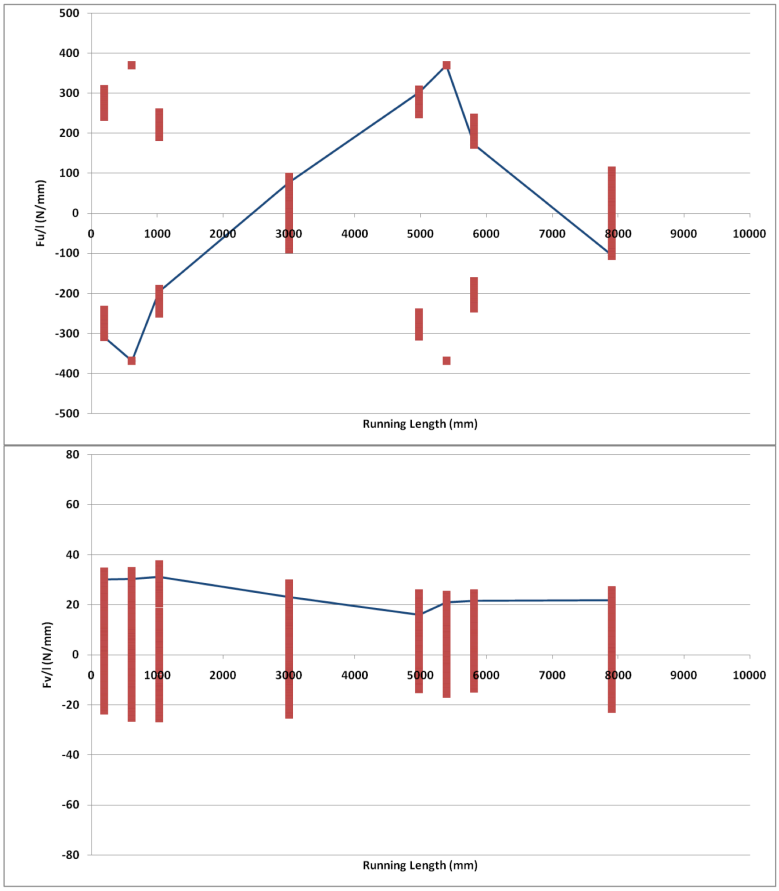

Figure AIII-14 Local force per unit length versus running length of the lower ELM for scenario 2010_03(v2)